TA7
W34
no.CERC-
91-15
v.1

y Corps
ers

LIBRARY
USE ONLY

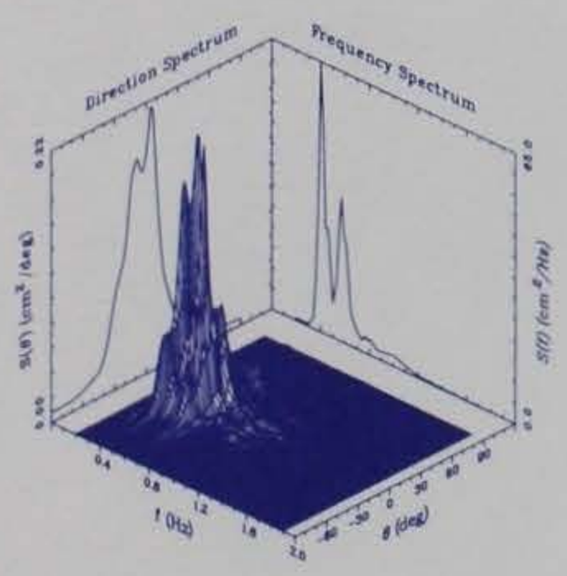

TECHNICAL REPORT CERC-91-15

WAVE TRANSFORMATION OVER A GENERALIZED BEACH

Volume I

MAIN TEXT AND APPENDIX A

by

Michael J. Briggs, Jane M. Smith, Debra R. Green

Coastal Engineering Research Center

DEPARTMENT OF THE ARMY
Waterways Experiment Station, Corps of Engineers
3909 Halls Ferry Road, Vicksburg, Mississippi 39180-6199

US-CE-C PROPERTY OF THE
UNITED STATES GOVERNMENT

September 1991
Final Report

Approved For Public Release; Distribution Unlimited

RESEARCH LIBRARY
US ARMY ENGINEER WATERWAYS
EXPERIMENT STATION
VICKSBURG, MISSISSIPPI

Prepared for DEPARTMENT OF THE ARMY
US Army Corps of Engineers
Washington, DC 20314-1000

Under Nearshore Waves and Currents Work Unit 31762
Laboratory Simulation of Nearshore Waves Work Unit 31672
Wave Estimation for Design Work Unit 31592

Destroy this report when no longer needed. Do not return it to the originator.

The findings in this report are not to be construed as an official Department of the Army position unless so designated by other authorized documents.

The contents of this report are not to be used for advertising, publication, or promotional purposes. Citation of trade names does not constitute an official endorsement or approval of the use of such commercial products.

USACEWES
3 5925 00244 6802

24641501

TA7
W34
no.CERC-91-15

REPORT DOCUMENTATION PAGE

Form Approved V.1
OMB No. 0704-0188

Public reporting burden for this collection of information is estimated to average 1 hour per response, including the time for reviewing instructions, searching existing data sources, gathering and maintaining the data needed, and completing and reviewing the collection of information. Send comments regarding this burden estimate or any other aspect of this collection of information, including suggestions for reducing this burden, to Washington Headquarters Services, Directorate for Information Operations and Reports, 1215 Jefferson Davis Highway, Suite 1204, Arlington, VA 22202-4302, and to the Office of Management and Budget, Paperwork Reduction Project (0704-0188), Washington, DC 20503.

1. AGENCY USE ONLY (Leave blank)	2. REPORT DATE	3. REPORT TYPE AND DATES COVERED
	September 1991	Final report (in 2 vols)

4. TITLE AND SUBTITLE
Wave Transformation Over a Generalized Beach;
Volume I, Main Text and Appendix A

5. FUNDING NUMBERS
WU 31762, 31672,
and 31592

6. AUTHOR(S)
Michael J. Briggs, Jane M. Smith, and Debra R. Green

7. PERFORMING ORGANIZATION NAME(S) AND ADDRESS(ES)
USAE Waterways Experiment Station
Coastal Engineering Research Center
3909 Halls Ferry Road
Vicksburg, MS 39180-6199

8. PERFORMING ORGANIZATION REPORT NUMBER
Technical Report
CERC-91-15

9. SPONSORING/MONITORING AGENCY NAME(S) AND ADDRESS(ES)
US Army Corps of Engineers
Washington, DC 20314-1000

10. SPONSORING/MONITORING AGENCY REPORT NUMBER

11. SUPPLEMENTARY NOTES
Available from National Technical Information Service, 5285 Port Royal Road, Springfield, VA 22161

12a. DISTRIBUTION/AVAILABILITY STATEMENT
Approved for public release; distribution unlimited

12b. DISTRIBUTION CODE

13. ABSTRACT (Maximum 200 words)

A three-dimensional, physical model study of the effects of wave directionality on wave transformation in the nearshore region was recently completed in the directional spectral wave basin. The model consisted of a 1:30 slope beach with plane-parallel contours, similar to the Torrey Pines Beach in southern California. Irregular waves, typical of unimodal and bimodal unidirectional and directional spectra, were created and tested. An array of 20 capacitance wave gages was used to measure surface wave elevations. This array consisted of offshore and nearshore, high-resolution linear arrays to quantify directional distributions and a cross-shore gage array along the center line to study wave transformation. Results are compared with two-dimensional flume test data of similar unidirectional waves and will be used to improve several existing numerical models. The goal of this research is to provide more realistic estimates of nearshore conditions by incorporating the effects of directional distributions in numerical models.

14. SUBJECT TERMS

Directional spectra	Shoaling waves	Wave nonlinearity
Directional spreading	Spectral evolution	Wave spectra
Hydraulic model test	Wave directionality	Wave transformation

15. NUMBER OF PAGES 122

16. PRICE CODE

17. SECURITY CLASSIFICATION OF REPORT	18. SECURITY CLASSIFICATION OF THIS PAGE	19. SECURITY CLASSIFICATION OF ABSTRACT	20. LIMITATION OF ABSTRACT
UNCLASSIFIED	UNCLASSIFIED		

SUMMARY

A three-dimensional, physical model study of the effects of wave directionality on wave transformation in the nearshore region was recently completed in the directional spectral wave basin. The model consisted of a 1:30 slope beach with plane-parallel contours, similar to the Torrey Pines Beach in southern California. Irregular waves, typical of unimodal and bimodal unidirectional and directional spectra, were created and tested. An array of 20 capacitance wave gages was used to measure surface wave elevations. This array consisted of offshore and nearshore, high-resolution linear arrays to quantify directional distributions and a cross-shore gage array along the center line to study wave transformation. Results are compared with two-dimensional flume test data of similar unidirectional waves and will be used to improve several existing numerical models. The goal of this research is to provide more realistic estimates of nearshore conditions by incorporating the effects of directional distributions in numerical models.

This report consists of two volumes: Volume I consisting of the main text and Appendix A and Volume II consisting of Appendices B-I. A limited number of copies of Volume II were published under separate cover. Copies of Volume I are available from the National Technical Information Service, 5285 Port Royal Road, Springfield, VA 22161.

A 3-1/2 min. videotape of each test case was made using a black-and-white, remote-controlled, overhead camera with pan, tilt, and zoom capabilities. Each of the nine, 3/4-in. format video cassettes contains approximately six cases. They are available for viewing and copying.

PREFACE

This report is a product of Work Units 31762, "Nearshore Waves and Currents"; 31672, "Laboratory Simulation of Nearshore Waves"; and 31592, "Wave Estimation for Design," of the Coastal Flooding and Storm Protection Program, Civil Works Research and Development, sponsored by Headquarters, US Army Corps of Engineers (HQUSACE). Testing was conducted from March to May 1989, and data reduction and report preparation were completed in September 1989 at the Coastal Engineering Research Center (CERC), US Army Engineer Waterways Experiment Station (WES). The HQUSACE Technical Monitors for the Coastal Flooding and Storm Protection Program were Messrs. John H. Lockhart, Jr.; John G. Housley; James E. Crews; and Robert H. Campbell. Dr. C. Linwood Vincent was Program Manager at CERC.

This report was prepared by Mr. Michael J. Briggs, Research Hydraulic Engineer; Mrs. Jane M. Smith, Research Hydraulic Engineer; and Mrs. Debra R. Green, Computer Analyst, Wave Processes Branch (WPB), Wave Dynamics Division (WDD), CERC, under the direct supervision of Mr. Douglas G. Outlaw, Chief, WPB, and Dr. Martin C. Miller, Chief, Oceanography Branch, Research Division (RD), CERC. General supervision was provided by Mr. C. E. Chatham, Jr., Chief, WDD; Mr. H. Lee Butler, Chief, RD; Mr. Charles C. Calhoun, Jr., Assistant Chief, CERC; and Dr. James R. Houston, Chief, CERC.

Numerous individuals contributed to the successful completion of this project. Mr. David A. Daily, Electronic Technician in the WES Instrumentation Services Division, maintained the directional spectral wave generator, current meters and wave gages, and associated electronics. Mr. Larry A. Barnes, Civil Engineering Technician, WPB, designed the model and interfaced with the WES shops; Dr. Charles E. Long, Research Scientist, Field Research Facility, CERC, reviewed the draft report and provided many helpful comments.

Commander and Director of WES during publication of this report was COL Larry B. Fulton, EN. Technical Director was Dr. Robert W. Whalin.

CONTENTS

	Page
PREFACE	2
CONVERSION FACTORS, NON-SI TO SI (METRIC) UNITS OF MEASUREMENT	4
PART I: INTRODUCTION	5
Background and Purpose	5
Report Organization	7
PART II: EXPERIMENTAL DESIGN	9
Model Setup	9
Wave Conditions	10
Testing Procedure and Data Analysis	14
PART III: PRELIMINARY TEST RESULTS AND ANALYSIS	22
Basin Circulation Phase	22
Test Duration Phase	22
Signal Calibration Phase	23
PART IV: WAVE TRANSFORMATION RESULTS AND ANALYSIS	35
Time Domain Analysis	35
Frequency Spectral Analysis of Cross-Shore Array	35
Directional Spectral Analysis of Longshore Arrays	42
PART V: SUMMARY AND CONCLUSIONS	50
REFERENCES	58
FIGURES 1-36	
APPENDIX A: NOTATION	A1
APPENDIX B*: TEST DURATION RESULTS	B1
APPENDIX C: MEASURED VERSUS PREDICTED DIRECTIONAL SPECTRA	C1
APPENDIX D: WAVE ELEVATION TIME SERIES	D1
APPENDIX E: ZERO-DOWNCROSSING RESULTS	E1
APPENDIX F: SPECTRAL ANALYSIS RESULTS	F1
APPENDIX G: LINEAR CROSS-SHORE ARRAY SPECTRA	G1
APPENDIX H: SEMILOG CROSS-SHORE ARRAY SPECTRA	H1
APPENDIX I: OFFSHORE AND NEARSHORE ARRAY DIRECTIONAL SPECTRA	I1

* A limited number of copies of Appendices B through I (Volume II) were published under separate cover. Copies are available from the National Technical Information Service, 5285 Port Royal Road, Springfield, VA 22161.

CONVERSION FACTORS, NON-SI TO SI (METRIC)
UNITS OF MEASUREMENT

Non-SI units of measurement used in this report can be converted to SI (metric) units as follows:

Multiply	By	To Obtain
degrees (angle)	0.01745329	radians
feet	0.3048	meters
inches	2.54	centimeters
square feet	0.09290304	square meters

WAVE TRANSFORMATION OVER A GENERALIZED BEACH

PART I: INTRODUCTION

Background and Purpose

1. The transformation of waves in shallow water is dependent on irregularity of the wave field. The wave field is composed of a variety of periods, heights, and directions, but little guidance exists on the combined effects of distribution of energy and direction on wave shoaling, refraction, and breaking. The Generalized Beach Model (GBM) tests were conducted to examine the effects of spectral shape (one or two peaks and relative energy distribution) and directional distribution (mean wave direction and directional spread) on wave transformation under controlled laboratory conditions. The results of these tests will be used to upgrade mathematical wave transformation models for predicting nearshore wave properties from offshore measurements or hindcasts. Accurate nearshore wave predictions are critical for estimating beach evolution and designing coastal structures.

2. The GBM three-dimensional (3-D), physical model study was conducted in the directional spectral wave basin of the US Army Engineer Waterways Experiment Station's (WES's) Coastal Engineering Research Center (CERC). The model consisted of a 1:30 concrete slope with plane, parallel contours. Irregular waves, typical of unimodal (i.e. single peak) and bimodal (i.e. two peaks) unidirectional and directional spectra, were created and tested. An array of 20 capacitance wave gages was used to measure water surface elevations. This array consisted of offshore and nearshore, high-resolution linear gage arrays to quantify directional distributions and a cross-shore gage array along the model center line to study wave transformation.

3. The GBM tests are an extension of flume tests on the shoaling and breaking of bimodal unidirectional wave fields (Smith and Vincent, in press). The flume tests were conducted on a plane, 1:30 slope in an 18-in.*-wide flume at CERC. The frequency spectra simulated in the flume study were reproduced in the GBM tests with added factors of wave direction and directional

---

* A table of factors for converting non-SI units of measurement to SI (metric) units is presented on page 4.

spread. The flume tests showed that during wave decay, wave energy is lost preferentially in the higher frequency mode. The flume results also showed that relative "closeness" and distribution of energy between modes are important. The GBM test results will be used to expand on flume results by including effects of directionality.

4. Elgar and Guza (1985, 1986) reported the results of field tests they conducted at Torrey Pines and Santa Barbara, California. Based on results with bispectral and cross-bispectral analysis, they found nonlinear coupling between frequencies to be a significant mechanism in the shoaling of ocean surface gravity waves. For unimodal, narrow-band spectra, nonlinear quadratic interactions between the peak and its higher frequency harmonics were the mechanism for cross-spectral energy transfers during wave shoaling. These harmonics were phase-coupled, and more of them interacted as the water depth decreased. Initially, the peak interacted with its first harmonic, but as the water got shallower, the harmonics would interact with each other. They saw the same phenomenon for unimodal, broad-banded spectra except that a mode might be involved in a myriad of interactions among a wide range of frequencies, not just harmonic frequencies. For bimodal spectra, they found that the excitation of modes at intermediate frequencies by both sum and difference interactions caused energy to increase in the "valley" between sea and swell peaks (i.e. spectral gap) as the wave traveled into shallower water. After breaking, the distinction between modes was lost, and the spectrum became unimodal in shape. They also found that the low-frequency phenomenon "surf beat," composed of infragravity modes with frequencies less than 0.04 Hz, was being generated by nonlinear coupling between neighboring frequencies within the spectral peak and their difference frequencies. Finally, cross-bispectral analysis showed that low-frequency modes in shallow water were nonlinearly coupled to higher frequency modes seaward of the surf zone. None of these results can be predicted with linear wave theory.

5. Thus, the purpose of this report is to describe the GBM tests and to present preliminary results and analyses. These analyses are not meant to be exhaustive, but rather a preliminary indication of the effects of linear and nonlinear interactions on wave transformation.

Report Organization

6. The report is divided into two volumes. Volume I contains the body of the report, discussion of results for representative cases, and overall summary. Volume II is composed of appendices that contain tabular listings and plots from all other cases.

7. Part II describes the model setup, wave conditions, testing procedure, and data analysis. The 37- by 18-m model consisted of a beach with plane-parallel contours on a 1:30 slope. Twenty capacitance wave gages were arranged in linear offshore (OGA) and nearshore (NGA) gage arrays for measuring directional distribution transformation and a cross-shore array (CGA) for wave transformation. A series of 54 unimodal and bimodal, unidirectional and directional spectra were simulated, iteratively corrected, and tested. Data were analyzed with zero-downcrossing, single-channel frequency spectral, and directional spectral analysis methods.

8. Part III describes test results from the first three preliminary phases: basin circulation, test duration, and signal calibration. In Phase 1, four Marsh McBirney, electromagnetic U-Velocity/V-Velocity (U/V) current meters were located along the basin perimeter to measure the presence of a wave-induced circulation in the basin. Measurements with current meters, dye tracer, and visual observations were all used during this phase. In Phase 2, preliminary tests of the first 12 cases were run to determine the proper sampling duration. Average measurements from the OGA were used to evaluate sample durations of 200 waves at the peak period versus durations of 400 waves. In Phase 3, control signals for each of the 54 wave conditions were iteratively corrected using a transfer function and a system gain factor to ensure reasonable generation of the desired directional spectra. Comparisons of measured OGA and predicted directional wave spectra parameters include peak wave period, zero-moment wave height, frequency spectrum, and directional distribution (composed of mean wave direction and directional spread).

9. Results from Phase 4, the wave transformation phase, are presented and discussed in Part IV. Time domain, single-channel frequency spectra, and directional spectral analyses were performed on the measured data. Time domain analysis results include time series plots of surface elevation for the CGA to illustrate wave profile evolution and tabular listings of zero-downcrossing average surface elevation, peak period, and significant wave height. Spectral analysis results include listings of measured peak wave

periods and zero-moment wave height for all gages, and linear and semilog spectral plots of the CGA illustrating wave transformation. The linear superposition assumption is evaluated based on height and spectral comparisons. Directional spectral analysis includes comparisons of measured directional spectra from the OGA and NGA to quantify effects of directional distribution on wave transformation. Results are presented in the same form as in the signal calibration phase.

10. Finally, Part V contains a summary of results and recommendations for future research and improvements.

11. A 3-1/2-min videotape of each test case was made using a black-and-white remote-controlled, overhead camera with pan, tilt, and zoom capabilities. Each of the nine, 3/4-in. format video cassettes contains approximately six cases. They are available for viewing and copying.

PART II: EXPERIMENTAL DESIGN

Model Setup

Physical model

12. A three-dimensional, physical model of a gently sloping beach with plane, parallel contours (i.e. homogeneous in the longshore direction) was constructed in CERC's directional spectral wave basin. The 1:30 slope physical model, 36.6 by 18.3 m, was patterned after the beach at Torrey Pines (1:40 slope) in southern California. The water depth at the directional spectral wave generator (DSWG) was 50 cm. The toe of the slope was located 4.48 m in front of the DSWG. Figure 1, a schematic of the basin layout, shows the DSWG, instrumentation, coordinate system, and grid locations. The right-hand, global coordinate system origin is located along the face of the DSWG at the beginning of paddle 1.

13. The rear of the basin behind the DSWG was lined with a permeable boundary of wave absorber frames backed by a concrete wall. The basin sides (i.e. slope edges) were lined with these absorber frames and a secondary row of horsehair rolls and were open to adjacent basins. Thus, wave energy was able to propagate away from the test area into the adjacent larger basins with minimal reflections from distant vertical walls.

Instrumentation

14. Instrumentation consisted of four current meters and 20 capacitance wave gages. The current meters (i.e. squares in Figure 1) were used in initial calibration tests to quantify wave-induced circulation within the basin. These meters were designed to measure average tidal velocities rather than wave orbital (i.e. particle) velocities. Thus, the gross circulation patterns produced by the waves were measured. The x- and y-axes of the current meters were aligned with the x- and y-axes of the DSWG. Current meter locations and corresponding water depths are listed in Table 1.

15. Twenty wave gages were arranged in patterns and water depths similar to the deep- and shallow-water arrays used in the field experiment at Torrey Pines in 1978.* The field deep array had lag spacings of 2-3-1-8-10

---

* Personal Communication, September 1989, Dr. Steve Elgar, Professor, Washington State University, Pullman, WA.

with a unit lag of 16 m. The field shallow-water array had lags of 8-1-3-2-5 with a unit lag spacing of 10 m. The model OGA and NGA 8-1-3-2-5 linear arrays (i.e. circles in Figure 1) were located in water depths of 40 and 16 cm, respectively. The OGA was composed of gages 1 to 6, and the NGA consisted og gages 12 to 17.

Table 1

Current Meter Coordinates

Gage No.	X m	Y m	Depth cm
CM1	-2.00	30.00	50.0
CM2	0.00	30.00	50.0
CM3	14.15	30.00	18.0
CM4	14.15	28.00	18.0

Unit lag spacings of 85 and 55 cm were selected for the OGA and NGA arrays, respectively, based on the field dimensions. Pawka (1982, 1983) had showed that the field arrays had a directional resolution of 10 deg for 16-sec waves. Imbedded in the two linear arrays was a CGA along the basin center line to measure wave transformation in spectral shape, wave period, and wave height. It was composed of the 10 gages: 4, 7 to 11, 15, and 18 to 20. Table 2 lists gage coordinates and corresponding water depths.

Wave Conditions

16. Unidirectional and directional wave spectra with a range of spectral parameters were selected for study and comparison. Both unimodal (i.e. single peak) and bimodal (i.e. double peak) frequency spectra were combined with different directional distributions. The unidirectional spectra were similar to earlier flume tests conducted by Smith and Vincent (in press).

17. Fifty-four wave conditions were organized in four groups consisting of (a) Unimodal, (b) Superposition, (c) Directional, and (d) Nonbreaking Series. Descriptions of these groups are given in the following paragraphs. Table 3 lists the target peak periods, significant wave heights, overall mean

Table 2

Capacitance Gage Coordinates

Gage No.	X m	Y m	Depth cm
C1	7.48	5.22	40.0
C2	7.48	9.47	40.0
C3	7.48	11.17	40.0
C4	7.48	13.72	40.0
C5	7.48	14.57	40.0
C6	7.48	21.37	40.0
C7	8.68	13.72	36.0
C8	10.68	13.72	29.3
C9	11.68	13.72	25.9
C10	12.68	13.72	22.6
C11	13.68	13.72	19.2
C12	14.68	8.22	16.0
C13	14.68	10.97	16.0
C14	14.68	12.07	16.0
C15	14.68	13.72	16.0
C16	14.68	14.27	16.0
C17	14.68	18.67	16.0
C18	15.68	13.72	12.8
C19	16.18	13.72	11.0
C20	16.68	13.72	9.4

wave directions (i.e. peak wave direction), and directional spreads* (i.e. full width at half power) for each wave case. Wave parameters for the unimodal cases are listed under the column with the "1" heading and under columns labeled "1" and "2" for the bimodal cases.

18. In the first group, the Unimodal Series, 12 broad-banded (i.e. spectral peakedness parameter $\gamma = 3.3$)** directional spectra were created to test the effect of wave directionality. Target peak periods $T_p = 1.25$ or 2.50 sec were selected. A significant wave height $H_{m0} = 15.2$ cm was used for the six $T_p = 2.50$ sec cases. This wave height was reduced by 20 percent to $H_{m0} = 12.2$ cm for the six $T_p = 1.25$ sec cases to prevent excessive wave breaking at the DSWG. Directional distributions consisted of combinations of

* The recommendations of the International Association of Hydraulic Research (IAHR) Working Group on Wave Generation and Analysis (1986) "List of Sea State Parameters" were followed wherever possible.

** For convenience, symbols and abbreviations are listed in the Notation (Appendix A).

Table 3

Target Directional Spectral Wave Parameters

Case ID	Period sec		Height cm		Direction deg		Spread deg	
	1	2	1	2	1	2	1	2
Unimodal Series								
S01	2.50	-	15.2	-	0.0	-	0.0	-
S09	2.50	-	15.2	-	0.0	-	40.0	-
S13	2.50	-	15.2	-	10.0	-	0.0	-
S21	2.50	-	15.2	-	10.0	-	40.0	-
S25	2.50	-	15.2	-	20.0	-	0.0	-
S33	2.50	-	15.2	-	20.0	-	40.0	-
S37	1.25	-	12.2	-	0.0	-	0.0	-
S45	1.25	-	12.2	-	0.0	-	40.0	-
S49	1.25	-	12.2	-	10.0	-	0.0	-
S57	1.25	-	12.2	-	10.0	-	40.0	-
S61	1.25	-	12.2	-	20.0	-	0.0	-
S69	1.25	-	12.2	-	20.0	-	40.0	-
Superposition Series								
D01	2.50	-	7.6	-	0.0	-	0.0	-
D02	1.75	-	13.2	-	0.0	-	0.0	-
D03	2.50	1.75	7.6	13.2	0.0	0.0	0.0	0.0
D04	2.50	-	10.8	-	0.0	-	0.0	-
D05	1.75	-	10.8	-	0.0	-	0.0	-
D06	2.50	1.75	10.8	10.8	0.0	0.0	0.0	0.0
D07	2.50	-	13.2	-	0.0	-	0.0	-
D08	1.75	-	7.6	-	0.0	-	0.0	-
D09	2.50	1.75	13.2	7.6	0.0	0.0	0.0	0.0
Directional Series								
D13	2.50	1.75	7.6	13.2	0.0	0.0	40.0	40.0
D16	2.50	1.75	10.8	10.8	0.0	0.0	40.0	40.0
D19	2.50	1.75	13.2	7.6	0.0	0.0	40.0	40.0
D23	2.50	1.75	7.6	13.2	0.0	0.0	20.0	40.0
D26	2.50	1.75	10.8	10.8	0.0	0.0	20.0	40.0
D29	2.50	1.75	13.2	7.6	0.0	0.0	20.0	40.0
D33	2.50	1.75	7.6	13.2	20.0	20.0	0.0	0.0
D36	2.50	1.75	10.8	10.8	20.0	20.0	0.0	0.0
D39	2.50	1.75	13.2	7.6	20.0	20.0	0.0	0.0
D43	2.50	1.75	7.6	13.2	20.0	20.0	40.0	40.0
D46	2.50	1.75	10.8	10.8	20.0	20.0	40.0	40.0
D49	2.50	1.75	13.2	7.6	20.0	20.0	40.0	40.0
D51	2.50	1.75	10.8	10.8	0.0	20.0	0.0	0.0
D52	2.50	1.75	10.8	10.8	0.0	20.0	40.0	40.0
D53	2.50	1.75	10.8	10.8	0.0	20.0	20.0	40.0
D61	2.50	1.25	10.8	10.8	0.0	0.0	0.0	0.0
D62	2.50	1.25	10.8	10.8	0.0	0.0	40.0	40.0
D63	2.50	1.25	10.8	10.8	20.0	20.0	0.0	0.0
D64	2.50	1.25	10.8	10.8	20.0	20.0	40.0	40.0
D65	2.50	1.25	10.8	10.8	0.0	20.0	0.0	0.0
D66	2.50	1.25	10.8	10.8	0.0	20.0	40.0	40.0
D67	2.50	1.25	10.8	10.8	0.0	20.0	20.0	40.0
D68	2.50	1.25	10.8	10.8	20.0	0.0	20.0	40.0
Nonbreaking Series								
D71	2.50	1.75	6.5	6.5	0.0	20.0	0.0	0.0
D72	2.50	1.75	6.5	6.5	0.0	20.0	40.0	40.0
D73	2.50	1.75	6.5	6.5	0.0	20.0	20.0	40.0
D81	2.50	1.25	6.5	6.5	0.0	0.0	0.0	0.0
D82	2.50	1.25	6.5	6.5	0.0	0.0	40.0	40.0
D83	2.50	1.25	6.5	6.5	20.0	20.0	0.0	0.0
D84	2.50	1.25	6.5	6.5	20.0	20.0	40.0	40.0
D85	2.50	1.25	6.5	6.5	0.0	20.0	0.0	0.0
D86	2.50	1.25	6.5	6.5	0.0	20.0	40.0	40.0
D87	2.50	1.25	6.5	6.5	0.0	20.0	20.0	40.0

Notes:
(1) Texel Marsden Arsloe (TMA) γ = 3.30 for Unimodal Series cases
TMA γ = 20.0 for all other cases
(2) TMA σ_α = 0.07 for all cases
TMA σ_β = 0.07 for bimodal modes with T_p = 2.50 sec
= 0.09 for unimodal and other bimodal modes
(3) Water depth = 50 cm

overall mean wave direction $\bar{\theta} = 0$ (i.e. normal incidence), 10, and 20 deg and full-width directional spreading $\sigma_m = 0$ (i.e. unidirectional) and 40 deg. Wave angle is the direction towards which the waves travel, with positive angles measured clockwise from the positive x-axis.

19. The second group, the Superposition Series, consisted of nine cases: three bimodal and six unimodal unidirectional spectra. Modal superposition was used to create the bimodal cases from two narrow (i.e. $\gamma = 20$) unimodal frequency spectra. For the bimodal cases, first mode (i.e. low-frequency) peak period $T_{p,1} = 2.5$ sec and second mode (i.e. high-frequency) peak period $T_{p,2} = 1.75$ sec were combined. The total energy in the bimodal spectra was adjusted to give a target wave height $H_{m0} = 15.2$ cm. The energy distribution was adjusted so that the ratio of energy in the two modes was 1/3:2/3, 1/2:1/2, or 2/3:1/3 corresponding to $H_{m0,1}:H_{m0,2} = 7.6:13.2$ cm, 10.8:10.8 cm, or 13.2:7.6 cm, respectively. Equivalent unimodal spectra, with $T_p = 2.5$ or 1.75 sec, were created for each of the six modes represented by these energy combinations. By comparing the sum of results from the two unimodal spectra to their equivalent bimodal spectra, the appropriateness of linear superposition of unimodal results and the effect of energy distribution and wave/wave interactions among the modes can be ascertained.

20. The third group or Directional Series consisted of 23 bimodal unidirectional and directional spectra to investigate the effect of wave directionality on wave transformation. All cases were narrow-banded ($\gamma = 20$) with target $H_{m0} = 15.2$ cm. In the first 15 cases (D13 to D53 in Table 3), modes with $T_{p,1} = 2.50$ sec and $T_{p,2} = 1.75$ sec were specified. Modal energy ratios of 1/3:2/3, 1/2:1/2, and 2/3:1/3 were used. The directional distributions were composed of different combinations of $\bar{\theta}$ (0 and 20 deg) and σ_m (0, 20, and 40 deg). In the last 8 cases (D61 to D68), $T_{p,1}$ was left unchanged and $T_{p,2} = 1.25$ sec to increase the frequency spreading between modes. In the last 11 cases (D51 to D68), equal energy distribution between modes (i.e. $H_{m0,1} = H_{m0,2} = 10.8$ cm) was specified. The same directional distribution combinations were selected in these cases. In 16 cases (D13 to D49 and D61 to D64), the same $\bar{\theta}$ or σ_m was used for both modes. Different directional parameters were selected for the remaining 7 cases (D51 to D53 and D65 to D68).

21. The final group, the Nonbreaking Series, consisted of 10 cases with reduced wave height to eliminate wave breaking outside the surf zone. For these 10 cases, the Directional Series cases D51 to D67 were repeated with

target $H_{m0,1} = H_{m0,2} = 6.5$ cm by using a gain factor of 60 percent. All other wave parameters remained unchanged.

Testing Procedure and Data Analysis

22. In this section, a description of the control signal simulation and generation, data collection, and data analyses are given.

Control signal simulation and generation

23. The 54 wave conditions were converted into control signals for each of the 61 paddles using a frequency domain, double summation, deterministic amplitude, random phase model (Briggs, Borgman, and Outlaw 1987). The directional spectra were simulated as the product of a TMA frequency spectra $S_{TMA}(f)$ and a wrapped normal directional spreading function $D(f,\Theta)$. The $S_{TMA}(f)$ was calculated at 30 discrete frequencies, selected to give good resolution about the modal peak frequency f_p. Similarly, 30 discrete directions were selected about $\bar{\Theta}$ to give good resolution. Uneven frequency and direction increments were used to define the spectral energy about the peaks more accurately. Full-width directional spread $\sigma_m = 0$, 20, and 40 deg were selected as a representative range. Equivalent wrapped normal directional spread $\sigma_m = 1$, 16.3, and 31.2 deg were used in the simulation (Jane M. Smith, unpublished data, March 1989).

24. The Digital/Analog (D/A) rate for the DSWG is 20 Hz, corresponding to a time increment $\Delta t = 0.05$ sec. Typically, a time series duration $T_r = 750$ sec (i.e. 15,000 points) was created for each paddle. After Fourier transformation in the frequency domain, this signal duration corresponds to an evenly spaced frequency increment $\Delta f = 0.00133$ Hz, or 1,464 frequencies between the lower and upper cutoff frequencies $f_l = 0.05$ and $f_u = 2.00$ Hz, respectively. A longer time series with $T_r = 1{,}500$ sec (i.e. 30,000 points) was created for the six unimodal cases with $T_p = 2.5$ sec. The frequency increment corresponds to $\Delta f = 0.000667$ Hz, or 2,926 frequencies between f_l and f_u.

Data collection

25. Gage and water depth calibration, data sampling, and control signal correction are discussed in the following paragraphs.

26. Gage and water depth calibration. Four Marsh McBirney current meters were borrowed from the WES Hydraulics Laboratory; these had been calibrated in previous tests. Depth of immersion of the current meter sphere was

8.9 cm, ample to measure average surface currents. This distance corresponds to the distance between the center line of the sphere and the change in diameter of the stinger or support rod.

27. The capacitance wave gages had 30.5- or 45.7-cm-long measurement rods, depending on local water depth. They were calibrated each day with the computer-controlled process IDCAL, which incorporates an 11-step procedure using a quadratic least squares fit. Table 4 lists the rod length and calibration range for each of the 20 gages. Individual gage rod lengths and calibration ranges were selected to adequately measure anticipated wave heights in a particular water depth. Generally, measurement accuracy is greater for shorter calibration ranges. Table 5 lists the percentage of full-scale errors for each gage and date based on the calibration ranges in Table 4.

Table 4

Gage Calibration Data

Gage No.	Rod Length cm	Cal Range cm
C1	45.72	25.40
C2	45.72	25.40
C3	45.72	25.40
C4	45.72	25.40
C5	45.72	25.40
C6	45.72	25.40
C7	45.72	25.40
C8	45.72	25.40
C9	45.72	21.59
C10	45.72	20.32
C11	30.48	16.51
C12	30.48	11.43
C13	30.48	12.70
C14	30.48	12.70
C15	30.48	11.43
C16	30.48	13.97
C17	30.48	11.43
C18	30.48	10.16
C19	30.48	8.89
C20	30.48	7.62

28. The water depth was maintained within $\pm$0.031 cm of the desired level by an automatic water level float control system.

29. Data sampling. Data were collected in four phases: basin circulation, test duration, signal calibration, and wave transformation. Table 6

Table 5

Calibration Error as Percentage of Full Scale for Capacitance Wave Gages

		Gage Number																					
No.	Date	C01 %	C02 %	C03 %	C04 %	C05 %	C06 %	C07 %	C08 %	C09 %	C10 %	C11 %	C12 %	C13 %	C14 %	C15 %	C16 %	C17 %	C18 %	C19 %	C20 %	Min %	Max %	Avg %
1	3/22/89	0.33	0.21	0.09	0.65	0.58	0.15	0.08	0.19	0.51	0.26	0.28	0.75	0.68	0.49	0.65	1.32	0.93	0.57	0.39	0.30	0.08	1.32	0.47
2	3/23/89	0.29	0.65	0.11	0.41	0.22	0.15	0.06	0.25	0.89	0.30	0.18	0.68	0.66	0.49	0.59	1.32	1.33	0.47	0.53	0.27	0.06	1.33	0.49
3	3/24/89	0.22	0.80	0.20	0.23	0.26	0.20	0.09	0.30	0.25	0.33	0.29	0.54	0.86	0.21	0.28	0.80	1.25	0.75	0.38	0.42	0.09	1.25	0.43
4	3/29/89	0.26	0.16	0.10	0.27	0.12	0.10	0.13	0.27	0.81	0.27	0.39	0.62	0.80	0.29	0.39	0.60	0.97	0.70	0.49	0.34	0.10	0.97	0.40
5	4/20/89	0.20	0.16	0.08	0.15	0.12	0.10	0.11	0.46	0.43	0.30	0.54	0.62	0.62	0.31	0.34	0.80	1.09	0.77	0.42	0.55	0.08	1.09	0.41
6	4/21/89	0.29	0.15	0.17	0.13	0.13	0.18	0.08	0.82	0.48	0.29	0.27	0.97	0.72	0.27	0.41	0.73	0.90	0.61	0.28	0.48	0.08	0.97	0.42
7	4/23/89	0.23	0.17	0.14	0.11	0.14	0.14	0.08	0.95	0.58	0.26	0.16	1.16	0.39	0.20	0.27	0.71	1.04	0.72	0.62	0.73	0.08	1.16	0.44
8	5/5/89	0.32	0.55	0.15	0.18	0.16	0.14	0.13	0.68	0.23	0.28	0.31	0.75	0.55	0.37	0.36	0.85	0.80	0.79	0.43	0.28	0.13	0.85	0.41
9	5/17/89	0.22	0.73	0.15	0.14	0.13	0.14	0.13	1.06	0.17	0.37	0.56	0.51	0.56	0.15	0.21	0.87	1.19	0.73	0.43	0.73	0.13	1.19	0.46
10	5/18/89	0.34	0.75	0.13	0.16	0.17	0.21	0.20	0.52	0.27	0.28	0.37	0.53	0.59	0.20	0.40	0.94	0.64	0.72	0.47	0.34	0.13	0.94	0.41
11	5/18/89	0.38	0.71	0.12	0.14	0.13	0.19	0.15	0.92	0.17	0.34	0.26	0.69	0.70	0.23	0.29	1.02	0.68	0.67	0.56	0.54	0.12	1.02	0.44
12	5/19/89	0.28	0.79	0.18	0.17	0.12	0.22	0.14	0.84	0.21	0.39	0.45	0.44	0.58	0.21	0.34	0.92	0.70	0.70	0.50	0.49	0.12	0.92	0.43
13	5/22/89	0.37	0.94	0.17	0.18	0.13	0.15	0.16	0.64	0.23	0.38	0.29	0.52	0.52	0.22	0.15	0.91	1.02	0.85	0.41	0.70	0.13	1.02	0.45
14	5/23/89	0.30	0.87	0.11	0.18	0.12	0.16	0.18	0.66	0.22	0.32	0.26	0.67	0.60	0.29	0.32	0.98	1.14	0.95	0.46	0.96	0.11	1.14	0.49
15	5/30/89	0.31	0.21	0.17	0.19	0.10	0.12	0.15	0.92	0.32	0.36	0.13	0.47	1.20	0.21	0.28	1.10	1.03	0.90	0.40	1.48	0.10	1.48	0.50
16	5/31/89	0.30	0.15	0.14	0.14	0.14	0.16	0.12	1.10	0.26	0.33	0.18	0.49	0.49	0.31	0.26	1.37	0.59	1.04	0.29	1.10	0.12	1.37	0.45
17	5/31/89	0.29	0.28	0.88	0.15	0.20	0.26	0.20	0.85	0.33	0.43	0.41	0.52	0.81	0.34	0.76	1.05	1.05	1.00	0.53	1.08	0.15	1.08	0.57
18	6/1/89	0.35	0.19	0.15	0.18	0.26	0.23	0.10	0.51	0.13	0.40	0.17	0.39	0.54	0.07	0.30	0.84	1.01	0.69	0.43	0.67	0.07	1.01	0.38
19	6/2/89	0.32	0.17	0.17	0.22	0.07	0.16	0.15	0.44	0.19	0.37	0.38	0.44	0.67	0.26	0.17	0.99	0.70	0.95	0.44	0.52	0.07	0.99	0.39
20	6/5/89	0.25	0.13	0.16	0.29	0.13	0.18	0.15	0.40	0.21	0.39	0.40	0.58	0.60	0.23	0.47	1.06	1.08	1.00	0.39	1.21	0.13	1.21	0.46
	Averages:	0.29	0.44	0.18	0.21	0.17	0.17	0.13	0.64	0.35	0.33	0.31	0.62	0.66	0.27	0.36	0.96	0.96	0.78	0.44	0.66	0.10	1.12	0.45

Table 6

Data Collection Parameters

Peak Period sec	Record Length sec	No. Points Record	Test Duration sec	Gain Factor Range
		Basin Circulation Phase		
2.50	1,200	12,000	1,260	1.0
1.25	600	6,000	660	1.0
		Test Duration Phase		
2.50	1,200	12,000	1,260	1.0
1.25	600	6,000	660	0.8-0.95
		Signal Calibration Phase		
2.50	650	6,500	700	0.93-1.0
1.25	350	3,500	400	0.8
		Wave Transformation Phase		
2.50	650	6,500	700	0.97-1.3
1.25	350	3,500	400	0.8

Note: S37 in Test Duration Phase had Gain = 0.60.

lists the data collection parameters for these four phases based on the peak period of the first mode. Parameters listed include record length of data collected, corresponding number of points collected in a record, test duration, and system gain factor range. Except for the gain factor range, values for the first two and last two phases were the same.

30. Experiments were conducted by starting the 9T magnetic tape containing the control signal and waiting 10 sec (timed by a stopwatch) to allow a common starting point for repeat tests. The DSWG was not actually making waves until this instant in time. Then, a 10-sec hardware ramp was automatically activated on the control signal to prevent damage to the DSWG. After the completion of this ramp at the beginning of the control signal (i.e. total delay of 20 sec), current meters or wave gages were sampled at 10 Hz (i.e. time increment $\Delta t = 0.10$ sec). The first pure (i.e. nonramped) wavelets reached the farthest gage 20 approximately 20 sec later. The first point in the data analysis was 100 sec into the records (see below).

31. Control signal correction. In Phase 3, the control signals were iteratively corrected using a response amplitude operator (RAO) transfer

function to compensate for observed variations in period, height, and spectral shape. The RAO is calculated in the frequency domain as the ratio of the average frequency spectral shape of the OGA to the target spectral shape. Calculated RAO values outside f_l and f_u cutoff frequencies were set to 1.0 because of low signal-to-noise ratios. Also, RAO's greater than 100.0 or less than 0.01 were set to these respective upper and lower limit values. Once the RAO is calculated, control signals are Fourier transformed to the frequency domain, divided by the appropriate RAO at each frequency, and then transformed back to the time domain to form the corrected control signal. Although the effect of RAO corrections on directional distributions have not been quantified, results with another physical model data set for the Yaquina Bay, Oregon, north jetty (Carver, Briggs, and Green, in preparation) produced a better match of the target distribution.

32. The DSWG has specified limits on displacement, velocity, and acceleration of the individual paddles. While attempting to produce large wave heights, these limit values were often exceeded in the control signals. Prior to running the tests, the control signals were checked for exceedance of these paddle limits and corrected if necessary. Typical locations of these exceedances were at the peaks and troughs (and corresponding positive and negative flanks) of large waves. The procedure consisted of rounding these peaks or troughs to lower values within the thresholds. If a value exceeded the threshold, a new value equal to half the distance between the threshold and the previous value was substituted. This procedure was used on successive steps until the exceedance was remedied. Because the threshold values are based on a displacement less than the maximum, the procedure usually converged after one or two iterations.

33. Although this procedure worked fairly well, the feedback sensors for some of the DSWG paddles (i.e. paddle 37) would shut them down after several minutes into a high energy case. Thus, it was necessary to reduce the entire signal by a small amount to complete the test. Gain factors were input at run time to control the amplitude of the control signal. The ideal gain has a value of "1.0," corresponding to 100 percent of the desired amplitude. The gain was successively reduced in increments of 0.01 (i.e. 0.99, 0.98, 0.97, etc.) until the control signal ran for the entire test duration. Table 6 lists the range of gain factors used to correct the control signals. Thus, stroke limitations of the DSWG played an important part in the signal generation.

Data analyses

34. Data analyses consisted of time domain zero-downcrossing, single-channel frequency spectra, and directional wave spectra. The Wave Dynamics Division TSAF22 package* was used for the first two and the program NUSPECGBM for the latter.

35. Zero-downcrossing analysis. Standard methods of zero-downcrossing analysis, as specified by the IAHR (1986), are incorporated in the TSAF22 software. Average surface elevation η, significant wave period $T_{H1/3,d}$, and significant wave height $H_{1/3,d}$ were calculated.

36. Single-channel frequency spectral analysis. For spectral analysis, data records were zero-meaned (quadratic trend removed for cases in Phase 1 only), tapered by a 10-percent cosine bell window, Fourier transformed, and band averaged between $f_l = 0.01$ Hz and $f_u = 2.50$ Hz. Table 7 lists the spectral analysis parameters for the four test phases. Included in the table are number of points in a record (NTIME), record length (T_r) in seconds, Δf in Hertzs, resolution bandwidth B_e in Hertzs, number of frequencies analyzed between f_l and f_u, number of smoothed frequencies in each band, and degrees of freedom υ. The first point analyzed in each record was 1,001 for all cases. To facilitate comparison of data in Phase 4, the number of spectral bands averaged was based on achieving the same $B_e = 0.024$ Hz in the flume tests.

37. Directional spectral analysis. A Fourier series expansion of the directional spectrum is used to estimate $S(f,\theta)$. This method is based on the relation that the autospectra and cross-spectra between all pairs of wave elevation time series can be expressed as a linear combination of the directional components of $S(f,\theta)$ at that frequency (Briggs 1988). The $S(f,\theta)$ is parameterized as the product of a frequency spectrum and a directional spreading function. The autospectral density $S_{ii}(f)$ for each of N gages is estimated, and a combined best estimate $S(f)$ is obtained using a harmonic mean. The directional spreading function is initially approximated by a truncated Fourier series expansion of L harmonics.

---

* Charles E. Long, 1986, "Laboratory Wave Generation and Analysis: An Instructional Report for Unidirectional Wave Generation and Analysis," unpublished report, US Army Engineer Waterways Experiment Station, Vicksburg, MS.

Table 7

Analysis Parameters

T_p sec	NTIME	T_r sec	Δf Hz	B_e Hz	No. Frequencies Anal.	No. Frequencies Smooth	ν
			Basin Circulation				
2.50	10,000	1,000	0.001	0.050	2,490	50	100
1.25	5,000	500	0.002	0.050	1,245	25	50
			Test Duration				
2.50	10,000	1,000	0.001	0.050	2,490	50	100
	5,000	500	0.002	0.050	1,245	25	50
1.25	5,000	500	0.002	0.050	1,245	25	50
	2,500	250	0.004	0.052	622	13	26
			Signal Calibration Phase				
2.50	5,000	500	0.002	0.050	1,245	25	50
1.25	2,500	250	0.004	0.052	622	13	26
			Wave Transformation				
2.50	5,000	500	0.002	0.024	1,245	12	24
1.25	2,500	250	0.004	0.024	622	6	12

Note: Same parameters used for T_p = 2.50 sec cases were used for three unimodal cases in Superposition Series with T_p = 1.75 sec.

38. The first step is to calculate measured autospectral and cross-spectral density estimates for each gage and each gage pair, respectively. The data are zero-meaned, tapered by a 10-percent cosine bell window, Fourier transformed using a "235" Fast Fourier Transform. Then a Gaussian smoothing function is used to smooth the estimates with an effective width of 0.024 Hz between the same f_l and f_u used for the single-channel spectral analysis. The equivalent number of Gaussian smoothed frequencies corresponding to T_p = 2.5 and 1.25 sec are 28 and 14, respectively.

39. The significant wave height H_σ is equal to 4 times the standard deviation of the time series of surface wave elevation σ_η. An average for the number of gages used to calculate the directional spectrum is calculated.

40. For N gages, a set of N^2 simultaneous linear equations can be solved for the full-circle Fourier coefficients a_m and b_m of the spreading

function. A least squares Fourier transform method for numerical integration is used to solve the set of available equations. A vector linear regression model inverts the matrix containing the spreading coefficients of $D(f,\theta)$.

41. Finally, a parameterized wrapped normal spreading function is fitted to $D(f,\theta)$ to improve the initial distorted estimate due to truncation of the Fourier series. A resolution of 2 deg (i.e. 180 increments in 360 deg) was used for the directional spreading function estimates. Once a_m and b_m are obtained, the mean wave direction $\theta(f)$ is calculated from the first harmonic a_1 and b_1 coefficients. The mean of all $\theta(f)$ equals the overall mean wave direction or peak wave direction $\bar{\theta}$.

42. A directional spread was calculated to give a relative indication of the width of the directional distribution. The directional spreading function was first normalized by its peak value. The spread then was calculated as half the width at the 50-percent level of the spreading function.

PART III: PRELIMINARY TEST RESULTS AND ANALYSIS

Basin Circulation Phase

43. Four current meters and dye tracer were used for cases S01 and S33 to monitor the presence of basin circulation due to wave conditions and basin configuration. Based on the lack of a significant circulation for these tests, further testing with the other cases was not deemed necessary.

Test Duration Phase

44. Table 8 lists normalized values of wave period and height for the 12 Unimodal Series cases. Measurements of T_p and H_{m0} from the OGA for durations of 200 waves at the peak period (half duration) were divided by durations of 400 waves (full duration) to obtain the normalized value. The duration of 200 waves is part of the longer duration time series of 400 waves duration. The starting point in the analysis is the same for both durations; 1,000 points (100 sec) are skipped from the beginning of the time series. Other analysis parameters are also identical. The actual measured values of T_p and H_{m0} are listed in Appendix B.

45. It is important to note that the control signals had not been calibrated or corrected during these tests, so the measured values did not always agree with the target or desired values. Based on the average of the six gages, the maximum period variation was 4 and 2 percent for T_p = 2.5 and 1.25 sec cases, respectively. The maximum height variation was 5 percent for both peak periods. The spectral estimates for T_p and H_{m0} are fairly stable statistics that should compare well for this type of test. The fact that there was little difference increased confidence that possible artifacts in the basin (i.e. circulation, long waves, etc.) were not significant.

46. The major effect of a short record is decreased confidence in spectral estimates as quantified by υ . Therefore, the spectral shapes for the different sampling durations were compared. Figure 2 shows an overlay of the measured frequency spectra for gages 1-4 of case S25. Variation in spectral shape for all 12 cases is illustrated in Figure 3 for the average of six gages. The spectral amplification ratio $S_{200}(f)/S_{400}(f)$ (i.e. ratio of spectral levels between long and short test durations) varies between 0.5 to 1.5, within the confidence limits for the spectral estimates. Since spectral

Table 8

Normalized Wave Parameters for Test Duration Phase

Test Case	OGA Gage Number 1	2	3	4	5	6	Ave.
	Normalized T_p Periods						
S01	0.94	0.94	1.00	0.94	0.94	1.00	0.96
S09	0.91	1.04	0.98	0.93	0.93	1.07	0.98
S13	0.94	0.99	1.03	0.98	0.98	1.03	0.99
S21	1.06	0.94	0.94	1.02	0.98	1.01	0.99
S25	0.94	0.94	1.00	1.03	1.02	0.94	0.98
S33	0.99	0.92	0.94	0.99	1.01	1.00	0.97
S37	1.06	1.06	0.98	0.98	1.02	0.99	1.02
S45	1.05	0.98	1.01	1.02	1.00	1.01	1.01
S49	1.00	0.99	1.00	1.04	1.00	1.00	1.00
S57	0.97	1.03	0.99	1.01	1.02	1.01	1.00
S61	0.93	1.05	1.02	1.02	1.05	1.02	1.01
S69	1.03	0.98	1.06	0.90	1.07	1.01	1.01
	Normalized H_{mO} Heights						
S01	0.97	0.97	0.99	0.97	0.97	0.97	0.97
S09	1.00	1.00	1.02	1.02	1.01	1.01	1.01
S13	0.95	0.95	0.96	0.95	0.92	0.95	0.95
S21	0.96	1.02	1.05	0.98	1.00	1.03	1.01
S25	1.00	1.01	1.03	0.97	0.98	1.00	1.00
S33	0.99	1.01	1.01	0.97	0.96	1.00	0.99
S37	0.94	0.96	0.96	0.96	0.94	0.95	0.95
S45	0.97	1.04	1.05	0.98	0.98	0.99	1.00
S49	0.97	1.00	0.97	0.96	0.97	0.98	0.98
S57	0.95	1.02	0.97	0.99	0.99	0.97	0.98
S61	0.99	1.03	0.99	1.00	0.99	1.00	1.00
S69	1.01	0.97	1.01	1.03	0.96	1.00	1.00

shape did not vary substantially due to record length, it was decided to test for the shorter duration for all future tests.

Signal Calibration Phase

47. In this phase of testing, each of the 54 control signals was corrected by iterating one to four times using the RAO transfer function and system gain factor to match the target directional spectra as closely as possible. Results from the directional spectral analysis of the OGA are compared

with predicted control signal values for peak frequency, significant wave height, frequency spectra, and directional distribution, which includes peak wave direction and directional spread.

Peak frequency

48. Table 9 summarizes measured and predicted peak frequency f_p for each of the 54 test cases, grouped by test series and mode number (in the case of bimodal spectra). To facilitate comparisons, the difference between predicted and measured frequency is shown for each mode. The maximum difference was ± 0.04 Hz, corresponding to a shift of ± 2 frequency bands, for cases S33 and S37 in the Unimodal Series. In most cases, the frequency shift was 0 to ± 1 band. The agreement is excellent since these small differences are insignificant relative to the inherent variability in the Fourier analysis for peak frequency.

Significant wave height

49. Figure 4 is a comparison of the three different methods for calculating significant wave height for the OGA: H_σ, $H_{1/3,d}$, and H_{m0}. The first two heights are from the time domain, and the last one from the frequency domain. Since the differences were small, the values for H_σ are used for comparison. Table 10 lists measured and predicted significant wave heights H_σ for the 54 cases. It has the same format as Table 9, except that no breakdown is given for individual modes since energy is computed for the total spectrum. The normalized ratio of measured wave height to predicted is included as a measure of the accuracy of spectral simulation.

50. In general, the match was very good, although measured wave heights were less than their target values. Measured wave height decreased as peak period, peak wave direction, and directional spreading increased. Given the problems previously cited concerning DSWG stroke limitations and earlier unidirectional spectra results (Briggs 1988), these results are not too surprising. The normalized height ratio ranged from a low of 0.80 (D49) to a high of 1.01 (D02 and D04) with an average for all cases of 0.92. Table 11 lists the minimum, maximum, and average normalized heights for each of the four test series.

51. In the first six cases of the Unimodal Series, wave height decreased slightly as wave direction increased from 0 deg. The next six cases had larger normalized heights because the target height was smaller (H_{m0} = 12.2 cm), with less associated wave breaking.

Table 9

Summary of Measured & Predicted Peak Frequency
Generalized Beach Model

Case ID	Gage Code*	Mode 1 Pred Hz	Mode 1 OGA Hz	Mode 1 Pred-OGA	Mode 2 Pred Hz	Mode 2 OGA Hz	Mode 2 Pred-OGA
			Unimodal Series				
S01	b	0.40	0.42	-0.02	-	-	-
S09	a	0.40	0.42	-0.02	-	-	-
S13	b	0.40	0.42	-0.02	-	-	-
S21	a	0.40	0.40	0.00	-	-	-
S25	b	0.40	0.42	-0.02	-	-	-
S33	b	0.40	0.44	-0.04	-	-	-
S37	b	0.80	0.76	0.04	-	-	-
S45	b	0.80	0.82	-0.02	-	-	-
S49	b	0.80	0.80	0.00	-	-	-
S57	b	0.80	0.82	-0.02	-	-	-
S61	b	0.80	0.82	-0.02	-	-	-
S69	a	0.80	0.78	0.02	-	-	-
			Superposition Series				
D01	b	0.40	0.40	0.00	-	-	-
D02	b	0.57	0.59	-0.02	-	-	-
D03	b	0.40	0.40	0.00	0.57	0.57	0.00
D04	b	0.40	0.40	0.00	-	-	-
D05	b	0.57	0.59	-0.02	-	-	-
D06	b	0.40	0.40	0.00	0.57	0.55	0.02
D07	b	0.40	0.40	0.00	-	-	-
D08	b	0.57	0.57	0.00	-	-	-
D09	b	0.40	0.40	0.00	0.57	0.55	0.02
			Directional Series				
D13	a	0.40	0.40	0.00	0.57	0.57	0.00
D16	a	0.40	0.40	0.00	0.57	0.57	0.00
D19	b	0.40	0.40	0.00	0.57	0.57	0.00
D23	b	0.40	0.40	0.00	0.57	0.57	0.00
D26	b	0.40	0.42	-0.02	0.57	0.57	0.00
D29	a	0.40	0.40	0.00	0.57	0.57	0.00
D33	b	0.40	0.42	-0.02	0.57	0.57	0.00
D36	b	0.40	0.40	0.00	0.57	0.57	0.00
D39	b	0.40	0.40	0.00	0.57	0.57	0.00
D43	a	0.40	0.40	0.00	0.57	0.59	-0.02
D46	a	0.40	0.42	-0.02	0.57	0.57	0.00
D49	a	0.40	0.42	-0.02	0.57	0.57	0.00
D51	b	0.40	0.40	0.00	0.57	0.57	0.00
D52	b	0.40	0.40	0.00	0.57	0.59	-0.02
D53	a	0.40	0.42	-0.02	0.57	0.57	0.00
D61	b	0.40	0.40	0.00	0.80	0.80	0.00
D62	b	0.40	0.40	0.00	0.80	0.80	0.00
D63	b	0.40	0.40	0.00	0.80	0.80	0.00
D64	b	0.40	0.40	0.00	0.80	0.80	0.00
D65	b	0.40	0.40	0.00	0.80	0.80	0.00
D66	b	0.40	0.40	0.00	0.80	0.80	0.00
D67	a	0.40	0.40	0.00	0.80	0.80	0.00
D68	a	0.40	0.40	0.00	0.80	0.82	-0.02
			Nonbreaking Series				
D71	b	0.40	0.40	0.00	0.57	0.57	0.00
D72	b	0.40	0.40	0.00	0.57	0.59	-0.02
D73	a	0.40	0.42	-0.02	0.57	0.57	0.00
D81	b	0.40	0.40	0.00	0.80	0.80	0.00
D82	b	0.40	0.40	0.00	0.80	0.80	0.00
D83	b	0.40	0.40	0.00	0.80	0.80	0.00
D84	b	0.40	0.40	0.00	0.80	0.80	0.00
D85	b	0.40	0.40	0.00	0.80	0.80	0.00
D86	b	0.40	0.40	0.00	0.80	0.80	0.00
D87	a	0.40	0.40	0.00	0.80	0.80	0.00

* OGA:
a = Gages 1-6, Gaussian Smooth
b = Gages 1-6, Raw Data
c = Gages 1-7, Gaussian Smooth
d = Gages 1-7, Raw Data

Table 10

Summary of Measured & Predicted Significant Wave Height

Generalized Beach Model

Case ID	Gage Code*	Pred. Cm	OGA Cm	OGA/Pred
		Unimodal Series		
S01	b	15.24	14.17	0.93
S09	b	15.24	13.81	0.91
S13	b	15.24	13.47	0.88
S21	b	15.24	13.74	0.90
S25	b	15.24	13.60	0.89
S33	b	15.24	13.52	0.89
S37	b	12.19	11.58	0.95
S45	b	12.19	11.92	0.98
S49	b	12.19	11.81	0.97
S57	b	12.19	11.90	0.98
S61	b	12.19	11.61	0.95
S69	b	12.19	11.71	0.96
		Superposition Series		
D01	b	7.62	7.50	0.98
D02	b	13.11	13.18	1.01
D03	b	15.16	13.87	0.91
D04	b	10.67	10.77	1.01
D05	b	10.67	10.34	0.97
D06	b	15.09	13.31	0.88
D07	b	13.11	12.18	0.93
D08	b	7.62	7.40	0.97
D09	b	15.16	12.38	0.82
		Directional Series		
D13	b	15.16	14.43	0.95
D16	b	15.09	13.93	0.92
D19	b	15.16	13.25	0.87
D23	b	15.16	14.14	0.93
D26	b	15.09	13.58	0.90
D29	b	15.16	13.14	0.87
D33	b	15.16	13.57	0.90
D36	b	15.09	12.96	0.86
D39	b	15.16	12.44	0.82
D43	b	15.16	13.60	0.90
D46	b	15.09	12.62	0.84
D49	b	15.16	12.13	0.80
D51	b	15.09	14.16	0.94
D52	b	15.09	13.57	0.90
D53	b	15.09	13.23	0.88
D61	b	15.09	14.38	0.95
D62	b	15.09	13.93	0.92
D63	b	15.09	14.03	0.93
D64	b	15.09	13.99	0.93
D65	b	15.09	14.32	0.95
D66	b	15.09	13.73	0.91
D67	b	15.09	13.71	0.91
D68	b	15.09	13.72	0.91
		Nonbreaking Series		
D71	b	9.05	8.43	0.93
D72	b	9.05	8.00	0.88
D73	b	9.05	7.89	0.87
D81	b	9.05	9.04	1.00
D82	b	9.05	8.48	0.94
D83	b	9.05	8.73	0.96
D84	b	9.05	8.45	0.93
D85	b	9.05	8.67	0.96
D86	b	9.05	8.35	0.92
D87	b	9.05	8.27	0.91

* OGA:
a = Gages 1-6, Gaussian Smooth
b = Gages 1-6, Raw Data
c = Gages 1-7, Gaussian Smooth
d = Gages 1-7, Raw Data

Table 11

Summary of Calibration Phase Normalized Wave Heights

Series	Minimum	Maximum	Average
Unimodal	0.88	0.98	0.93
Superposition	0.82	1.01	0.94
Directional	0.80	0.95	0.90
Nonbreaking	0.87	1.00	0.93

52. In the Superposition Series, the unimodal cases with higher frequency modes (T_p = 1.75 sec) more closely matched the desired wave height. The three bimodal cases D03, D06, and D09 did not match target wave heights as well as their unimodal counterparts. Reproduction was most accurate for case D03, which had more energy in the higher frequency mode. The low-frequency peaks were harder to reproduce than the higher frequency peak, even when the lower frequency had more energy (case D09).

53. In the Directional Series, the first 12 cases (D13 through D49) experienced the same pattern of increasing accuracy as the energy in the high-frequency mode increased relative to the low-frequency mode. The next three cases, D51 to D53, all had even energy distribution between modes with constant $\bar{\theta}_1$ = 0 deg and $\bar{\theta}_2$ = 20 deg and varying directional spreading. The unidirectional case D51 had significantly better accuracy than case D36 with $\bar{\theta}$ = 20 deg for both modes. Comparisons of three cases D52 with D16 and D46, with $\sigma_{m,1} = \sigma_{m,2}$ = 40 deg, indicate that height decreased as wave direction increased for one or both modes. Cases D53 and D26, both with $\sigma_{m,1}$ = 20 deg and $\sigma_{m,2}$ = 40 deg, also show this trend. The final eight cases, D61 to D68, had $T_{p,2}$ = 1.25 sec versus $T_{p,2}$ = 1.75 sec for the earlier cases. Energy distribution was equal between modes while wave direction and spreading were varied. Comparisons of cases D61 with D62 and D65 with D66 show a trend of reduced height as spreading increases. Only the unidirectional case D61 with $\bar{\theta}$ = 0 deg showed slightly better low-frequency mode simulation.

54. In the Nonbreaking Series, cases D71 to D73 are analogous to Directional Series cases D51 to D53 and cases D81 to D87 are similar to cases D61 to D67. The normalized wave heights for cases D71 to D73 are slightly reduced relative to cases D51 to D53. Normalized heights in cases D81 to D86 are the same or slightly larger than D61 to D66, indicating that breaking did occur in the Directional Series to reduce measured wave heights. In cases D83 and D84,

an increase in spreading caused a decrease in wave height, whereas wave breaking in cases D63 and D64 disguised this effect.

Frequency spectra

55. Figures 4 and 5 are examples of the measured and predicted frequency spectra for the unimodal case S25 and the bimodal case D29, respectively. In each figure, the dashed line is the predicted spectrum, and the solid line is the measured spectrum. Both spectra are normalized by the peak value of the predicted spectrum, so that shape and relative magnitudes are preserved. Plots of the other cases are contained in Appendix C.

56. The measured spectral ordinates at the peak frequency were smaller than predicted for all cases except S45, S49, S57, and S61. This smaller shape is in keeping with the smaller than desired wave heights since most of the energy is contained in the peak frequency. One explanation is the smaller frequency increment of the predicted spectra produces a more peaked spectra since frequency resolution is finer. As was true for wave height, higher frequency modes were more easily simulated for both unimodal and bimodal cases. In some cases, there was more energy in the higher frequencies of the measured spectra than desired. Cases D04 and D05 in Figure 6 illustrate both of these trends.

57. In general, the agreement between measured and predicted spectral shapes was very good for bimodal spectra to excellent for unimodal spectra. Based on chi-squared random variables and the limited number of degrees of freedom, the measured and predicted spectra are indistinguishable at the 95-percent level of confidence. For cases with $T_p = 1.25$ sec and $\upsilon = 12$, the estimated spectral ordinate can range between 0.51 to 2.74 of the true value. Similarly, for $T_p = 1.75$ and 2.50 sec and $\upsilon = 24$, the 95-percent confidence limits are 0.61 to 1.94.

Directional distributions

58. As previously discussed, directional distributions are represented by the directional spreading function that is centered at a peak wave direction with a width described by its directional spread.

59. Directional spreading function. The agreement between measured and predicted directional spreading functions for the unidirectional cases (a spike centered at the peak wave direction) was excellent. Figure 7 for case S25 is a good example. The dashed line is the predicted spreading function, and the solid line is the measured spreading. Each curve is normalized by its own maximum spreading value. Truncation of the Fourier series based on the

limited number of independent measurements tends to produce negative side lobes in the directional spreading function. These negative values have been suppressed and set to zero on these plots. The legend lists peak frequency for the mode, peak wave direction, and a relative directional spread for each curve.

60. The measured shapes of the directional cases were much more erratic, however, often displaying only one-third to one-half the desired directional width. In general, cases with narrower spreads matched predicted values better than those with wider spreads. Case D29 (Figure 8) is an example of a bimodal case with narrow and wide directional spread ($\sigma_{m,1}$ = 20 deg, $\sigma_{m,2}$ = 40 deg) illustrating this point.

61. Since cases with wider directional distributions did not match target values very well, it was decided to see what effect, if any, the addition of more gages and Gaussian smoothing would have on the measured directional distribution estimates. To maximize spatial homogeneity of the array due to different water depths, only gage C7 was included in the analysis with the six original linear offshore array gages. Gaussian smoothing is a weighted moving average with overlapping of the directional spreading function estimates (Briggs 1988). Different combinations of number of gages and smoothing produced four options for analyzing the directional distributions. A gage analysis code for each of these options is summarized in Table 12.

62. The four options were tried on all directional cases. Figures 9a to 9d illustrate the effect of the four different options for the unimodal case S33. Figures 10a to 10d are for the bimodal case D68. Gaussian smoothing tends to smooth and widen the distribution with little or no change in the peak direction. The addition of another gage has the same effects on measured values.

Table 12

Gage Analysis Code

Offshore Gage Array

Code	Gages	Smoothing
a	1 to 6	Yes
b	1 to 6	No
c	1 to 7	Yes
d	1 to 7	No

63. Since the effect of an additional gage and smoothing was not as profound as had been hoped, preference was given to the original OGA with no smoothing unless a significant improvement in the directional distributions for all modes was obvious. Thus, only 10 broad-banded cases have directional distributions based on a seven gage array with smoothing. The option selected is listed by gage code in Tables 13 and 14 giving measured and predicted directional spectral parameters. Since the peak frequency and significant wave height are affected by the number of gages, only the gage code "b" values for six gages are reported for these quantities.

64. Measured directional distributions were narrower than desired in most cases. Typical examples with about one-third the directional spread are cases S09, first mode of D26, and the second mode of D52 (Figures 11a to 11c). Figures 12a to 12c show examples with about one-half the desired spread in S21, first mode of D52, and the second mode of D13, respectively. Cases that matched target spreading function shapes reasonably well were S57, first mode of D68, and second mode of D19 (Figures 13a to 13c). The measured directional spread would have been wider in some cases if side lobes with energy levels less than the 50-percent criteria were included. Figures 14a to 14c illustrate typical examples for cases S69, first mode of D16, and second mode of D53, respectively. Plots of the remaining cases are contained in Appendix C.

65. As shown for the wider directional distributions, the energy appears to be more focused than desired. Array tuning (i.e. length of array and individual gage spacings) and refraction are possible explanations for some of this disparity. The linear arrays were modeled after arrays used in field experiments to measure narrower directional distributions. As wavelength increases and angle of incidence decreases, the required array length to adequately resolve the directional distribution increases. The directional resolution of the linear gage arrays varied from 4 to 8 deg for the range of peak frequencies from 0.80 to 0.40 Hz, respectively. This resolution is based on the theory of Oltman-Shay (1987) for the unit lag spacing and the maximum 19 lags available. Although the directional resolution could have been better, at least the linear arrays were reasonably well tuned for the directional distributions tested.

66. The waves were generated in 50-cm depth, and the OGA was located in 40-cm depth. For the wide directional spreads of σ_m = 40 deg, a wave ray refracts approximately 3 to 5 deg for the range of peak frequencies tested. If one can assume that an equal amount of narrowing would occur on both sides

Table 13

Summary of Measured & Predicted Peak Wave Direction

Generalized Beach Model

Case ID	Gage Code*	Mode 1 Pred. Deg	Mode 1 OGA Deg	Mode 1 Pred-OGA	Mode 2 Pred. Deg	Mode 2 OGA Deg	Mode 2 Pred-OGA
			Unimodal Series				
S01	b	0	0	0	-	-	-
S09	a	0	-2	2	-	-	-
S13	b	10	8	2	-	-	-
S21	a	10	-6	16	-	-	-
S25	b	20	18	2	-	-	-
S33	c	20	6	14	-	-	-
S37	b	0	0	0	-	-	-
S45	c	0	2	-2	-	-	-
S49	b	10	8	2	-	-	-
S57	c	10	-4	14	-	-	-
S61	b	20	18	2	-	-	-
S69	a	20	0	20	-	-	-
			Superposition Series				
D01	b	0	0	0	-	-	-
D02	b	0	0	0	-	-	-
D03	b	0	0	0	0	0	0
D04	b	0	0	0	-	-	-
D05	b	0	0	0	-	-	-
D06	b	0	0	0	0	0	0
D07	b	0	0	0	-	-	-
D08	b	0	0	0	-	-	-
D09	b	0	0	0	0	0	0
			Directional Series				
D13	a	0	-2	2	0	0	0
D16	a	0	-2	2	0	2	-2
D19	c	0	0	0	0	6	-6
D23	b	0	-4	4	0	-24	24
D26	d	0	-2	2	0	-8	8
D29	a	0	-10	10	0	2	-2
D33	b	20	18	2	20	18	2
D36	b	20	18	2	20	18	2
D39	b	20	18	2	20	18	2
D43	a	20	4	16	20	2	18
D46	a	20	8	12	20	2	18
D49	a	20	8	12	20	8	12
D51	b	0	0	0	20	18	2
D52	c	0	4	-4	20	18	2
D53	a	0	8	-8	16	4	12
D61	b	0	0	0	0	0	0
D62	c	0	6	-6	0	-2	2
D63	b	20	18	2	20	18	2
D64	b	20	22	-2	20	20	0
D65	b	0	0	0	20	18	2
D66	c	0	6	-6	20	10	10
D67	a	0	6	-6	18	2	16
D68	a	20	20	0	2	16	-14
			Nonbreaking Series				
D71	b	0	0	0	20	18	2
D72	c	0	2	-2	20	18	2
D73	a	0	8	-8	16	6	10
D81	b	0	0	0	0	0	0
D82	c	0	2	-2	0	-4	4
D83	b	20	18	2	20	18	2
D84	b	20	22	-2	20	20	0
D85	b	0	0	0	20	18	2
D86	c	0	0	0	20	12	8
D87	a	0	6	-6	18	2	16

* OGA:
a = Gages 1-6, Gaussian Smooth
b = Gages 1-6, Raw Data
c = Gages 1-7, Gaussian Smooth
d = Gages 1-7, Raw Data

Table 14

Summary of Measured & Predicted Directional Spread

Generalized Beach Model

Case ID	Gage Code*	Mode 1 Pred. Deg	Mode 1 OGA Deg	Mode 1 Pred-OGA	Mode 2 Pred. Deg	Mode 2 OGA Deg	Mode 2 Pred-OGA
			Unimodal Series				
S01	b	1.00	5.00	-4.00	-	-	-
S09	a	37.00	12.00	25.00	-	-	-
S13	b	2.00	5.00	-3.00	-	-	-
S21	a	37.00	17.00	20.00	-	-	-
S25	b	4.00	5.00	-1.00	-	-	-
S33	c	37.00	18.00	19.00	-	-	-
S37	b	1.00	3.00	-2.00	-	-	-
S45	c	37.00	15.00	22.00	-	-	-
S49	b	2.00	3.00	-1.00	-	-	-
S57	c	37.00	31.00	6.00	-	-	-
S61	b	4.00	3.00	1.00	-	-	-
S69	a	37.00	25.00	12.00	-	-	-
			Superposition Series				
D01	b	1.00	4.00	-3.00	-	-	-
D02	b	1.00	4.00	-3.00	-	-	-
D03	b	1.00	4.00	-3.00	1.00	4.00	-3.00
D04	b	1.00	4.00	-3.00	-	-	-
D05	b	1.00	4.00	-3.00	-	-	-
D06	b	1.00	4.00	-3.00	1.00	4.00	-3.00
D07	b	1.00	4.00	-3.00	-	-	-
D08	b	1.00	4.00	-3.00	-	-	-
D09	b	1.00	4.00	-3.00	1.00	4.00	-3.00
			Directional Series				
D13	a	37.00	14.00	23.00	37.00	19.00	18.00
D16	a	37.00	16.00	21.00	37.00	15.00	22.00
D19	c	37.00	12.00	25.00	37.00	26.00	11.00
D23	b	19.00	12.00	7.00	36.00	32.00	4.00
D26	d	19.00	8.00	11.00	35.00	38.00	-3.00
D29	a	19.00	17.00	2.00	31.00	9.00	22.00
D33	b	4.00	5.00	-1.00	4.00	4.00	0.00
D36	b	4.00	5.00	-1.00	4.00	4.00	0.00
D39	b	4.00	5.00	-1.00	4.00	4.00	0.00
D43	a	37.00	15.00	22.00	37.00	14.00	23.00
D46	a	37.00	28.00	9.00	37.00	17.00	20.00
D49	a	37.00	21.00	16.00	37.00	8.00	29.00
D51	b	1.00	4.00	-3.00	1.00	4.00	-3.00
D52	c	37.00	21.00	16.00	37.00	11.00	26.00
D53	a	19.00	12.00	7.00	37.00	14.00	23.00
D61	b	1.00	4.00	-3.00	1.00	3.00	-2.00
D62	c	37.00	21.00	16.00	37.00	17.00	20.00
D63	b	1.00	5.00	-4.00	1.00	3.00	-2.00
D64	b	37.00	15.00	22.00	37.00	17.00	20.00
D65	b	1.00	4.00	-3.00	1.00	3.00	-2.00
D66	c	37.00	23.00	14.00	37.00	28.00	9.00
D67	a	19.00	10.00	9.00	37.00	8.00	29.00
D68	a	19.00	16.00	3.00	37.00	17.00	20.00
			Nonbreaking Series				
D71	b	1.00	4.00	-3.00	1.00	4.00	-3.00
D72	c	37.00	19.00	18.00	37.00	10.00	27.00
D73	a	19.00	11.00	8.00	37.00	15.00	22.00
D81	b	1.00	4.00	-3.00	1.00	3.00	-2.00
D82	c	37.00	18.00	19.00	37.00	16.00	21.00
D83	b	1.00	5.00	-4.00	1.00	3.00	-2.00
D84	b	37.00	15.00	22.00	37.00	17.00	20.00
D85	b	1.00	4.00	-3.00	1.00	3.00	-2.00
D86	c	37.00	19.00	18.00	37.00	18.00	19.00
D87	a	19.00	10.00	9.00	37.00	9.00	28.00

* OGA:
a = Gages 1-6, Gaussian Smooth
b = Gages 1-6, Raw Data
c = Gages 1-7, Gaussian Smooth
d = Gages 1-7, Raw Data

of the symmetric directional distributions, then refraction explains a good deal of the observed disparity in directional spreading functions.

67. Peak wave direction. Table 13 lists the measured and predicted peak wave directions for each of the cases. The format is the same as Table 9 for peak frequency. The agreement was excellent for both unimodal and bimodal unidirectional cases. The differences ranged from 0 to $\pm$2 deg, equivalent to $\pm$1 directional increment. For the cases with directional spreading, the agreement showed a high degree of variability. Cases with a target wave direction of 0 deg varied from 0 to $\pm$10 deg (five directional bands). Cases with nonzero wave directions varied from a perfect match to extremes of -14 (D68) and +24 (D23) deg. Looking at measured directional distributions for the extreme cases (appendices) shows that although the maximum value in the spreading function estimate is picked, spreading actually encompasses the desired peak wave direction. This is typical of other cases that had peak wave directions significantly different from their intended values. Hydraulic laboratories in other countries (Sand and Mynett 1987) have reported differences of $\pm$10 deg, so this amount of variation is not too alarming.

68. Directional spread. Table 14 lists measured and predicted directional spread for the 54 cases. Again, the format is the same as previous tables. As seen in the measured directional spreading functions, agreement between measured and predicted directional spread is excellent for the unidirectional cases, both unimodal and bimodal. The differences for these cases range from perfect match to -4 deg (2 bands). Measured unidirectional spreads are wider than predicted in all cases except for case S61 and the second mode of cases D33 to D39. This small amount of difference is due to the Fourier series truncation inherent in the directional spectral analysis and is not considered significant. As discussed previously, cases with directional spreading show much more variability, usually being only one-third to one-half as wide as desired. Extreme differences of 29 deg occurred in the second modes of cases D49 and D67, both having $\bar{\theta}_2 = 20$ deg and $\sigma_{m,2} = 40$ deg.

Discussion and summary

69. As has been discussed, the peak frequency, wave height, and frequency spectral shapes matched target values very well. There was quite a bit more variability in the measured directional distributions, especially for the wider cases at nonzero wave direction. The match between measured and predicted distributions for the unidirectional cases was excellent, however. Thus, the question is whether the target directional spectra were actually

simulated or the gage array was not able to correctly resolve the true shapes. Previous experience leads one to believe that the proper directional spectra were generated.

70. Some explanations of this disparity are listed in the following:

a. Variability is inherent in any laboratory simulations. Differences in peak wave directions are one example.

b. The control signals were generated in a water depth of 50 cm while they were measured in 40-cm depth. Refraction definitely affected the measured directional spectra, narrowing the wider distributions by 6 to 10 deg depending on peak frequency.

c. The waves experienced some breaking in traveling between the two water depths. This breaking was true for most of the cases.

d. Although the linear array was reasonably tuned, directional resolution could have been improved with the addition of more gages, especially for the wider directional distributions. The design was modeled after a linear array used in field measurements for narrower directional distributions. The 2-3-1-7-5 CERC Field Research Facility linear array has proved to be reasonably robust in previous laboratory experiments and should be used in future tests. Also, new triaxial, ultrasonic current meters to measure directional spectra at a single location might eliminate some of the spatial tuning problems.

e. Stroke limitations on the DSWG prevented the corrected control signal from being generated as prescribed. Even though the RAO corrected the control signals, displacement, velocity, and acceleration limits on the DSWG often prevented the intended signal from being generated.

f. Although reflections from the beach should be minimal because of the 1:30 slope, some could be canceling energy in some directions.

71. Finally, better analysis methods should be investigated. The Maximum Likelihood Method (MLM) and Maximum Entropy Method (MEM) and other higher resolution methods could give better estimates of measured directional spectra.

PART IV: WAVE TRANSFORMATION RESULTS AND ANALYSIS

72. In this section, time and frequency domain results are presented to study the effects of nonlinearity and directionality on wave transformation in the nearshore region.

Time Domain Analysis

Time series plots

73. Measured surface elevation time series plots for the broad-banded unimodal case 525 for gages 4, 8, 10, 15, and 20 are shown in Figures 15a to 15e. Figures 16a to 16e show the time series for the same gages for the bimodal case D29. Only 15 sec of data for each gage, representative of 6 to 12 waves, are shown to illustrate wave profile evolution in the cross-shore direction. Common x-axis and y-axis scales and starting points (after elapsed time of 100 sec to allow the waves to reach the farthest gage) are used. The classic, nonlinear "sawtooth" wave shape of steep front faces and flat rear slopes in very shallow water reported by Elgar and Guza (1985) is seen for both narrow and broad frequency spectra cases. Appendix D contains surface elevation time series plots for all 10 CGA gages in the 54 cases.

Zero-downcrossing statistics

74. Results from the zero-downcrossing analysis for each gage of each case are listed in Appendix E. Values of average surface elevation η, significant wave period $T_{1/3,d}$, and significant wave height $H_{1/3,d}$ are grouped by test case within each of the four test series. The average of the first six gages is also given to facilitate comparisons with the OGA.

Frequency Spectral Analysis of Cross-Shore Array

Peak wave period

75. Tabular listings of the peak period by the CERC method $T_{p,c}$ for all gages in each case are contained in Appendix F. The format is the same as the downcrossing results. A detailed analysis of spectral period transformation remains to be performed. However, general trends are that unimodal spectra peaks remain constant or shift to slightly lower frequency. The same pattern occurs for bimodal spectra with peak period remaining relatively

invariant or shifting to the lower frequency peak. Since B_e = 0.024 Hz, some of this peak frequency variation is due to natural variability.

Zero-moment wave height

76. Appendix F also contains tabular listings of H_{m0} for all gages in each case. The format is the same as the downcrossing results. Wave height information was the most extensively analyzed. First, measured wave heights are compared with the two-dimensional (2-D) flume tests to see if the same trend of shoaling and decay is produced, given the difference in experimental setup. Next, the effects of energy and directional distributions on wave height transformation are presented and discussed. Finally, the effect of a smaller deepwater wave height is evaluated.

77. Comparison with flume trend. The 2-D flume tests provided important insight into the problem of wave transformation for unimodal and bimodal, unidirectional spectra. As the waves shoaled, wave height remained fairly flat or increased slightly. Inside the surf zone, wave height became locally depth controlled, no longer governed by outside conditions, as the waves became saturated. These results are in agreement with field data reported by Seymour (1989). The 3-D GBM tests provide a natural extension to these flume tests.

78. Flume comparisons are presented for the 12 Unimodal Series spectra in Figures 17a and 17b. Figure 17a is a comparison of wave height versus depth for the flume and six basin cases (S01 to S33) with target T_p = 2.5 sec, H_{m0} = 15.2 cm, and σ_m = 0 deg. The basin cases with $\bar{\theta}$ = 0, 10, and 20 deg are included because the reduction in wave height due to refraction for these cases is expected to be negligible (less than 2 percent based on linear theory). The top half of the plot is the measured wave height, and the bottom half is a normalized (nondimensional) wave height obtained by dividing measured height by the wave height at the 40-cm depth (gage 4 in the GBM basin tests). The normalized plots facilitate comparisons because measured heights differed somewhat from target values. In the shoaling region (i.e. region of constant or increasing height), the flume and basin results compare very well (within 5 percent). In the decay region (i.e. region of decreasing height), the wave heights from the three basin cases are very close, following an approximately linear decay. The flume case decays more slowly at first and then matches the basin cases. The maximum difference in measured wave height is 1 cm (within 7 percent).

79. Figure 17b is a similar plot of measured and normalized wave height for the flume case and six basin cases (S37 to S69) with target T_p = 1.25 sec and H_{m0} = 12.2 cm. The normalized plot shows that flume and basin case S49 with $\bar{\theta}$ = 10 deg agree closely, but basin cases with $\bar{\theta}$ = 0 (S37) and $\bar{\theta}$ = 20 deg (S61) begin decay much sooner. The maximum difference between cases is 15 percent. These two basin cases may decay due to steepness-induced breaking because they had larger incident heights relative to the flume (see measured height plot). In the decay region, flume and all basin cases are close, and again the decay is approximately linear with depth. Although basin tests do not exactly reproduce flume tests, maximum differences are generally 5 to 10 percent.

80. Energy distribution. The effect of energy distribution on wave height transformation is illustrated in Figures 18a to 18d. Bimodal cases with $T_{p,1}$ = 2.5 and $T_{p,2}$ = 1.75 sec from the Superposition (D03, D06, and D09) and Directional (D13 to D49) Series are grouped by directional distribution ($\bar{\theta}$ = 0 or 20 deg, σ_m = 0 or 40 deg) and compared. Unimodal Series cases (S01, S09, S25 and S33) with T_p = 2.50 sec and H_{m0} = 15.2 cm are included in the plots for reference.

81. Flume experiments showed a strong trend of larger wave heights in the shoaling region for cases with more energy in the low-frequency mode relative to the high-frequency mode. Normalized plots show the same trend, with maximum differences of 10 percent for any energy distribution. Based on trends in the bimodal cases, unimodal cases (with all energy in the first mode) would be expected to show greater shoaling than bimodal cases. However, the spectral shape of the unimodal cases is much broader (γ = 3.3), in agreement with the earlier flume tests, which confuses the comparison.

82. Directional distribution. The effect of directional distribution on transformed wave height for the Unimodal Series cases (S01 to S33) with T_p = 2.5 sec and H_{m0} = 15.2 cm is presented in Figure 19. Figure 19b shows measured and normalized height for the Unimodal Series cases (S37 to S69) with T_p = 1.25 sec and H_{m0} = 12.2 cm. Directional distribution parameters are $\bar{\theta}$ = 0, 10, and 20 deg and σ_m = 10 and 40 deg. In general, wave direction and spreading do not appear to have a significant effect on the transformed wave height for these broad-banded unimodal cases. Directional spreading tends to increase height in the decay region, which appears to dominate in the cases with T_p = 1.25 sec (Figure 19b). Measured wave heights in the unidirectional cases (S13 and S49) with $\bar{\theta}$ = 10 deg are 10 percent lower than the other

cases and therefore shoal more before breaking dominates. The wave height appears to be more sensitive to small differences in deepwater wave height than to differences in incident wave direction or spreading. In the region of decay, all cases follow a common trend of approximate linear decay with depth, in agreement with earlier results.

83. The effect of directional spreading for a constant wave direction for the bimodal cases from the Superposition (D03, D06, and D09) and Directional Series (D13 to D49) is seen by comparing Figures 18a and 18b ($\bar{\theta}$ = 0 deg, σ = 0 and 40 deg) and Figures 18c and 18d ($\bar{\theta}$ = 20 deg, σ = 0 and 40 deg). An increase in spreading reduces the effect (paragraph 80) of modal energy variation, especially in the shoaling region.

84. Figures 20a to 20c show the effect of directional distribution on the same bimodal cases from the Superposition and Directional Series ($T_{p,1}$ = 2.5 sec, $T_{p,2}$ = 1.75 sec) for the three different energy distributions (shown by the H_{m0} associated with each mode). Figure 20d shows transformed heights for Directional Series cases (D61 to D68) with $T_{p,1}$ = 2.50 and $T_{p,2}$ = 1.25 sec and equal modal energy distribution. Directional distribution parameters are $\bar{\theta}$ = 0, 10, and 20 deg and σ_m = 10 and 40 deg. The legend shows two values for wave direction and spreading: the value to the left of the slash corresponds to the first mode, and the value to the right corresponds to the second mode.

85. An increase in wave direction produces an apparent increase in wave height over the entire nearshore region (nondimensional height in Figure 20). The effect of an increase in spreading is less obvious. Spreading appears to be frequency-dependent, as it tends to increase transformed height in the shoaling region for cases with $T_{p,2}$ = 1.75 sec and in the decay region for cases with $T_{p,2}$ = 1.25 sec. The most variation due to spreading occurs for the cases with $T_{p,2}$ = 1.75 sec and equal energy distribution (Figure 20b). Again, deepwater wave height appears to be more important than other factors, i.e., cases with slightly larger deepwater height tend to stay constant or decrease, and cases with slightly lower deepwater height tend to increase. Maximum differences in normalized heights are 10 to 15 percent for cases with $T_{p,2}$ = 1.75 sec and 20 percent for cases with $T_{p,2}$ = 1.25 sec. The larger difference for cases with $T_{p,2}$ = 1.25 sec (Figure 20d) is probably due to higher wave steepness.

86. Effect of deepwater height. Measured wave heights from the Nonbreaking Series with reduced deepwater height are plotted in Figure 21a for

the three cases (D71 to D73) with $T_{p,2}$ = 1.75 sec and in Figure 21b for the seven cases (D81 to D87) with $T_{p,2}$ = 1.25 sec. The first mode period is the same in both figures. The cases in Figure 21b are analogous to the first seven cases in Figure 20c with larger deepwater wave heights. In general, the shoaling region is much greater when the deepwater height is reduced, extending throughout most of the surf zone. The decay region is less steep and shorter. This is not surprising, given that wave height is depth-dependent (Seymour 1989). The cases in Figure 21a do not show significant effect due to spreading for constant wave directions of $\bar{\theta}_1$ = 0 deg and $\bar{\theta}_2$ = 20 deg, although the unidirectional case is slightly higher. In Figure 21b, two of the three unidirectional cases show an increase in wave height. Even though all three cases have the same deepwater energy, the two non-normally incident cases show a significant increase in height, whereas the normally incident case does not.

87. Linear superposition assumption. If the linear superposition assumption is correct, the height and spectral transformation of two superimposed unimodal spectra should match that of their equivalent bimodal spectrum. The flume experiments showed linear superposition worked well in the shoaling region, but poorly in the decay region. Measured and normalized wave heights from the Superposition Series (D01 to D09) are shown in Figures 22a to 22c for the three energy distributions, respectively. Directional distributions in all cases are $\bar{\theta}$ = 0 deg and σ_m = 0 deg. Normalized plots show the same trend as the flume tests: close comparisons in the shoaling region and overprediction of wave height by linear superposition in the decay region (overprediction throughout surf zone in equal energy distribution case, Figure 20b).

88. Figures 23a to 23c compare the two superposed unimodal spectra and corresponding bimodal spectra from the Superposition Series for the three different energy distributions, respectively. Each panel represents a different gage and water depth d in the CGA. The solid line is the bimodal spectrum, and the dashed line is the linear combination of the unimodal spectra. If the relative magnitudes of the curves are preserved during transformation, then the superposition assumption can be supported. In Figure 23a, the first mode (i.e. low-frequency) of the bimodal spectrum maintains about one-half to one-third the area of the superimposed spectra for all depths, but the second mode (i.e. high-frequency) of the bimodal spectrum decays much faster than the superimposed spectra. This is consistent with

flume test results and the findings of Elgar and Guza (1985, 1986) that the higher frequency mode decays faster in the presence of a lower frequency mode. Figures 23b and 23c show the same trend. Thus, based on this limited set of wave height and spectra comparisons, the linear superposition assumption can not be supported everywhere in the nearshore region.

Frequency spectra

89. Case S25 (T_p = 2.5 sec, γ = 3.3) is a good example of the transformation that occurs for a broad-banded unimodal spectrum. Figure 24a is a linear plot of the transformed spectrum from the 10 gages in the CGA. Each panel contains the measured spectra for two adjacent gages, starting with gage 4 in 40-cm depth. All spectra in a test case are normalized by the peak spectral ordinate of gage 4 to illustrate relative changes due to depth. Figure 24b shows the same information, but with semilog axes and without normalization. The linear plots show relative features of wave transformation, especially regions of shoaling and breaking. Changes in energy distribution between frequencies, especially transfers to subharmonics and super-harmonics (i.e. f_p divided by or multiplied by an integer, respectively), are more easily seen on the semilog plots. Appendices G and H contain linear and semilog plots, respectively, for all cases.

90. In case S25, energy increases at the subharmonic and higher harmonic frequencies as the waves travel into shallower water. During shoaling, the first (f ≈ 0.80 Hz) and second (f ≈ 1.20 Hz) harmonics experience an energy increase (panels 2 and 3). As the wave breaks (panels 4 and 5), multiple nonlinear interactions among a wide range of frequencies produce smaller, less well-defined peaks. The third subharmonic (f ≈ 0.10 Hz) of the peak also tends to grow (two to three times) as the wave transforms, more so than the first subharmonic (f ≈ 0.20 Hz). These results agree qualitatively with the findings of Elgar and Guza (1985, 1986).

91. For a narrow-band unimodal spectrum, case D08 (T_p = 1.75 sec, γ = 20) is a good example of spectral transformation. Figures 25a and 25b for the linear and semilog plots, respectively, show that shoaling continues to the 16-cm depth (panel 4) in this case. The first (f ≈ 1.14 Hz) and second (f ≈ 1.71 Hz) harmonics grow as the wave travels from 22.6- to 9.5-cm depth (panels 3 to 5). The third subharmonic (f ≈ 0.14 Hz) experiences a fivefold increase in energy, similar to the broad-banded spectral case.

92. Case D29 ($T_{p,1}$ = 2.50 sec, $T_{p,2}$ = 1.75 sec, γ = 20) is an example of a narrow-band bimodal spectrum with more energy in the first mode, typical of

sea and swell spectra. Linear and semilog plots are shown in Figures 26a and 26b, respectively. As the wave breaks, energy is initially transferred to the frequency corresponding to the summation of mode frequencies (i.e. $f \approx 0.97$ Hz, panel 2). As the wave continues to decay, energy is transferred out of this harmonic mode and the second peak mode to the harmonic modes located at $f \approx 0.80$ and 1.20 Hz (panels 3 to 5). This transference agrees with Elgar and Guza's (1985, 1986) findings that a bimodal sea and swell peak spectrum would become unimodal as it transformed. Again, the subharmonic peak at $f \approx 0.17$ Hz grows due to the nonlinear difference interactions between the sea and swell peaks.

93. The subharmonic peaks in each of these examples suggest the naturally occurring surf beat or nonlinear difference interactions between frequencies observed in the field. However, these peaks might be due to seiching between the DSWG and the beach and just an artifact of the physical modeling process. For a standing wave in a basin with constant and varying depth, the seiche frequency is approximately 0.06 Hz (15.6 sec). It is improbable that the low-frequency peaks are first or second harmonics of the seiche frequency and not true subharmonics.

94. In cross-bispectral analysis of waves undergoing transformation in the breaking region, Elgar and Guza (1985) found that high-frequency energy was reduced and low-frequency energy increased relative to their levels seaward of the surf zone. They found that there was a significant nonlinear coupling of the shallow low-frequency modes to the seaward high-frequency modes. Unidirectional cases D36 and D63, with greater energy in the high-frequency sea peak than the low-frequency swell peak, are examples illustrating this behavior. Figures 27a and 27b contain the linear spectral transformation plots for cases D36 and D63, respectively. Both cases have the following directional spectral parameters: $T_{p,1} = 2.50$ sec, $H_{m0,1} = H_{m0,2} = 10.8$ cm, and $\bar{\theta}_1 = \bar{\theta}_2 = 20$ deg. The only difference is $T_{p,2} = 1.75$ sec in case D36 and $T_{p,2} = 1.25$ sec in case D63. The first mode has less energy than the second mode in deeper water, but the first mode dominates in shallower depths. The dominance of the first mode is more pronounced in case D63 because of greater frequency separation between modes.

95. Figure 28 shows the linear spectral plot for the unidirectional case D61. It has the same target directional spectral parameters as case D63 except $\bar{\theta}_1 = \bar{\theta}_2 = 0$ deg. A comparison of cases D61 and D63 shows that an

increase in wave direction from shore-normal tends to increase the energy in the first mode.

96. Comparison of cases with constant wave direction ($\bar{\theta}$ = 0 deg) and varied spreading (σ_m = 0 or 40 deg) suggests that inclusion of directional spreading inhibits the growth of subharmonics. Figures 29a and 29b for cases D06 and D16 ($T_{p,2}$ = 1.75 sec), respectively, illustrate this behavior. Cases D61 and D62 have the same directional spectral parameters as cases D06 and D16 except $T_{p,2}$ = 1.25 sec. Figure 28 for case D61 and Figure 29c for case D62 show the same trend.

97. If wave directions are different between modes ($\bar{\theta}_1$ = 0 deg, $\bar{\theta}_2$ = 20 deg) and directional spreading is included, the first mode energy level is reduced, and the second mode peak is split as the wave transforms. Figures 30a and 30b for cases D65 and D66 ($T_{p,1}$ = 2.50 sec, $T_{p,2}$ = 1.25 sec), respectively, demonstrate this behavior.

98. The effect of reduced deepwater wave heights on the transformed spectral shapes is shown in Figures 31a and 31b for the unidirectional cases D51 and D71, respectively. Directional spectral parameters are the same in both cases ($T_{p,1}$ = 2.50 sec, $T_{p,2}$ = 1.75 sec, $\bar{\theta}_1$ = 0 deg, $\bar{\theta}_2$ = 20 deg), except deepwater wave height is reduced 60 percent in case D71. Whereas case D51 has begun decay by d = 29.3 cm, case D71 continues to shoal until d = 19.2 cm, before beginning to decay. Spectral shapes match if the panels for D71 are linearly translated from the shallower depths to deeper water panels of case D51.

Directional Spectral Analysis of Longshore Arrays

99. For directional spectral analysis of the two longshore arrays, OGA and NGA, six gages were used to calculate peak frequency and wave height estimates. The directional distributions were estimated with six or seven gages, similar to the OGA analysis described in Part III.

Peak frequency

100. Table 15 lists measured peak frequency for the OGA and NGA for each case. The format is the same as Table 9. The maximum change occurred for cases S13 (0.04 Hz) and S49 (-0.04 Hz) in the Unimodal Series. Typical changes, if they occurred, were only $\pm$0.02 Hz (i.e. $\pm$1 frequency band). Thus, the average shift in peak frequency due to wave transformation between the two

Table 15

Summary of Measured Peak Frequency

Case Id	Gage Code*	Mode 1 OGA Hz	Mode 1 NGA Hz	Mode 1 OGA-NGA	Mode 2 OGA Hz	Mode 2 NGA Hz	Mode 2 OGA-NGA
			Unimodal Series				
S01	b	0.42	0.42	0.00	-	-	-
S09	a	0.42	0.42	0.00	-	-	-
S13	b	0.42	0.38	0.04	-	-	-
S21	a	0.40	0.42	-0.02	-	-	-
S25	b	0.42	0.44	-0.02	-	-	-
S33	b	0.44	0.44	0.00	-	-	-
S37	b	0.76	0.78	-0.02	-	-	-
S45	b	0.82	0.80	0.02	-	-	-
S49	b	0.80	0.84	-0.04	-	-	-
S57	b	0.82	0.80	0.02	-	-	-
S61	b	0.82	0.82	0.00	-	-	-
S69	a	0.78	0.78	0.00	-	-	-
			Superposition Series				
D01	b	0.40	0.40	0.00	-	-	-
D02	b	0.59	0.57	0.02	-	-	-
D03	b	0.40	0.40	0.00	0.57	0.57	0.00
D04	b	0.40	0.40	0.00	-	-	-
D05	b	0.59	0.59	0.00	-	-	-
D06	b	0.40	0.40	0.00	0.55	0.55	0.00
D07	b	0.40	0.40	0.00	-	-	-
D08	b	0.57	0.57	0.00	-	-	-
D09	b	0.40	0.40	0.00	0.55	0.57	-0.02
			Directional Series				
D13	a	0.40	0.40	0.00	0.57	0.57	0.00
D16	a	0.40	0.40	0.00	0.57	0.57	0.00
D19	b	0.40	0.40	0.00	0.57	0.59	-0.02
D23	b	0.40	0.40	0.00	0.57	0.59	-0.02
D26	b	0.42	0.42	0.00	0.57	0.57	0.00
D29	a	0.40	0.40	0.00	0.57	0.59	-0.02
D33	b	0.42	0.42	0.00	0.57	0.57	0.00
D36	b	0.40	0.40	0.00	0.57	0.57	0.00
D39	b	0.40	0.42	-0.02	0.57	0.57	0.00
D43	a	0.40	0.40	0.00	0.59	0.59	0.00
D46	a	0.42	0.40	0.02	0.57	0.59	-0.02
D49	a	0.42	0.40	0.02	0.57	0.59	-0.02
D51	b	0.40	0.40	0.00	0.57	0.57	0.00
D52	b	0.40	0.40	0.00	0.59	0.55	0.04
D53	a	0.42	0.42	0.00	0.57	0.57	0.00
D61	b	0.40	0.40	0.00	0.80	0.80	0.00
D62	b	0.40	0.40	0.00	0.80	0.80	0.00
D63	b	0.40	0.40	0.00	0.80	0.78	0.02
D64	b	0.40	0.40	0.00	0.80	0.80	0.00
D65	b	0.40	0.40	0.00	0.80	0.80	0.00
D66	b	0.40	0.40	0.00	0.80	0.78	0.02
D67	a	0.40	0.40	0.00	0.80	0.82	-0.02
D68	a	0.40	0.40	0.00	0.82	0.80	0.02
			Nonbreaking Series				
D71	b	0.40	0.40	0.00	0.57	0.57	0.00
D72	b	0.40	0.40	0.00	0.59	0.57	0.02
D73	a	0.42	0.42	0.00	0.57	0.57	0.00
D81	b	0.40	0.40	0.00	0.80	0.80	0.00
D82	b	0.40	0.42	-0.02	0.80	0.80	0.00
D83	b	0.40	0.40	0.00	0.80	0.80	0.00
D84	b	0.40	0.40	0.00	0.80	0.80	0.00
D85	b	0.40	0.40	0.00	0.80	0.80	0.00
D86	b	0.40	0.40	0.00	0.80	0.80	0.00
D87	a	0.40	0.40	0.00	0.80	0.82	-0.02

* OGA:
a = Gages 1-6, Gaussian Smooth
b = Gages 1-6, Raw Data
c = Gages 1-7, Gaussian Smooth
d = Gages 1-7, Raw Data

NGA:
a = Gages 12-17, Gaussian Smooth
b = Gages 12-17, Raw Data
c = Gages 11-18, Gaussian Smooth
d = Gages 11-18, Raw Data

linear arrays was insignificant. This is in agreement with the results from the CGA measurements.

Significant wave height

101. Table 16 lists average H_σ measured with OGA and NGA for the 54 cases. It has the same format as Table 10. Normalized height is the measured NGA height divided by the measured OGA height. In general, wave heights were reduced between the OGA and the NGA due to wave breaking and decay. The normalized height ratio ranged from a low of 0.79 (D61) to a high of 1.08 (D01), with an average for all cases of 0.90. Values greater than one indicate that the shoaling region extended at least to the NGA depth. Table 17 lists the minimum, maximum, and average for each of the four test series. The standard deviation is given for the average as an indication of the variability.

Frequency spectra

102. Figures 32a and 32b are examples of measured average frequency spectra of the OGA and NGA for the unimodal S25 and bimodal D29 cases, respectively. The format is the same as the figures for the calibration phase. The dashed line is the OGA spectrum, and the solid line is the NGA spectrum. Again, the measured frequency spectra are normalized by the spectral ordinate at the peak of the predicted spectrum. Thus, the relative size to the predicted spectrum is preserved. The trends discussed earlier from the single-channel spectral analysis of the CGA are observed. Plots for the remaining cases are contained in Appendix I.

Directional distributions

103. Directional spreading function. Measured directional spreading functions for the NGA were analyzed with the method selected for the OGA. The only difference was inclusion of two additional gages in options "c" and "d" for the NGA. Since water depth did not change appreciably for the gage immediately in front of (gage 11) and the gage behind (gage 18) the NGA, it was felt that spatial homogeneity of the array would not be compromised significantly if these two gages were included in analysis of the directional distributions. Table 18 summarizes the gage analysis code for the NGA.

104. In most cases, the central tendency of the directional distributions remained consistent during wave transformation. Unidirectional cases did not change, and wider directional distributions tended to narrow as they traveled into shallower water due to refraction. Because of uncertainty in the directional spectral analysis and resolution of the linear array, peak

Table 16

Summary of Measured Significant Wave Heights

Case Id	Gage Code*	OGA Cm	NGA Cm	NGA/OGA
		Unimodal Series		
S01	b	14.17	12.11	0.85
S09	b	13.81	11.71	0.85
S13	b	13.47	11.80	0.88
S21	b	13.74	11.70	0.85
S25	b	13.60	11.38	0.84
S33	b	13.52	11.79	0.87
S37	b	11.58	10.05	0.87
S45	b	11.92	10.11	0.85
S49	b	11.81	9.82	0.83
S57	b	11.90	10.00	0.84
S61	b	11.61	9.37	0.81
S69	b	11.71	10.06	0.86
		Superposition Series		
D01	b	7.50	8.07	1.08
D02	b	13.18	11.50	0.87
D03	b	13.87	11.56	0.83
D04	b	10.77	10.58	0.98
D05	b	10.34	10.08	0.97
D06	b	13.31	11.38	0.85
D07	b	12.18	11.21	0.92
D08	b	7.40	7.77	1.05
D09	b	12.38	11.25	0.91
		Directional Series		
D13	b	14.43	11.94	0.83
D16	b	13.93	11.80	0.85
D19	b	13.25	11.82	0.89
D23	b	14.14	11.89	0.84
D26	b	13.58	11.78	0.87
D29	b	13.14	11.68	0.89
D33	b	13.57	11.48	0.85
D36	b	12.96	11.40	0.88
D39	b	12.44	11.26	0.91
D43	b	13.60	11.70	0.86
D46	b	12.62	11.39	0.90
D49	b	12.13	11.14	0.92
D51	b	14.16	11.82	0.83
D52	b	13.57	12.00	0.88
D53	b	13.23	11.69	0.88
D61	b	14.38	11.30	0.79
D62	b	13.93	11.52	0.83
D63	b	14.03	11.62	0.83
D64	b	13.99	11.72	0.84
D65	b	14.32	11.47	0.80
D66	b	13.73	11.45	0.83
D67	b	13.71	11.68	0.85
D68	b	13.72	11.53	0.84
		Nonbreaking Series		
D71	b	8.43	8.74	1.04
D72	b	8.00	8.59	1.07
D73	b	7.89	8.38	1.06
D81	b	9.04	9.05	1.00
D82	b	8.48	8.34	0.98
D83	b	8.73	8.79	1.01
D84	b	8.45	8.50	1.01
D85	b	8.67	8.64	1.00
D86	b	8.35	8.35	1.00
D87	b	8.27	8.62	1.04

* OGA:
a = Gages 1-6, Gaussian Smooth
b = Gages 1-6, Raw Data
c = Gages 1-7, Gaussian Smooth
d = Gages 1-7, Raw Data

NGA:
a = Gages 12-17, Gaussian Smooth
b = Gages 12-17, Raw Data
c = Gages 11-18, Gaussian Smooth
d = Gages 11-18, Raw Data

Table 17

Summary of Wave Transformation Phase Wave Heights

Series	Minimum	Maximum	Average, Std Dev
Unimodal	0.81	0.88	0.85, ±0.02
Superposition	0.83	1.08	0.94, ±0.09
Directional	0.79	0.92	0.86, ±0.03
Nonbreaking	0.98	1.07	1.02, ±0.03

Table 18

Gage Analysis Code

Nearshore Gage Array

Code	Gages	Smoothing
a	12 to 17	Yes
b	12 to 17	No
c	11 to 18	Yes
d	11 to 18	No

direction and directional spread estimates can have errors in the range of ±4 to 8 deg.

105. Figure 33a illustrates this trend for the unimodal, unidirectional case D08. Figure 33b shows significant narrowing for the unimodal case S57 with wide directional spreading (σ_m = 40 deg). The bimodal case D29 ($\bar{\theta}_1 = \bar{\theta}_2$ = 0 deg, $\sigma_{m,1}$ = 20 deg, $\sigma_{m,2}$ = 40 deg) illustrates a narrowing in the first mode and widening in the second mode (Figure 34a). Case D26 has the same target directional distribution as case D29. The main difference between the two cases is energy distribution in frequency: case D26 has even modal distribution and case D29 has more energy in the low-frequency mode. Figure 34b, for case D26, is an example where the directional distribution remains fairly constant. Plots of remaining cases are contained in Appendix I. The format is the same as directional spectral plots for the Signal Calibration Phase in Appendix C.

106. Peak wave direction. Table 19 lists the measured OGA and NGA mean wave directions for each of the cases. The format is the same as Table 13. The largest directional shift was in the cases with $\bar{\theta}$ = 20 deg. Figure 35a illustrates this shift in wave direction for the unimodal, unidirectional case S25. In the bimodal cases, the maximum variation was 12 deg in

Table 19

Summary of Measured Peak Wave Direction

Case Id	Gage Code*	Mode 1 OGA Deg	Mode 1 NGA Deg	Mode 1 OGA-NGA	Mode 2 OGA Deg	Mode 2 NGA Deg	Mode 2 OGA-NGA
			Unimodal Series				
S01	b	0	0	0	-	-	-
S09	a	-2	-2	0	-	-	-
S13	b	8	6	2	-	-	-
S21	a	-6	0	-6	-	-	-
S25	b	18	12	6	-	-	-
S33	c	6	0	6	-	-	-
S37	b	0	0	0	-	-	-
S45	c	2	-4	6	-	-	-
S49	b	8	6	2	-	-	-
S57	c	-4	-4	0	-	-	-
S61	b	18	14	4	-	-	-
S69	a	0	0	0	-	-	-
			Superposition Series				
D01	b	0	0	0	-	-	-
D02	b	0	0	0	-	-	-
D03	b	0	0	0	0	0	0
D04	b	0	0	0	-	-	-
D05	b	0	0	0	-	-	-
D06	b	0	0	0	0	0	0
D07	b	0	0	0	-	-	-
D08	b	0	0	0	-	-	-
D09	b	0	0	0	0	0	0
			Directional Series				
D13	a	-2	-2	0	0	2	-2
D16	a	-2	0	-2	2	0	2
D19	c	0	6	-6	6	2	4
D23	b	-4	-4	0	-24	-6	-18
D26	d	-2	0	-2	-8	2	-10
D29	a	-10	-2	-8	2	0	2
D33	b	18	12	6	18	12	6
D36	b	18	12	6	18	12	6
D39	b	18	10	8	18	12	6
D43	a	4	2	2	2	2	0
D46	a	8	6	2	2	6	-4
D49	a	8	0	8	8	6	2
D51	b	0	0	0	18	12	6
D52	c	4	4	0	18	8	10
D53	a	8	4	4	4	0	4
D61	b	0	0	0	0	0	0
D62	c	6	6	0	-2	-6	4
D63	b	18	12	6	18	12	6
D64	b	22	16	6	20	4	16
D65	b	0	0	0	18	14	4
D66	c	6	8	-2	10	-10	20
D67	a	6	6	0	2	6	-4
D68	a	20	8	12	16	2	14
			Nonbreaking Series				
D71	b	0	0	0	18	12	6
D72	c	2	6	-4	18	10	8
D73	a	8	4	4	6	2	4
D81	b	0	0	0	0	0	0
D82	c	2	6	-4	-4	2	-6
D83	b	18	12	6	18	12	6
D84	b	22	16	6	20	4	16
D85	b	0	0	0	18	14	4
D86	c	0	6	-6	12	-2	14
D87	a	6	6	0	2	6	-4

* OGA:
a = Gages 1-6, Gaussian Smooth
b = Gages 1-6, Raw Data
c = Gages 1-7, Gaussian Smooth
d = Gages 1-7, Raw Data

NGA:
a = Gages 12-17, Gaussian Smooth
b = Gages 12-17, Raw Data
c = Gages 11-18, Gaussian Smooth
d = Gages 11-18, Raw Data

case D68 for the first mode and 20 deg in case D66 for the second mode. The target energy distributions are the same for both cases, but the directional distributions are different. Figures 35b and 35c illustrate this behavior for case D68 ($\bar{\theta}_1$ = 20 deg, $\bar{\theta}_2$ = 0 deg, $\sigma_{m,1}$ = 20 deg, $\sigma_{m,2}$ = 40 deg) and case D66 ($\bar{\theta}_1$ = 0 deg, $\bar{\theta}_2$ = 20 deg, $\sigma_{m,1} = \sigma_{m,2}$ = 40 deg), respectively.

107. Directional spread. Table 20 lists measured OGA and NGA directional spread for the 54 cases. It has the same format as Table 14. The unidirectional cases basically did not change. The slight widening of 1 deg for some unidirectional cases is probably not significant. One anomaly occurred for the second mode of the unidirectional case D65 ($\bar{\theta}_2$ = 20 deg). A secondary unidirectional peak formed at $\bar{\theta}$ = 0 deg (Figure 36). This is a good example of a nonlinear interaction: second mode energy shifted to the direction of the first mode. The maximum change of 22 deg occurred for case S57 with $\sigma_{m,1}$ = 40 deg (see Figure 33b).

108. Discussion. In general, directional distribution estimates for the 26 unidirectional cases were excellent. The 28 directionally spread cases, however, exhibited much more variability although central tendencies matched reasonably well. Explanations of this variability are:

a. Changes in peak direction and narrowing of the distributions were primarily due to wave refraction. For example, a wave with σ_m = 35 deg at the OGA would refract to a σ_m = 22 to 24 deg at the NGA for the range of f_p tested.

b. The directional resolution of the linear NGA was the same as the OGA: 4 to 8 deg for the range of f_p = 0.80 to 0.40 Hz, respectively. The NGA design was based on earlier field tests with different design requirements. An optimum design would provide better resolution.

c. The FFT-based analysis algorithm might not be capable of resolving the wide directional distributions. Additional analysis with the high-resolution MLM should be undertaken.

Table 20
Summary of Measured Directional Spread

Case Id	Gage Code*	Mode 1 OGA Deg	Mode 1 NGA Deg	Mode 1 OGA-NGA	Mode 2 OGA Deg	Mode 2 NGA Deg	Mode 2 OGA-NGA
			Unimodal Series				
S01	b	5.00	5.00	0.00	-	-	-
S09	a	12.00	10.00	2.00	-	-	-
S13	b	5.00	5.00	0.00	-	-	-
S21	a	17.00	9.00	8.00	-	-	-
S25	b	5.00	5.00	0.00	-	-	-
S33	c	18.00	13.00	5.00	-	-	-
S37	b	3.00	3.00	0.00	-	-	-
S45	c	15.00	10.00	5.00	-	-	-
S49	b	3.00	3.00	0.00	-	-	-
S57	c	31.00	9.00	22.00	-	-	-
S61	b	3.00	3.00	0.00	-	-	-
S69	a	25.00	8.00	17.00	-	-	-
			Superposition Series				
D01	b	4.00	5.00	-1.00	-	-	-
D02	b	4.00	4.00	0.00	-	-	-
D03	b	4.00	5.00	-1.00	4.00	4.00	0.00
D04	b	4.00	5.00	-1.00	-	-	-
D05	b	4.00	4.00	0.00	-	-	-
D06	b	4.00	5.00	-1.00	4.00	4.00	0.00
D07	b	4.00	5.00	-1.00	-	-	-
D08	b	4.00	4.00	0.00	-	-	-
D09	b	4.00	5.00	-1.00	4.00	4.00	0.00
			Directional Series				
D13	a	14.00	9.00	5.00	19.00	10.00	9.00
D16	a	16.00	16.00	0.00	15.00	13.00	2.00
D19	c	12.00	13.00	-1.00	26.00	33.00	-7.00
D23	b	12.00	11.00	1.00	32.00	19.00	13.00
D26	d	8.00	7.00	1.00	38.00	39.00	-1.00
D29	a	17.00	11.00	6.00	9.00	15.00	-6.00
D33	b	5.00	6.00	-1.00	4.00	4.00	0.00
D36	b	5.00	5.00	0.00	4.00	4.00	0.00
D39	b	5.00	5.00	0.00	4.00	4.00	0.00
D43	a	15.00	9.00	6.00	14.00	14.00	0.00
D46	a	28.00	8.00	20.00	17.00	15.00	2.00
D49	a	21.00	21.00	0.00	8.00	15.00	-7.00
D51	b	4.00	5.00	-1.00	4.00	4.00	0.00
D52	c	21.00	13.00	8.00	11.00	14.00	-3.00
D53	a	12.00	9.00	3.00	14.00	9.00	5.00
D61	b	4.00	5.00	-1.00	3.00	3.00	0.00
D62	c	21.00	12.00	9.00	17.00	22.00	-5.00
D63	b	5.00	5.00	0.00	3.00	3.00	0.00
D64	b	15.00	15.00	0.00	17.00	9.00	8.00
D65	b	4.00	5.00	-1.00	3.00	9.00	-6.00
D66	c	23.00	10.00	13.00	28.00	22.00	6.00
D67	a	10.00	11.00	-1.00	8.00	10.00	-2.00
D68	a	16.00	11.00	5.00	17.00	12.00	5.00
			Nonbreaking Series				
D71	b	4.00	5.00	-1.00	4.00	4.00	0.00
D72	c	19.00	12.00	7.00	10.00	14.00	-4.00
D73	a	11.00	9.00	2.00	15.00	10.00	5.00
D81	b	4.00	4.00	0.00	3.00	3.00	0.00
D82	c	18.00	12.00	6.00	16.00	13.00	3.00
D83	b	5.00	5.00	0.00	3.00	3.00	0.00
D84	b	15.00	14.00	1.00	17.00	10.00	7.00
D85	b	4.00	5.00	-1.00	3.00	3.00	0.00
D86	c	19.00	11.00	8.00	18.00	23.00	-5.00
D87	a	10.00	10.00	0.00	9.00	11.00	-2.00

* OGA:
a = Gages 1-6, Gaussian Smooth
b = Gages 1-6, Raw Data
c = Gages 1-7, Gaussian Smooth
d = Gages 1-7, Raw Data

NGA:
a = Gages 12-17, Gaussian Smooth
b = Gages 12-17, Raw Data
c = Gages 11-18, Gaussian Smooth
d = Gages 11-18, Raw Data

PART V: SUMMARY AND CONCLUSIONS

109. The GBM tests were conducted to study transformation of directional wave spectra propagating over a gently sloping beach in a controlled laboratory environment. Little guidance exists on the combined effects of frequency-directional energy distributions on wave shoaling, refraction, and breaking. Knowledge of transformed wave conditions is critical for estimating beach evolution and designing coastal structures. Results from this research will be used to upgrade numerical models for predicting nearshore wave properties from offshore measurements or hindcasts.

110. A fixed-bed model with bathymetry consisting of plane, parallel contours with a 1:30 slope was patterned after Torrey Pines Beach in southern California. The rectangular model measured 36.6 by 18.3 m and had an offshore water depth of 50 cm. The toe of the beach was 4.5-m in front of the DSWG.

111. A total of 54 directional spectra was simulated as the product of the TMA spectral form and a wrapped normal spreading function. Both unimodal (single peak) and bimodal (double peak) frequency spectra with varying energy distributions were simulated. The ratios of energy between modes in the bimodal cases were 1/3:2/3, 1/2:1/2, and 2/3:1/3. Directional distributions (combination of peak wave direction and directional spread) were both narrow (unidirectional) and wide (directional) and were varied between modes. Peak wave periods were 1.25, 1.75, and 2.50 sec; wave heights were 6.5, 7.6, 10.8, 12.2, 13.2, and 15.2 cm; spectral peakedness parameters were 3.3 and 20.0; peak wave directions were 0 (shore-normal) and 20 deg; and full-width spread parameters were 1, (unidirectional), 20, and 40 deg.

112. Twenty capacitance wave gages were arranged in patterns and water depths similar to the prototype arrays used in 1978 and 1980 experiments at Torrey Pines Beach. The gage pattern consisted of two 8-1-3-2-5 alongshore linear arrays to measure changes in directional distributions and a cross-shore array to study transformation of wave frequency spectra. The linear OGA and NGA were located in water depths of 40 and 16 cm (0.52 ft), respectively. Lag spacings between gages for the OGA and NGA were 85 and 55 cm, respectively. The design of these linear arrays allowed measurements of waves with a directional resolution of 4 to 8 deg for the range of peak periods tested. The CGA was nested within these two linear arrays, transverse to their axes and aligned with the physical model center line.

113. The 54 wave conditions were converted into stroke control signals for each of the 61 paddles of the DSWG using a frequency domain, double summation, deterministic amplitude, random phase model. Typically, control signals were digitized at 20 Hz for 750-sec duration. Data were sampled at 10 Hz for a minimum duration corresponding to 200 waves of the mode with the longest peak period.

114. Data analyses consisted of time domain zero-downcrossing, frequency domain single-channel spectral analysis, and directional spectral analysis. For the spectral analysis, the wave gage data were zero-meaned, tapered by a 10-percent cosine bell window, Fourier transformed, and band averaged between lower and upper cutoff frequencies of 0.01 and 2.50 Hz, respectively. This process yielded a resolution bandwidth of 0.024 Hz. The directional spectral analysis is based on a Fourier series expansion of the directional spreading function. The measured data again were zero-meaned, windowed, and Fourier transformed to the frequency domain. A Gaussian smoothing function then was used to smooth the cross-spectral matrix of autospectra and cross-spectra. A linear, stepwise regression model was used to solve for the Fourier coefficients of spreading function.

115. Prior to wave transformation tests, three preliminary test phases were conducted: basin circulation, test duration, and signal calibration. In Phase 1, four current meters were positioned along the basin perimeter to measure the presence (if any) of wave-induced circulation in the basin. Based on these measurements, dye tracer, and visual observations for two cases, wave-induced circulation was not judged to be significant, and further tests with the other cases were not deemed necessary.

116. In Phase 2, test durations of 200 and 400 waves at the peak period for the first 12 unimodal cases were compared to determine the proper sampling duration. For the OGA, the maximum peak period variation was 4 and 2 percent for the 2.50- and 1.25-sec period cases, respectively. Maximum wave height variation was 5 percent for both periods. Spectral shapes did not vary significantly due to changes in sampling duration. The amplification factor (ratio of spectral ordinate for 200 wave duration divided by ordinate for 400 wave duration) clustered around 1.0 with a range between 0.5 to 1.5, within the 95-percent confidence limits for the spectral estimates. Thus, it was decided to test for the shorter duration for the last two test phases of signal calibration and wave transformation.

117. In the signal calibration phase (Phase 3), each of the 54 control signals was iteratively corrected one to four times using an RAO transfer function and system gain factor to match the target directional wave spectra as closely as possible. The RAO is calculated in the frequency domain as the ratio of average measured frequency spectrum from the OGA to target spectrum. The control signal that produced measured spectra then is corrected in the frequency domain before being transformed back to the time domain for the next iteration. The RAO seems to work well up to two or three iterations, after which improvement in the generated signal is less substantial.

118. Results from this signal calibration phase are presented in the form of plots of measured and predicted frequency spectra and directional spreading functions and tabular listings of four parameters: peak frequency, significant wave height, peak wave direction, and directional spread. Results are averages for the gages in the OGA. In general, the match between measured and predicted directional wave spectra was good to excellent.

119. The maximum variation in peak frequency was $\pm$0.04 Hz, occurring in only two cases. In most cases, there was no significant frequency shift.

120. Wave heights matched target values very well. Normalized height ratios (measured height divided by target height) averaged 0.92 for all cases with a minimum of 0.80 and a maximum of 1.01. Wave breaking and DSWG stroke limitations explain most of these energy losses.

121. The agreement between measured and predicted frequency spectra was very good to excellent. The peak of the measured spectrum was usually slightly smaller than the target spectral ordinate, but within the 95-percent confidence level. Also, since wave height was generally less than desired, one would expect the measured spectrum to be smaller. There also tended to be more energy in the high-frequency region of the measured spectrum, possibly due to energy transfers seaward of the OGA.

122. The greatest disparity was in the directional distributions. For unidirectional cases, agreement was excellent. Peak wave directions experienced differences of no more than $\pm$2 deg, directional spread ranged from a perfect match to a difference of -4 deg, and spreading functions matched target shapes in all cases. For directional cases, directional distributions showed a high degree of variability. Attempts to correct measured directional distributions using analysis techniques did not produce a substantial improvement. The effects of adding another gage (No. 7) to the OGA and the use of Gaussian smoothing on the measured directional distribution were evaluated for

all cases. Both of these techniques tended to smooth and widen the measured distribution without affecting wave direction. Peak wave directions varied from a perfect match to an extreme difference of +24 deg. In general, measured directional spread and spreading functions were narrower than desired, usually, only one-third to one-half target widths. In most cases, wave direction and spreading were contained within the measured directional distribution. In some cases, the magnitude of the side lobes was less than the 50-percent criterion, leading to narrower calculated directional spread.

123. Some explanations for the differences in measured and predicted directional spectra are listed below:

a. Accurate measurement of directional distributions in laboratory models is difficult at best. Other laboratories have reported variations of ±10 deg in peak wave directions based on differences just in the analysis method. Thus, much of the variation in these measurements is accounted for.

b. The control signals were generated in a depth of 50 cm and measured in 40-cm depth over the slope of the model. Wave refraction explains much of the observed changes in wave direction and directional spread.

c. Some of the waves experienced some minor breaking in traveling between the two water depths, producing a loss of energy.

d. Stroke limitations on the DSWG displacement, velocity, and acceleration prevented corrected control signals from being generated as prescribed. If the control signal for a particular paddle happens to contain directional information that is suppressed due to these limitations, the measured directional distribution would be altered.

e. The tuning of the OGA was not sufficient to accurately measure the wider directional distributions, especially when coupled with the larger peak wave direction. The design of the OGA was modeled after a field experiment linear array that did not necessarily experience the range of directional characteristics. Typically, a 2-3-1-7-5 linear array, patterned after the FRF, is used in physical model experiments.

f. It is possible that the OGA was in the "near field" of the DSWG. The directional wave fields did not have enough space to properly form before encountering the beach toe and being measured. The location of the OGA was a trade-off with available model space.

g. The waves were not sampled long enough for good statistical stability. The number of degrees of freedom in the analysis would have increased by a factor of two if

a duration of 400 waves had been used instead of only 200 waves.

h. Reflections from the beach might be interacting with the spectrum producing alternate reinforcement and cancellation in the energy and directional distributions. Testing this hypothesis would involve additional tests with different gage setups to accurately resolve the reflection coefficients.

124. Thus, based on experience in measuring wide directional distributions with different linear and spatial gage arrays, it is felt that the target energy and directional distributions were generated within reasonable limits. Data adaptive, high-resolution analysis techniques, such as MEM or MLM, should be investigated to see what effect they might have on the measured OGA data.

125. The unique emphasis of these tests was the study of wave transformation of bimodal directional wave spectra due to shoaling, refraction, wave breaking, and decay. Many of the cases in the GBM tests were repeats of earlier flume tests with unidirectional wave spectra on a similar beach. Analyses in this report are not meant to be exhaustive, but rather a preliminary indication of effects of linear and nonlinear interactions on wave transformation.

126. Time domain results include time series plots of surface wave elevation for the CGA and tabular listings of zero-downcrossing average elevation and significant wave period and height. Time series plots revealed the classic, nonlinear "sawtooth" wave shape of steep front faces and flat rear slopes in very shallow water due to wave transformation.

127. Frequency domain results include single-channel spectral analysis of the CGA. Spectral analysis results include listings of measured peak wave periods and zero-moment wave height for all gages, and linear and semilog spectral plots of gages in the CGA.

128. Peak wave periods in the CGA showed little change due to wave transformation. Typically, they remained invariant or shifted slightly to a lower frequency.

129. The wave height data were the most extensively analyzed. Zero-moment wave height values were used for comparisons because there was no significant difference with zero-downcrossing and time series derived wave heights. A summary of results is presented below:

a. Measured wave heights in the CGA display a trend of a flat shoaling region followed by a linearly decreasing

decay region. Extent of the shoaling region varies according to initial height. Smaller initial heights have longer shoaling regions with less steep decay through the breaker zone. Agreement with the flume tests is very good, varying no more than 5 to 15 percent.

b. The effect of energy distribution between modes was evaluated. When more energy is in the low-frequency mode relative to the high-frequency mode (swell and sea), larger wave heights are recorded in the shoaling region. This effect is in agreement with flume test results.

c. The effect of directional distribution on unimodal cases did not appear to be significant. An increase in wave direction did produce an increase in measured wave height in the bimodal series. The effect of directional spreading was less obvious, although it did reduce the effect of variations in modal energy distribution. Maximum variations in measured height are 10 to 20 percent, with the larger value for cases with wider frequency separation between modes.

130. The linear superposition assumption was tested and compared with results from the flume tests. If this assumption was correct, measured wave heights and spectra of two unimodal spectra should match their bimodal counterparts during all stages of wave transformation. The assumption worked well in the shoaling region, but poorly in the decay region. In the decay region, wave height is overpredicted, and bimodal spectra experience faster second mode decay in the presence of the lower frequency mode. These findings are in agreement with the flume tests.

131. Elgar and Guza (1985) found nonlinear coupling between frequencies to be a significant mechanism in the transformation of ocean surface gravity waves. Results from the transformation of the CGA frequency spectra support these conclusions. Nonlinear interactions and other mechanisms are described below:

a. For unimodal broad-banded spectra, energy shifts from the peak frequency to subharmonics and harmonics as the wave travels into shallow water. During shoaling, first and second harmonics increase in magnitude. As the wave breaks, multiple nonlinear interactions among a wide range of frequencies produce smaller harmonic peaks. The third subharmonic grows as the wave transforms.

b. For unimodal narrow-banded spectra, the same pattern of spectral evolution occurs, except that fewer frequencies are involved and harmonics remain stronger throughout the wave transformation.

c. The bimodal sea and swell peak spectrum, represented by greater energy in the low-frequency mode, becomes unimodal as it transforms. Energy is initially transferred to the harmonic located at the frequency corresponding to the summation of mode frequencies. As the wave continues to decay, energy is transferred out of this mode and higher frequency mode to harmonics. The spectral "valley" between sea and swell peaks disappears. The subharmonic grows due to nonlinear difference interactions between sea and swell peaks.

d. The opposite condition, a bimodal spectrum with greater energy in the sea peak, suggests a significant nonlinear coupling of the low-frequency mode in shallow water to the high-frequency mode seaward of the surf zone. During wave transformation, energy is transferred from the sea peak to the swell peak. The dominance of the low-frequency mode is more pronounced for greater frequency separation between peaks.

e. Seiching between the DSWG and the beach was suggested as a source of the observed subharmonic growth in the frequency spectra. For a standing wave in the DSWG basin with both fixed and varying depth, the seiche frequency is approximately 0.06 Hz (15.6 sec). Although possible, it is improbable that the observed low-frequency peaks are first or second harmonics of the seiche frequency rather than true subharmonics of the peak frequency.

f. Cross-basin oscillations due to sidewall reflections can also affect the low-frequency modes in the DSWG basin. Although these reflections were minimized during the GBM study, they might have had a slight impact on the measured spectra.

132. Bispectral and cross-bispectral analysis would allow more precise location of nonlinear interactions among frequencies in measured wave spectra in the nearshore region. Bispectral analysis is used on measured data from single gages. Cross-bispectral analysis is used on two gages (as in cross-spectral coherence analysis) to detect nonlinear energy transfers between frequencies in one location to frequencies in the other location. The GBM data should be studied with these types of analyses.

133. Conclusions regarding the effect of directional distribution on wave transformation are suggested from the spectral analysis of the CGA. They are listed below:

a. For bimodal unidirectional spectra, an increase in wave direction tends to increase energy in the low-frequency mode.

b. Just the opposite occurs if the wave directions are different between modes and directional spreading is included. The energy in the low-frequency mode is decreased.

c. The inclusion of directional spreading tends to suppress the formation and growth of subharmonics in the directional spectrum.

134. Directional spectral analysis also was part of the frequency domain analysis. Results from this analysis consist of tables and plots comparing measured directional spectra for the OGA and NGA to quantify directional distribution changes due to wave transformation. This is an area that is very important for researchers in nearshore processes since not much information is available. In general, trends for the peak frequency, significant wave height, and frequency spectra are consistent with the single-channel frequency spectral analysis results. A summary of results is presented below:

a. The shape of the directional distribution remained consistent between offshore and nearshore locations. Observed changes in peak wave direction and directional spreading can be explained by refraction theory. The nonlinear interactions affecting the shape of the frequency spectrum did not appear to be a significant factor in transforming directional distributions.

b. Directional spreading did not change for the unidirectional cases. The cases with wider directional spreading tended to narrow as they traveled into shallower water. The maximum change was 22 deg.

135. The GBM tests were very successful in providing a first step in WES's attempts to understand and quantify the mechanisms that affect wave transformation over a generalized beach in a laboratory experiment. Realistic wave conditions with a range of energy and directional distributions were created and tested. Results compared well with earlier flume tests of similar unidirectional wave conditions. The extensive data set will be used to upgrade numerical models for predicting nearshore wave properties that are critical for estimating beach evolution and designing coastal structures.

REFERENCES

Briggs, M. J. 1988. "Unidirectional Spectral Wave Generation and Analysis in Wave Basins, Vol I," Technical Report CERC-88-11, US Army Engineer Waterways Experiment Station, Vicksburg, MS, pp 1-69.

Briggs, M. J., Borgman, L. E., and Outlaw, D. G. 1987. "Generation and Analysis of Directional Spectral Waves in a Laboratory Basin," OTC 5416, Offshore Technology Conference, Houston, TX, pp 495-502.

Briggs, M. J., and Jensen, R. E. 1988. "Simulation of Extreme Storm Events in Coastal Structural Models," Proceedings of the Offshore Structural Dynamics Symposium, Corvallis, OR, pp 119-133.

Carver, R. D., Briggs, M. J., and Green, D. R. "Stability Study of the 1978 Jetty Rehabilitation, Yaquina Bay, Oregon, Coastal Model Investigation," Technical Report, in preparation, US Army Engineer Waterways Experiment Station, Vicksburg, MS.

Elgar, S., and Guza, R. T. 1985. "Observations of Bispectra of Shoaling Surface Gravity Waves," Journal of Fluid Mechanics, Great Britain, Vol 161, pp 425-448.

_____. 1986. "Nonlinear Model Predictions of Bispectra of Shoaling Surface Gravity Waves," Journal of Fluid Mechanics, Great Britain, Vol 167, pp 1-18.

International Association of Hydraulic Research Working Group on Wave Generation and Analysis. 1986 (Jan). "List of Sea State Parameters," Supplement to Bulletin No. 52, pp 1-24.

Oltman-Shay, J. M. 1987. "Linear Arrays: Wind Wave Directional Measurement Systems," Seminar at US Army Engineer Waterways Experiment Station, Vicksburg, MS, pp 1-28.

Pawka, S. S. 1982. "Wave Directional Characteristics on a Partially Sheltered Coast," Ph.D. Dissertation, Scripps Institute of Oceanography, University of California, San Diego, pp 1-246.

_____. 1983. "Island Shadows in Wave Directional Spectra," Journal of Geophysical Research, Vol 88, pp 2579-2591.

Sand, S. E., and Mynett, A. E. 1987. "Directional Wave Generation and Analysis," IAHR Seminar on Wave Analysis and Generation in Laboratory Basins, Lausanne, Switzerland, pp 209-235.

Seymour, R. J., Ed. 1989. Nearshore Sediment Transport, Plenum Press, New York.

Smith, J. M., and Vincent, C. L. "Shoaling and Decay of Two Wavetrains on a Beach," Journal of Waterway, Port, Coastal and Ocean Engineering, American Society of Civil Engineers, in press.

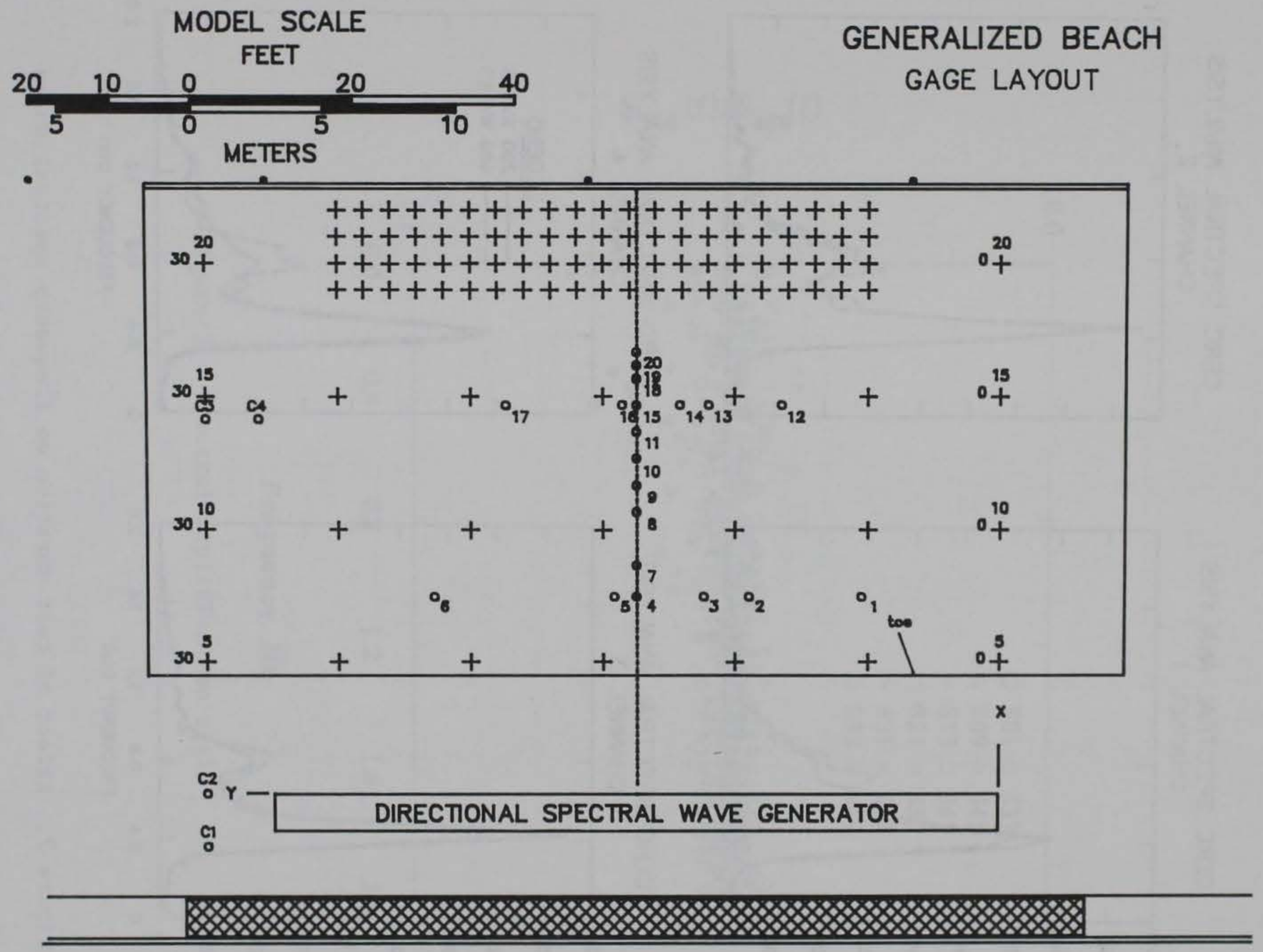

Figure 1. Model Setup

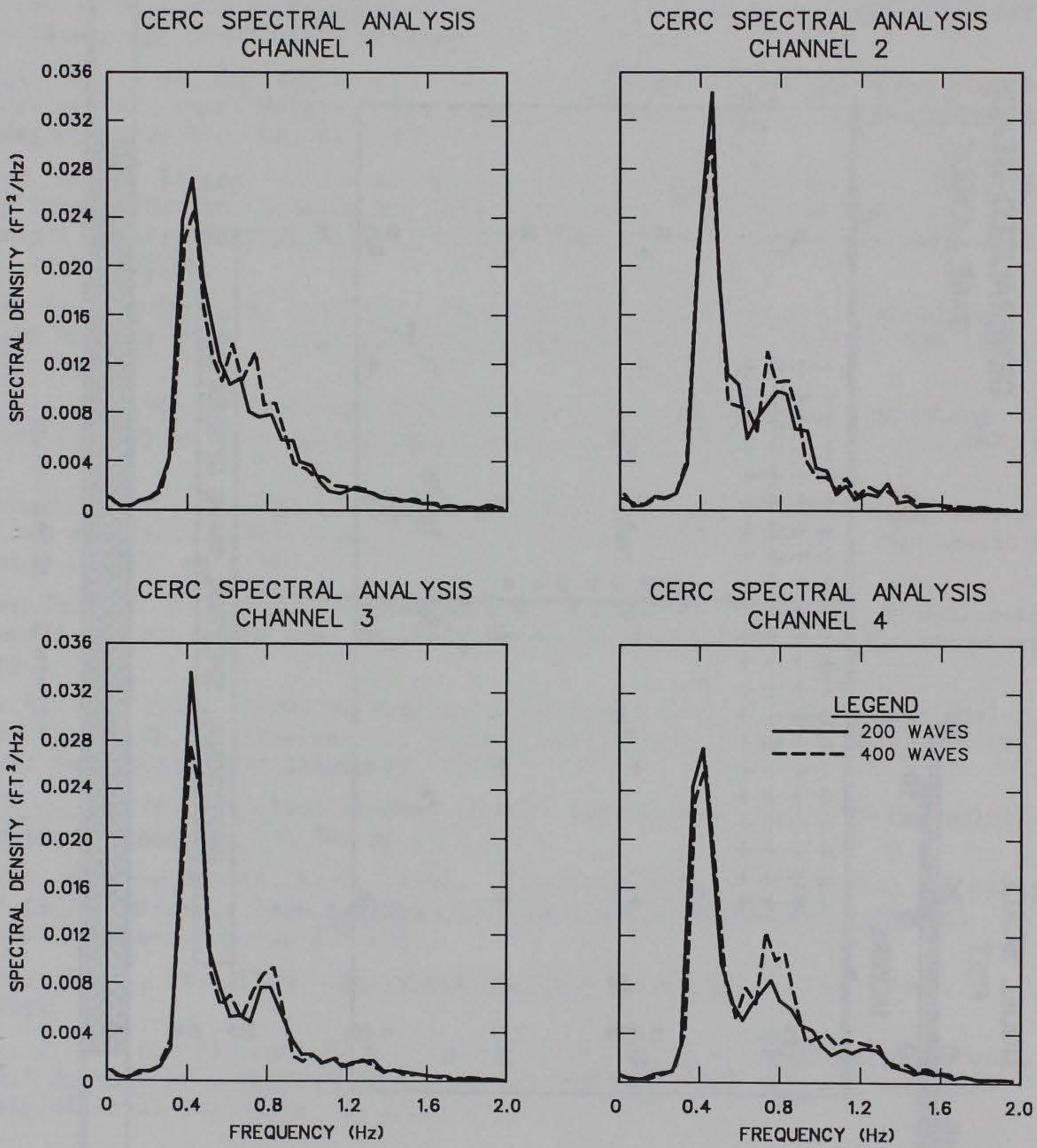

Figure 2. Effect of test duration on frequency spectral shape

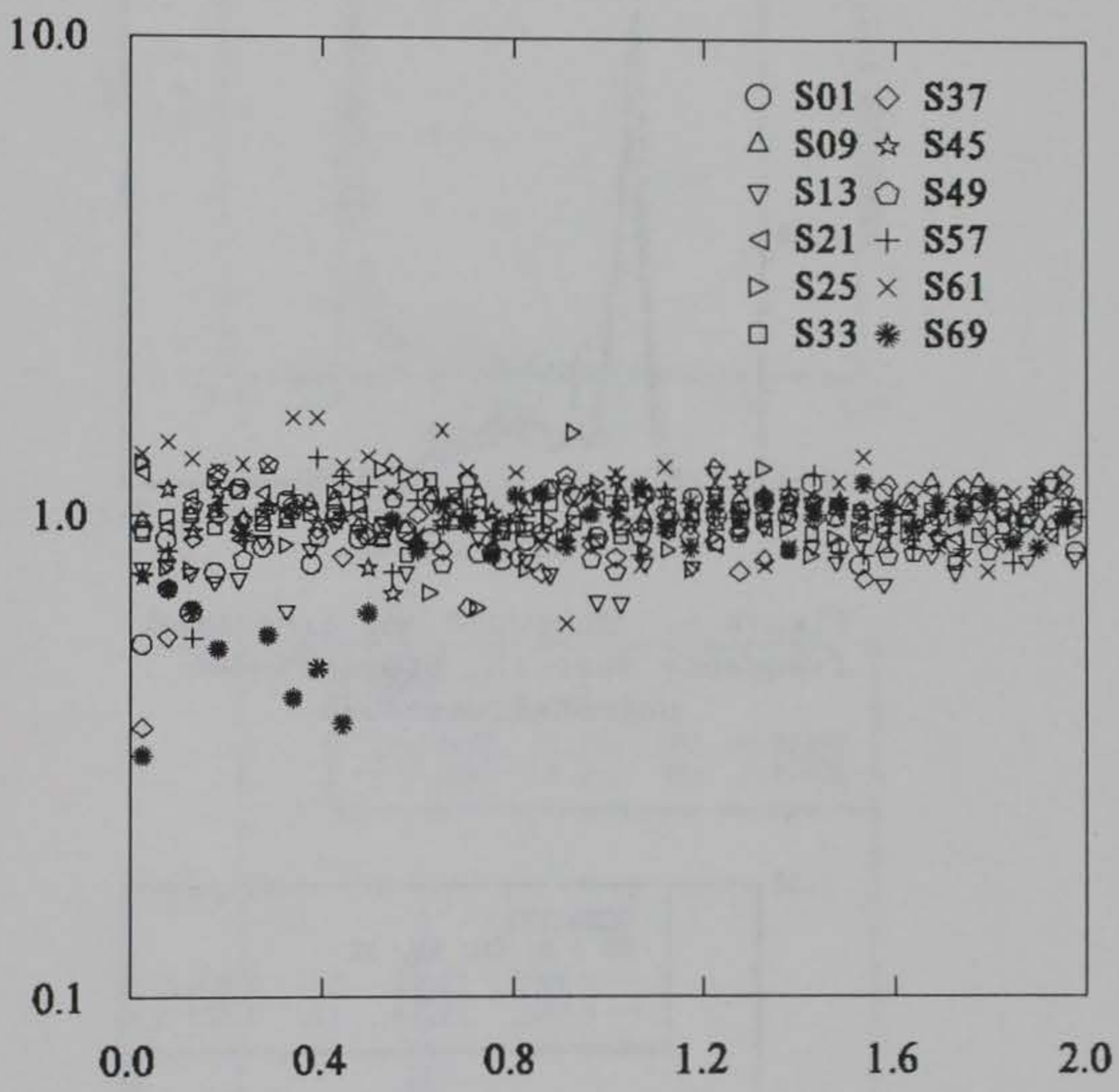

Figure 3. Spectral amplification ratio

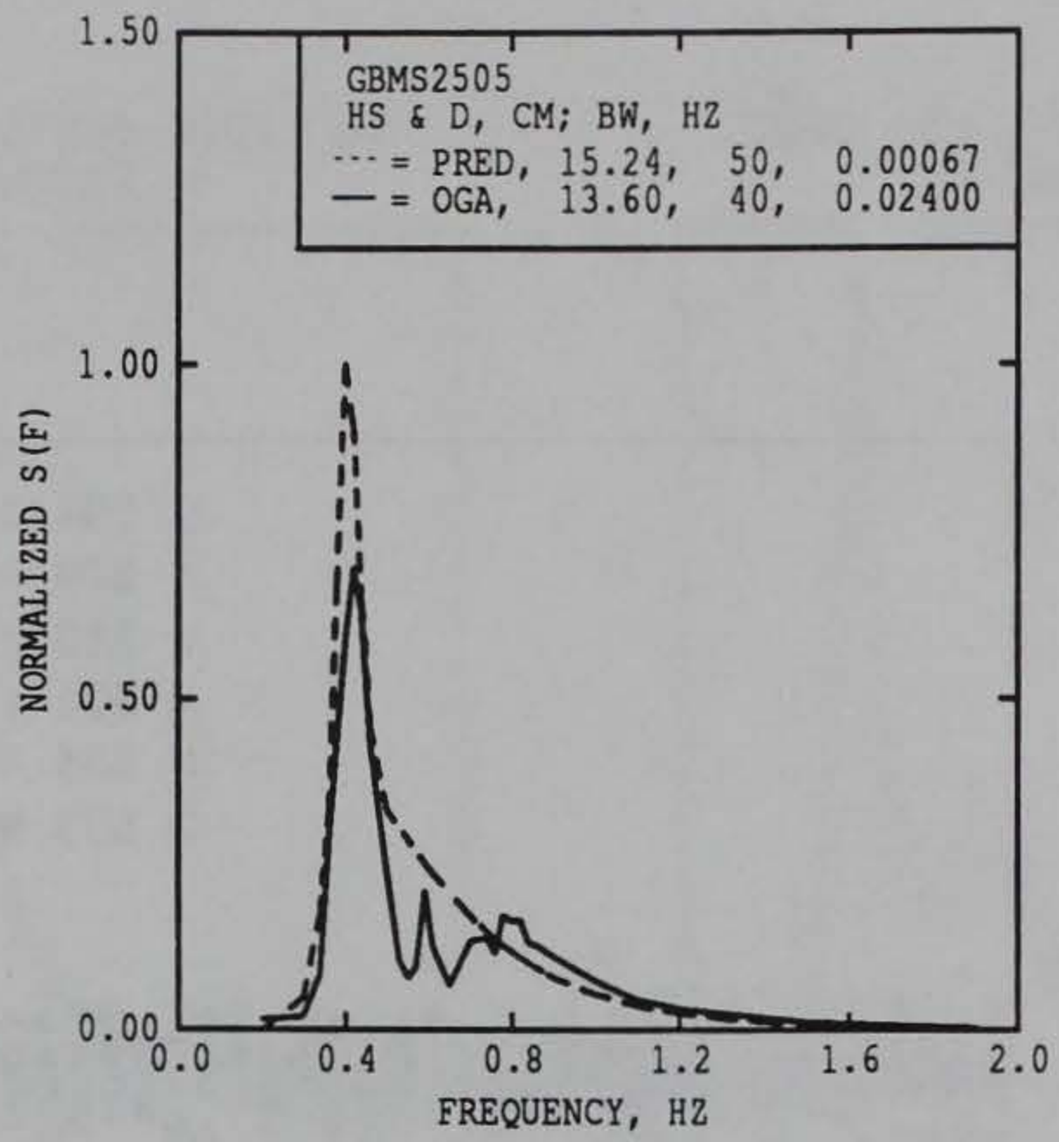

Figure 4. Measured and predicted frequency spectra, broad-banded unimodal case S25

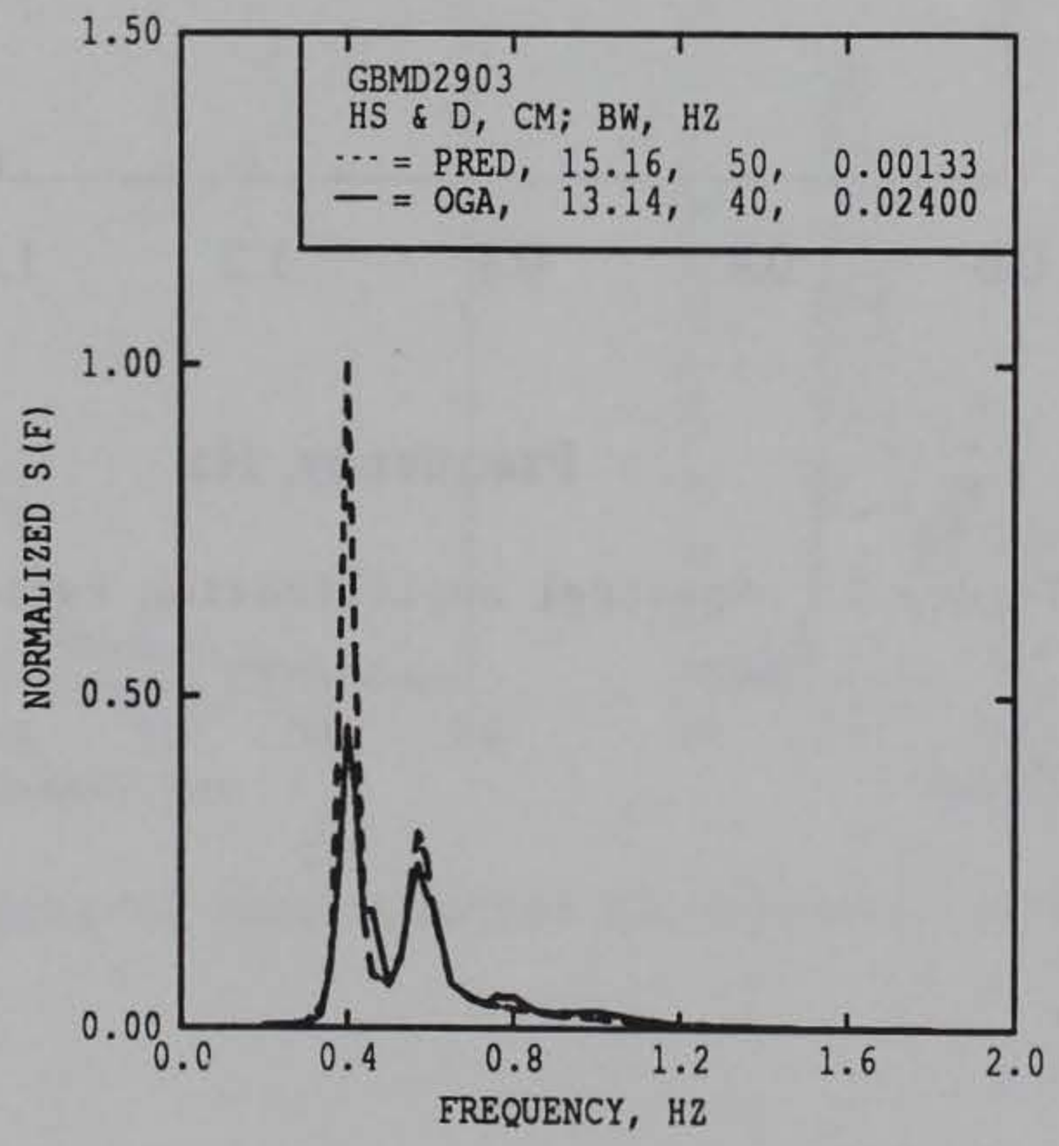

Figure 5. Measured and predicted frequency spectra, bimodal case D29

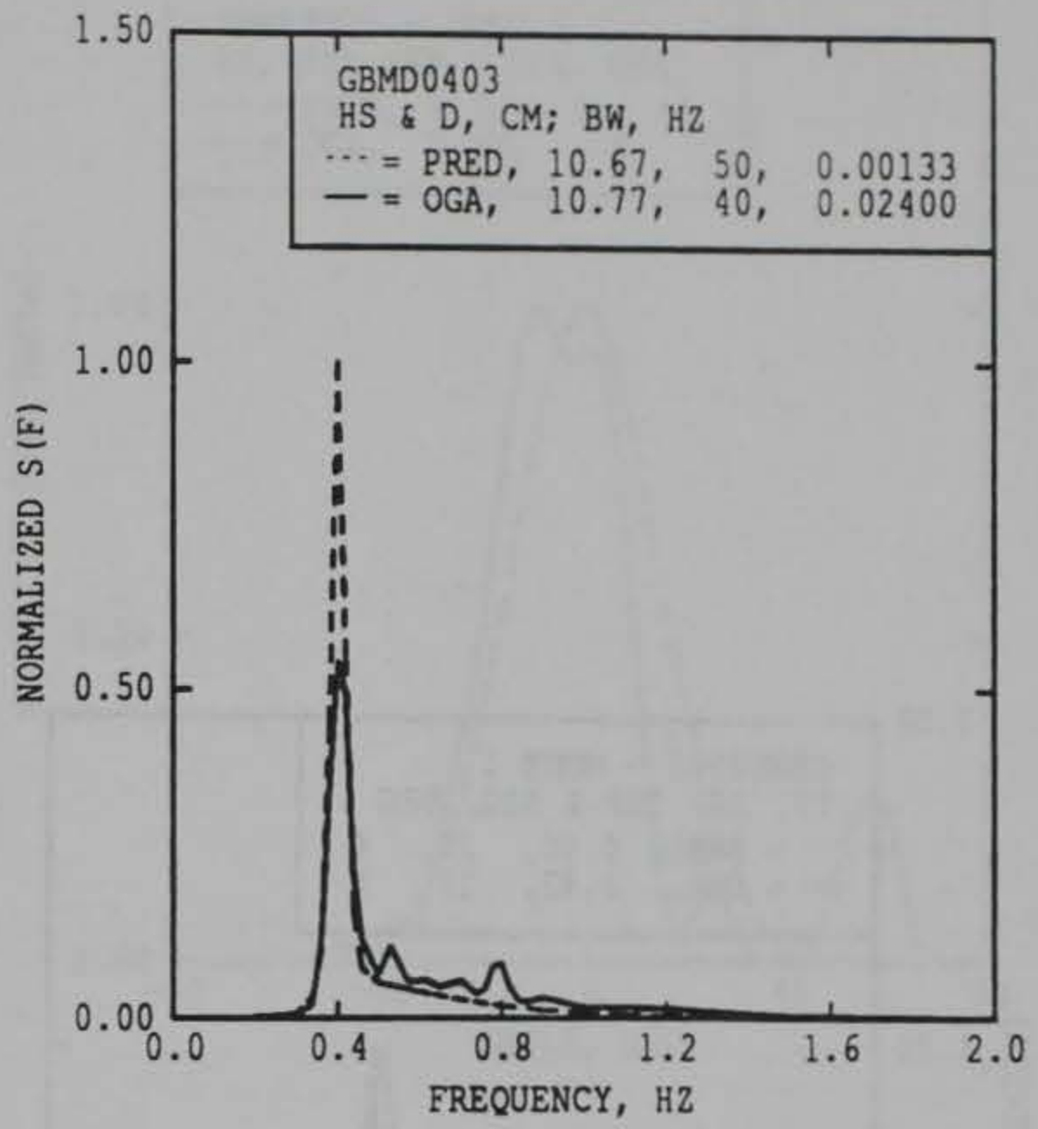

a. Case D04

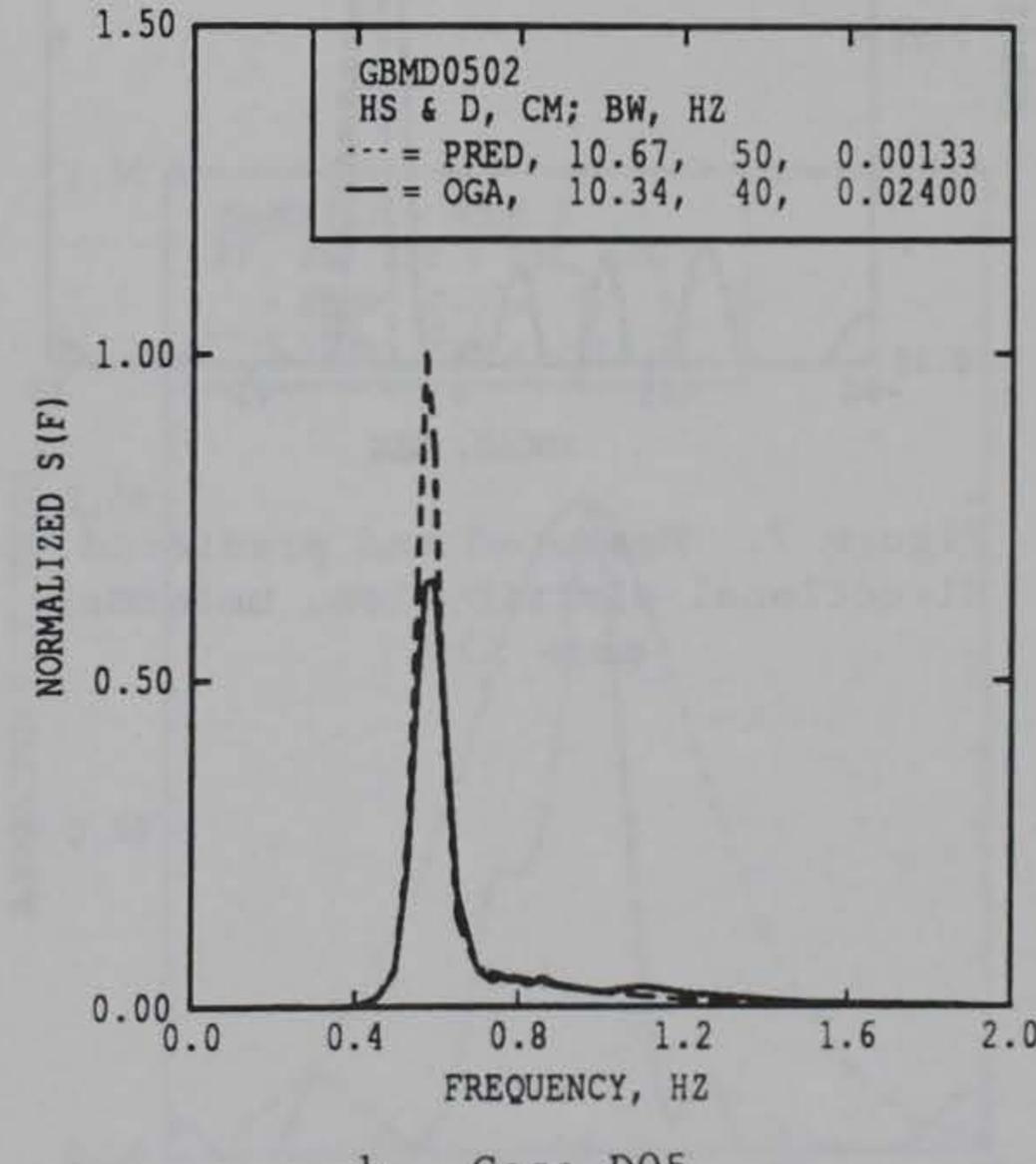

b. Case D05

Figure 6. Measured and predicted frequency spectra, narrow-banded unimodal cases

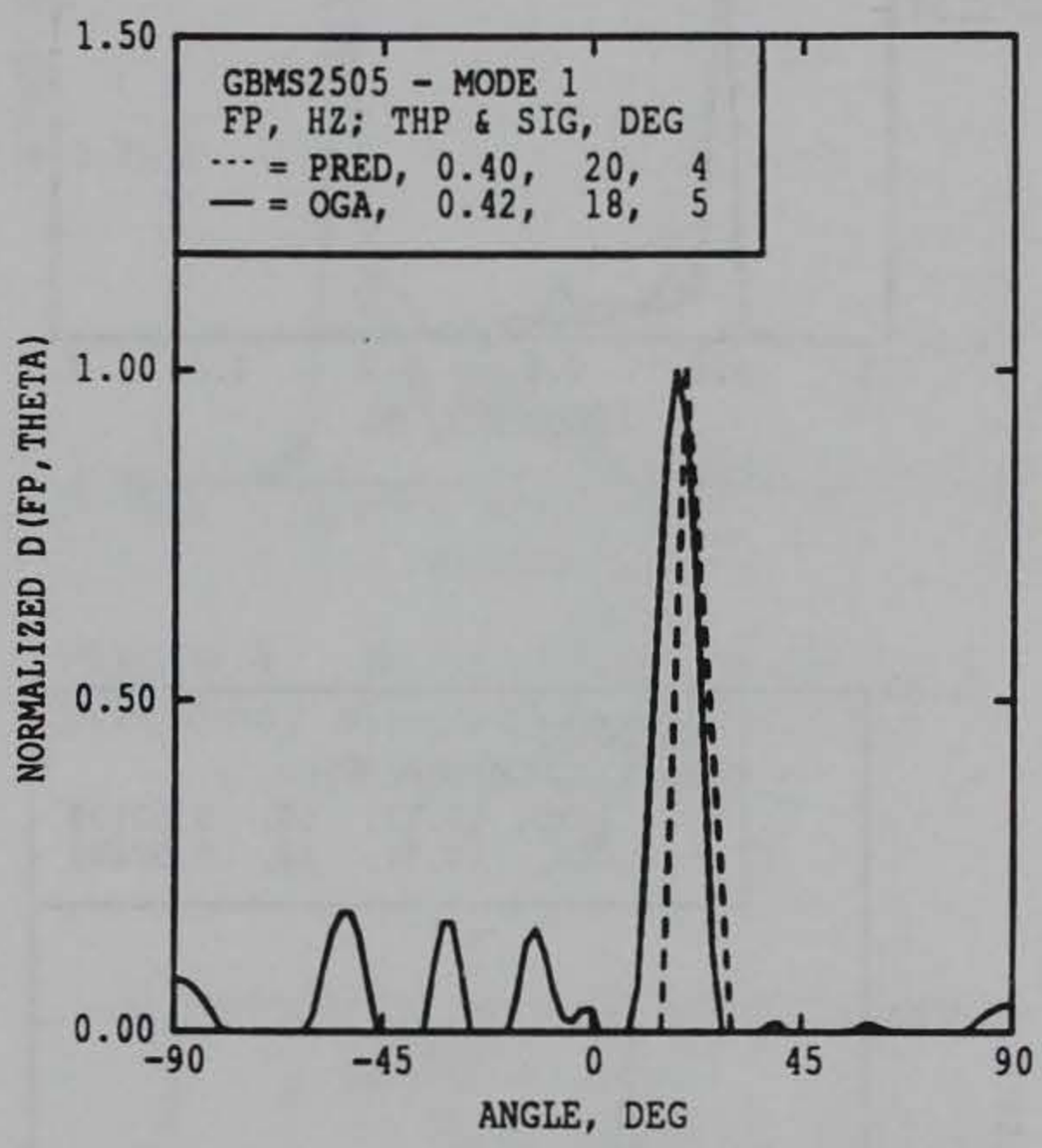

Figure 7. Measured and predicted directional distribution, unimodal case S25

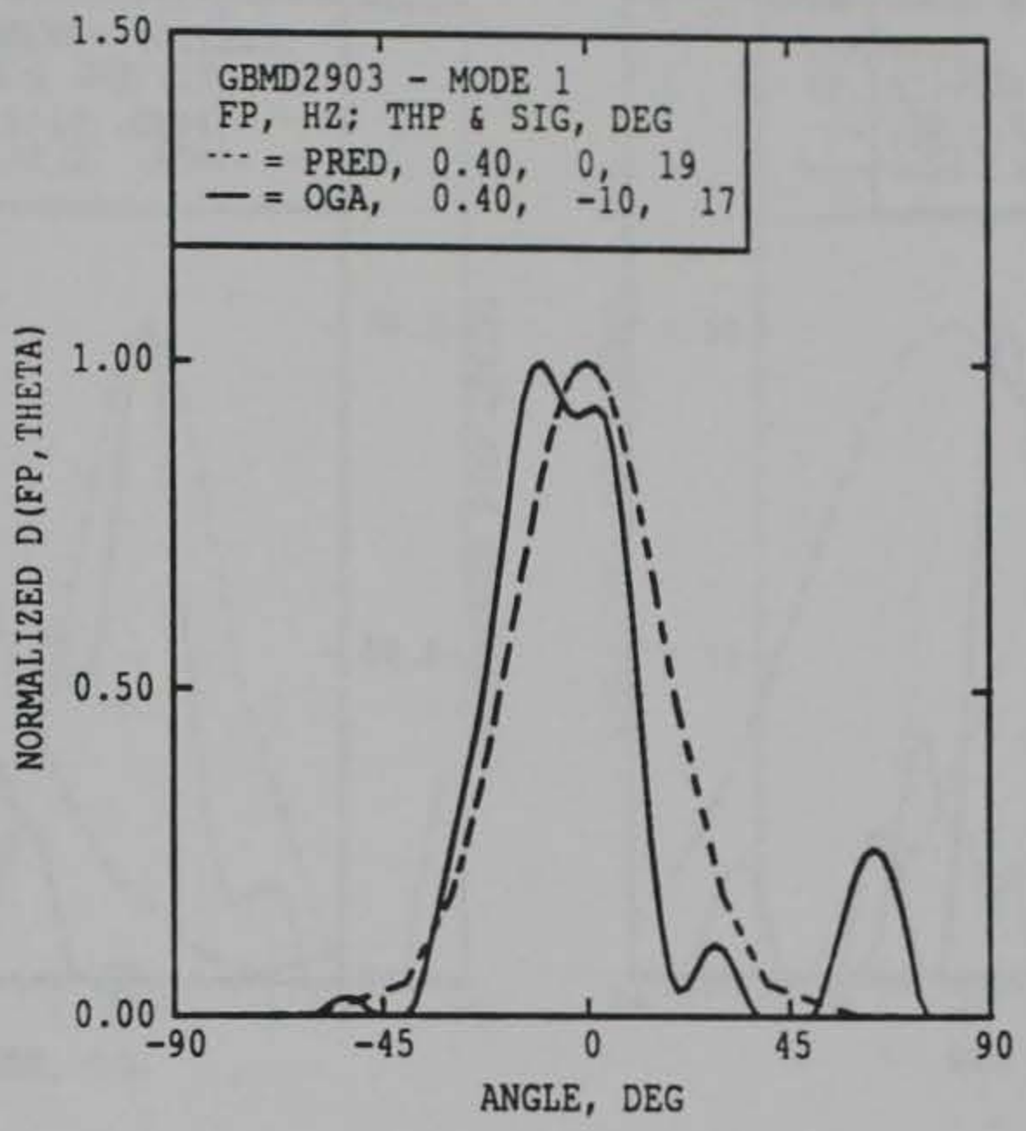

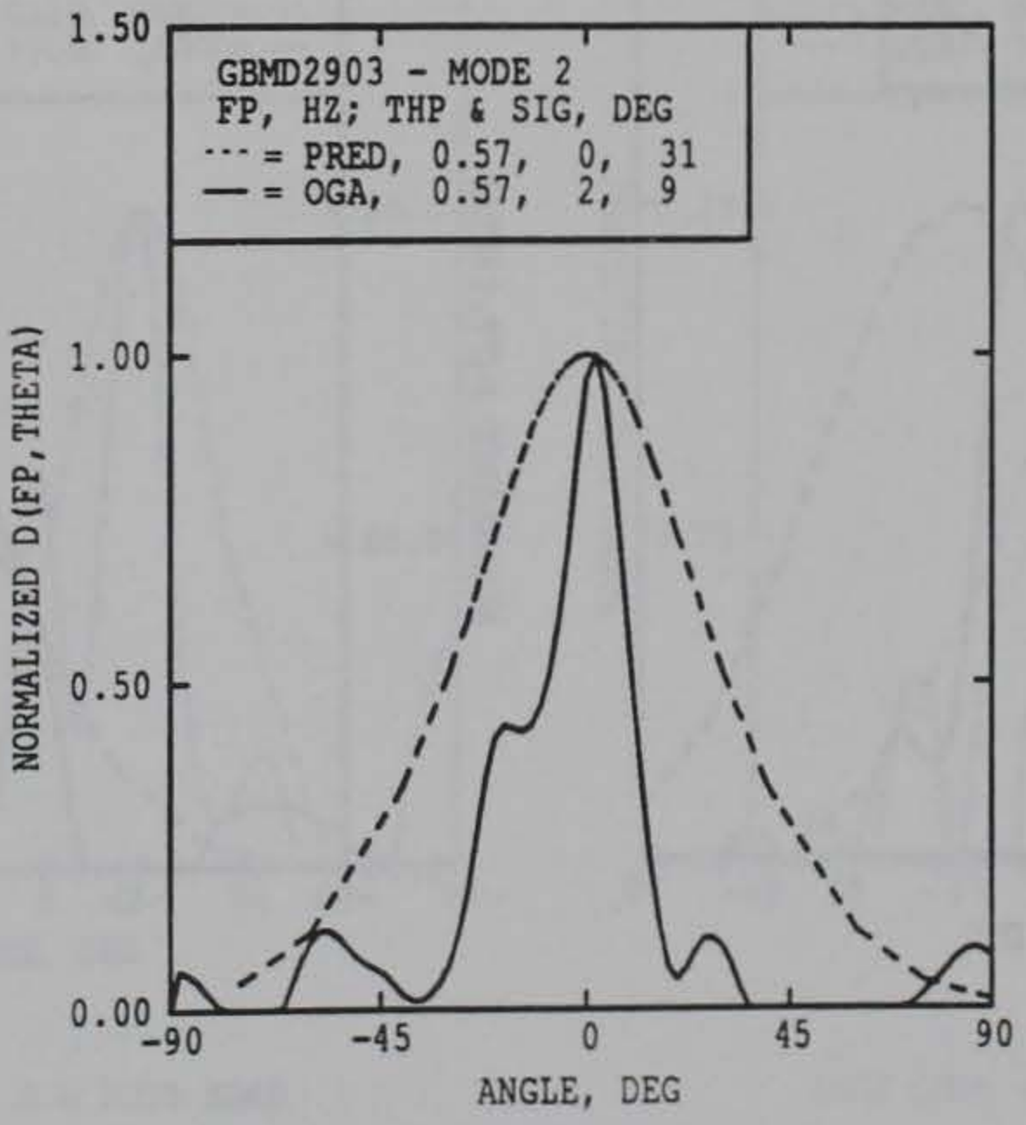

Figure 8. Measured and predicted directional distribution, bimodal case D29

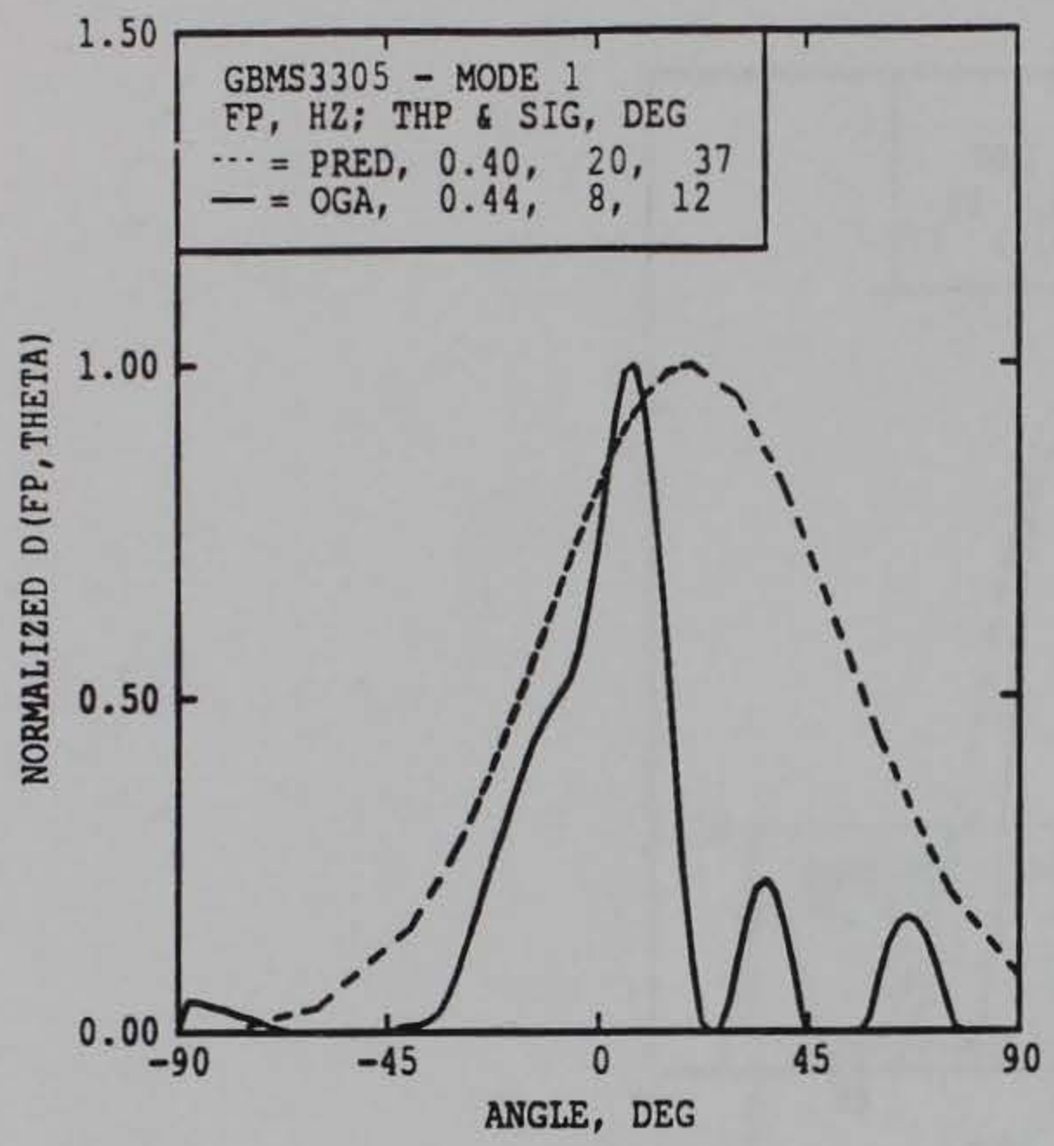

GAGE CODE = A

a. Option A

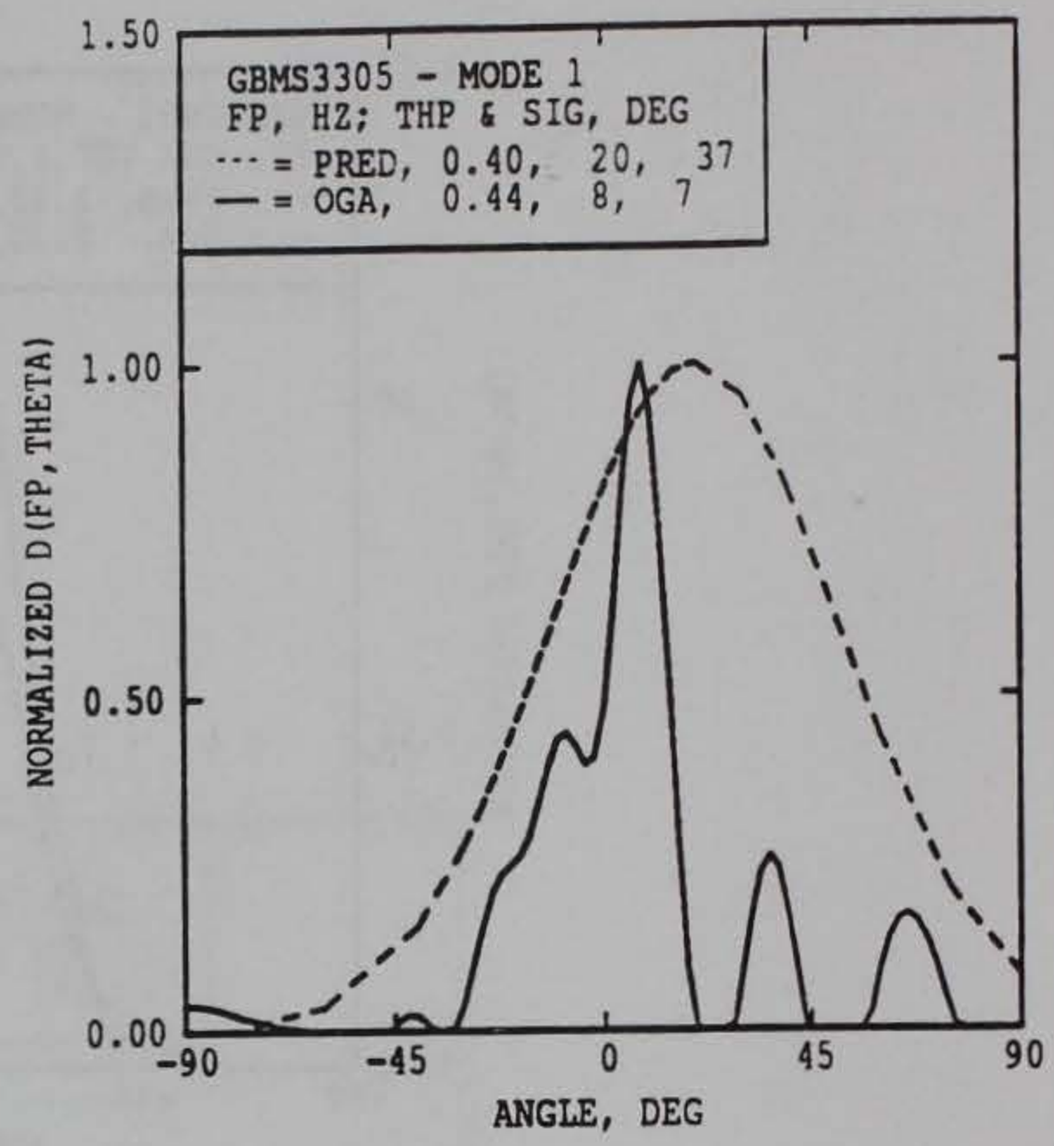

GAGE CODE = B

b. Option B

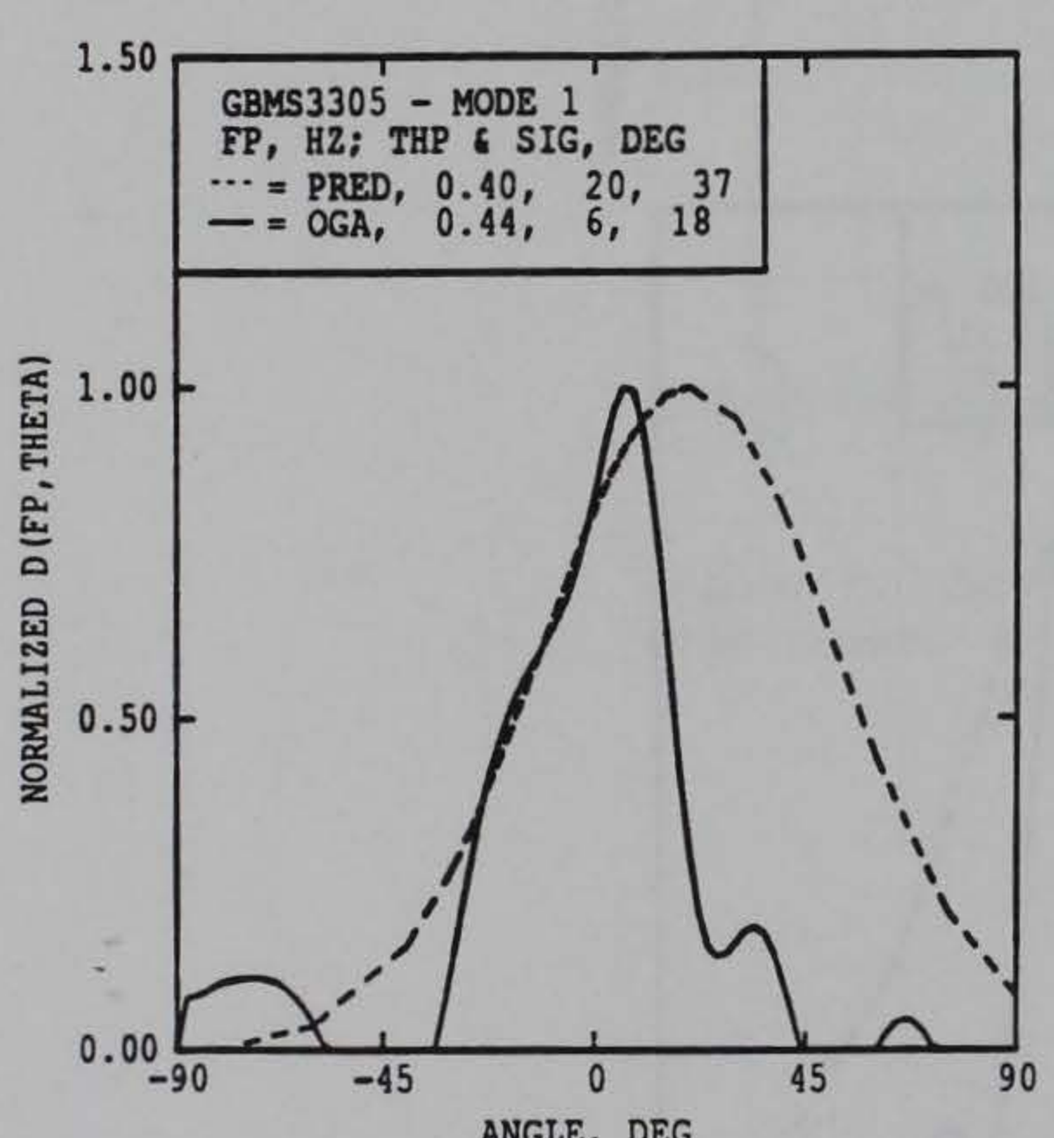

GAGE CODE = C

c. Option C

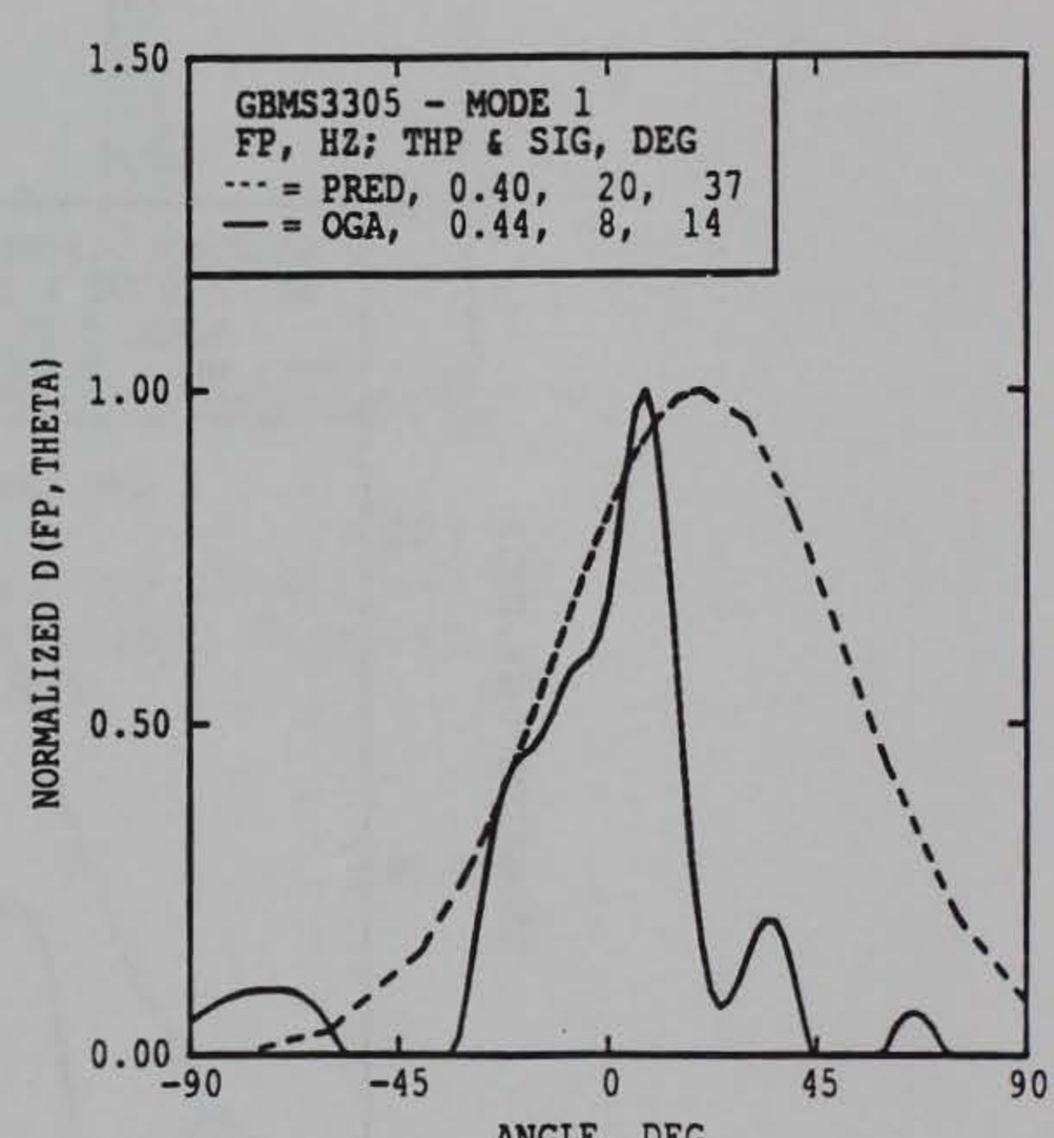

GAGE CODE = D

d. Option D

Figure 9. Directional distribution analysis results, unimodal case S33

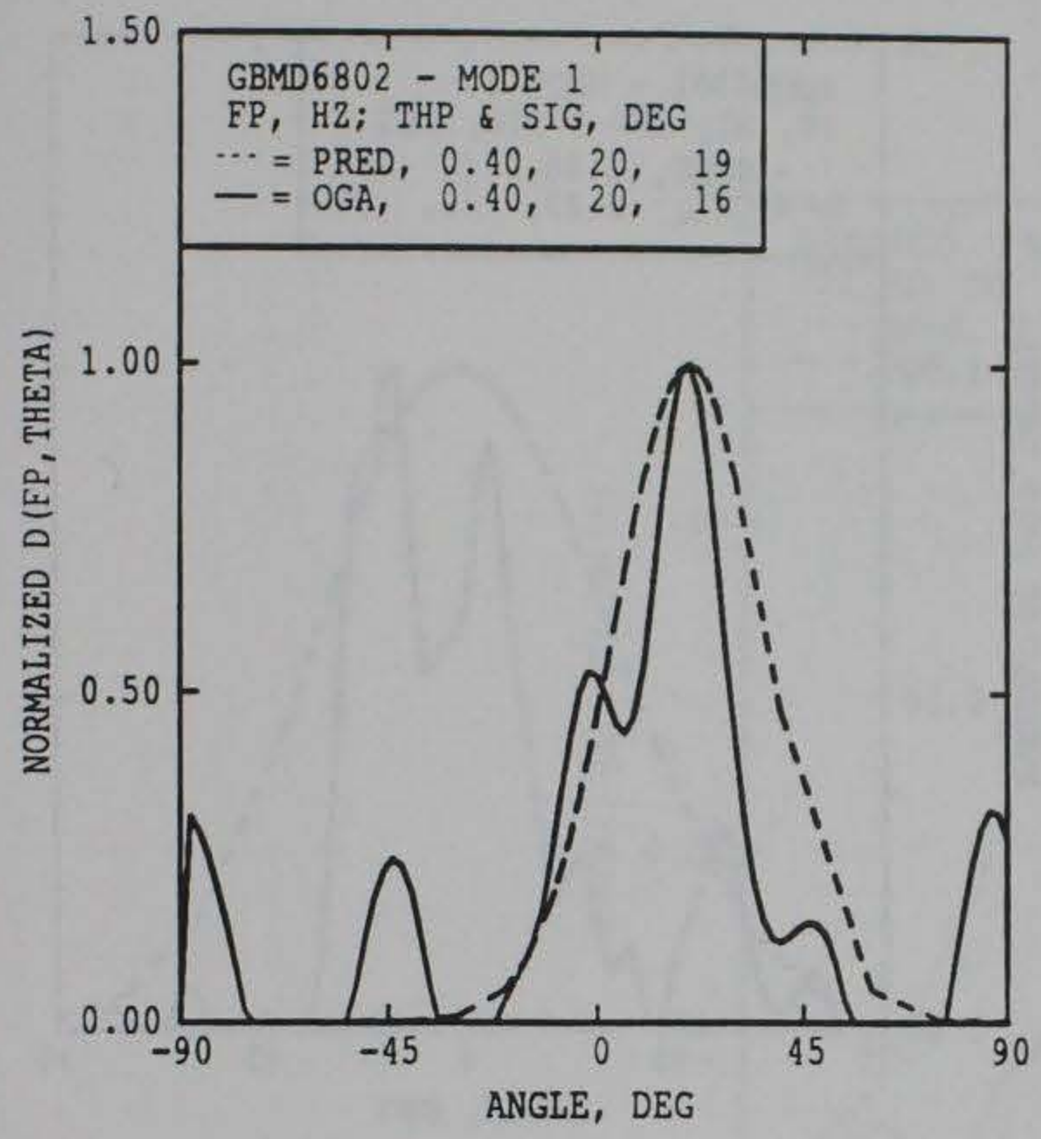

GAGE CODE = A

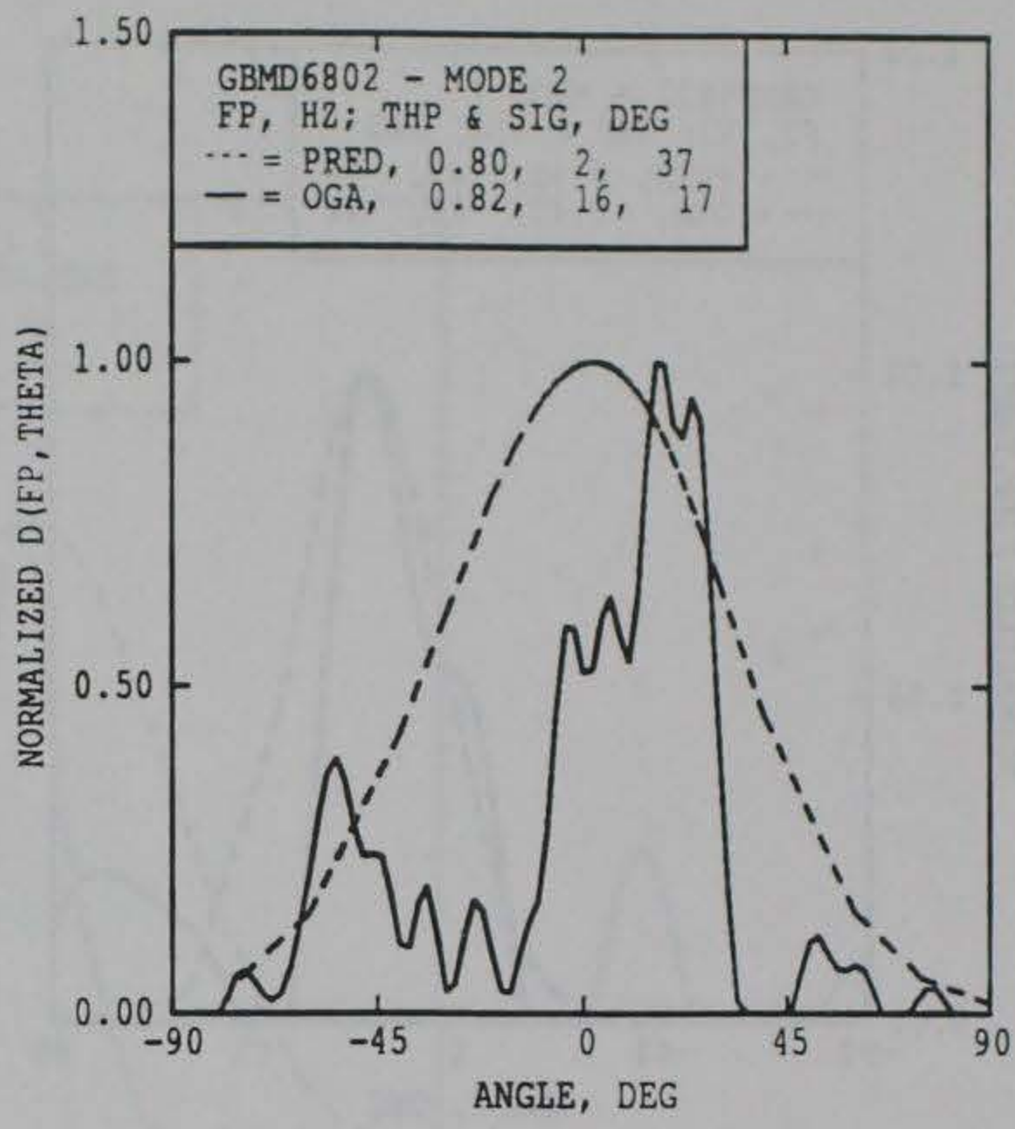

GAGE CODE = A

a. Option A

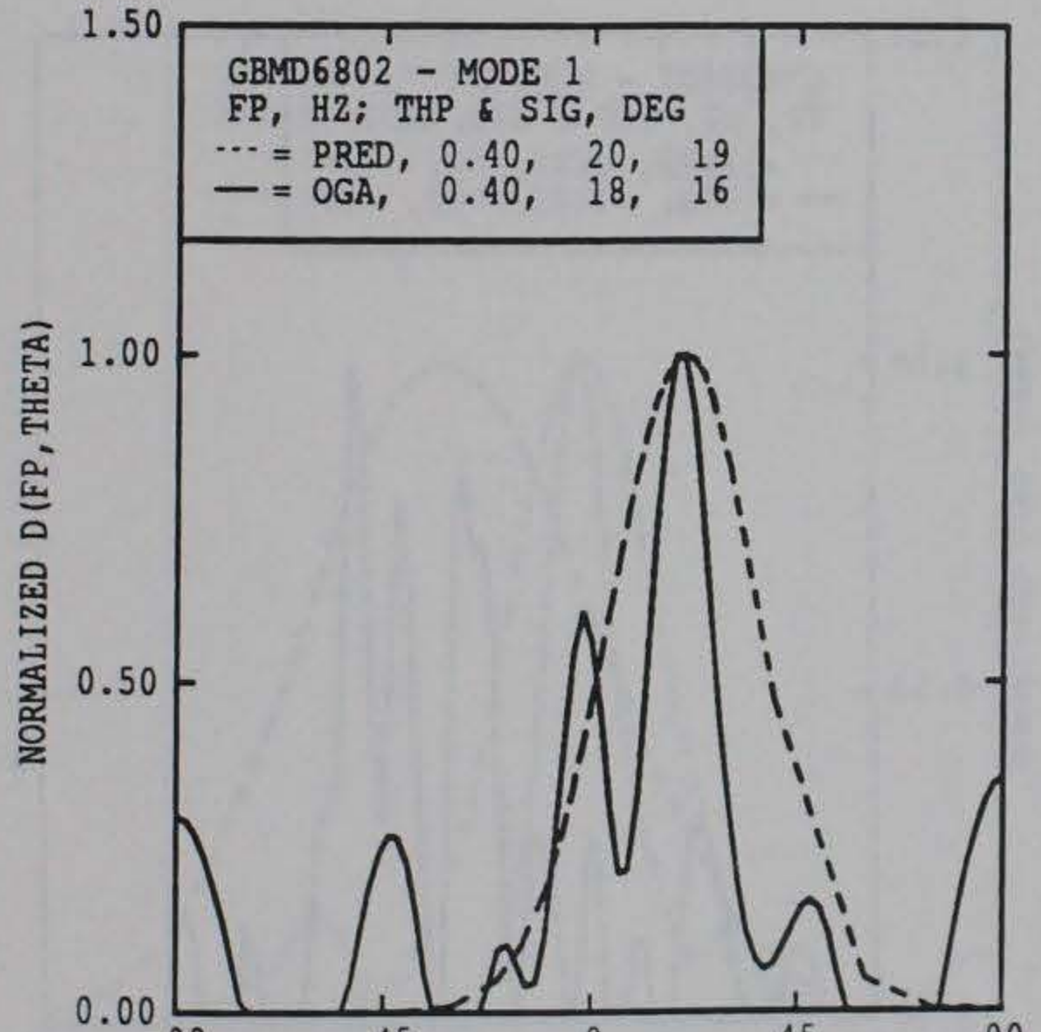

GAGE CODE = B

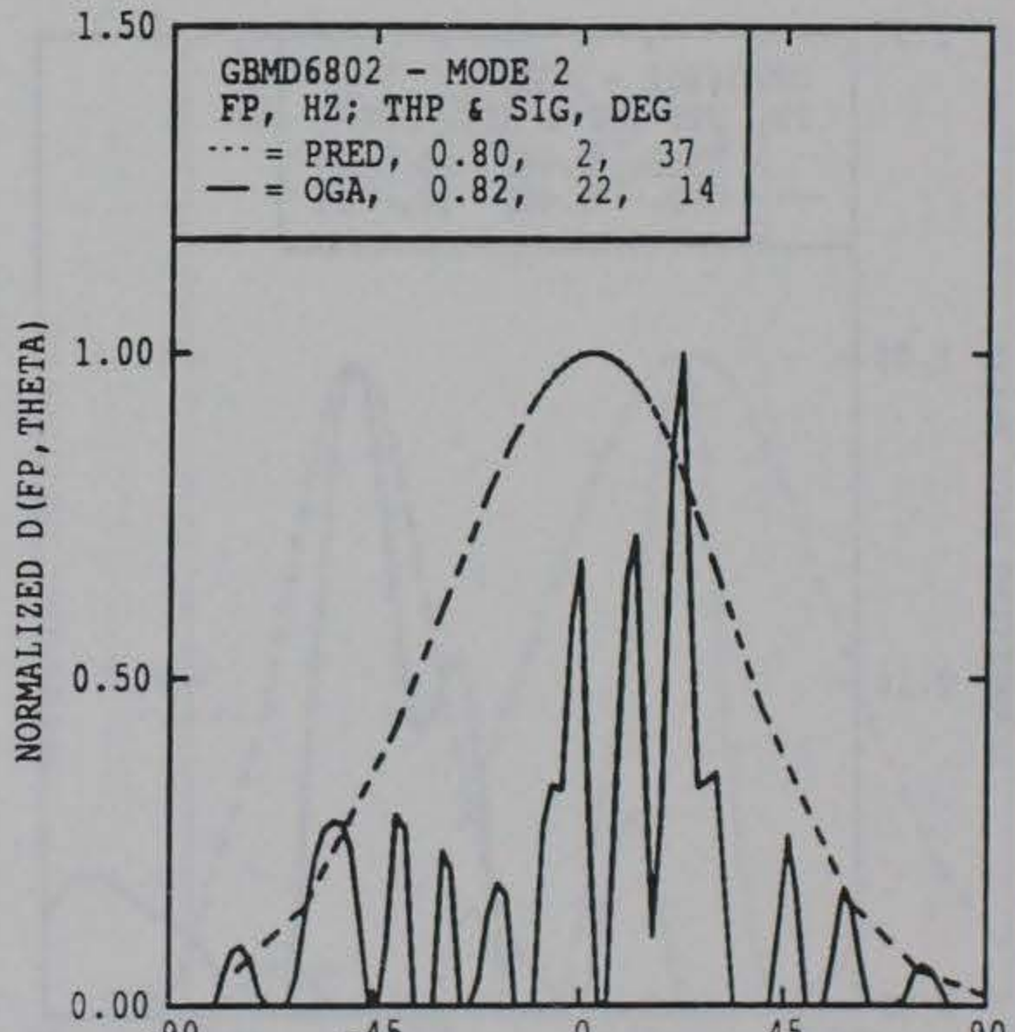

GAGE CODE = B

b. Option B

Figure 10. Directional distribution analysis results, bimodal case D68 (Continued)

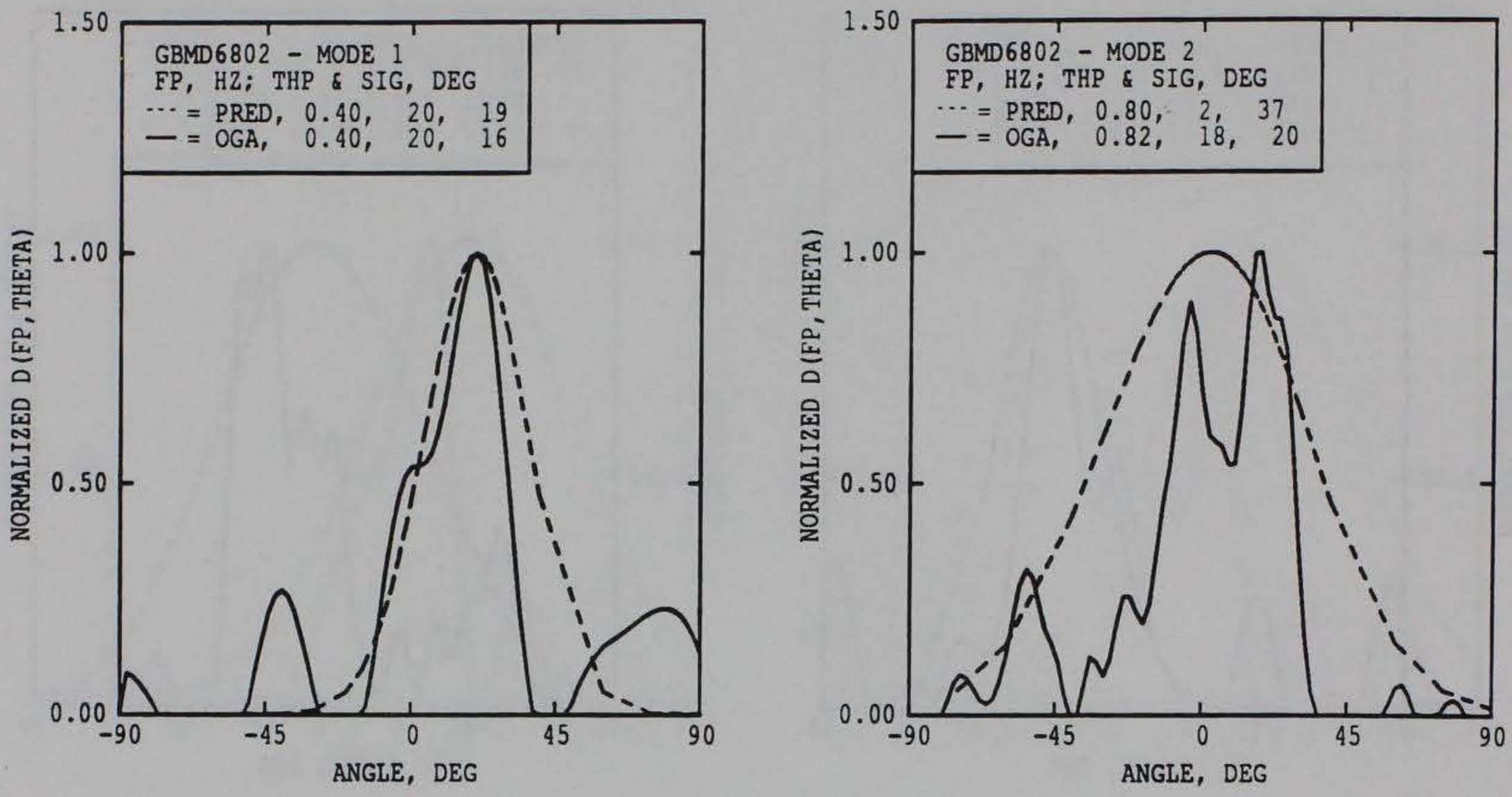

GAGE CODE = C

GAGE CODE = C

c. Option C

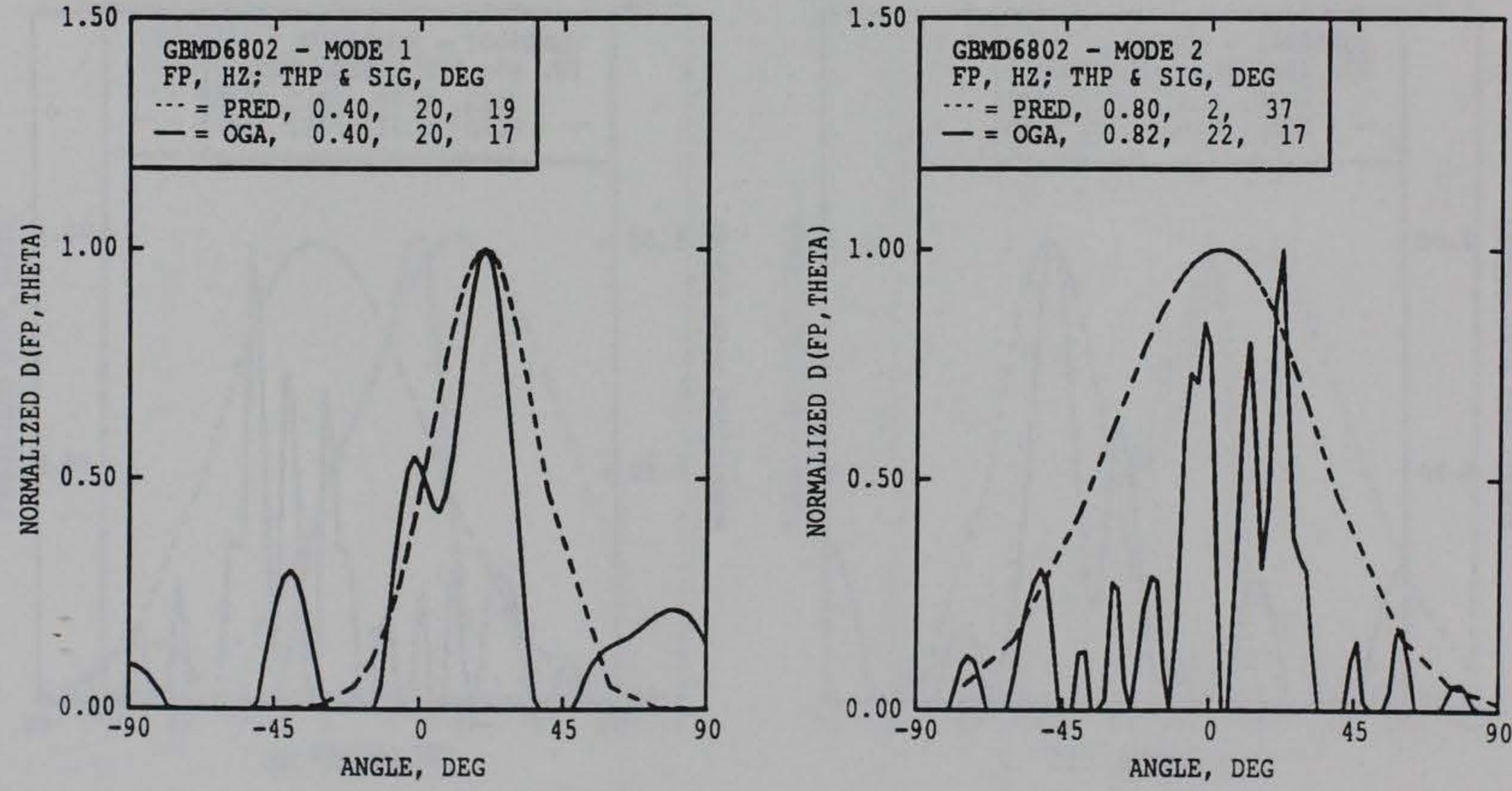

GAGE CODE = D

GAGE CODE = D

d. Option D

Figure 10. (Concluded)

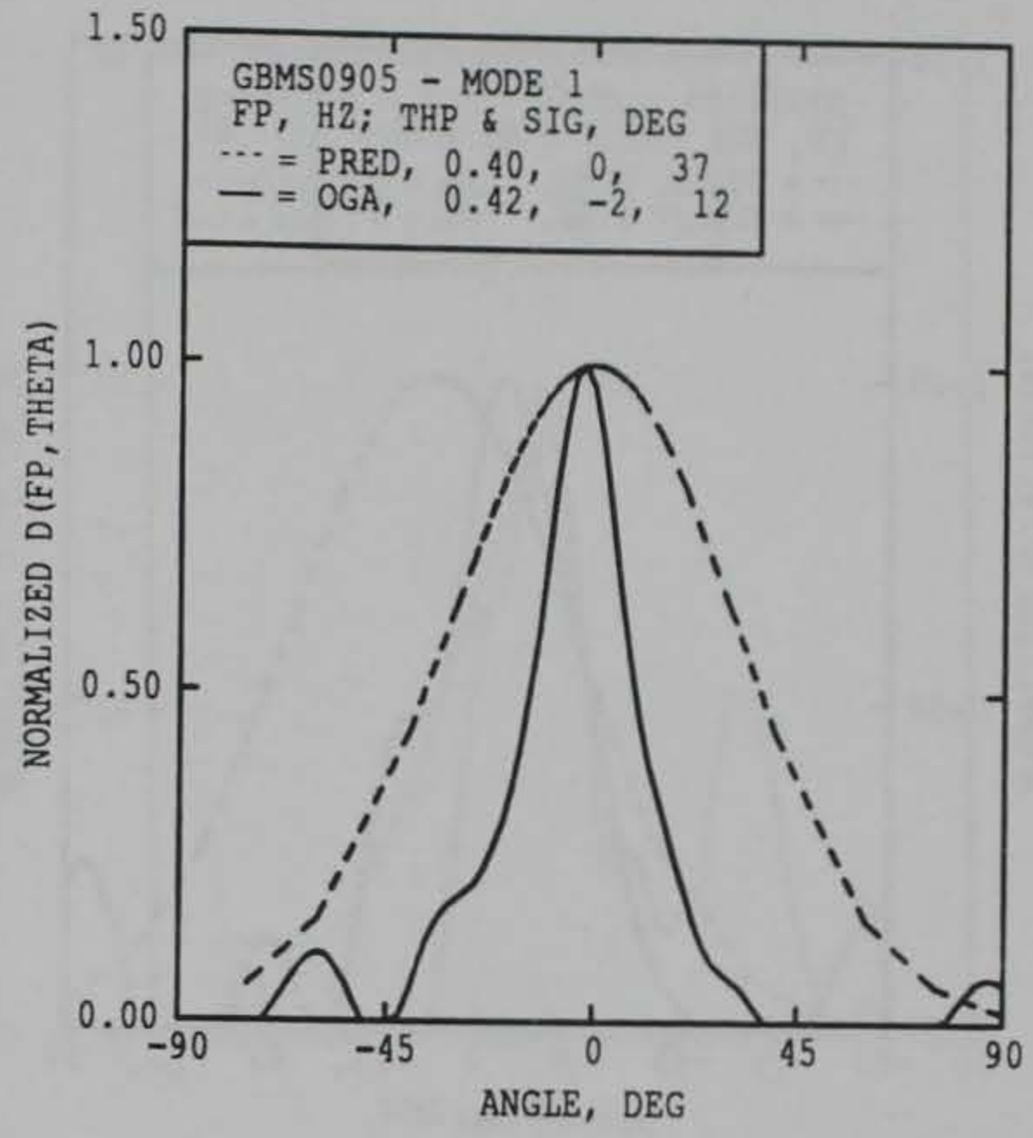

a. Unimodal case S09

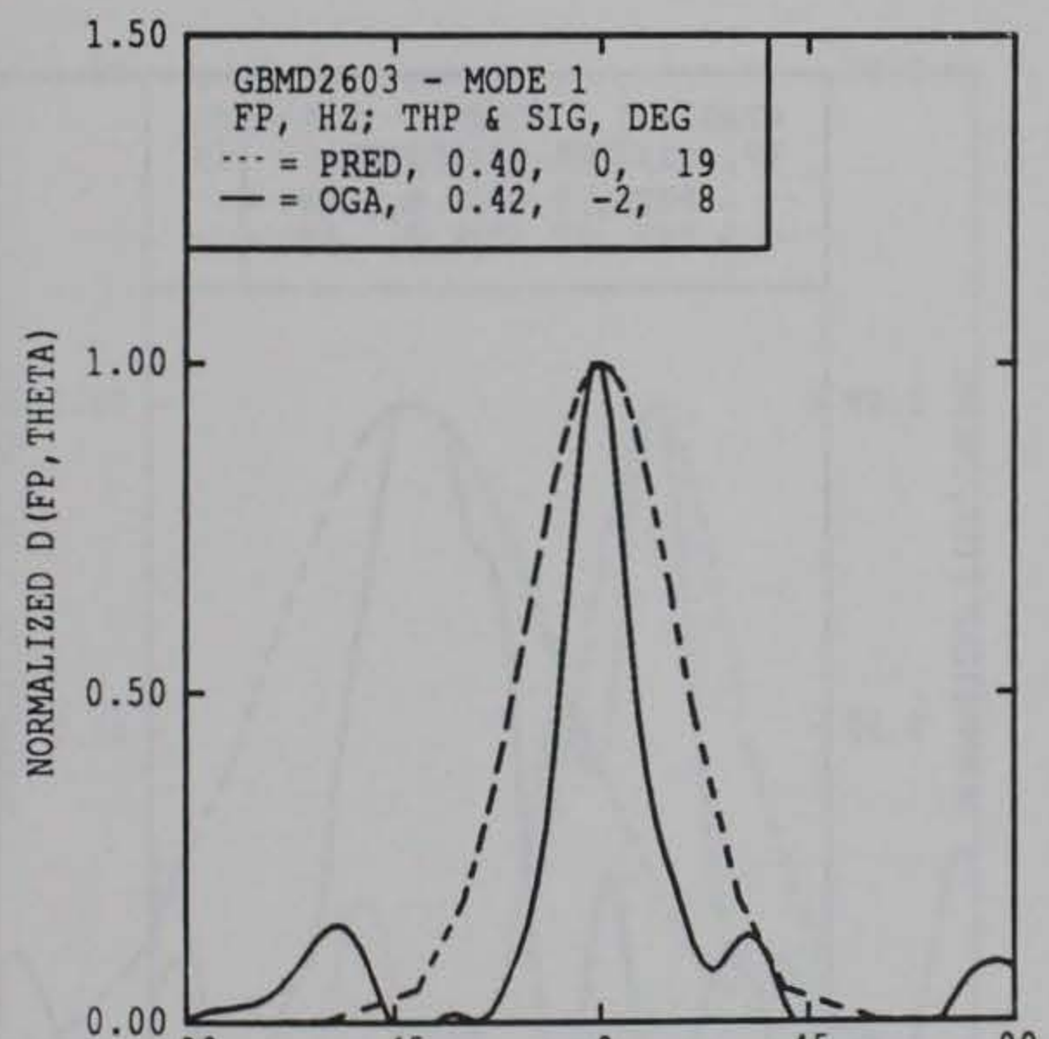

b. Bimodal case D26, mode 1

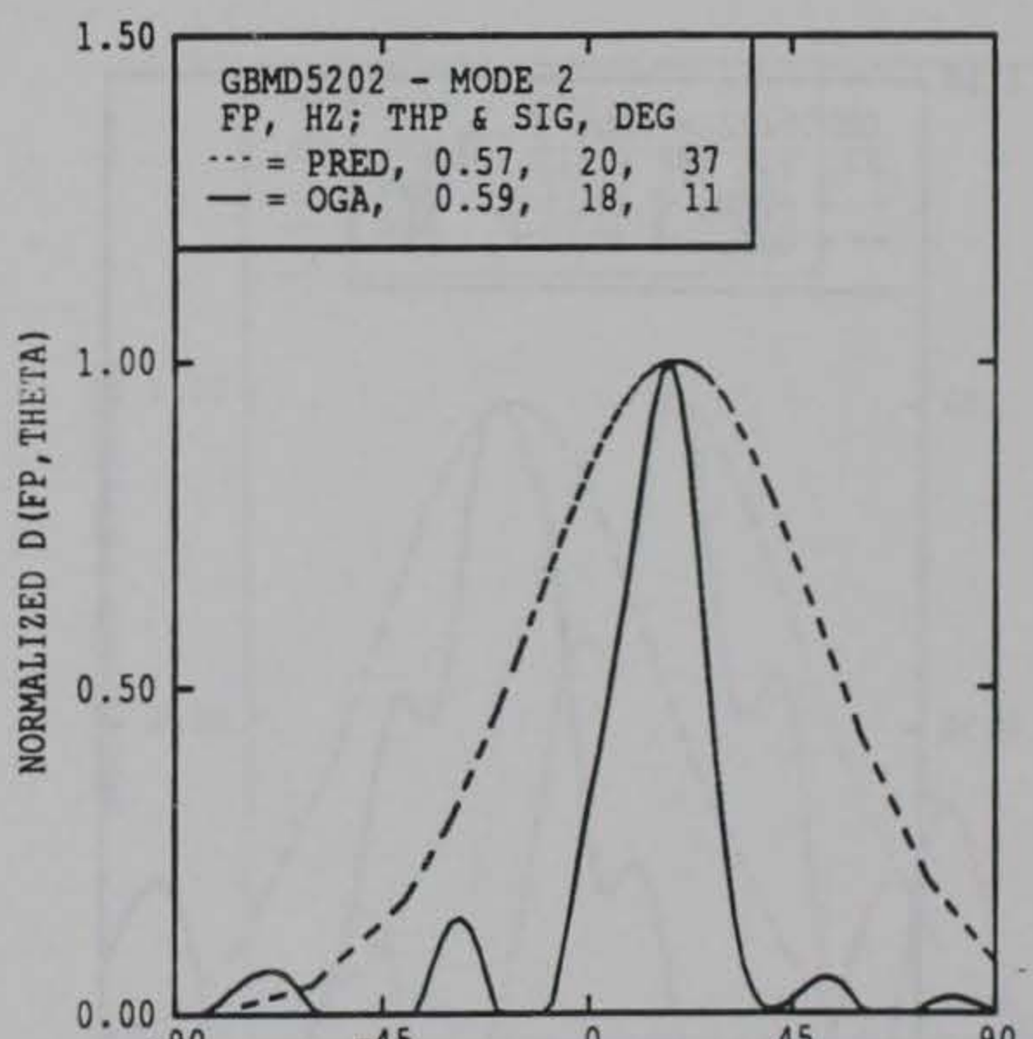

c. Bimodal case D52, mode 2

Figure 11. Measured directional distributions with one-third desired spread

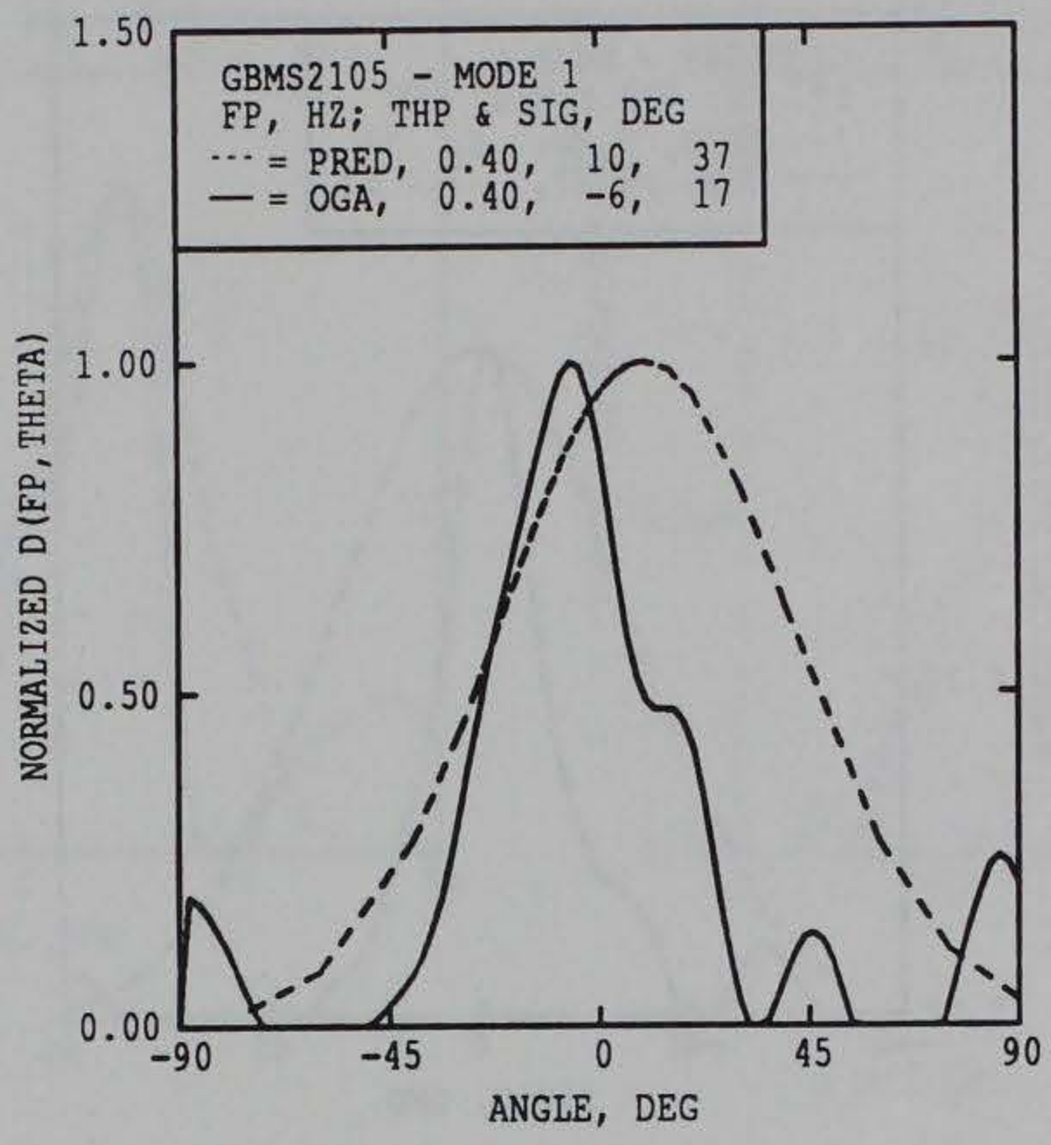

a. Unimodal case S21

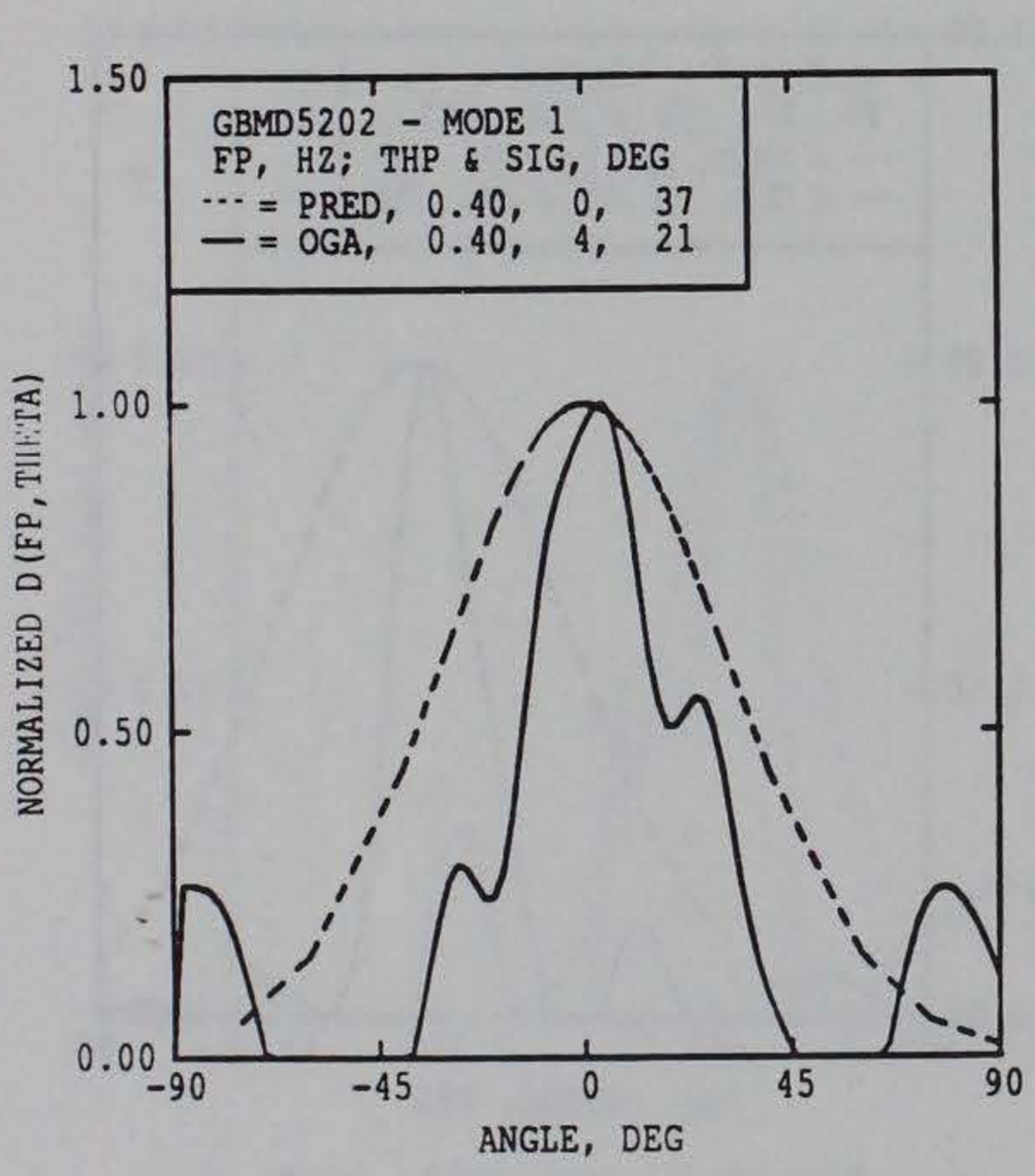

b. Bimodal case D52, mode 1

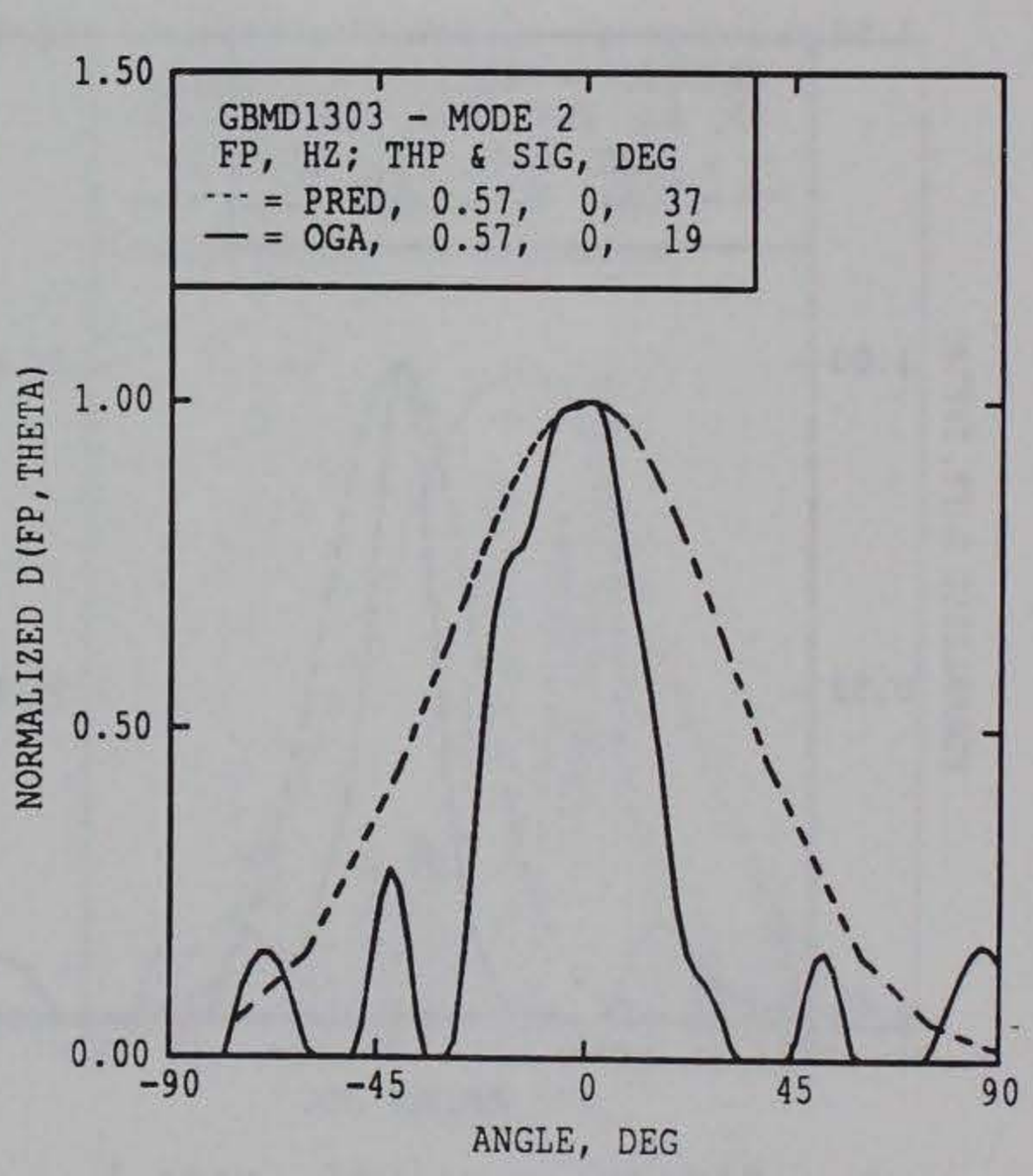

c. Bimodal case D13, mode 2

Figure 12. Measured directional distributions with one-half desired spread

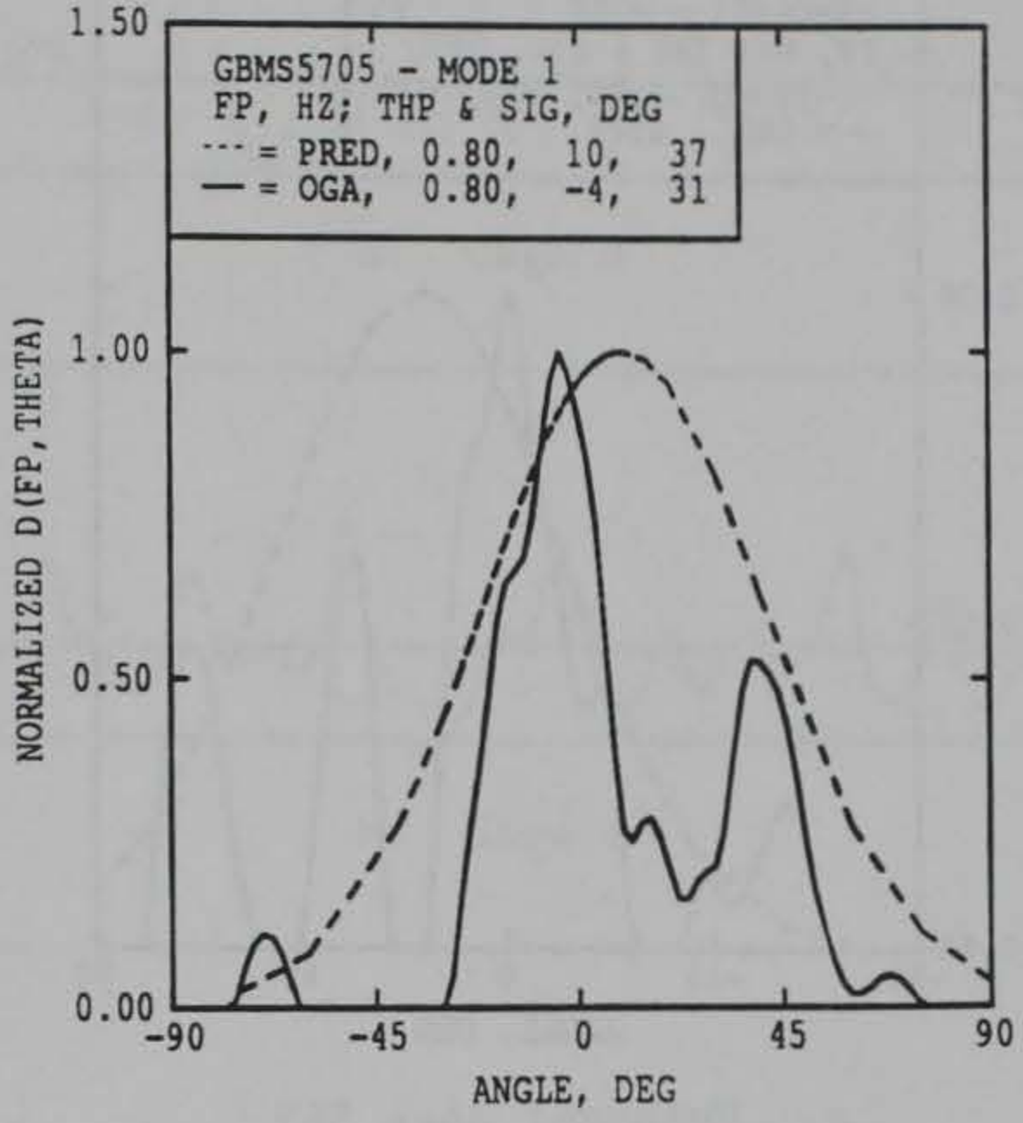

a. Unimodal case S57

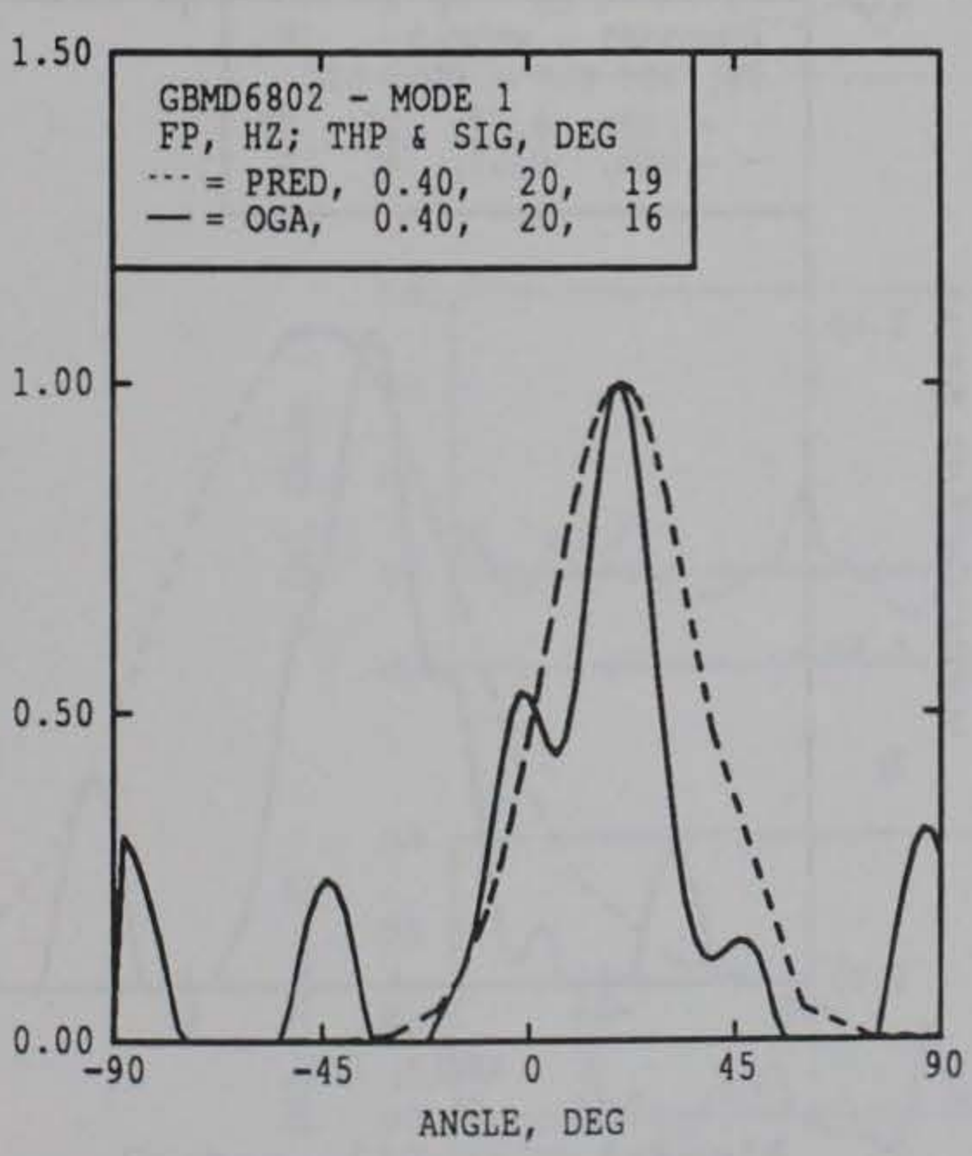

b. Bimodal case D68, mode 1

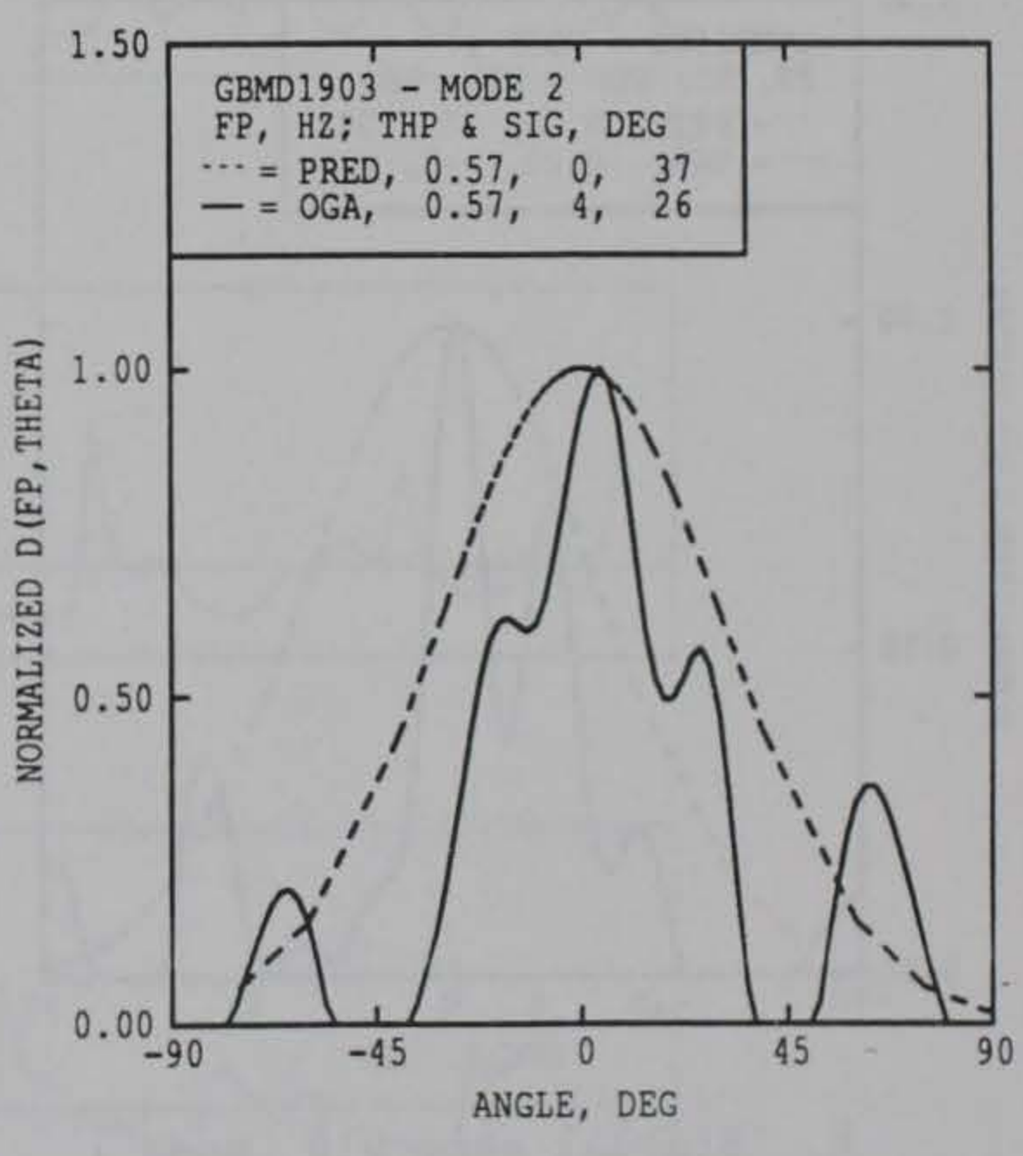

c. Bimodal case D19, mode 2

Figure 13. Measured directional distributions with desired spread

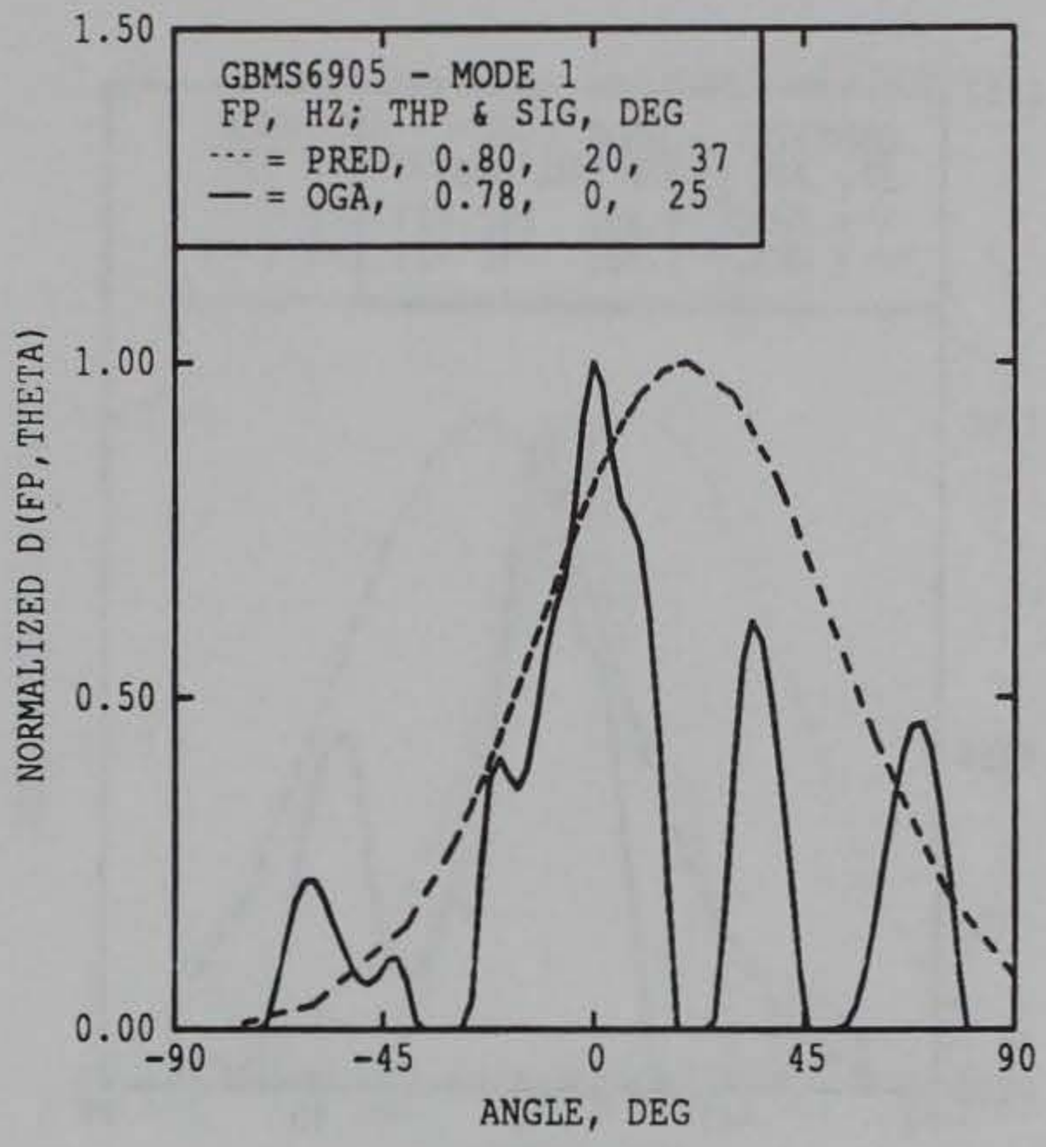

a. Unimodal case S69

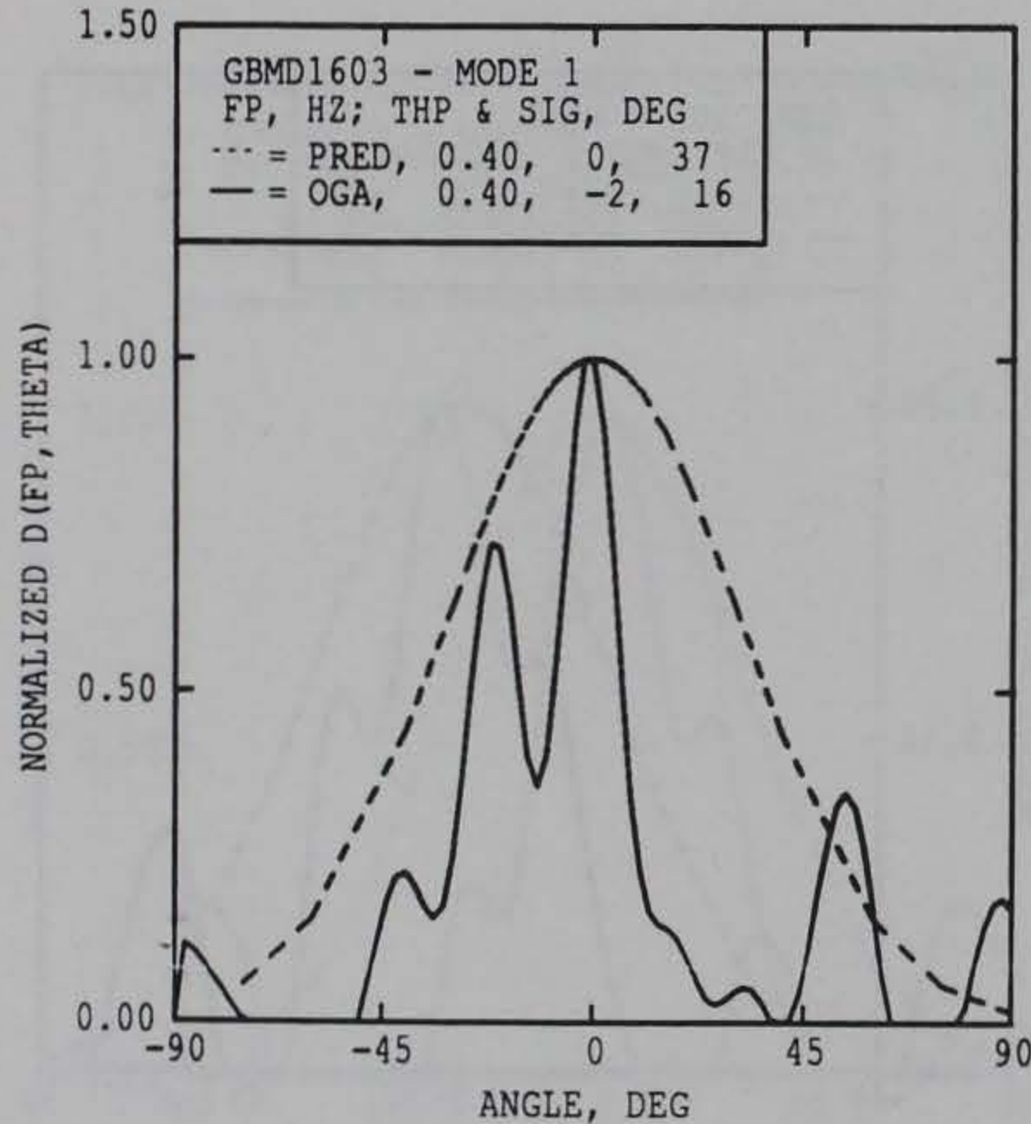

b. Bimodal case D16, mode 1

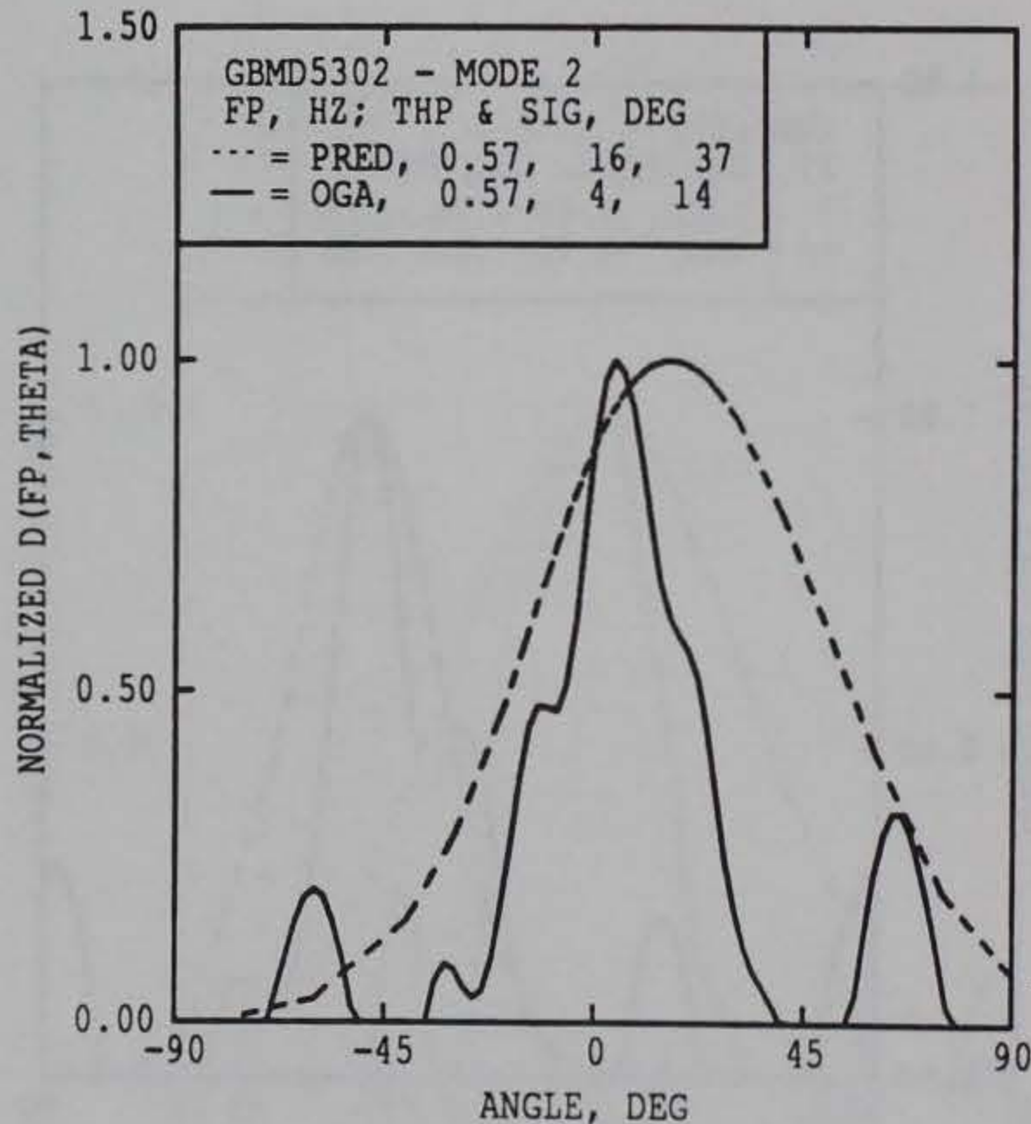

c. Bimodal case D53, mode 2

Figure 14. Measured directional distributions with significant side band energy

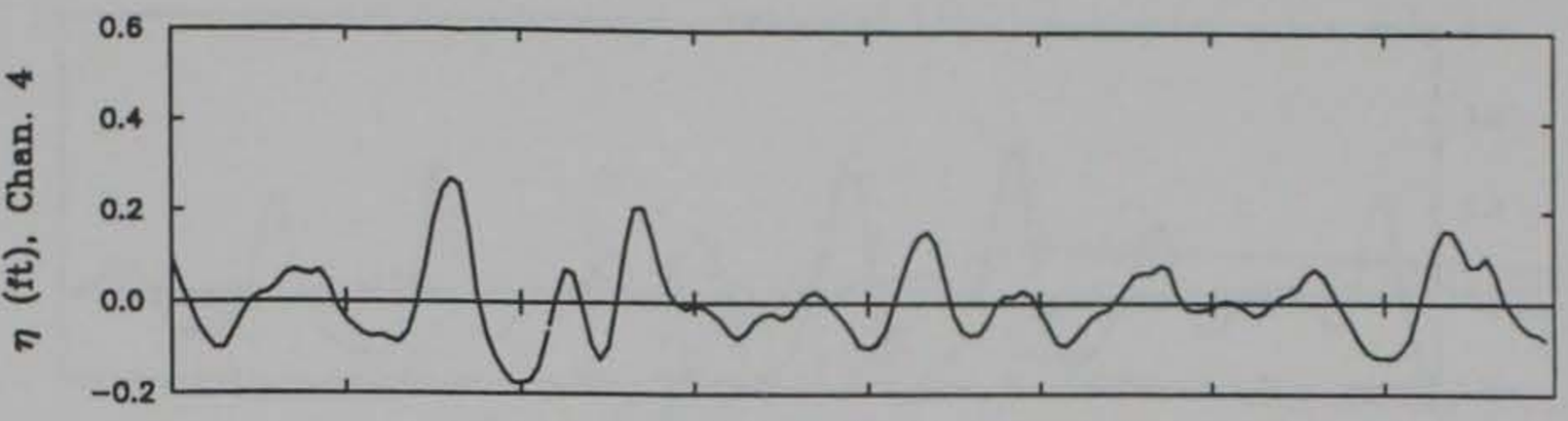

a. Gage 4

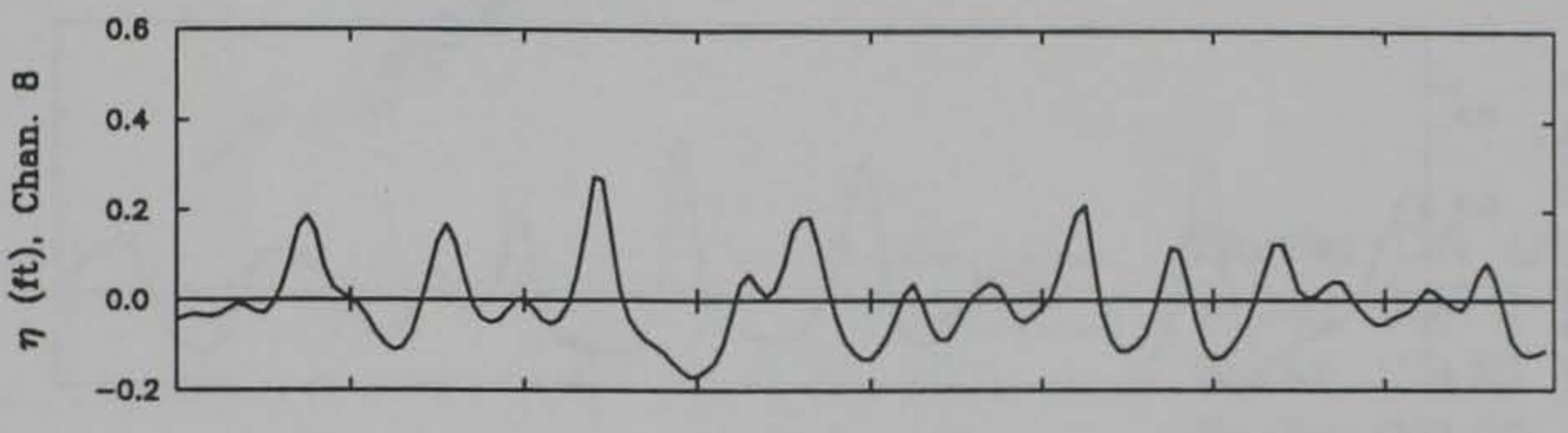

b. Gage 8

c. Gage 10

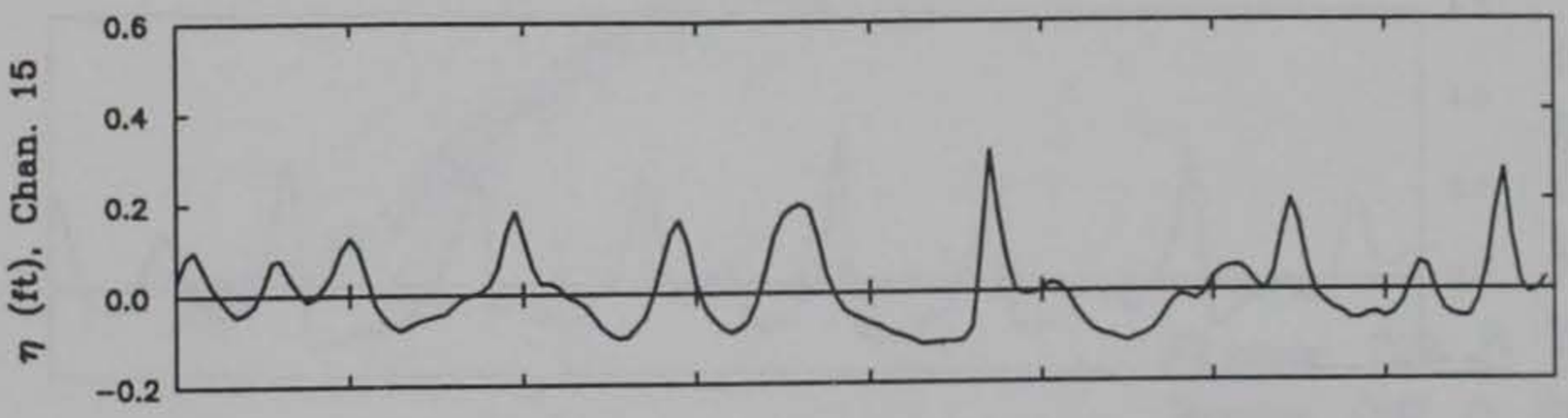

d. Gage 15

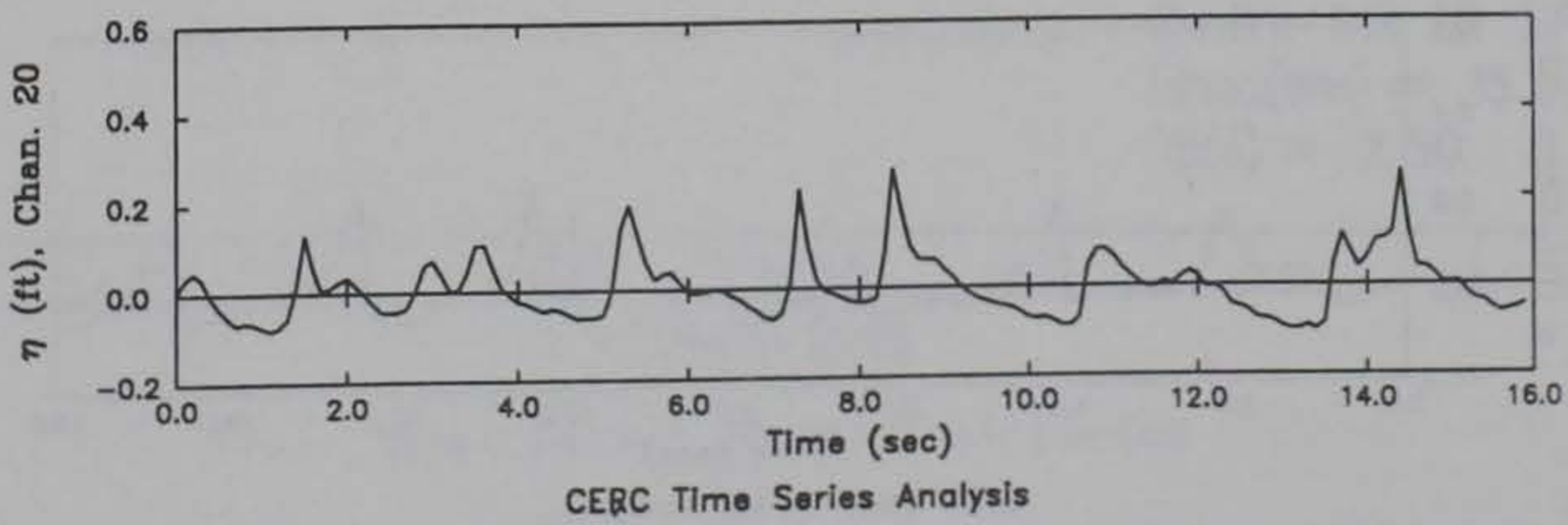

e. Gage 20

Figure 15. Measured wave profile, broad-banded unimodal case S25

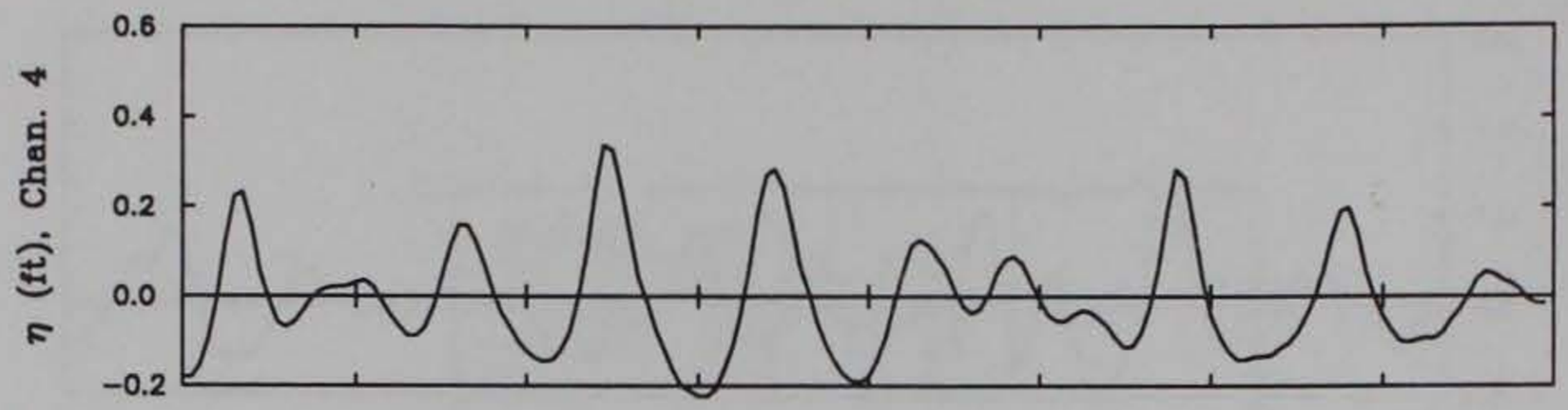

a. Gage 4

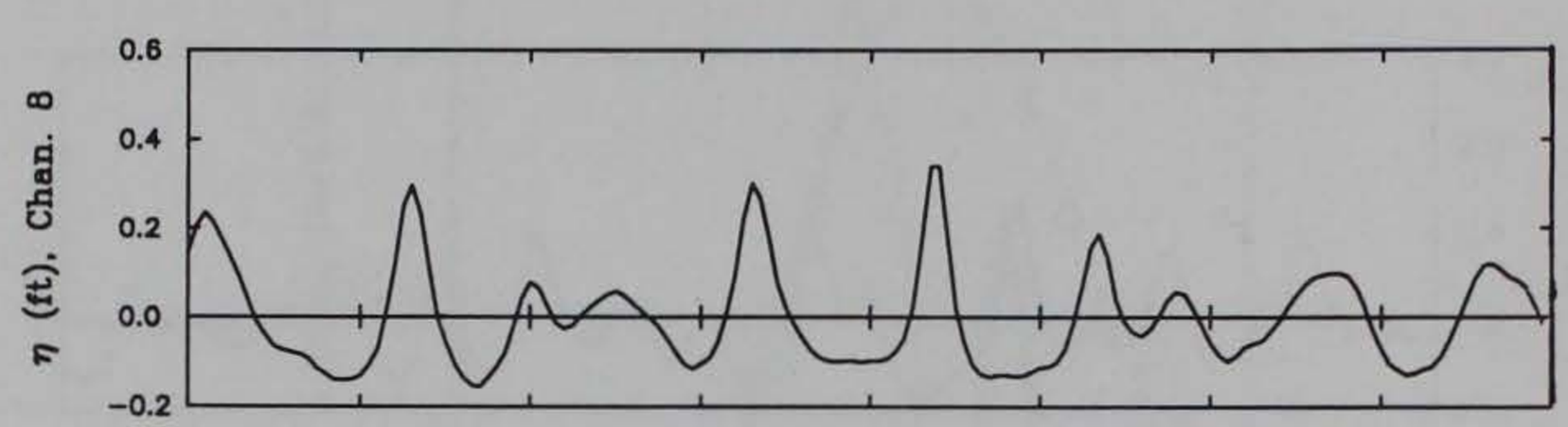

b. Gage 8

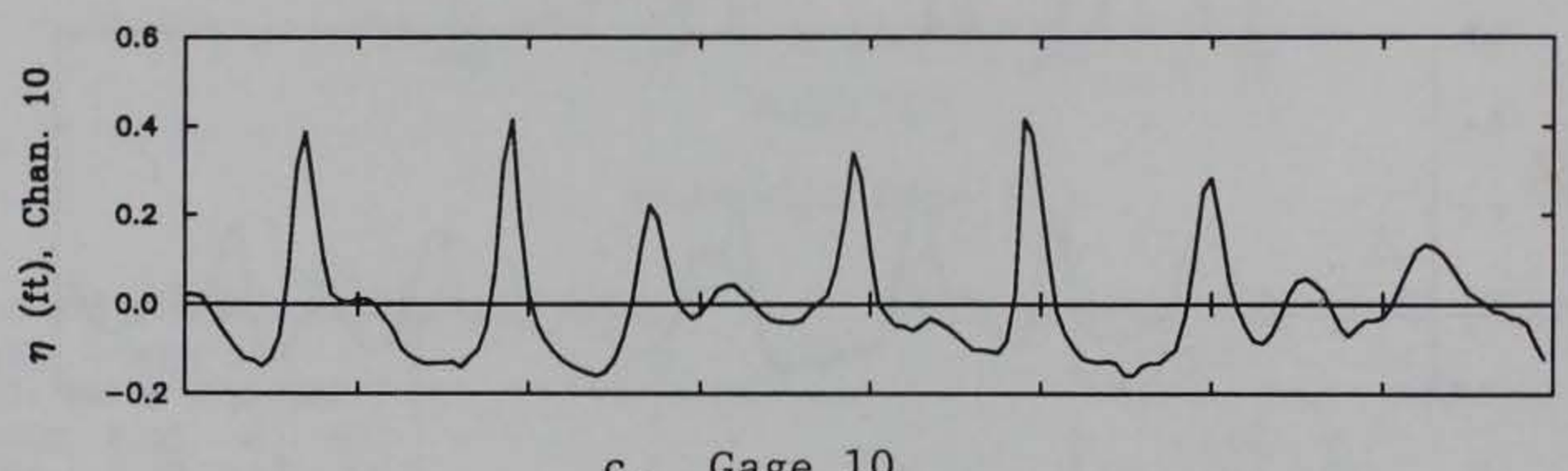

c. Gage 10

d. Gage 15

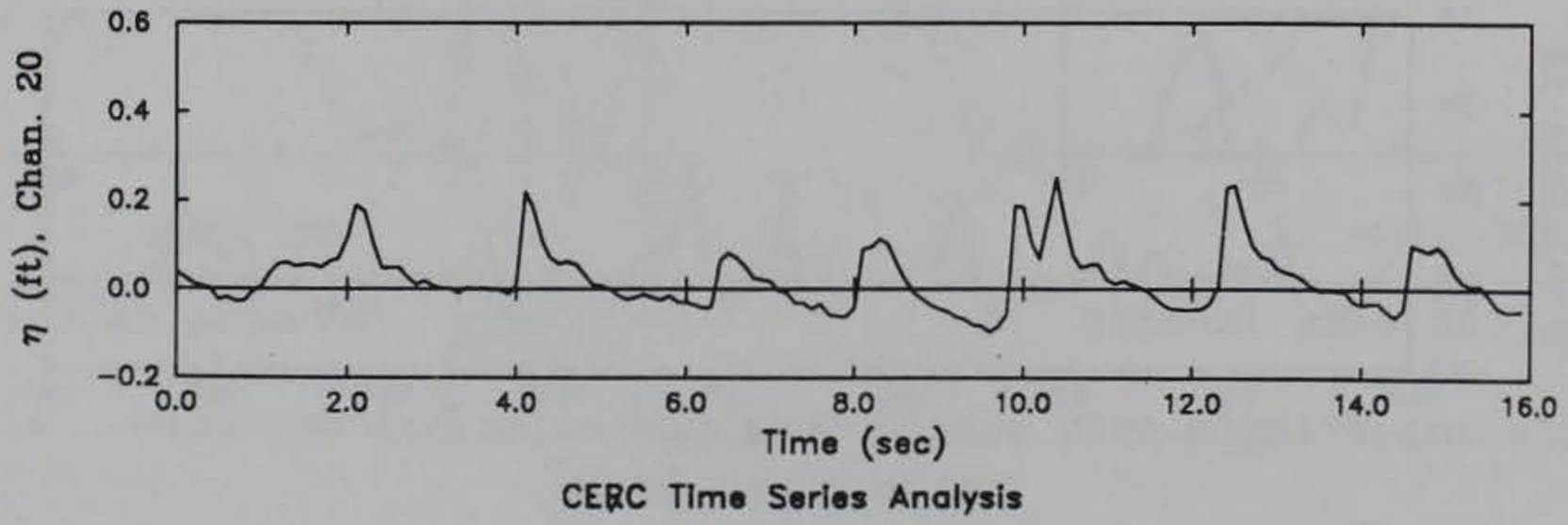

e. Gage 20

Figure 16. Measured wave profile, bimodal case D29

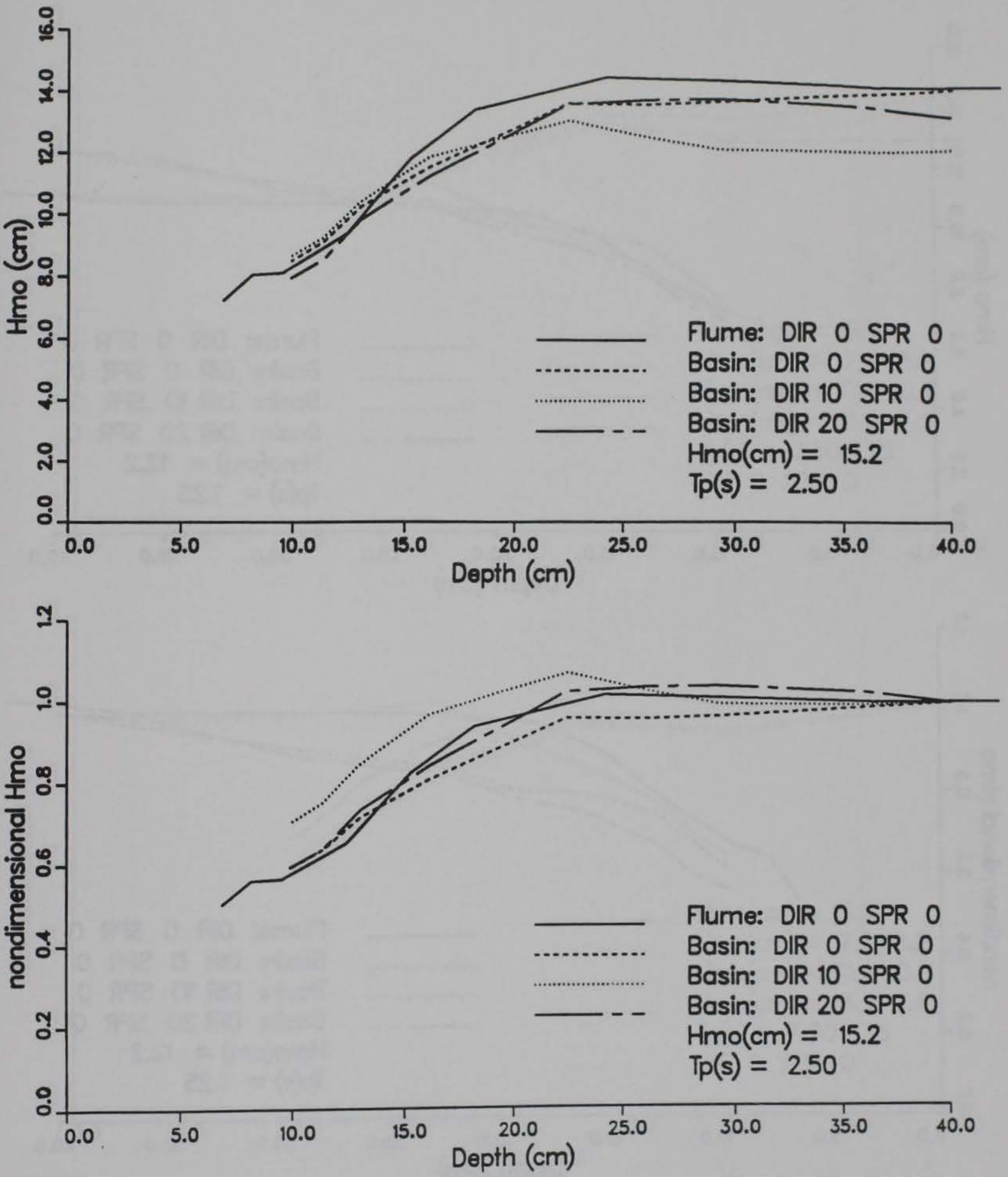

a. Cases with 2.50 sec peak period

Figure 17. Flume and basin wave height comparisons, unimodal spectra (Continued)

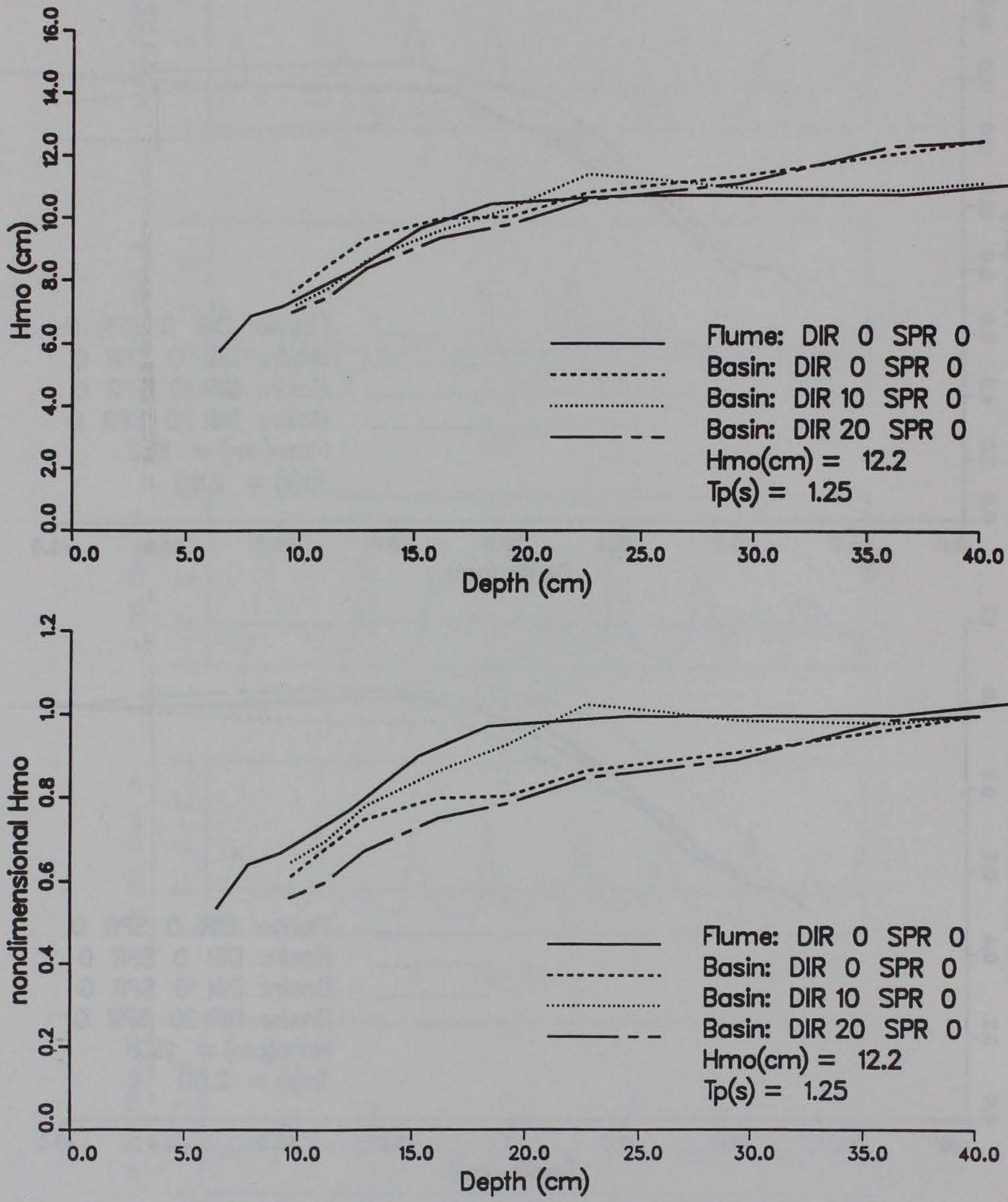

b. Cases with 1.25 sec peak period

Figure 17. (Concluded)

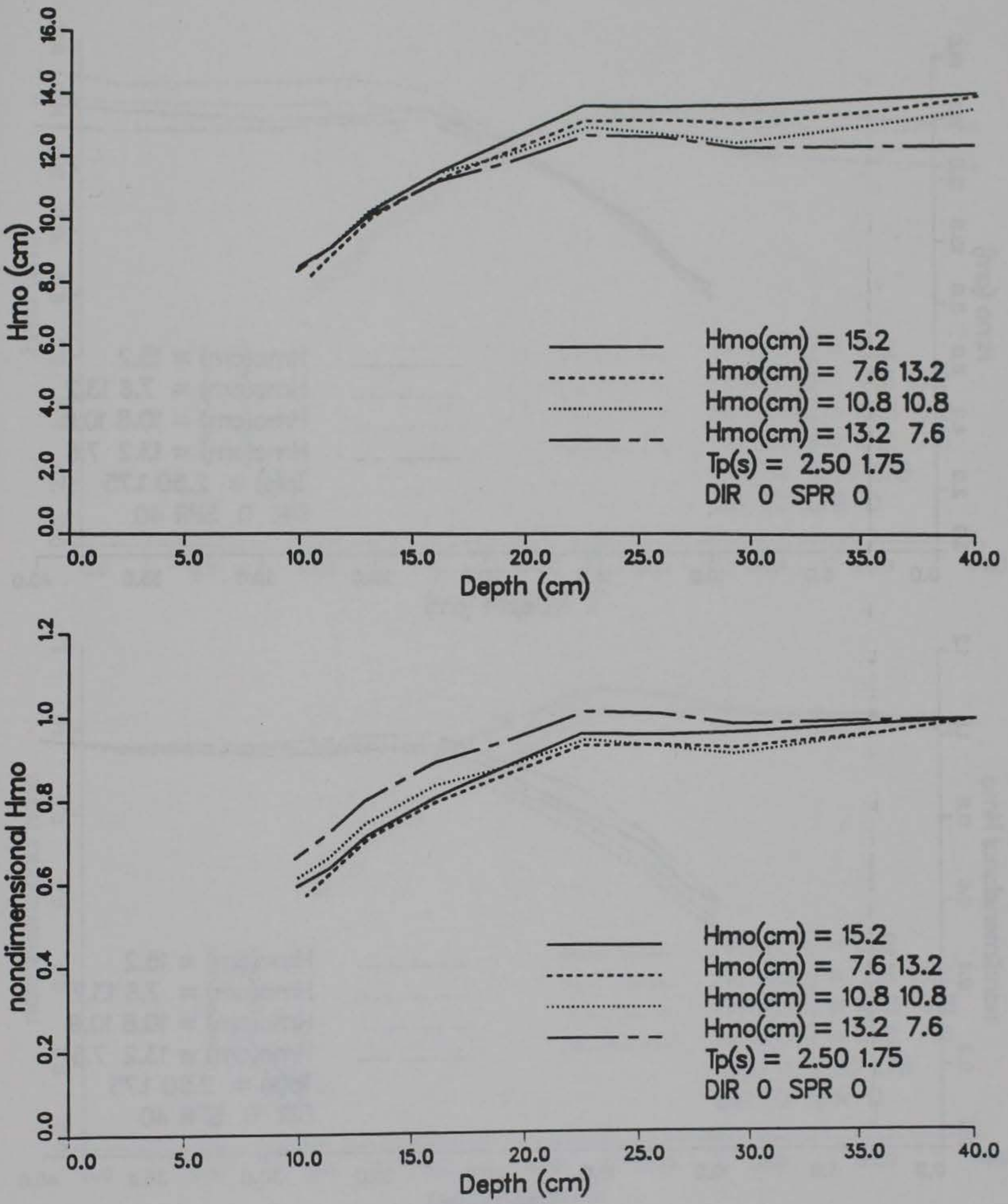

a. Cases with 0-deg wave direction, 0-deg directional spread

Figure 18. Energy distribution effect on wave height, unimodal and bimodal spectra (Sheet 1 of 4)

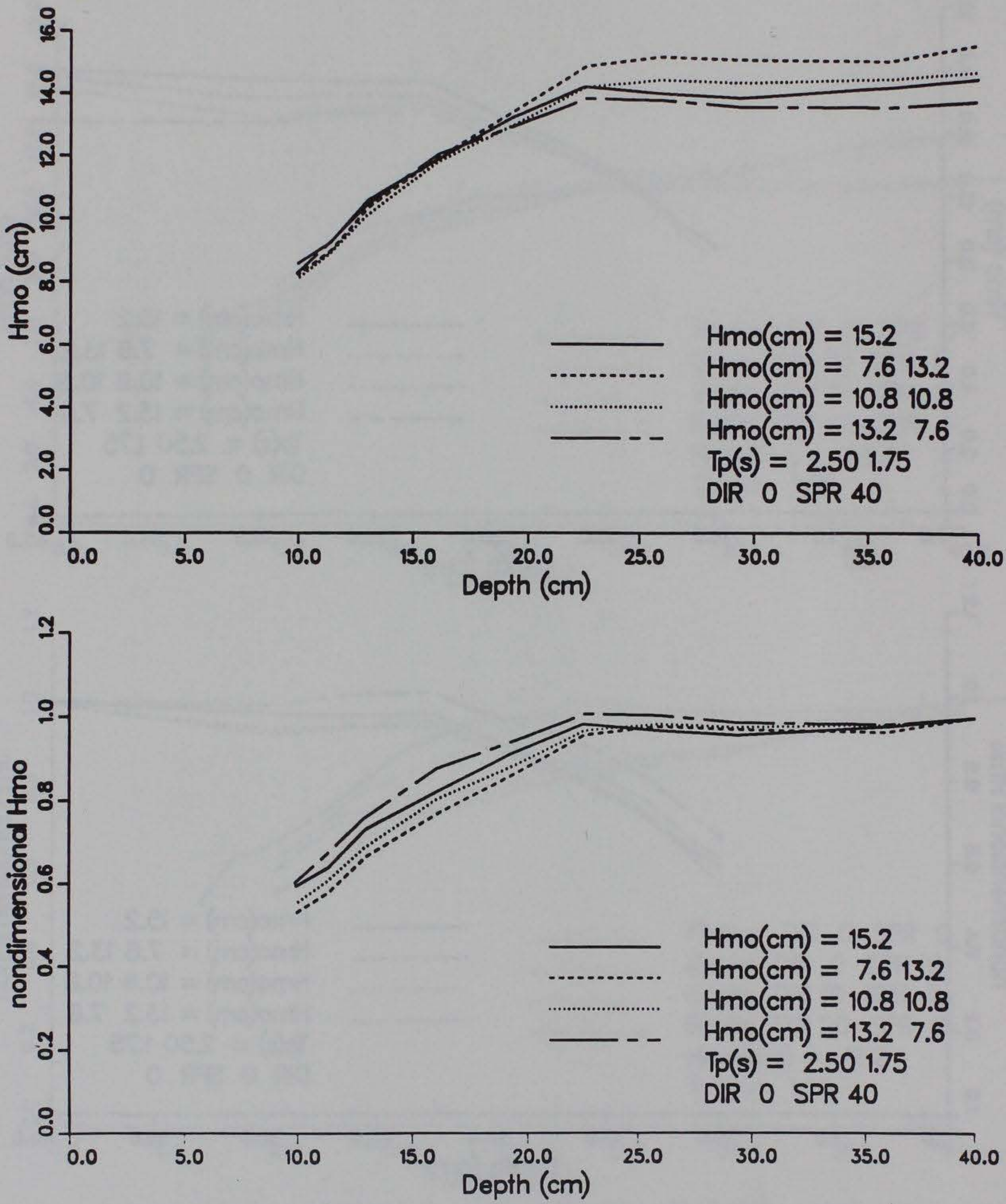

b. Cases with 0-deg wave direction, 40-deg directional spread

Figure 18. (Sheet 2 of 4)

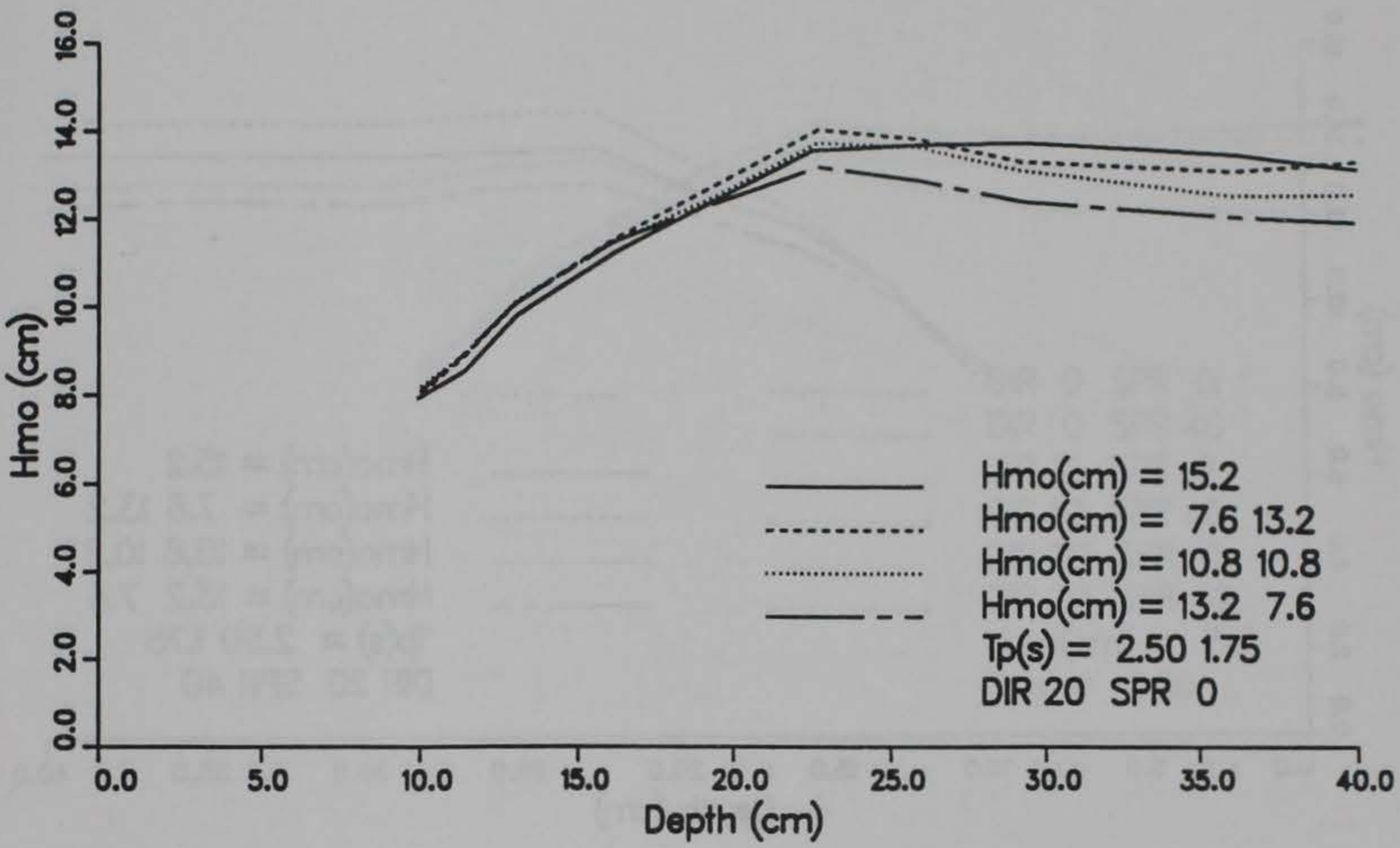

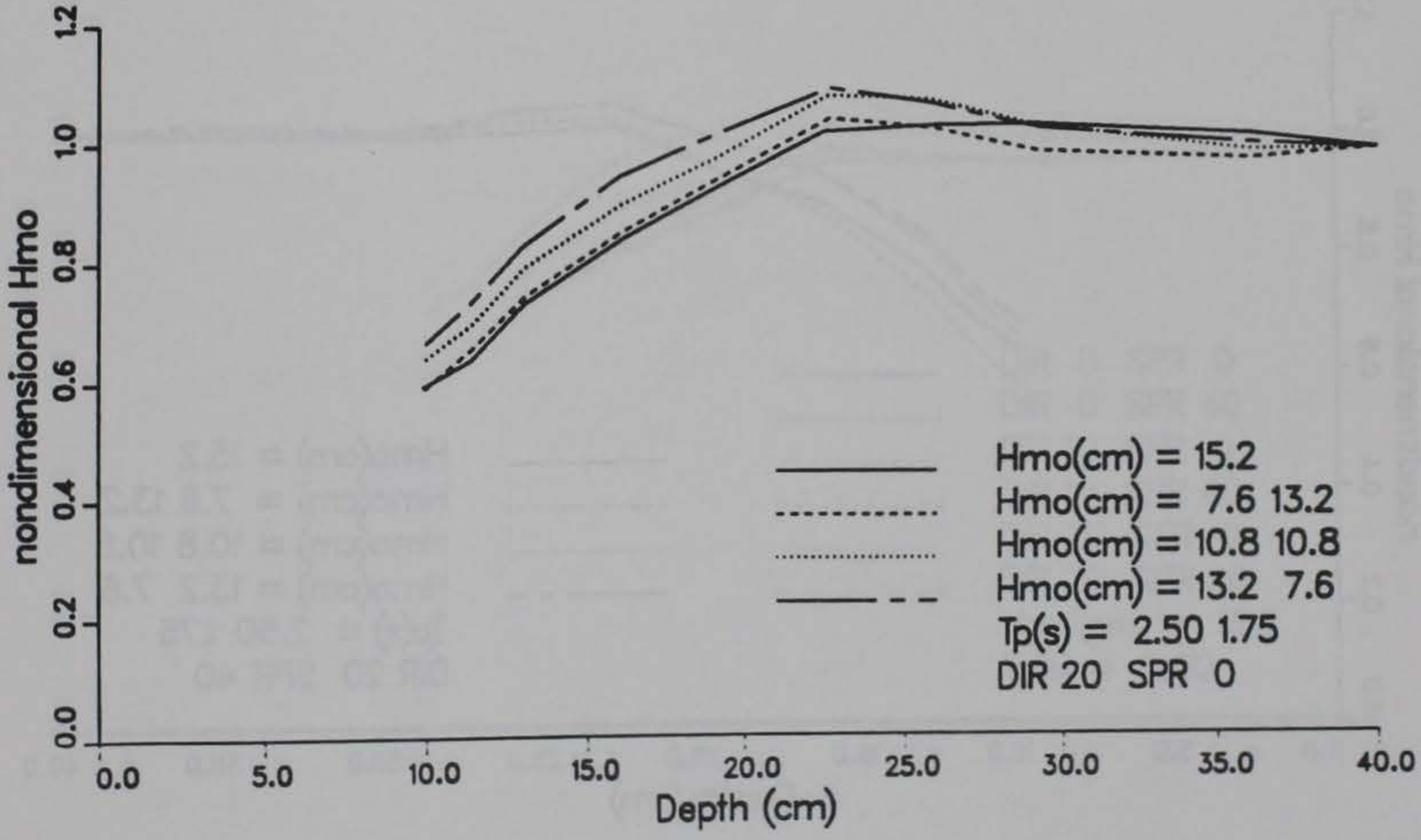

c. Cases with 20-deg wave direction, 0-deg directional spread

Figure 18. (Sheet 3 of 4)

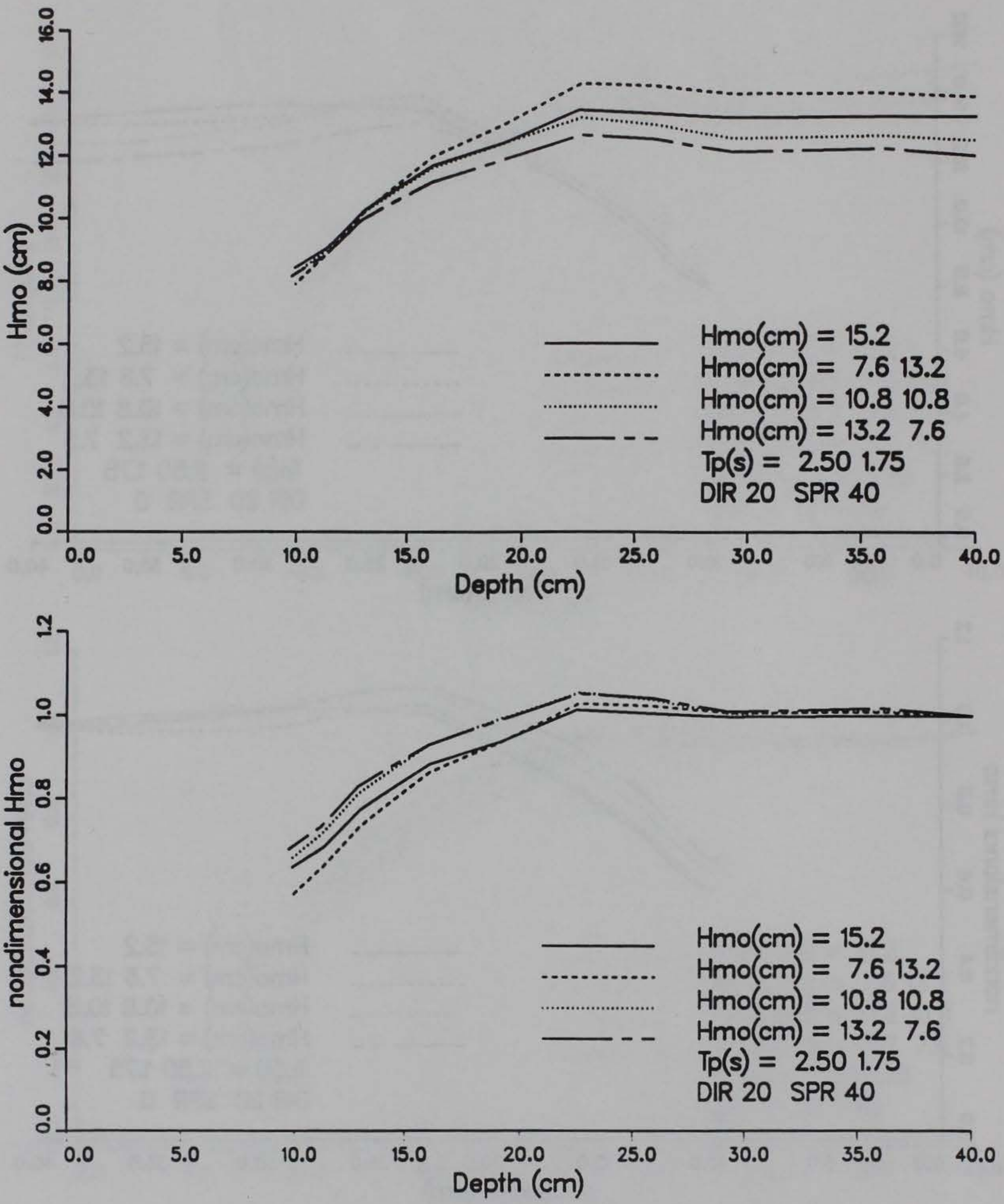

d. Cases with 20-deg direction and 40-deg spread

Figure 18. (Sheet 4 of 4)

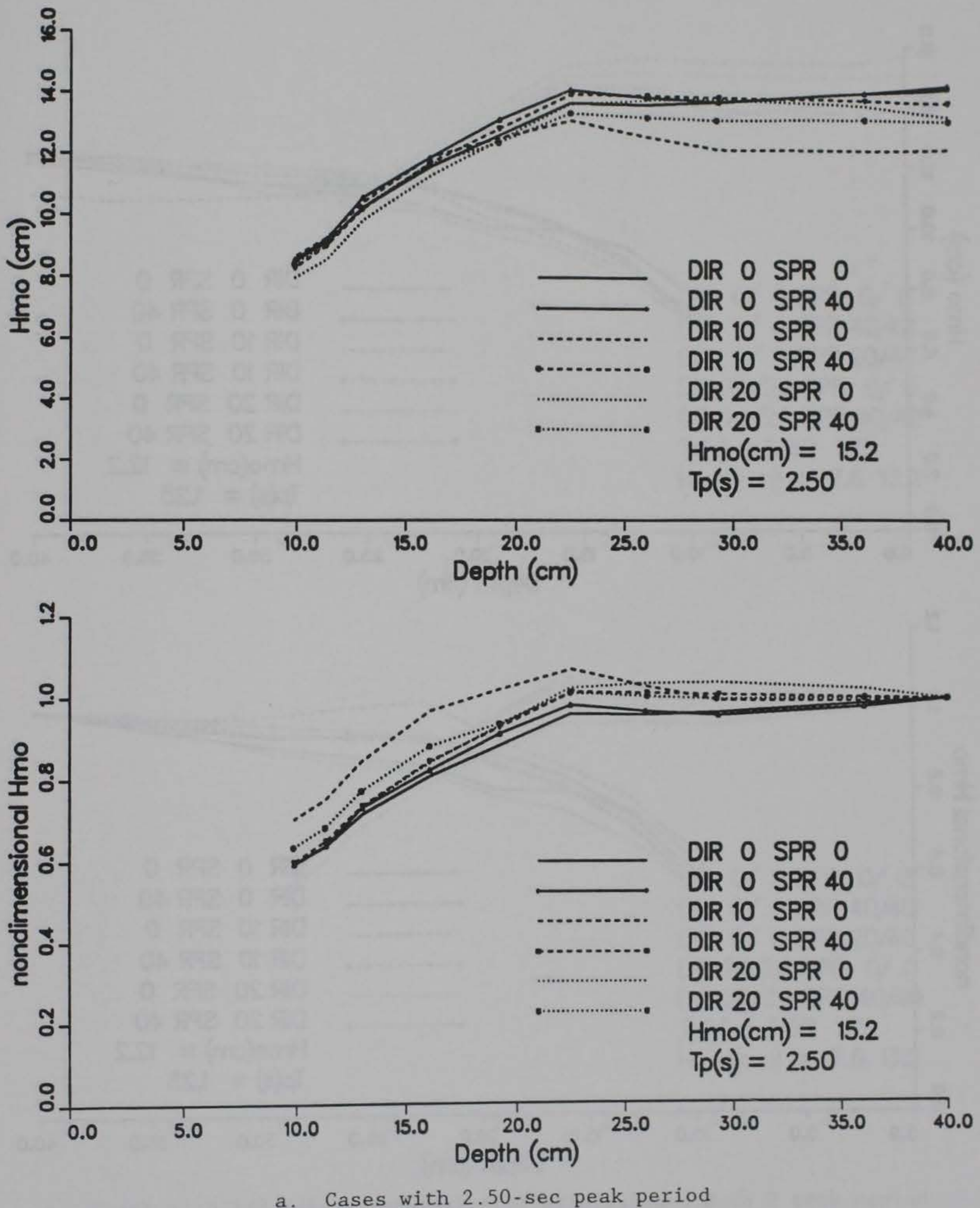

a. Cases with 2.50-sec peak period

Figure 19. Directional distribution effect on wave height, unimodal spectra (Continued)

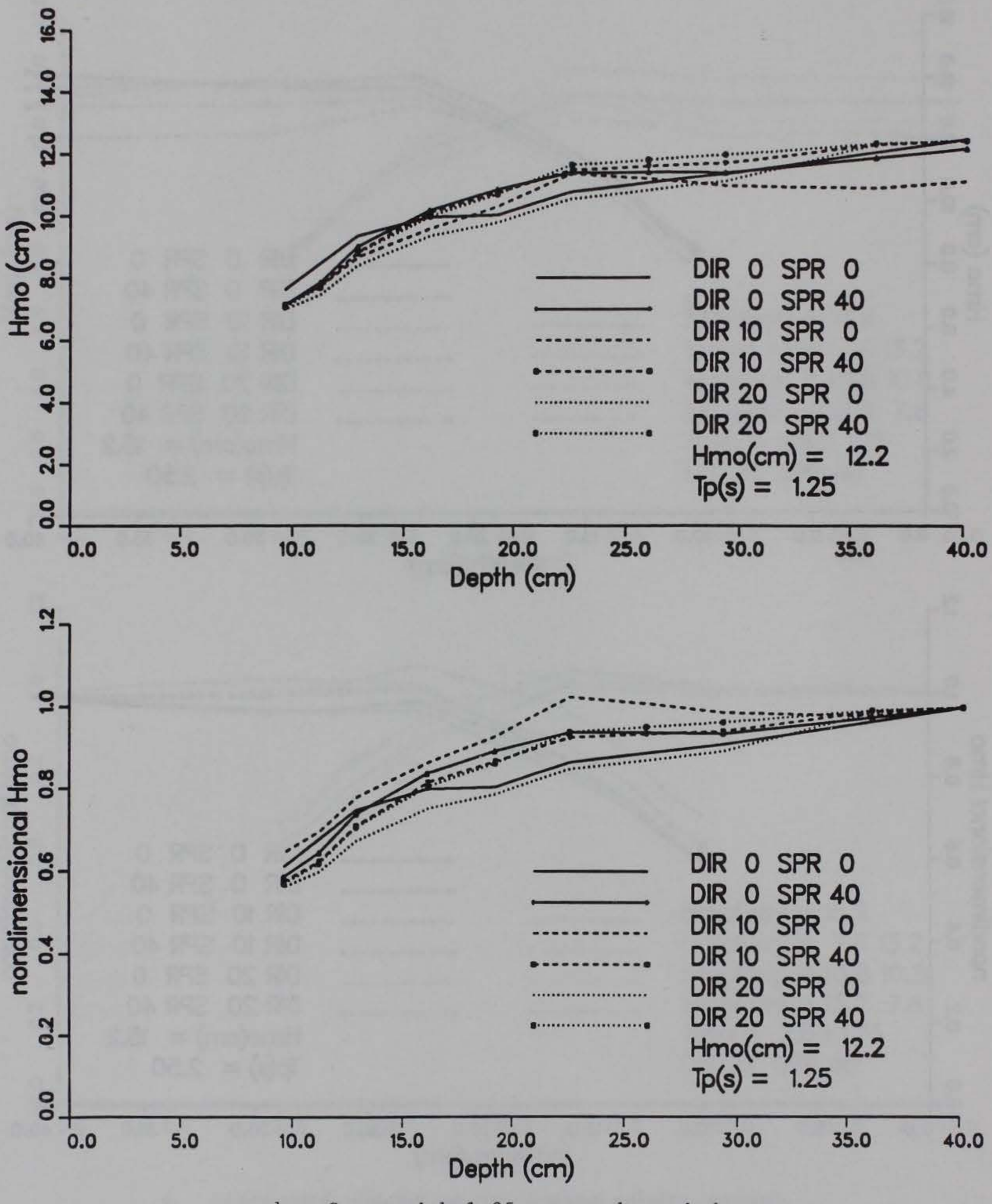

b. Cases with 1.25-sec peak period

Figure 19. (Concluded)

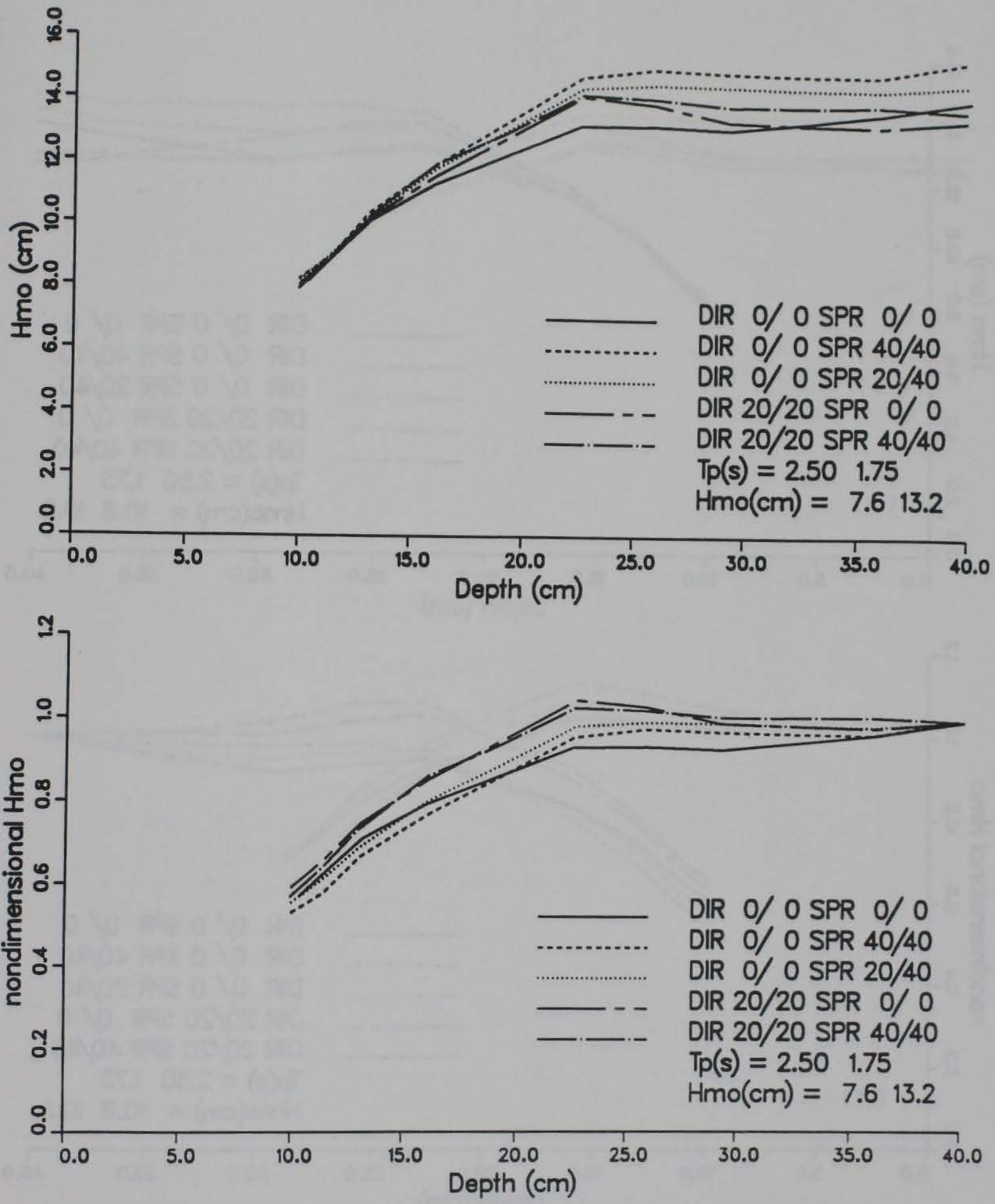

a. Cases with 1/3:2/3 energy distribution, 1.75-sec mode 2 peak period

Figure 20. Directional distribution effect on wave height, bimodal spectra (Sheet 1 of 4)

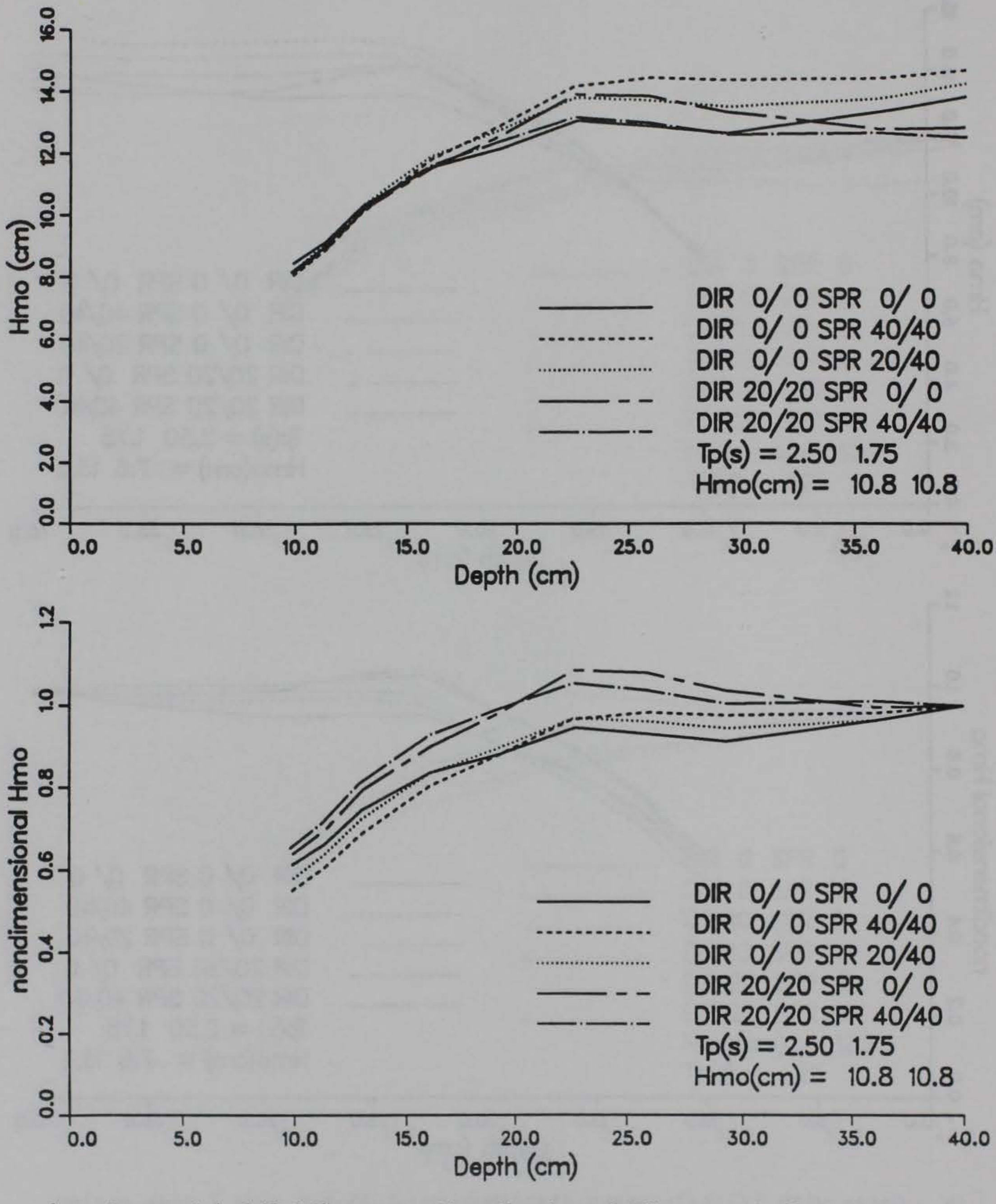

b. Cases with 1/2:1/2 energy distribution, 1.75-sec mode 2 peak period

Figure 20. (Sheet 2 of 4)

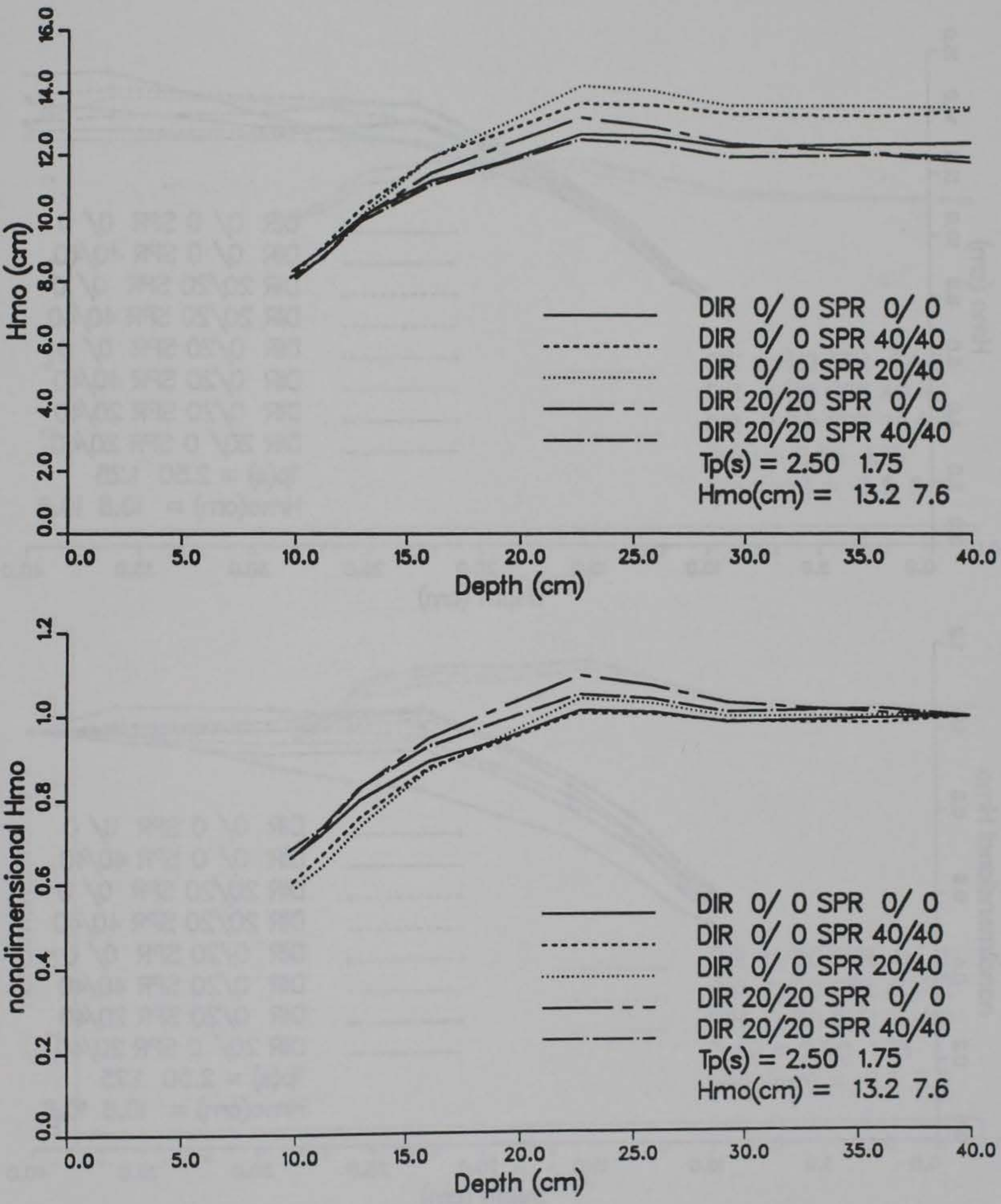

c. Cases with 2/3:1/3 energy distribution, 1.75-sec mode 2 peak period

Figure 20. (Sheet 3 of 4)

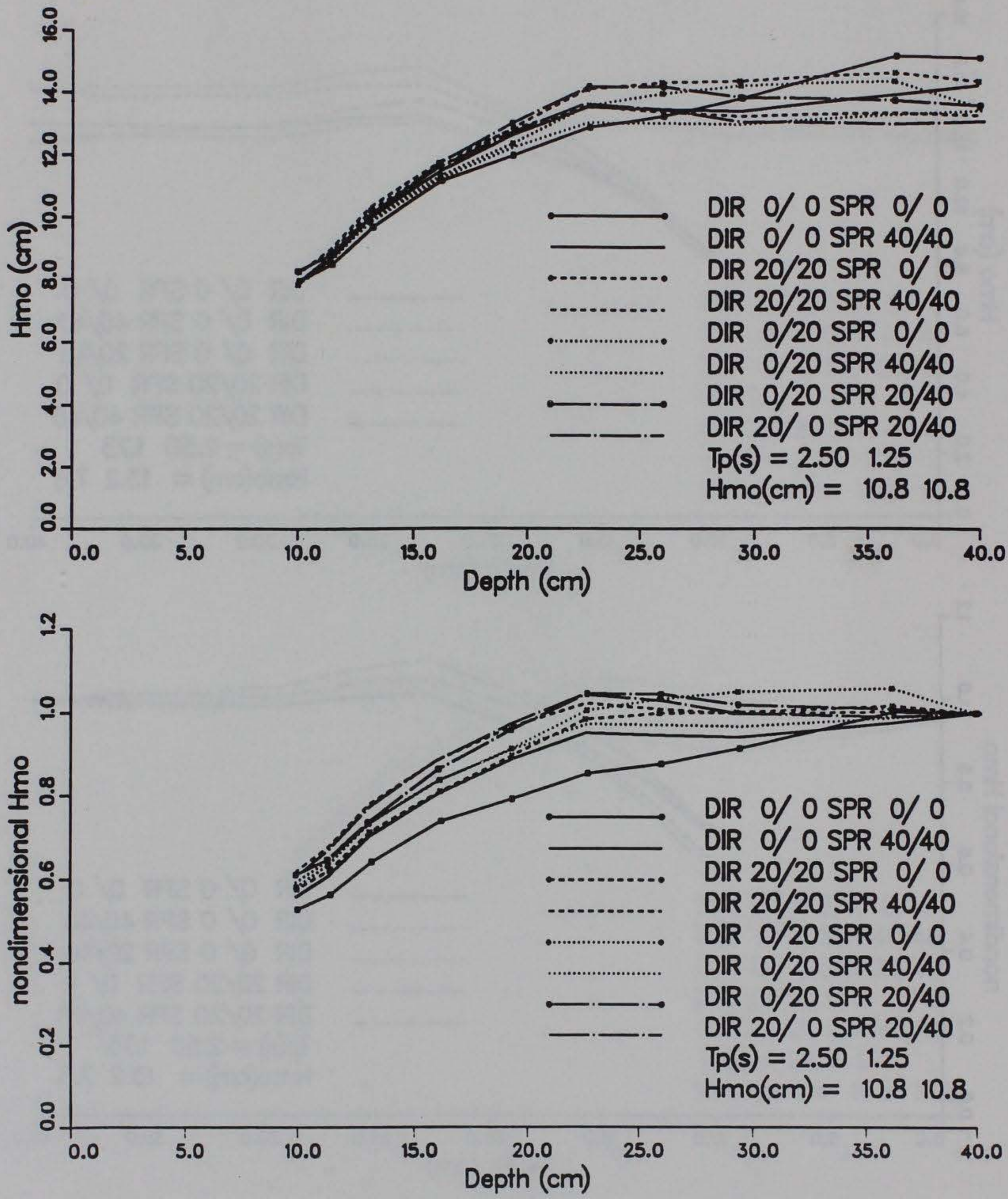

d. Cases with 1/2:1/2 energy distribution, 1.25-sec mode 2 peak period

Figure 20. (Sheet 4 of 4)

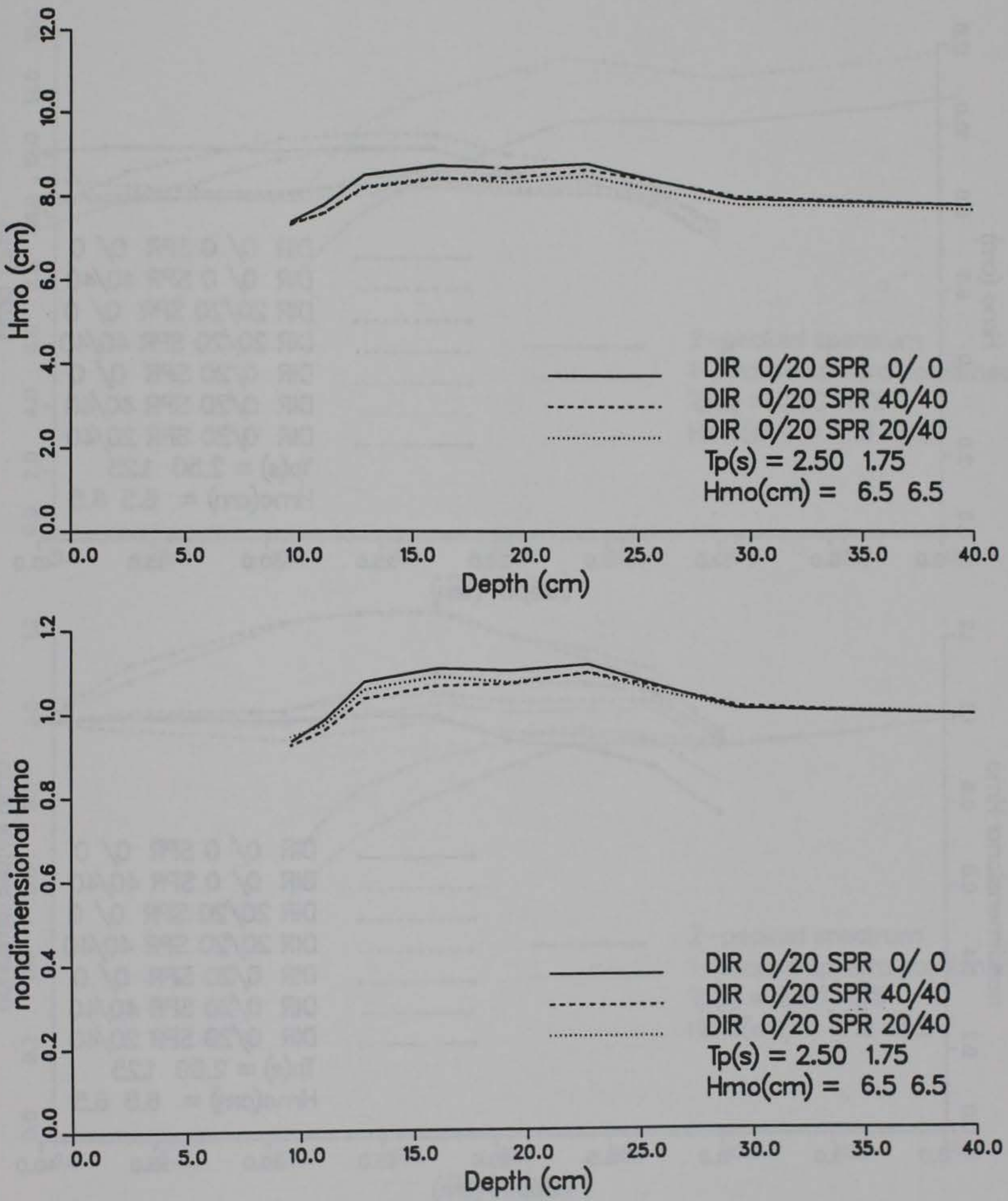

a. Cases with 1.75-sec mode 2 peak period

Figure 21. Initial height effect on wave height, bimodal spectra (Continued)

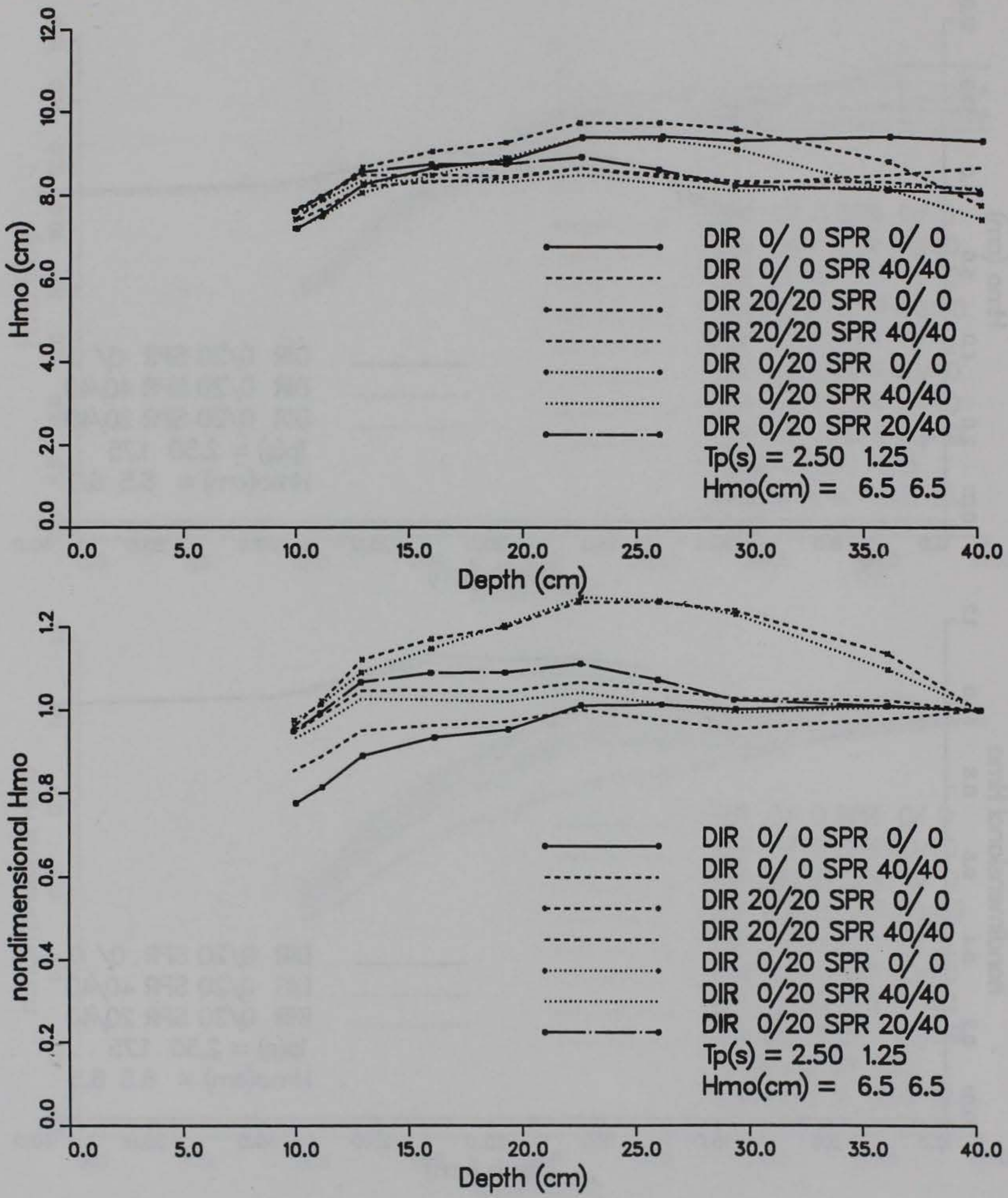

b. Cases with 1.25-sec mode 2 peak period

Figure 21. (Concluded)

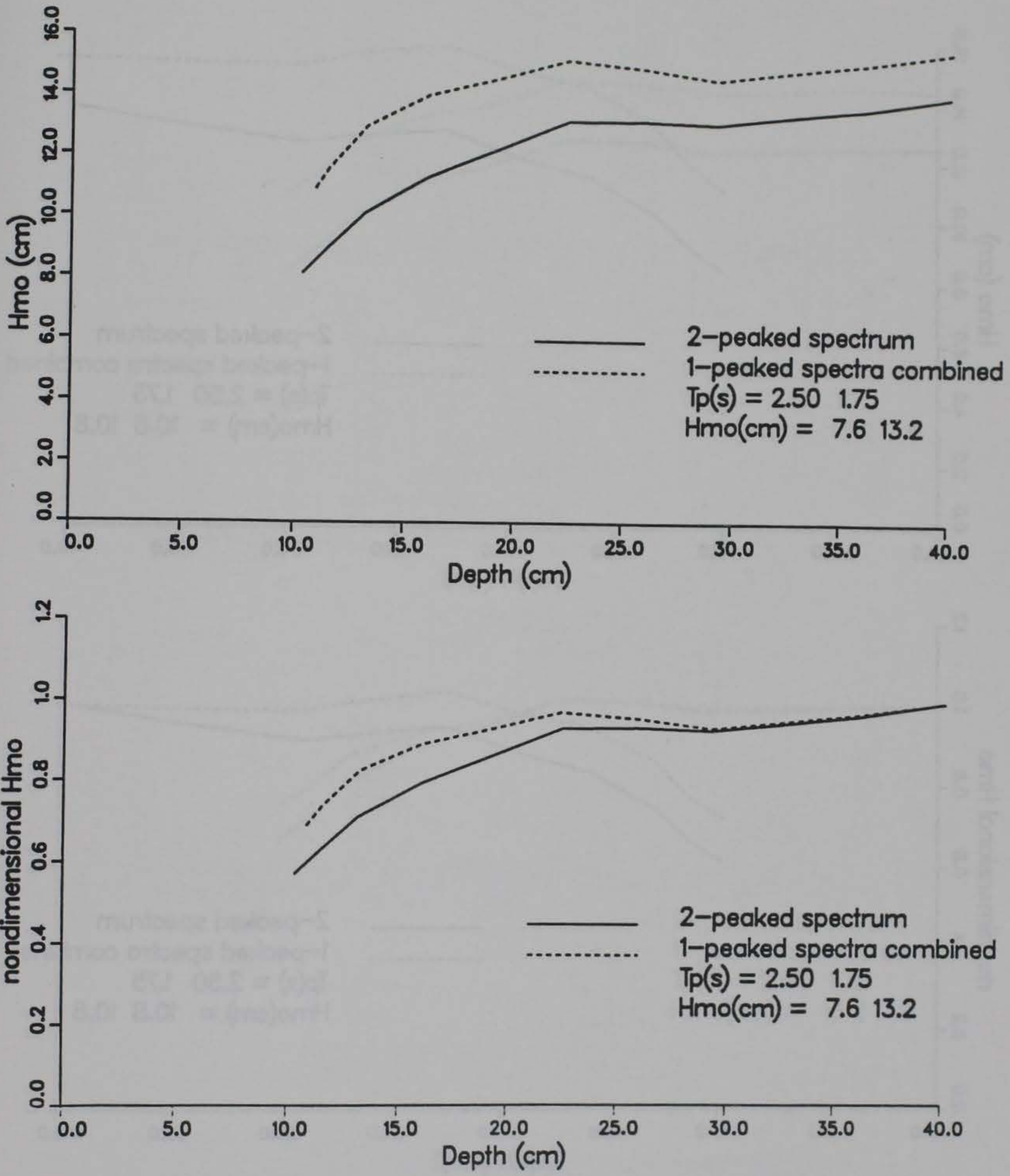

a. Cases with 1/3:2/3 energy distribution

Figure 22. Linear superposition assumption effect on wave height
(Sheet 1 of 3)

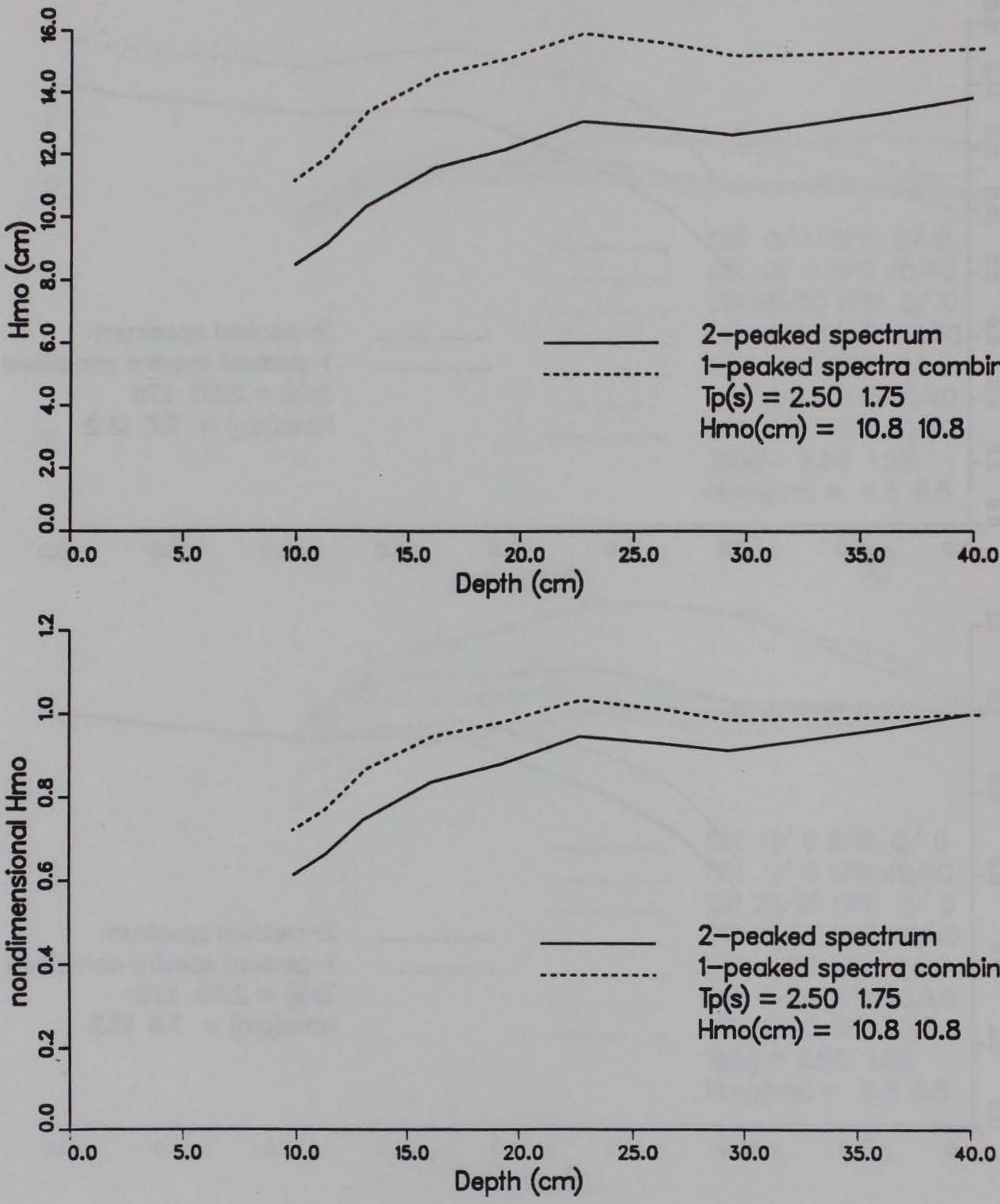

b. Cases with 1/2:1/2 energy distribution

Figure 22. (Sheet 2 of 3)

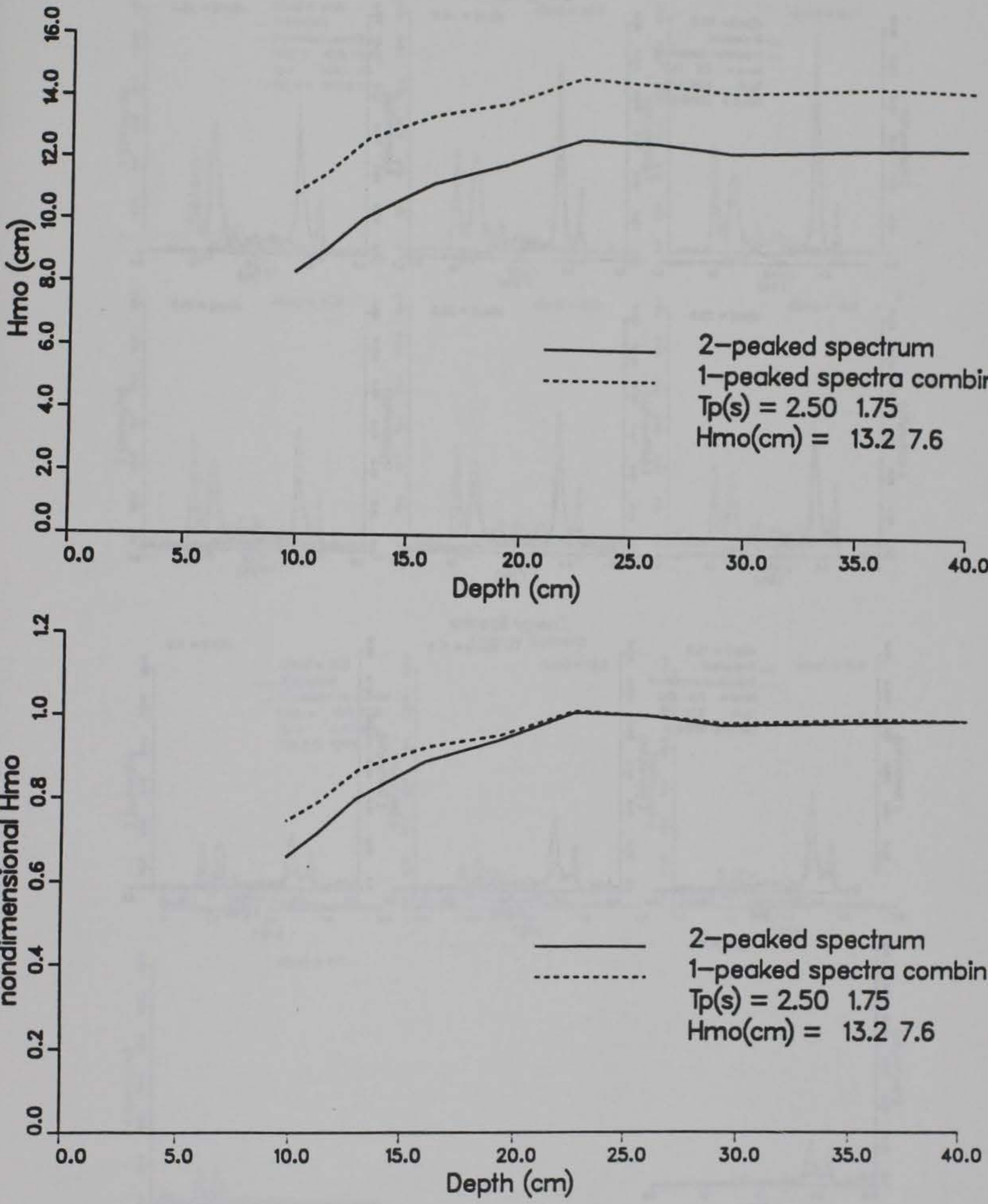

c. Cases with 2/3:1/3 energy distribution

Figure 22. (Sheet 3 of 3)

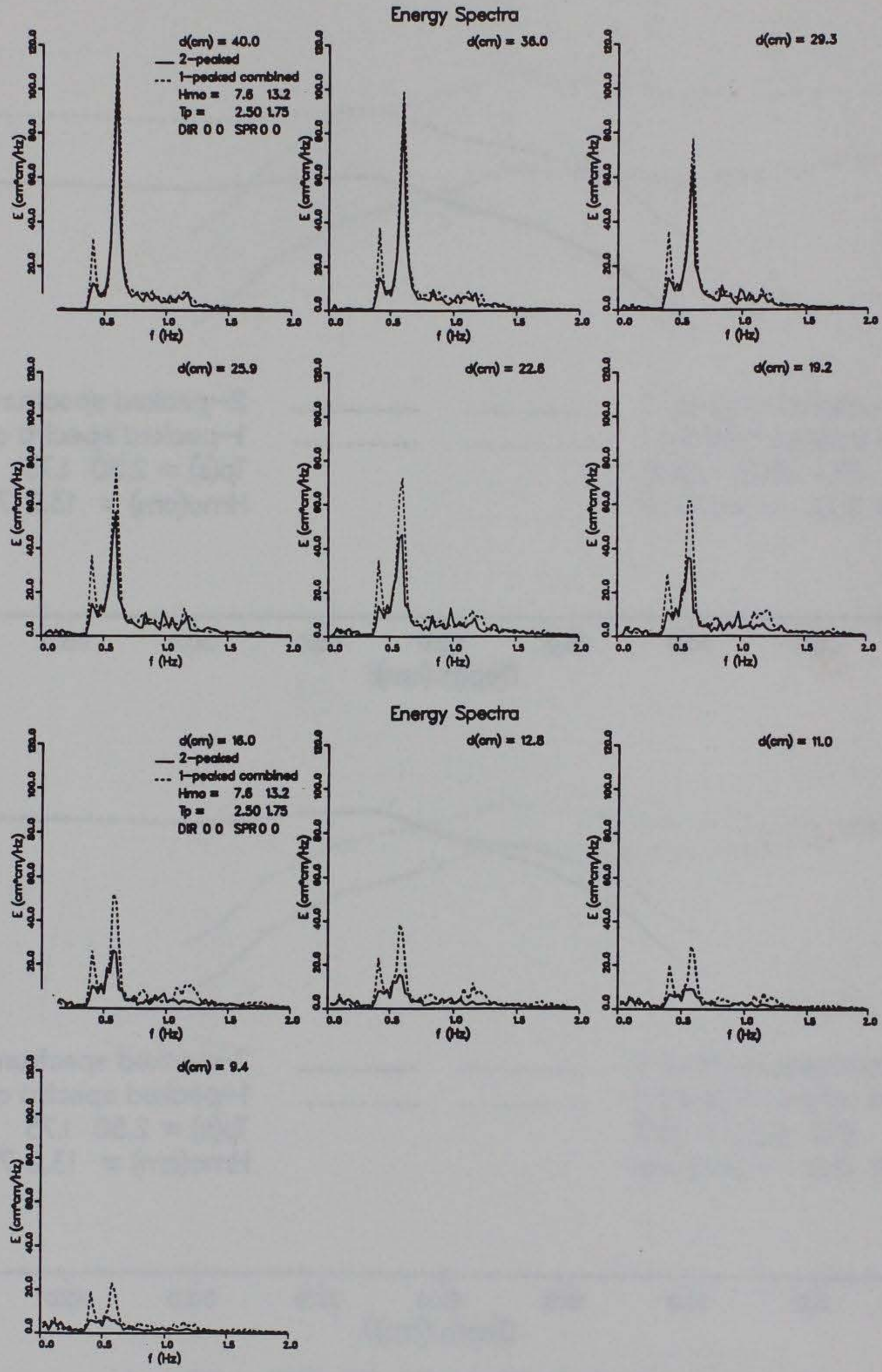

a. Cases with 1/3:2/3 energy distribution

Figure 23. Linear superposition assumption effect on wave spectra (Sheet 1 of 3)

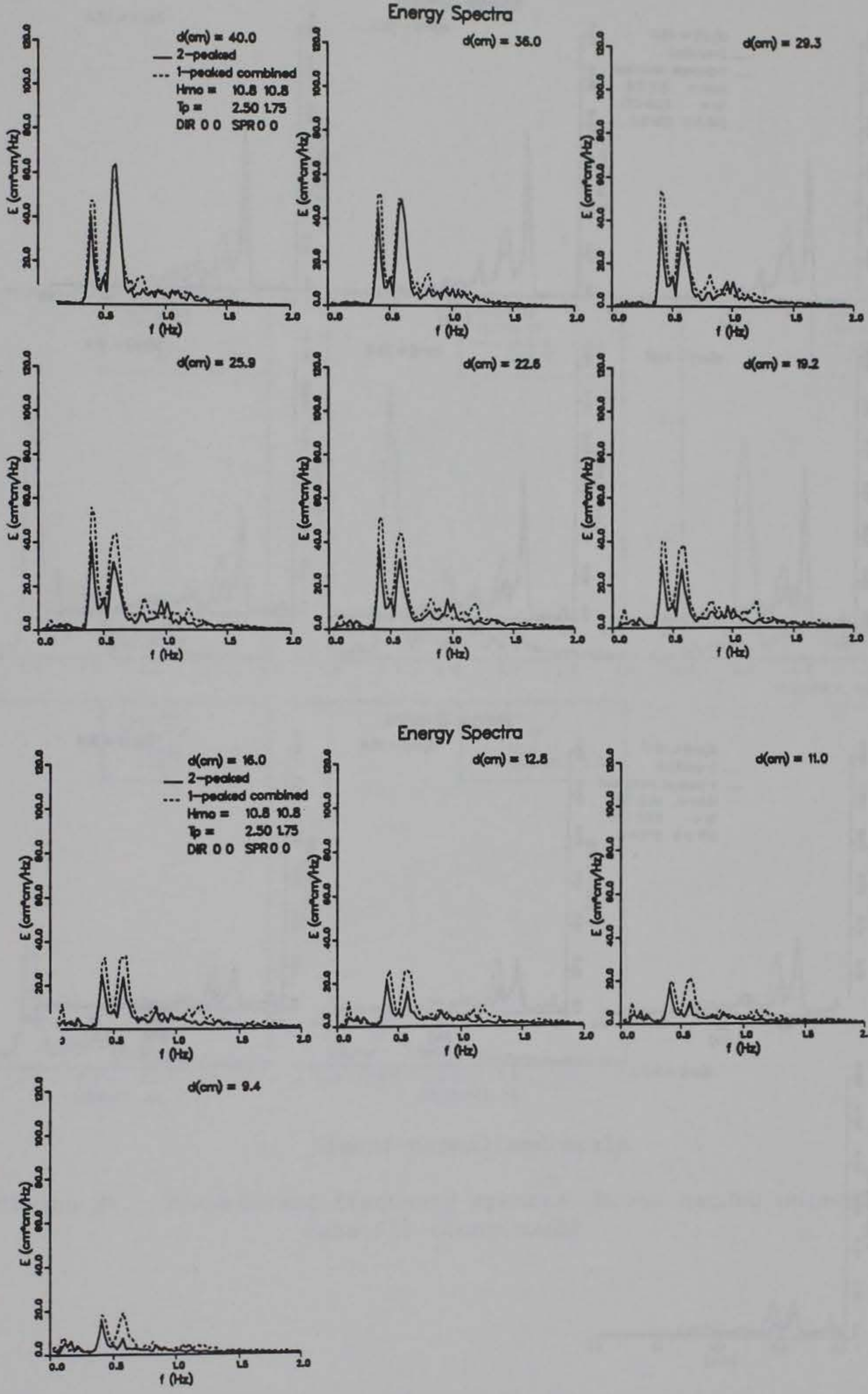

b. Cases with 1/2:1/2 energy distribution

Figure 23. (Sheet 2 of 3)

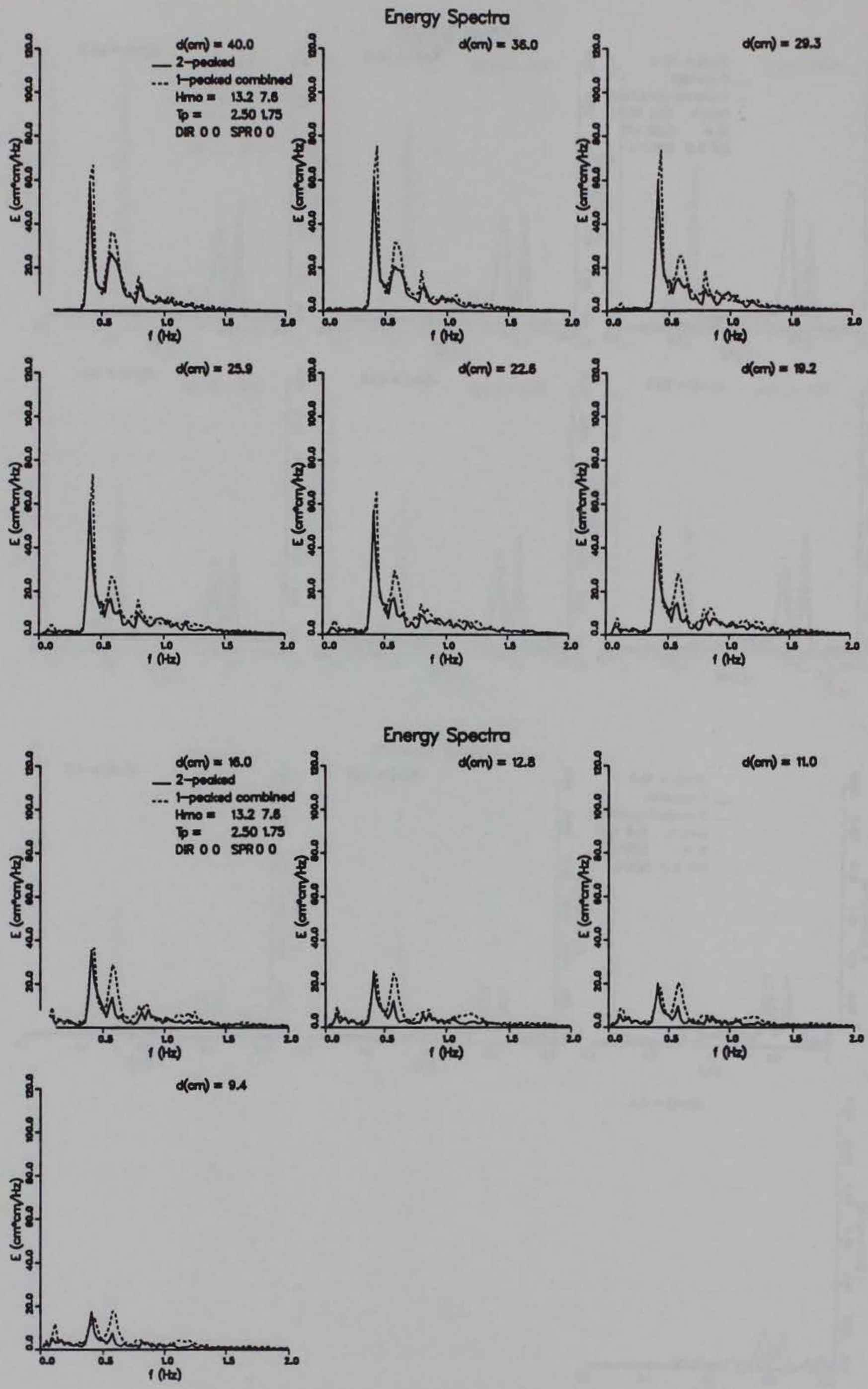

c. Cases with 2/3:1/3 energy distribution

Figure 23. (Sheet 3 of 3)

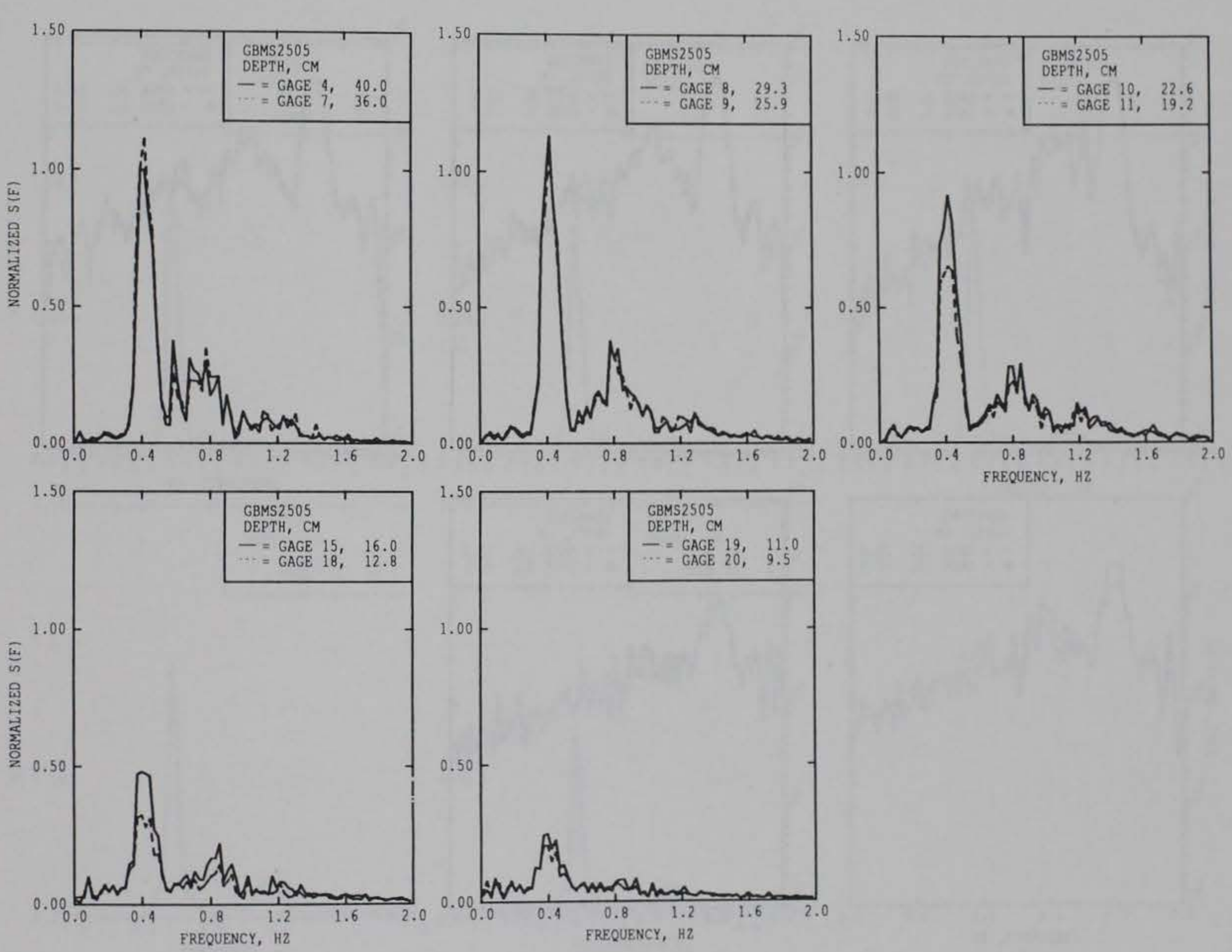

a. Linear normalized scale

Figure 24. Transformed frequency spectra, broad-banded unimodal case S25 (Continued)

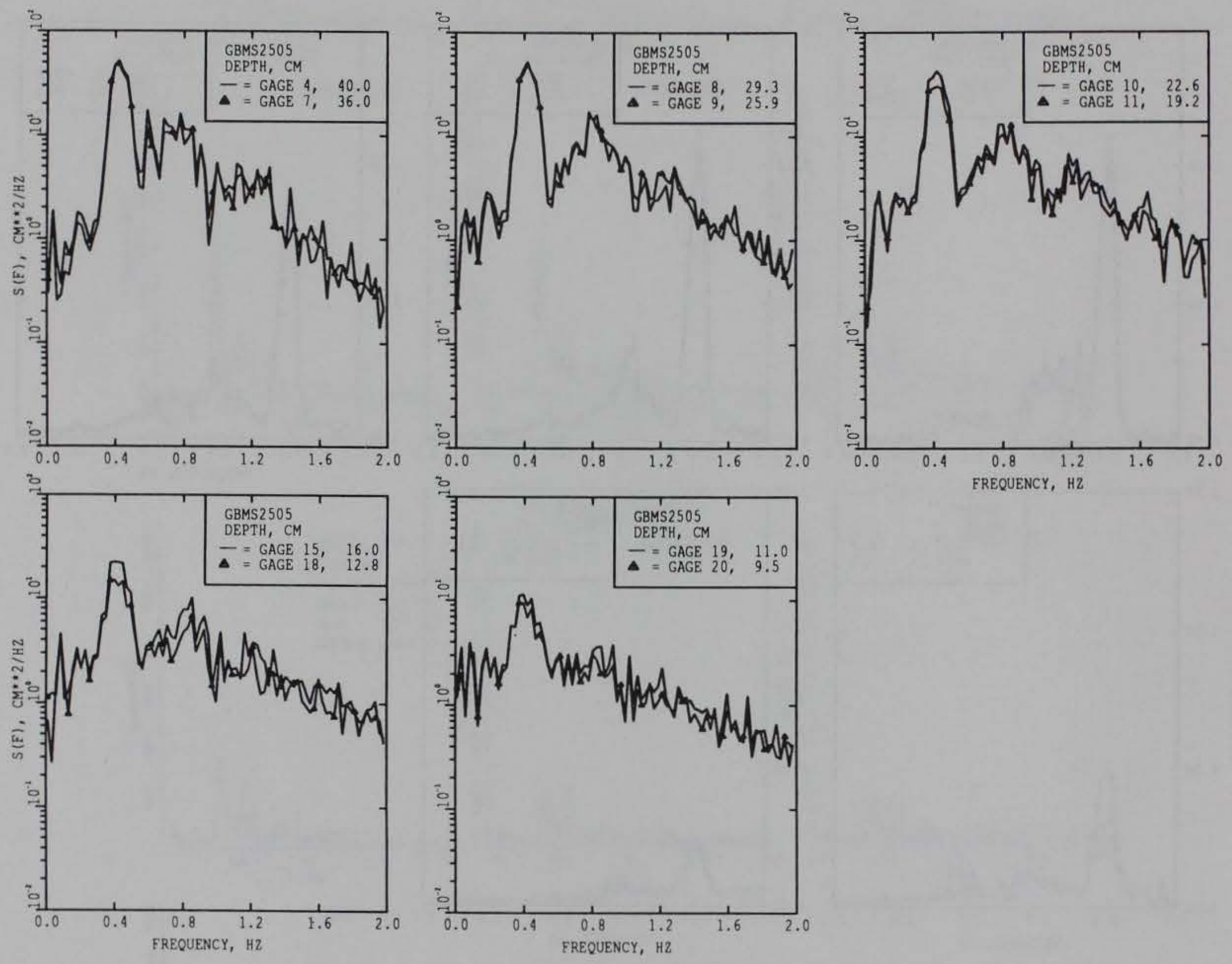

b. Semilog scale

Figure 24. (Concluded)

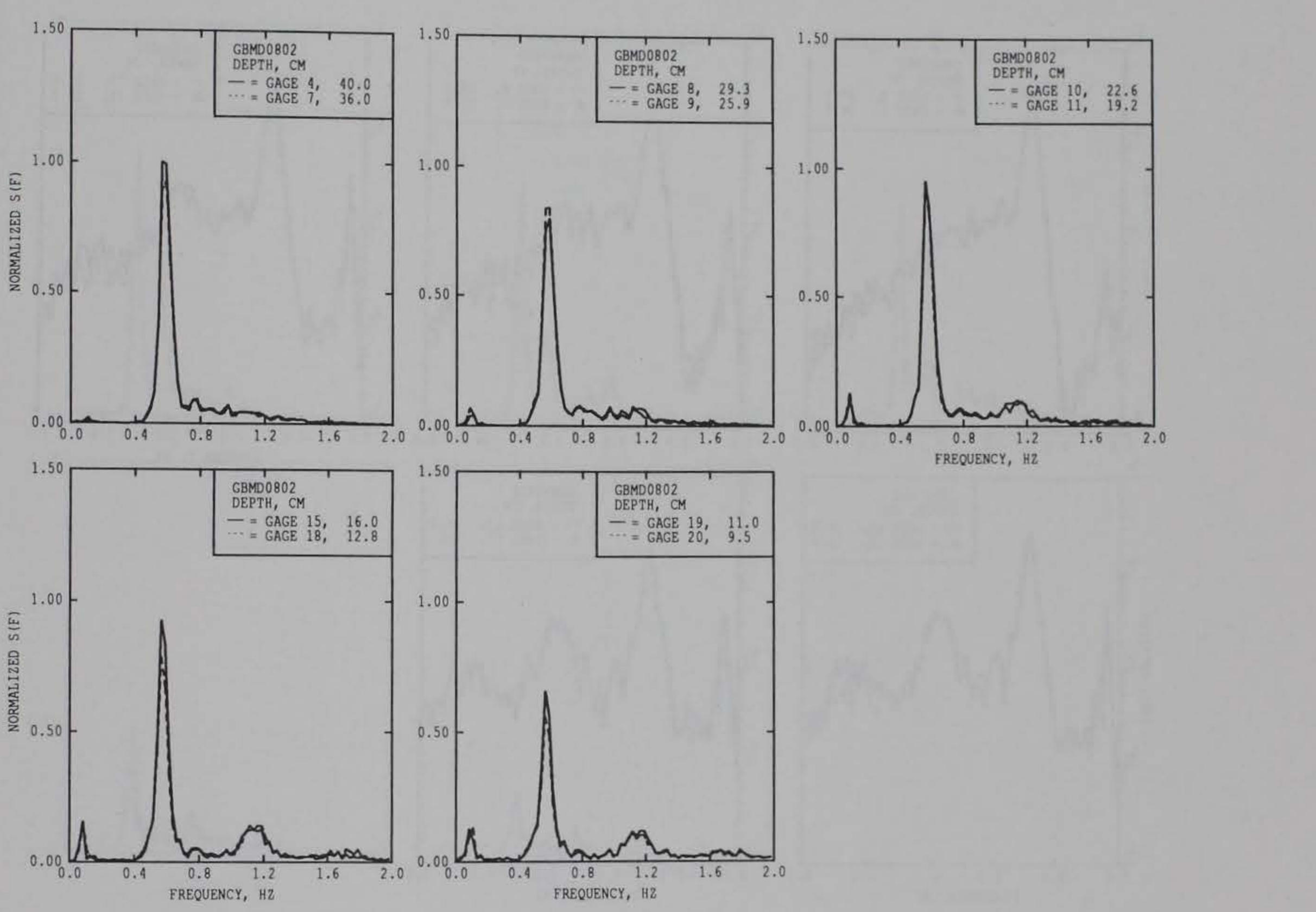

a. Linear normalized scale

Figure 25. Transformed frequency spectra, narrow-banded unimodal case D08 (Continued)

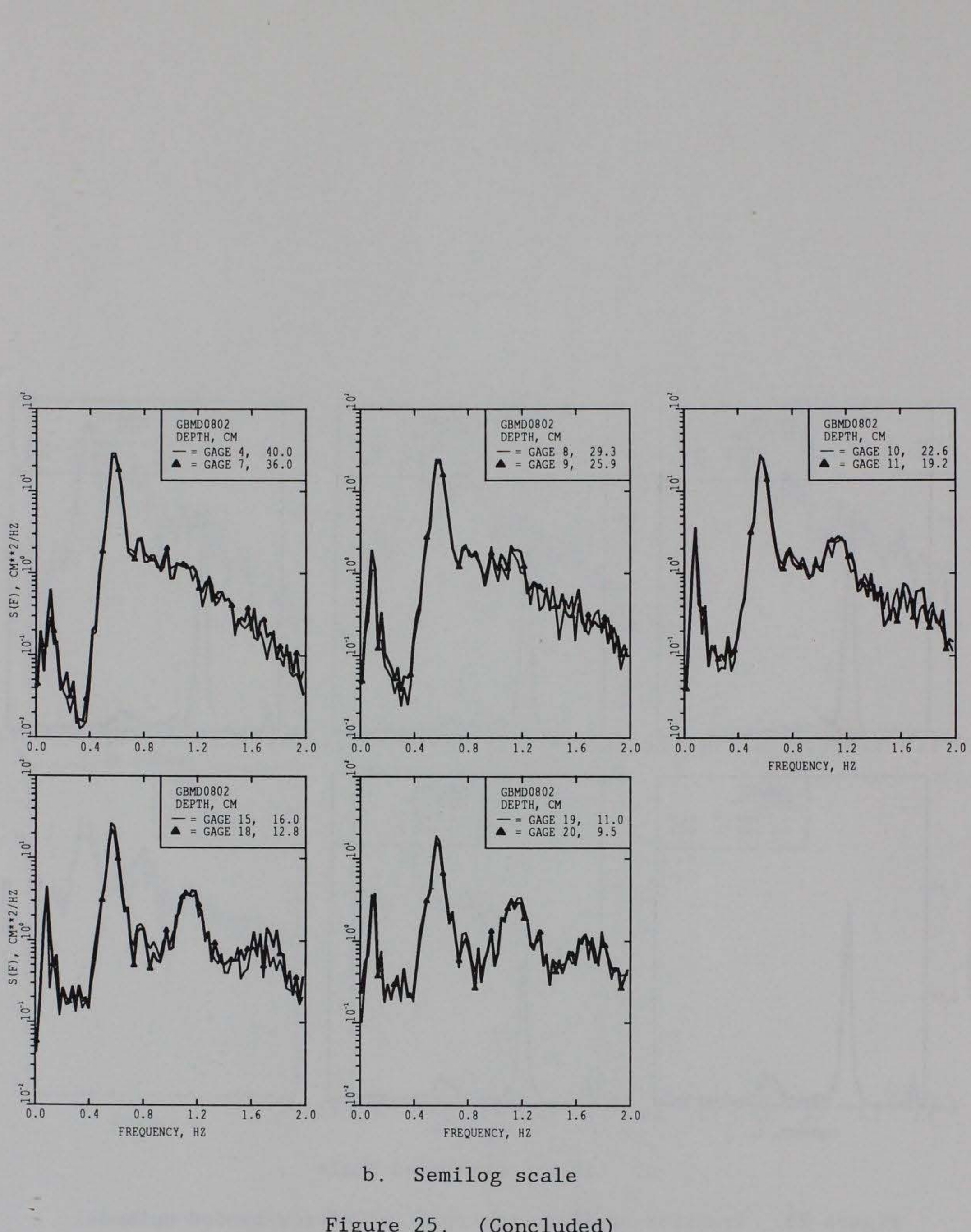

b. Semilog scale

Figure 25. (Concluded)

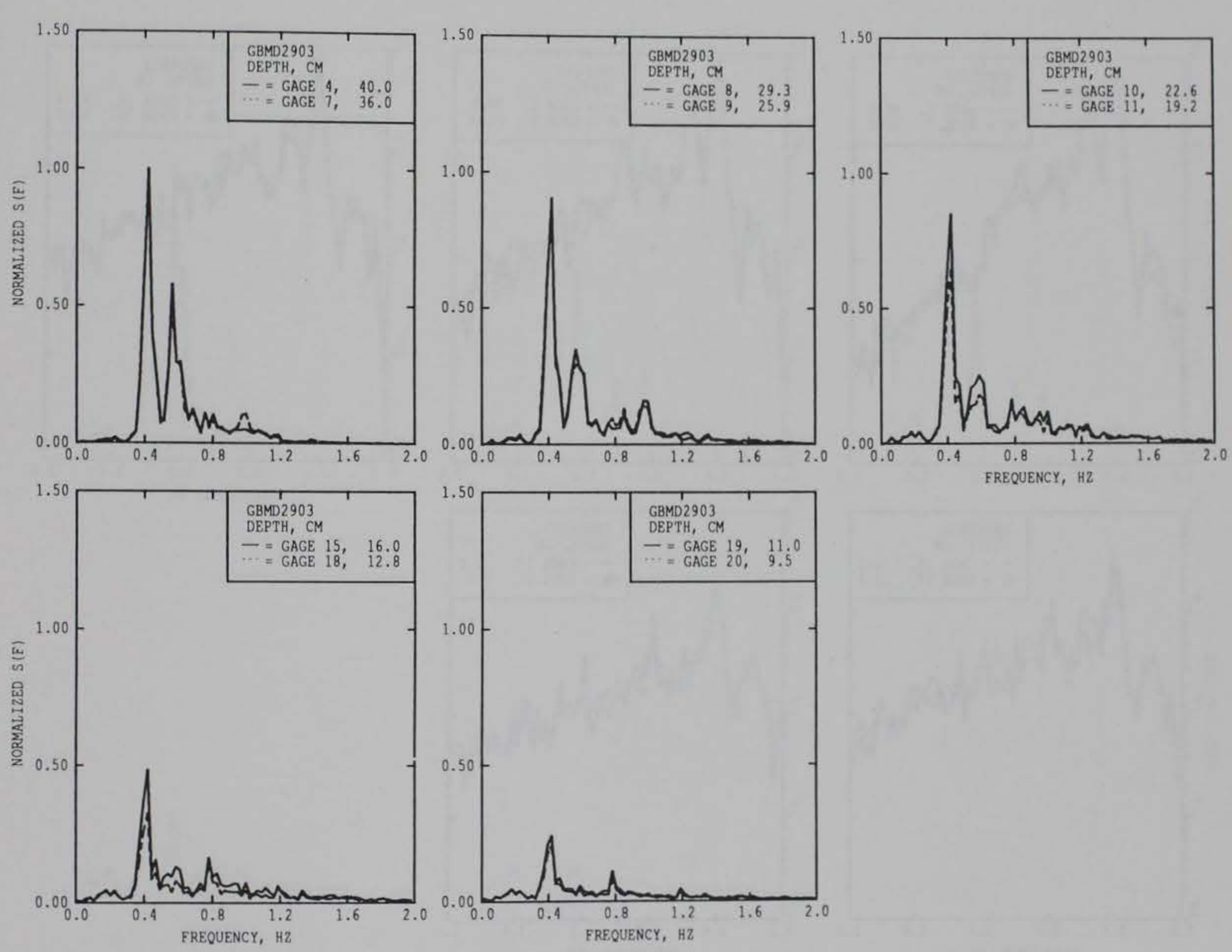

a. Linear normalized scale

Figure 26. Transformed frequency spectra, bimodal case D29 (Continued)

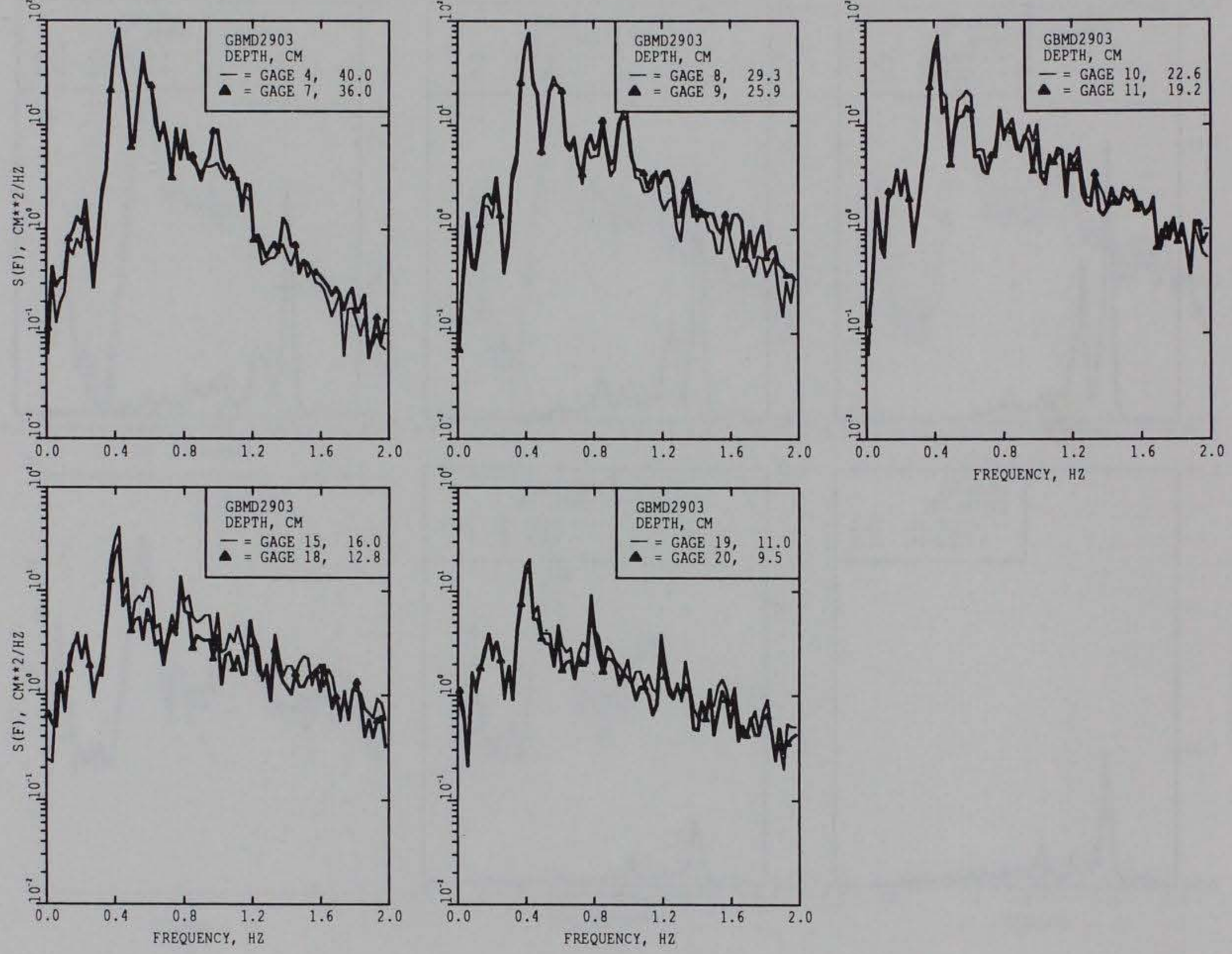

b. Semilog scale

Figure 26. (Concluded)

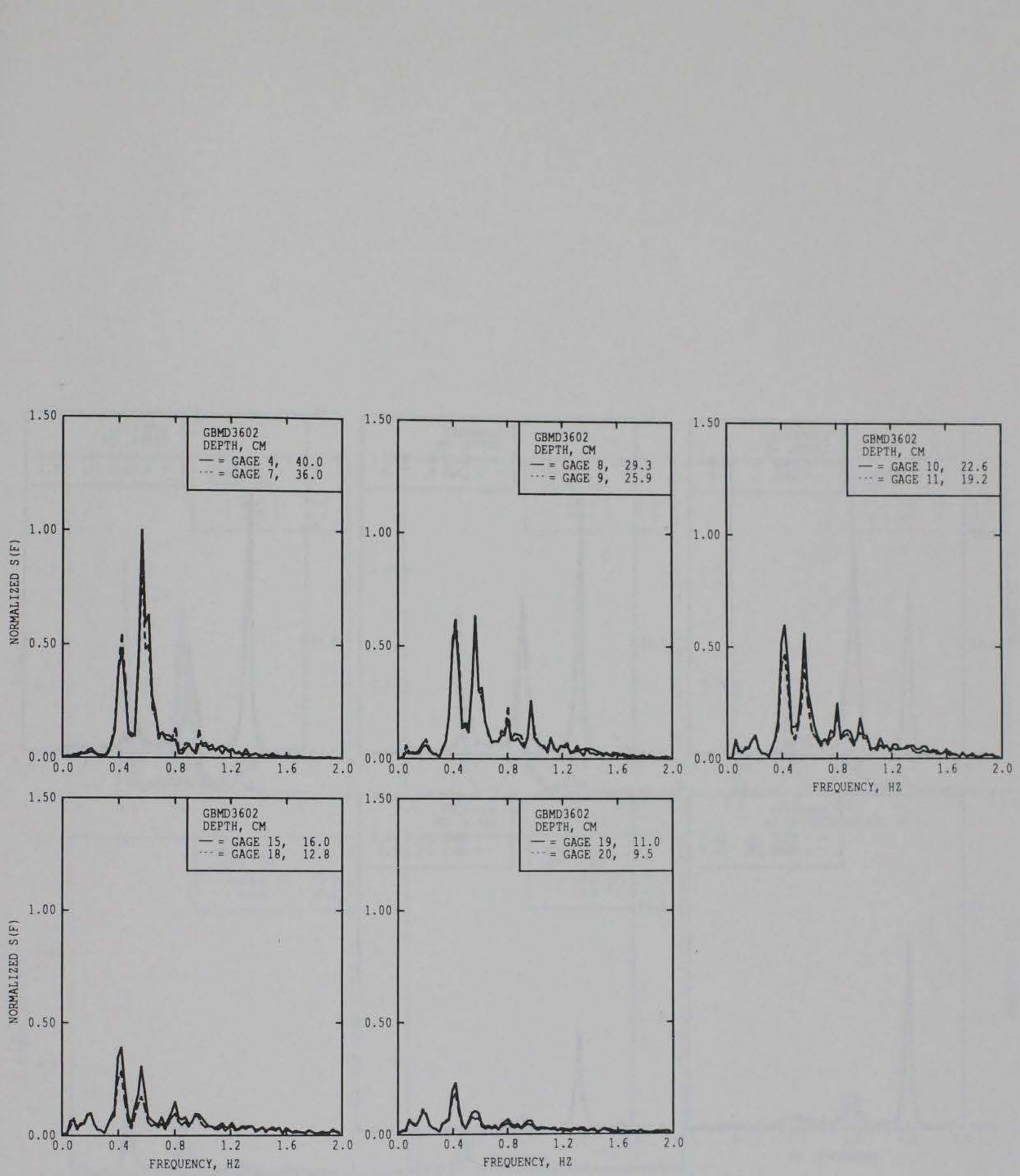

a. Case D36 with 1.75-sec mode 2 peak period

Figure 27. Nonlinear interaction effect on spectral transformation (Continued)

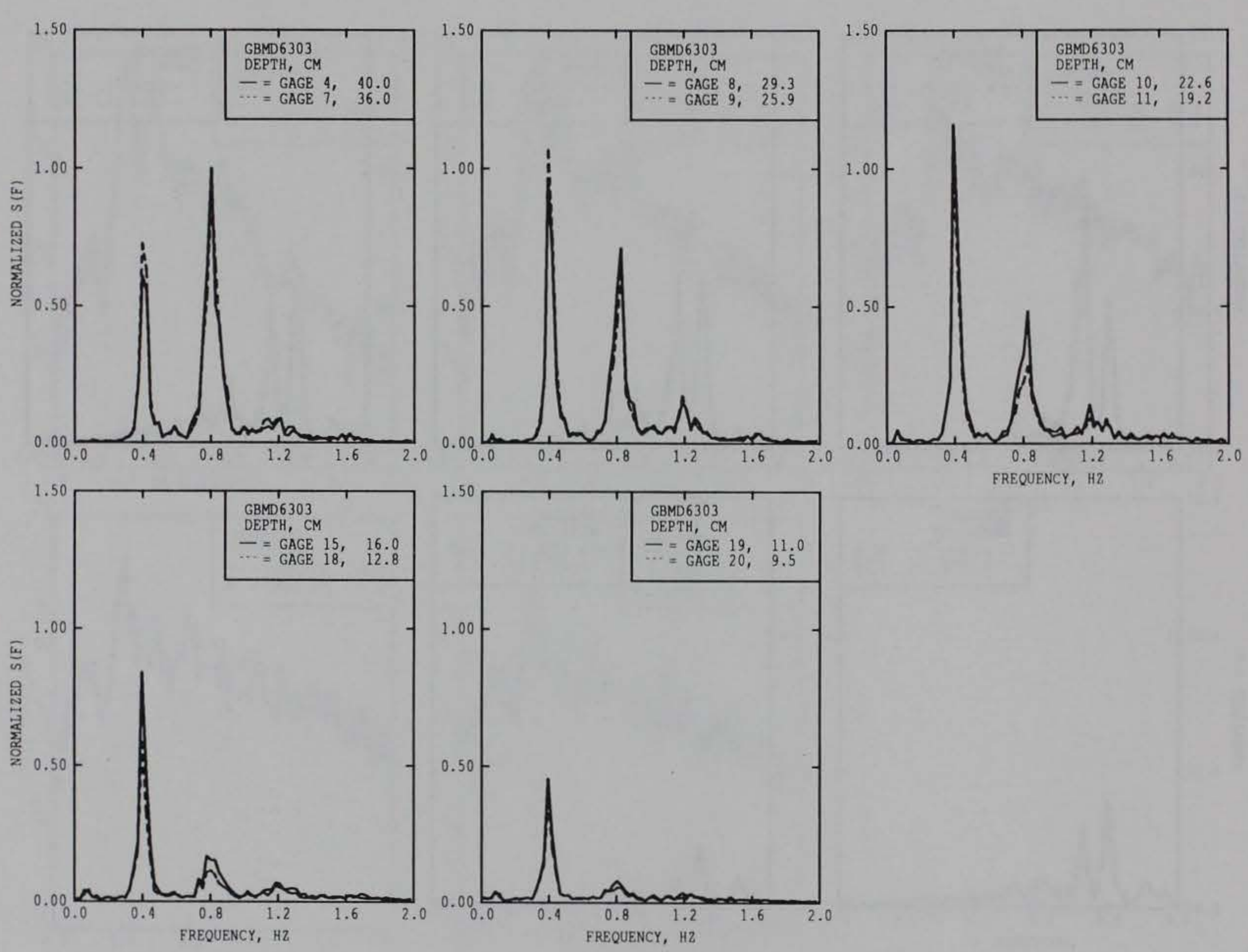

b. Case D63 with 1.25-sec mode 2 peak period

Figure 27. (Concluded)

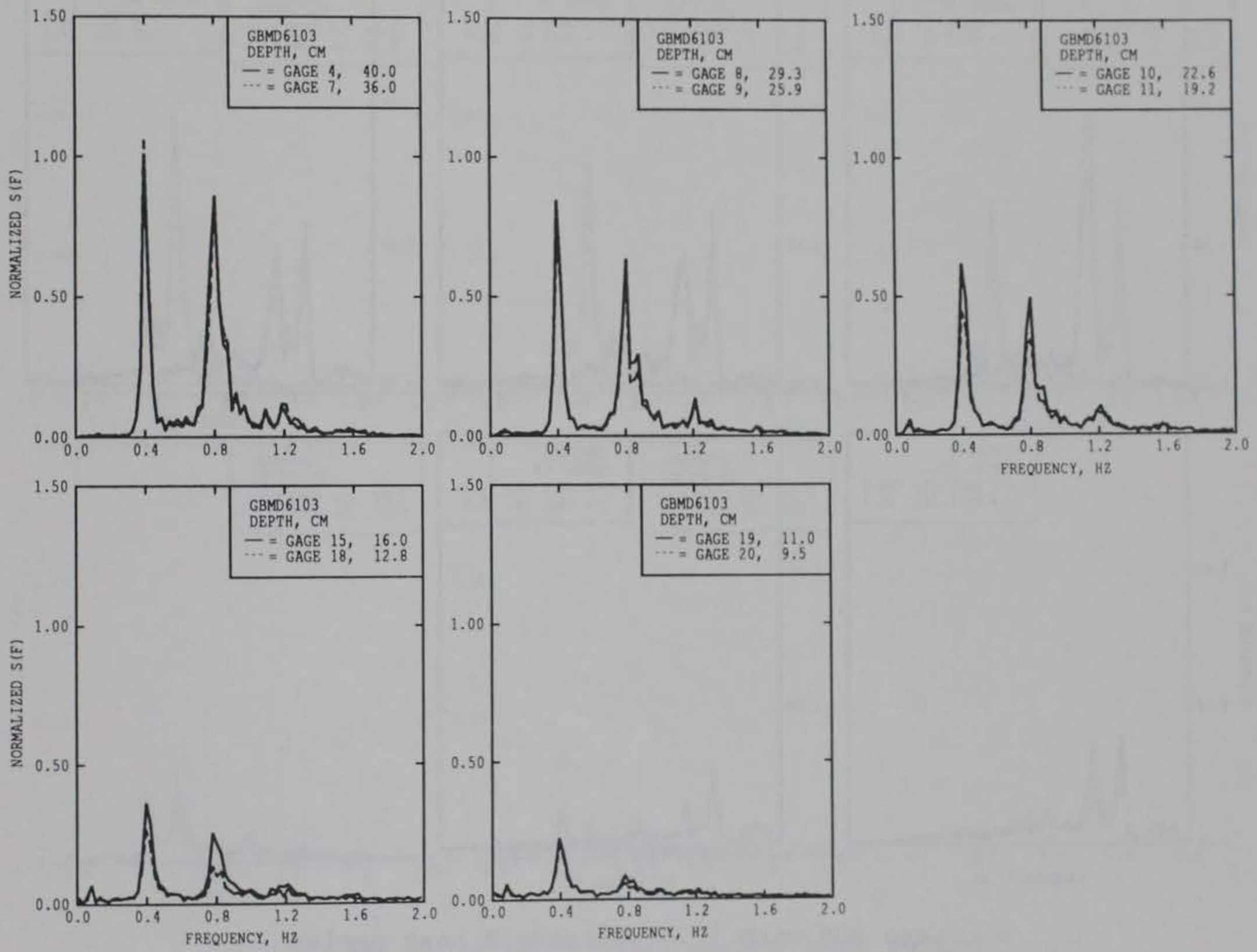

Figure 28. Transformed frequency spectra, case D61

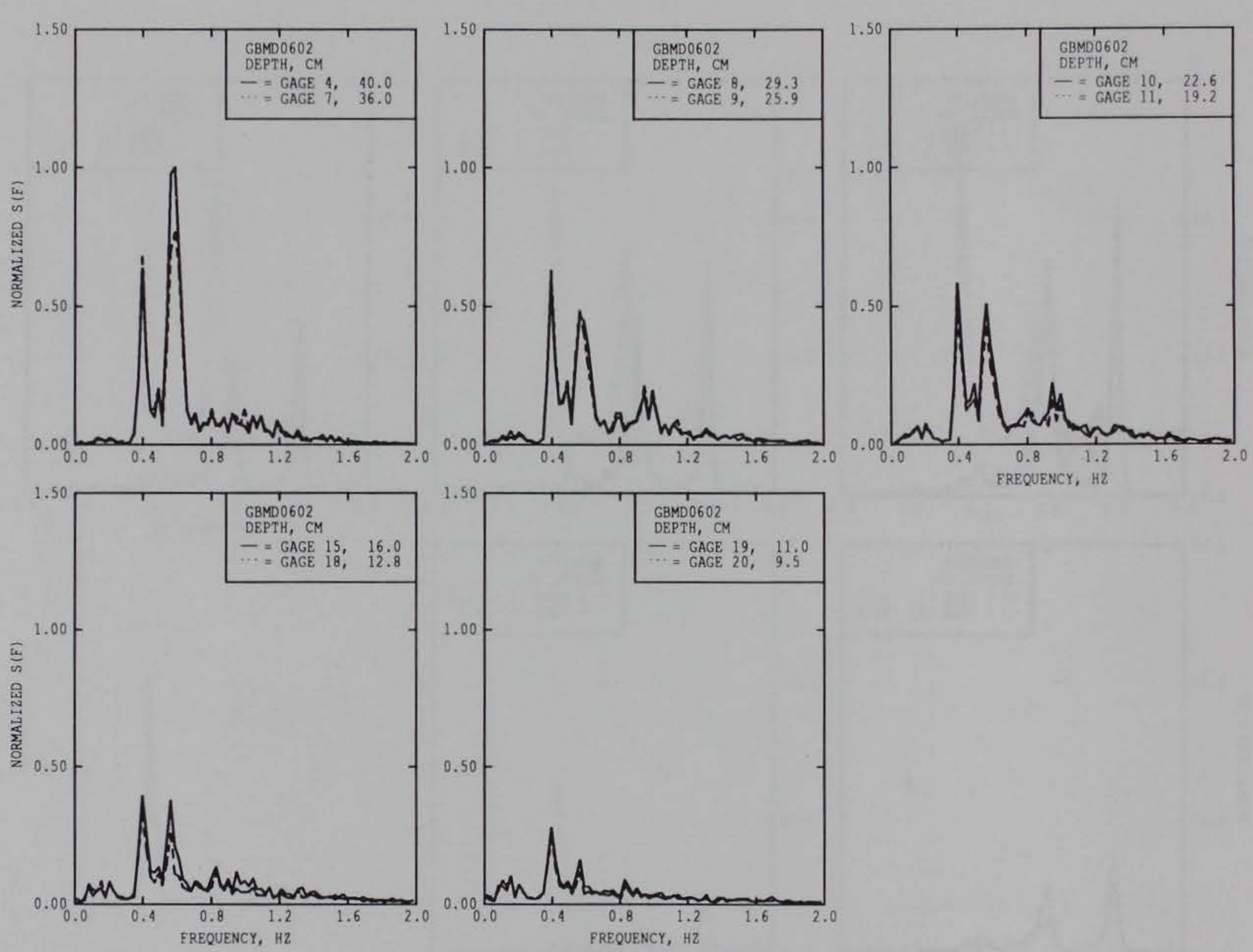

a. Case D06 with 1.75-sec mode 2 peak period

Figure 29. Directional spreading effect on subharmonic growth
(Sheet 1 of 3)

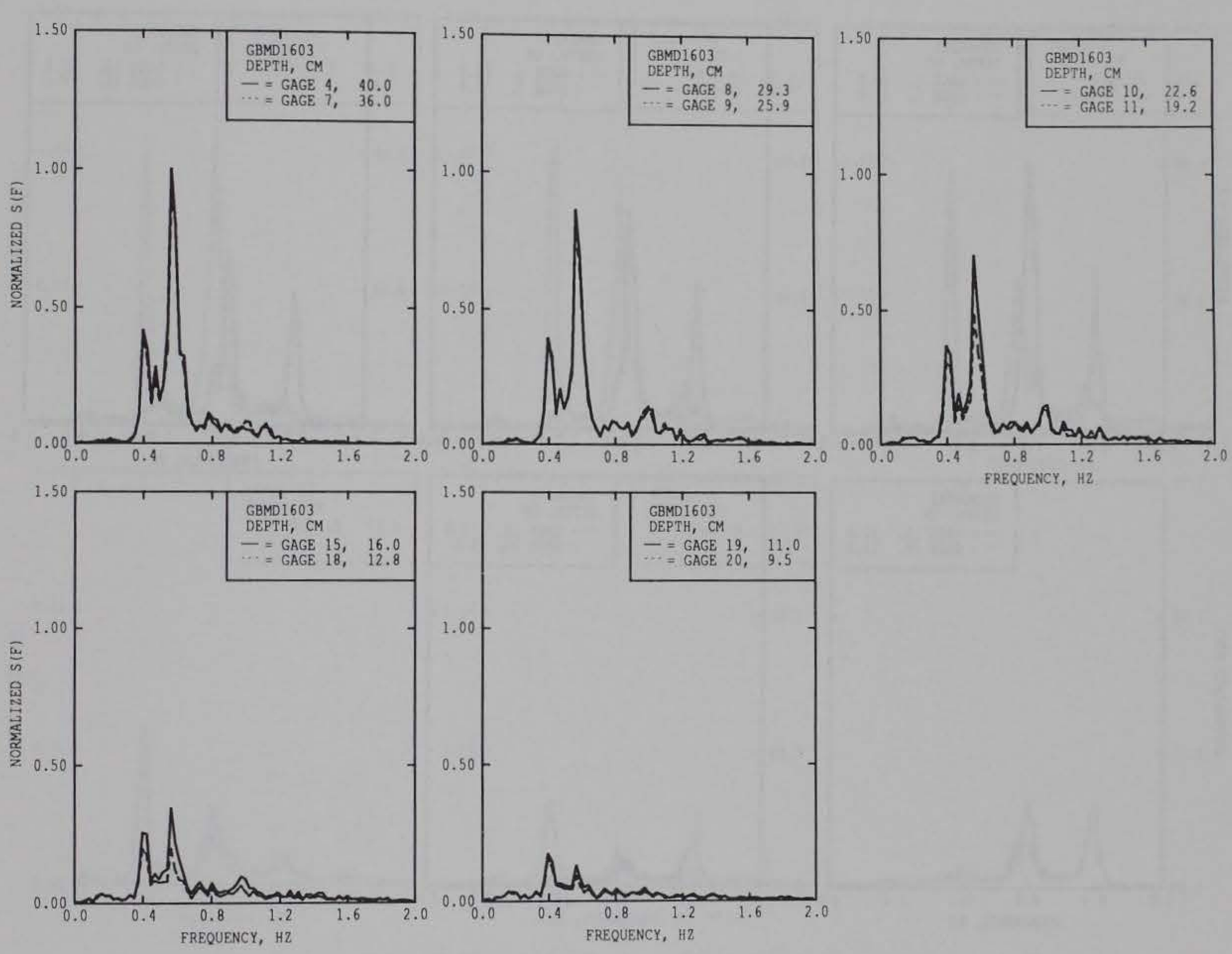

b. Case D16 with 1.75-sec mode 2 peak period

Figure 29. (Sheet 2 of 3)

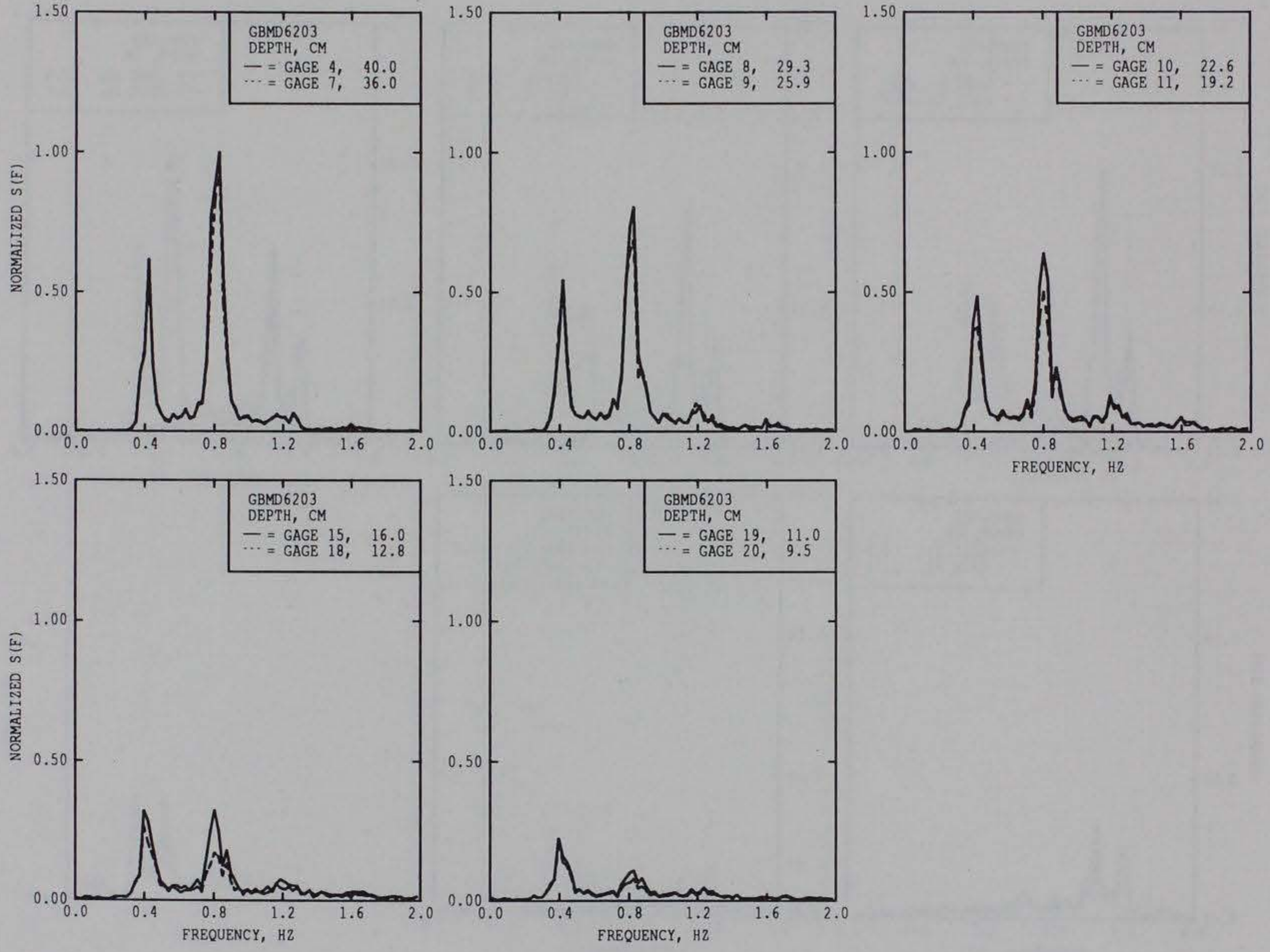

c. Case D62 with 1.25-sec mode 2 peak period

Figure 29. (Sheet 3 of 3)

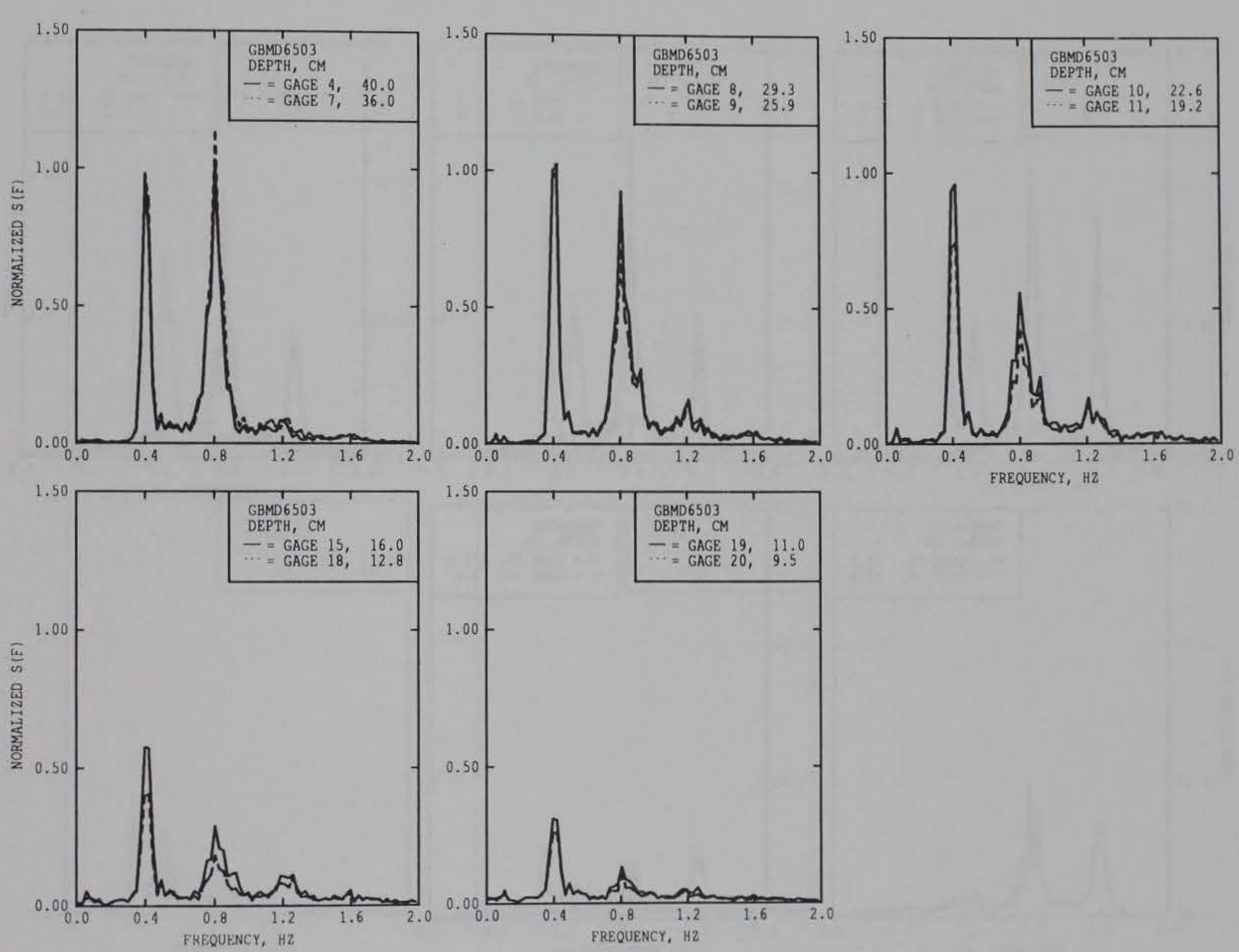

a. Case D65 with 0-deg directional spread

Figure 30. Directional spreading effect on first mode energy (Continued)

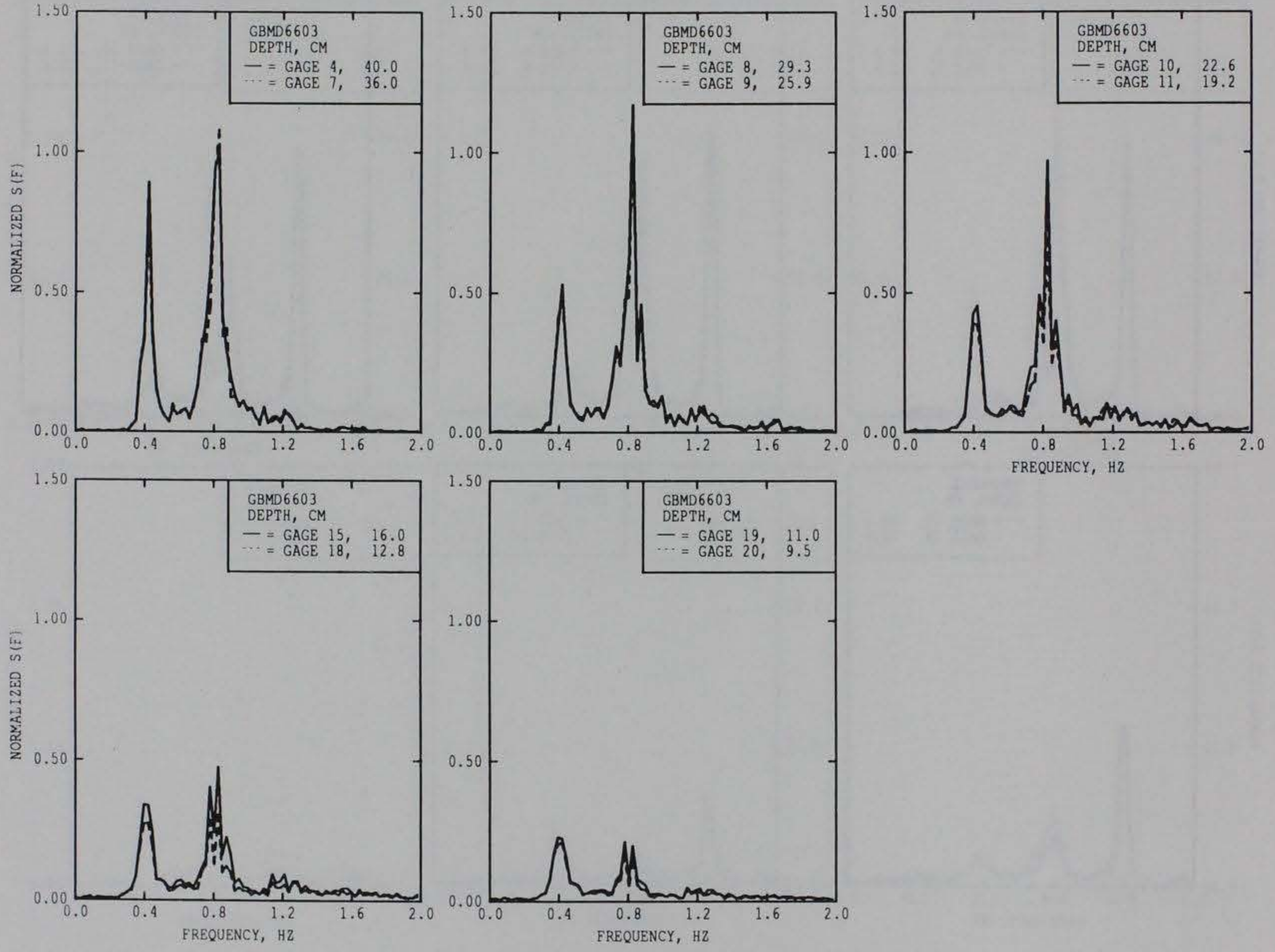

b. Case D66 with 40-deg directional spread

Figure 30. (Concluded)

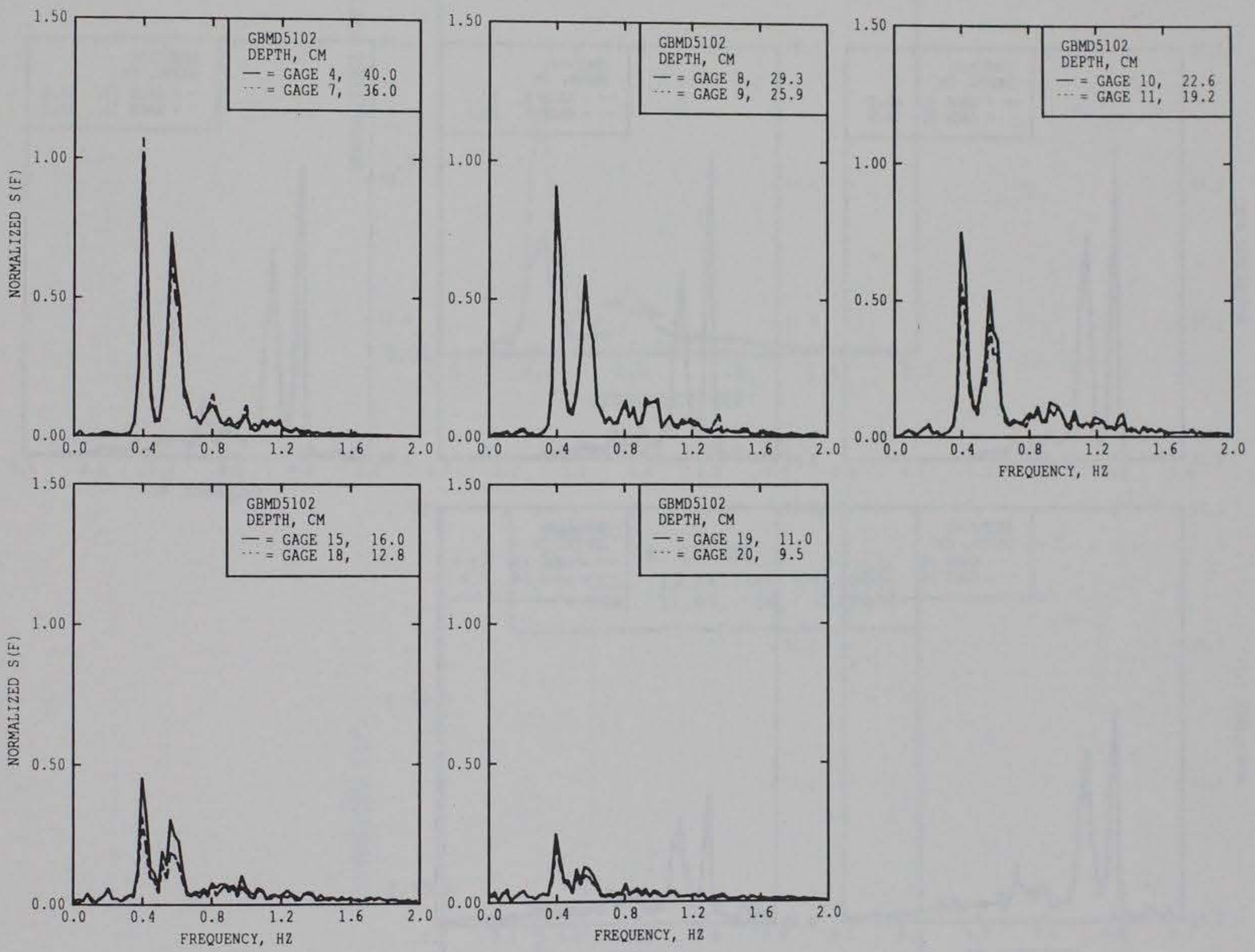

a. Case D51 with 10.8-cm wave height

Figure 31. Initial height effect on spectral transformation (Continued)

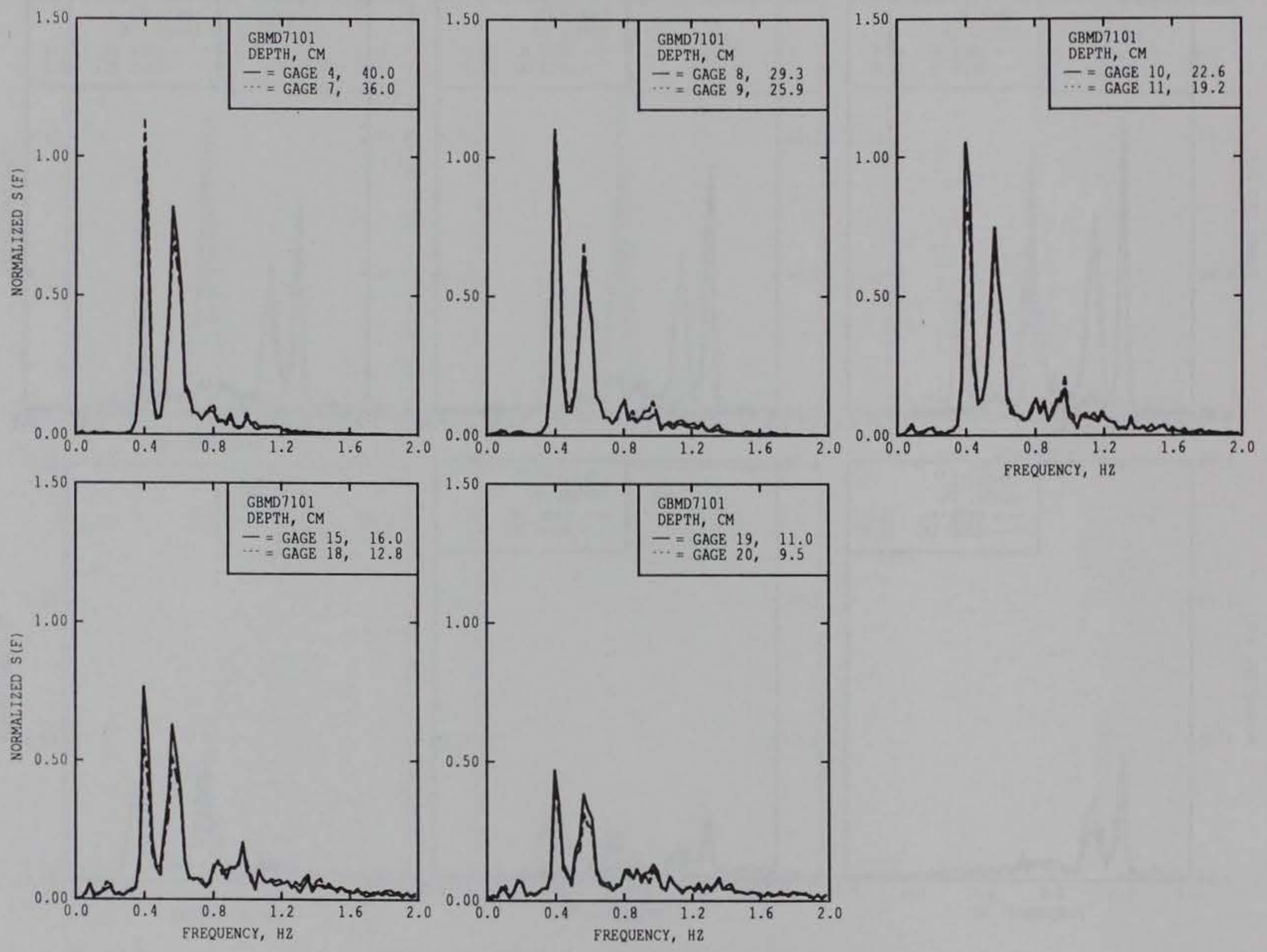

b. Case D71 with 6.5-cm wave height

Figure 31. (Concluded)

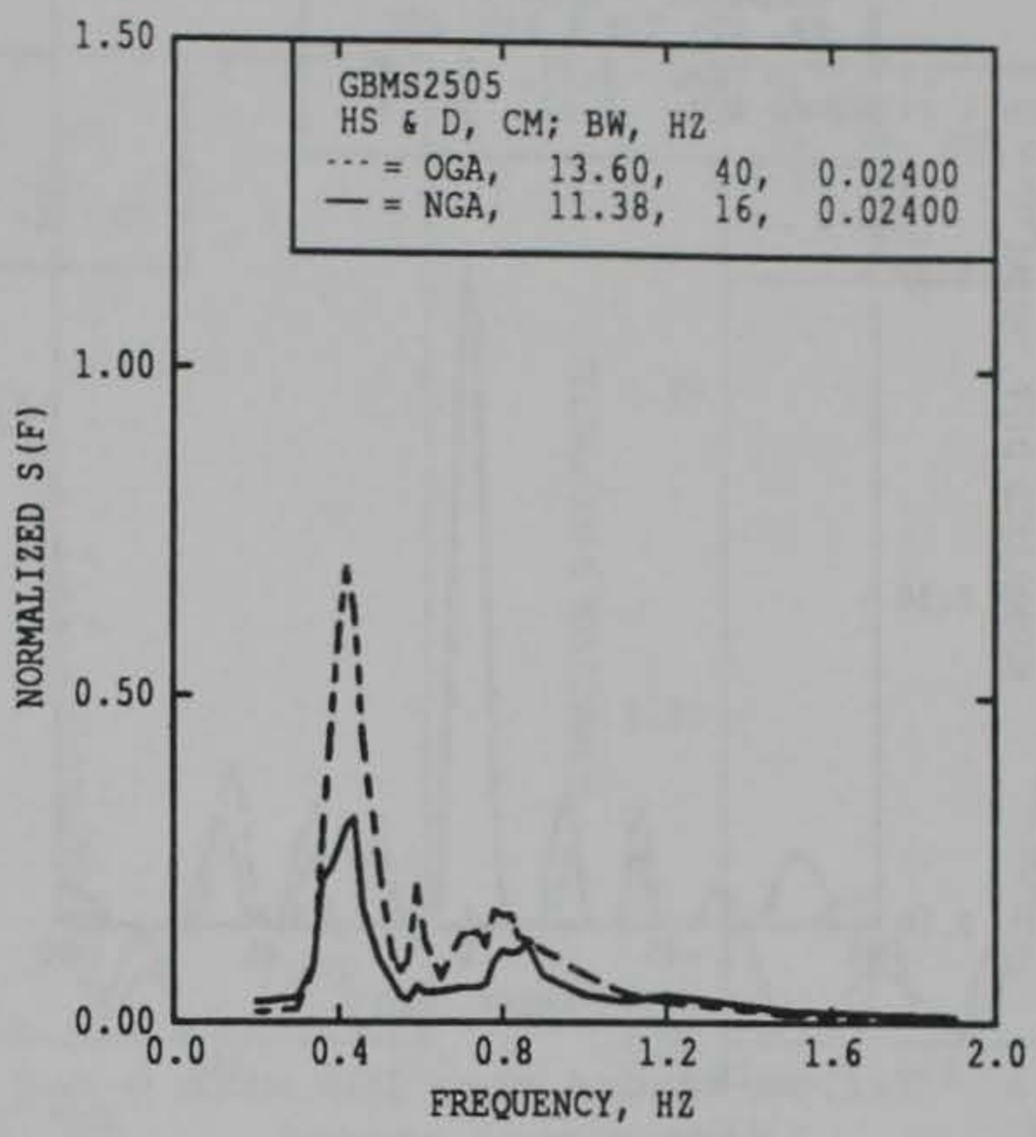

a. Unimodal case S25

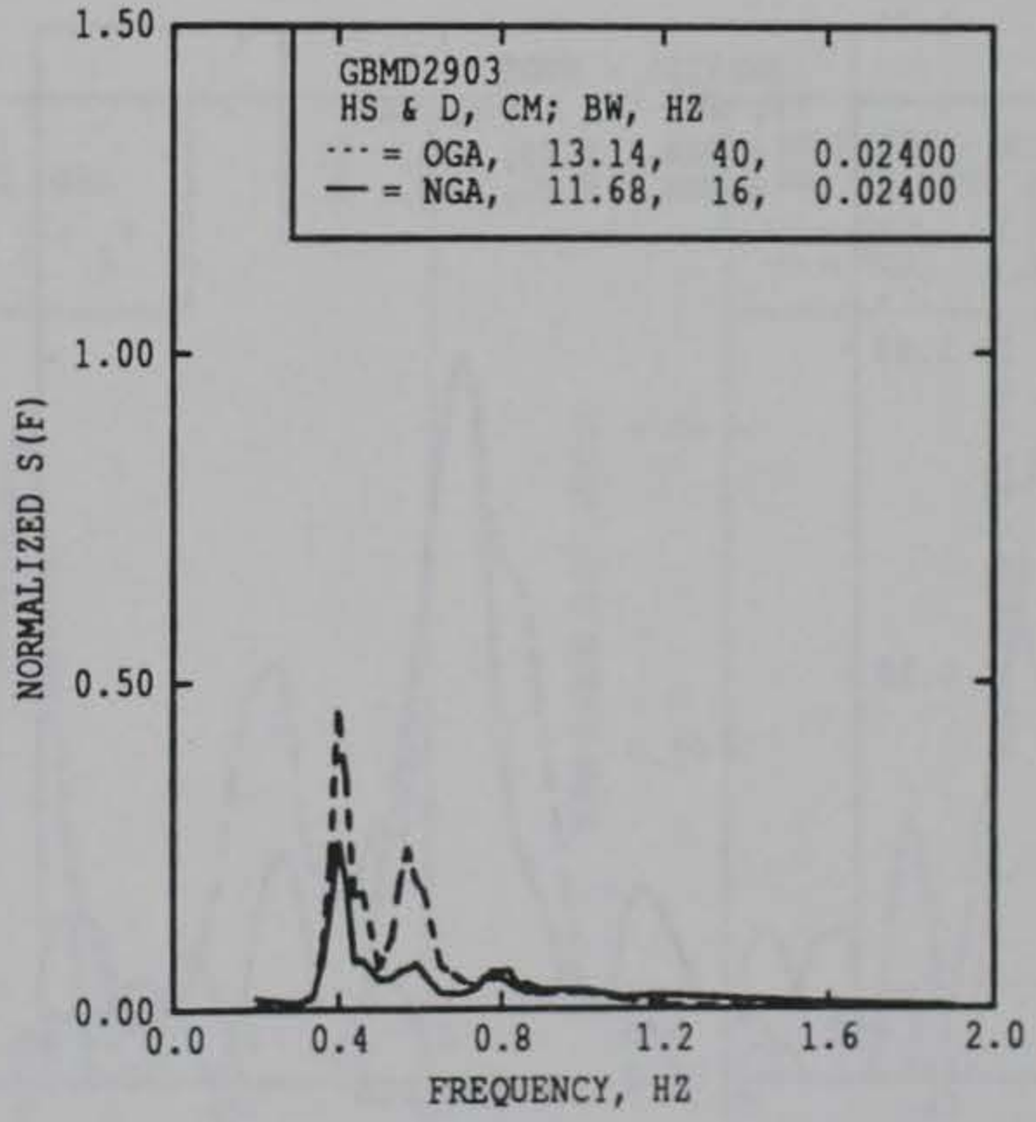

b. Bimodal case D29

Figure 32. Measured average spectra for offshore and nearshore linear arrays

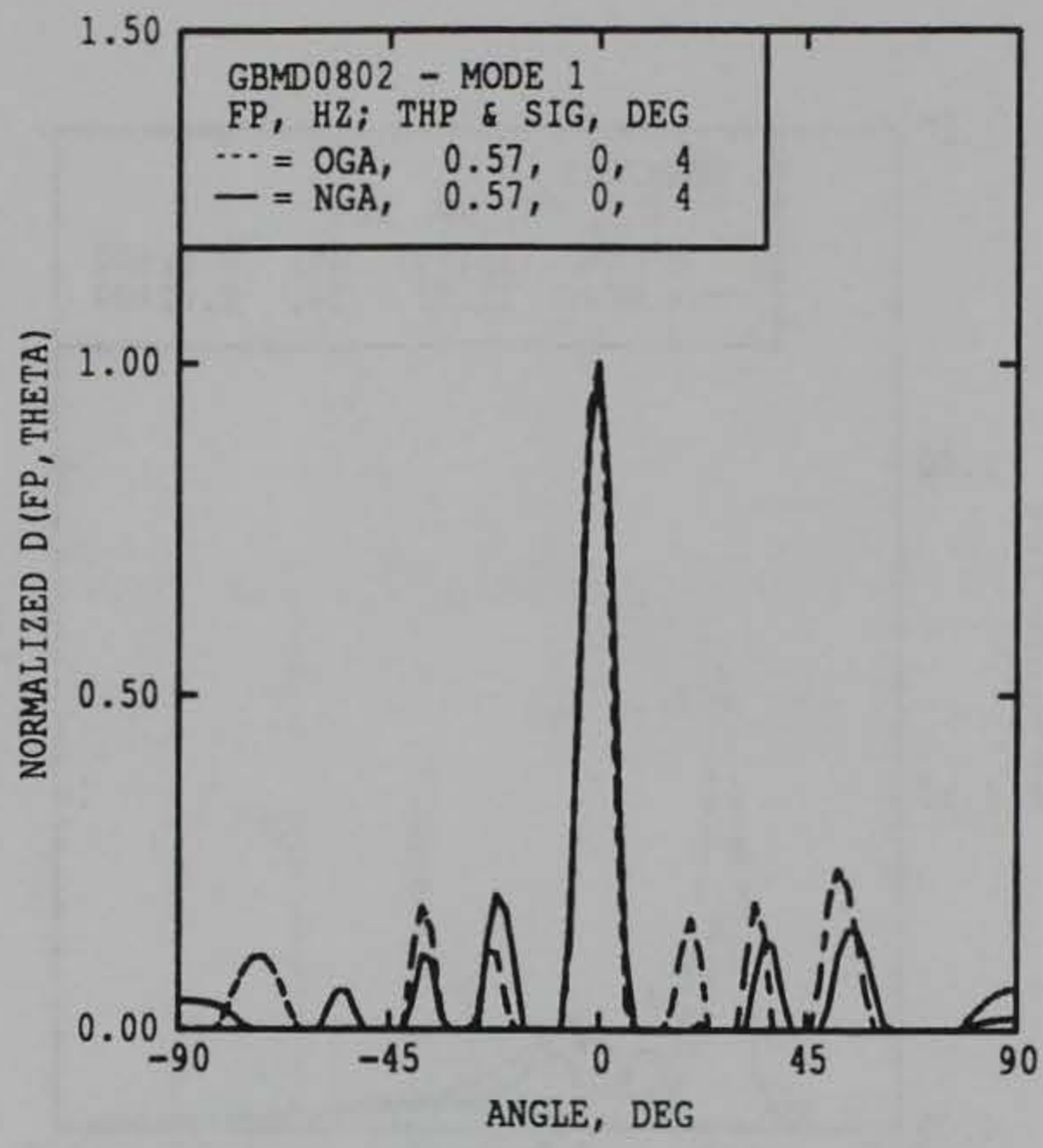

a. Narrow-banded case D08 with 0-deg directional spread

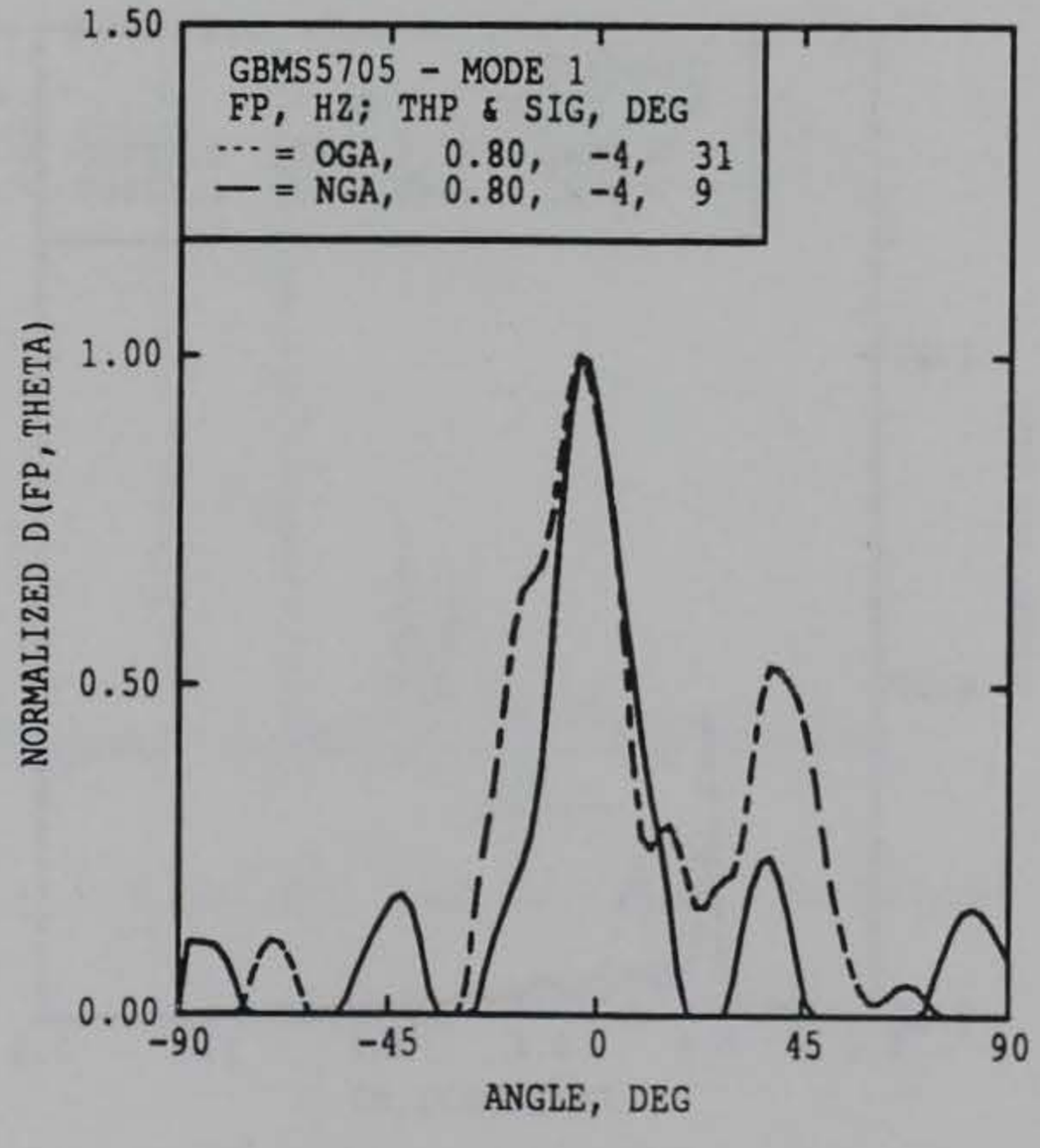

b. Broad-banded case S57 with 40-deg directional spread

Figure 33. Measured directional distribution transformation for unimodal spectra

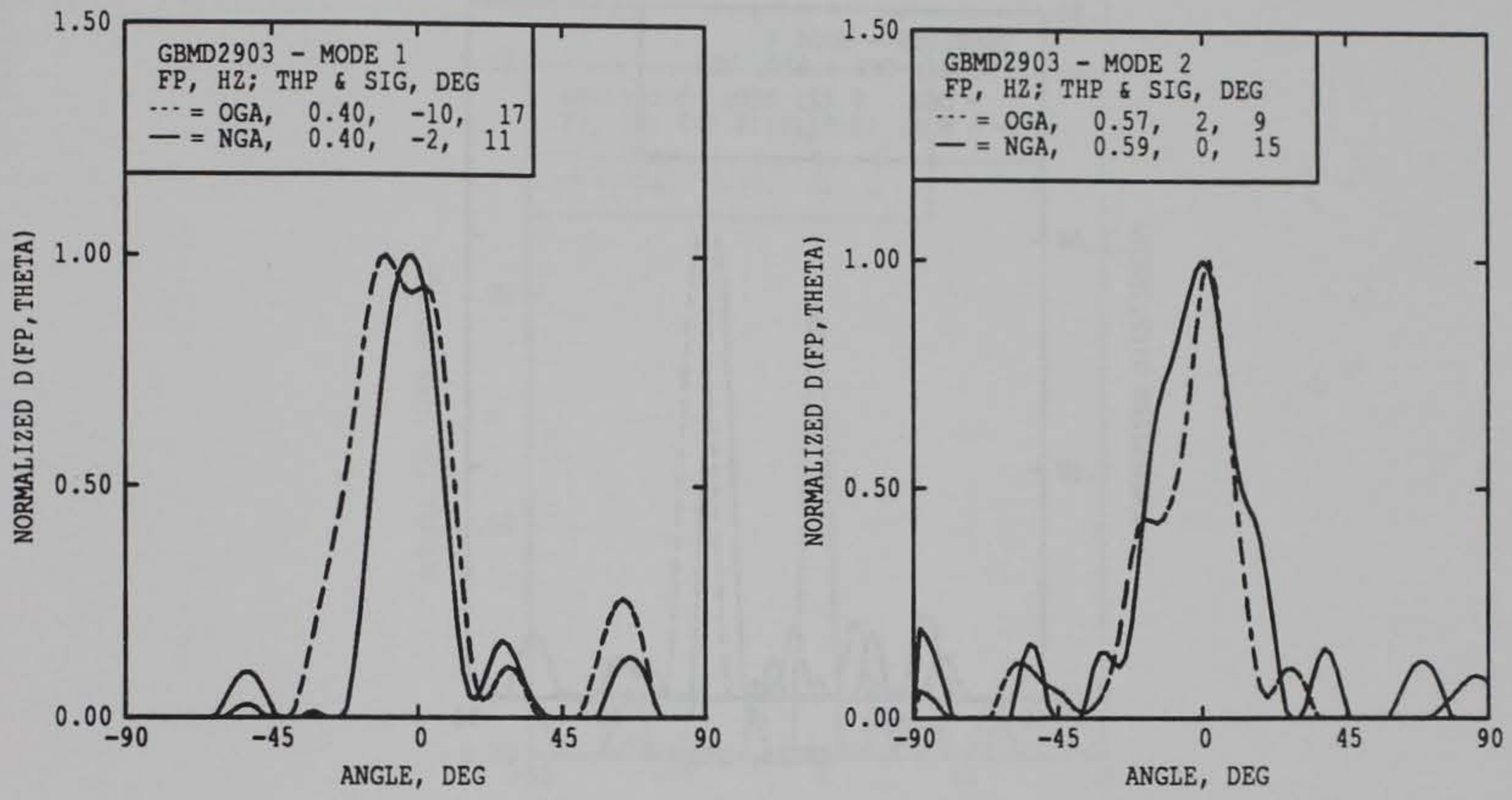

a. Case D29 with first mode dominant

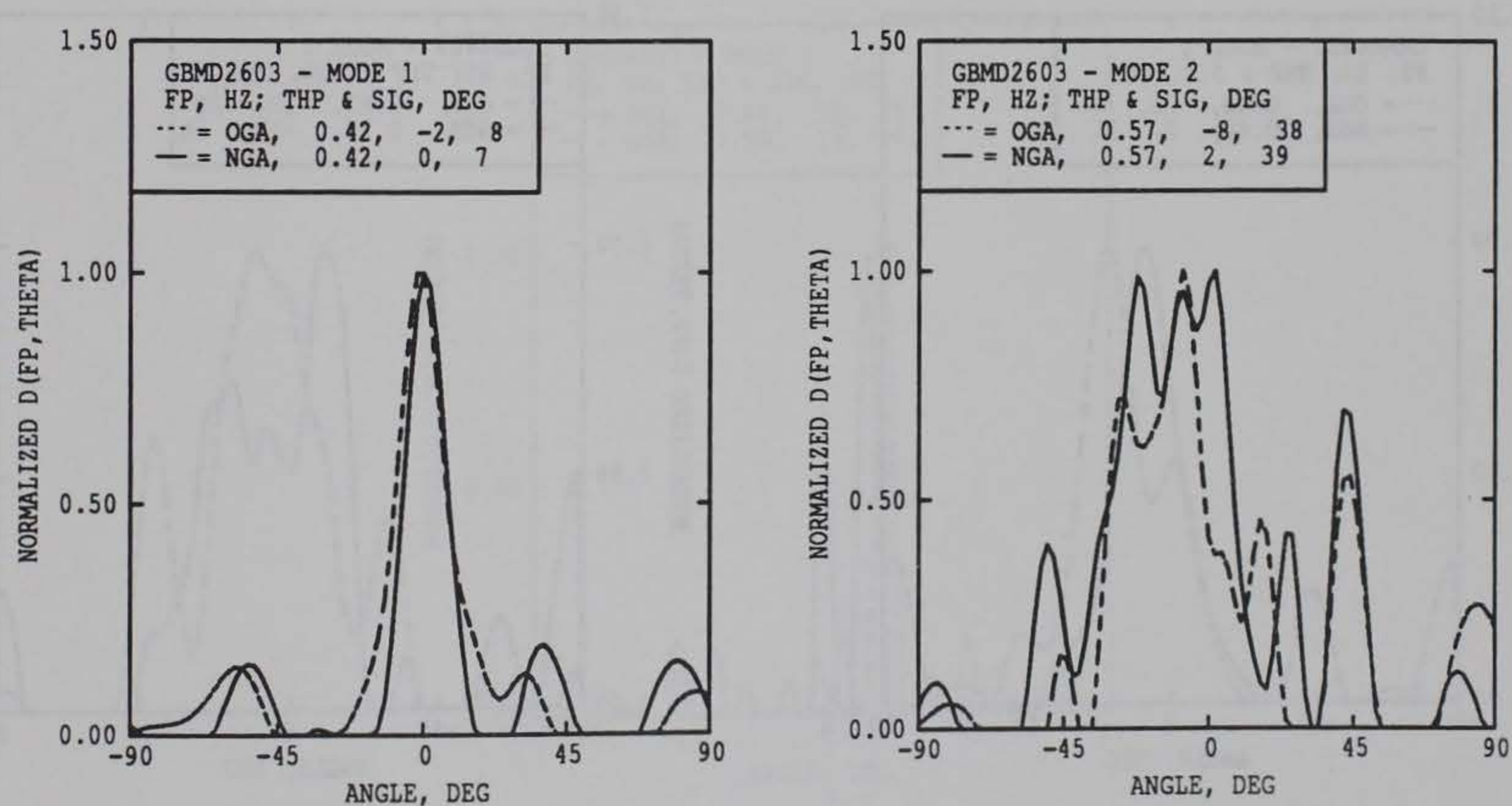

b. Case D26 with equal energy distribution

Figure 34. Measured directional distribution transformation for bimodal spectra

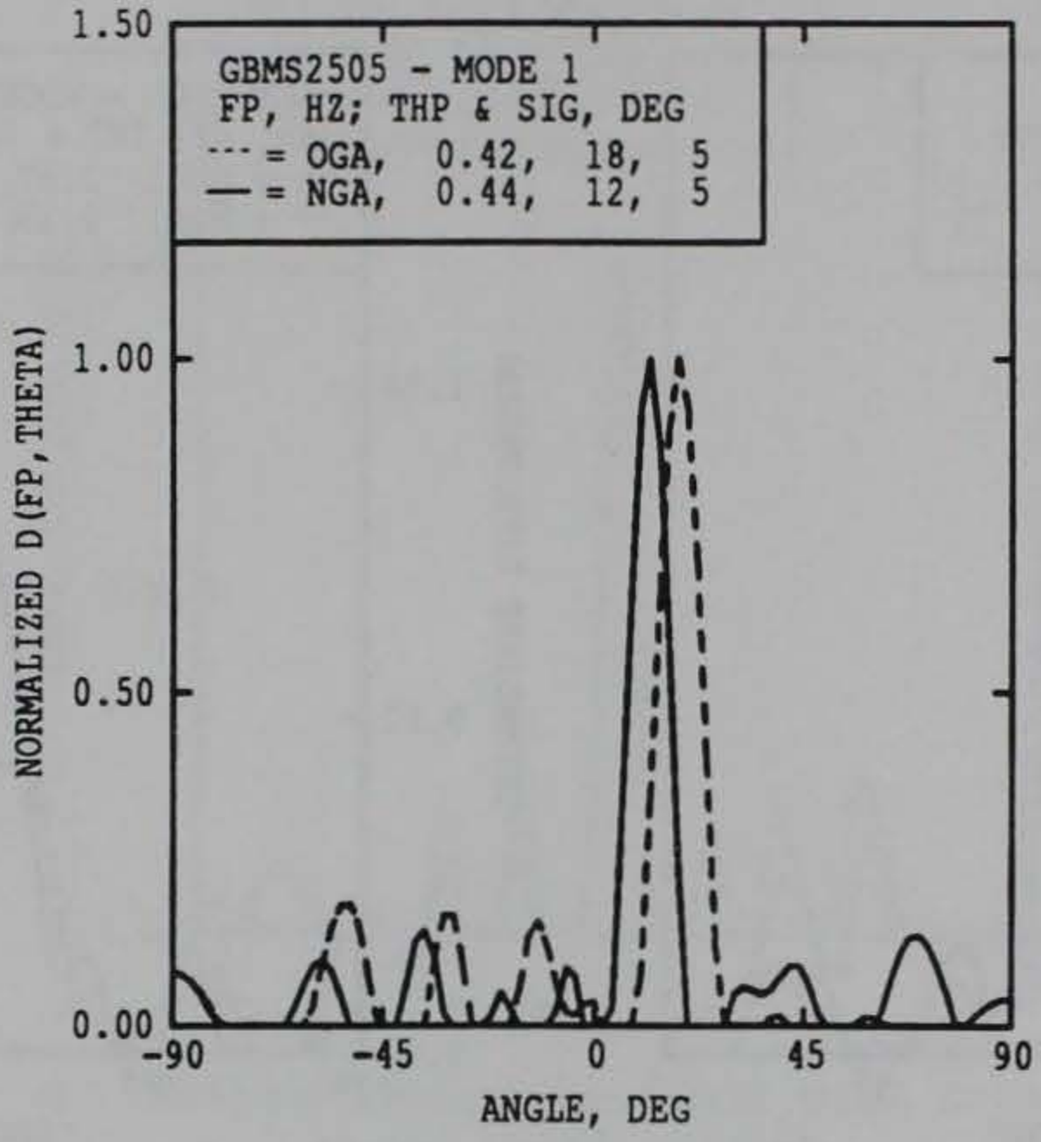

a. Unidirectional case S25

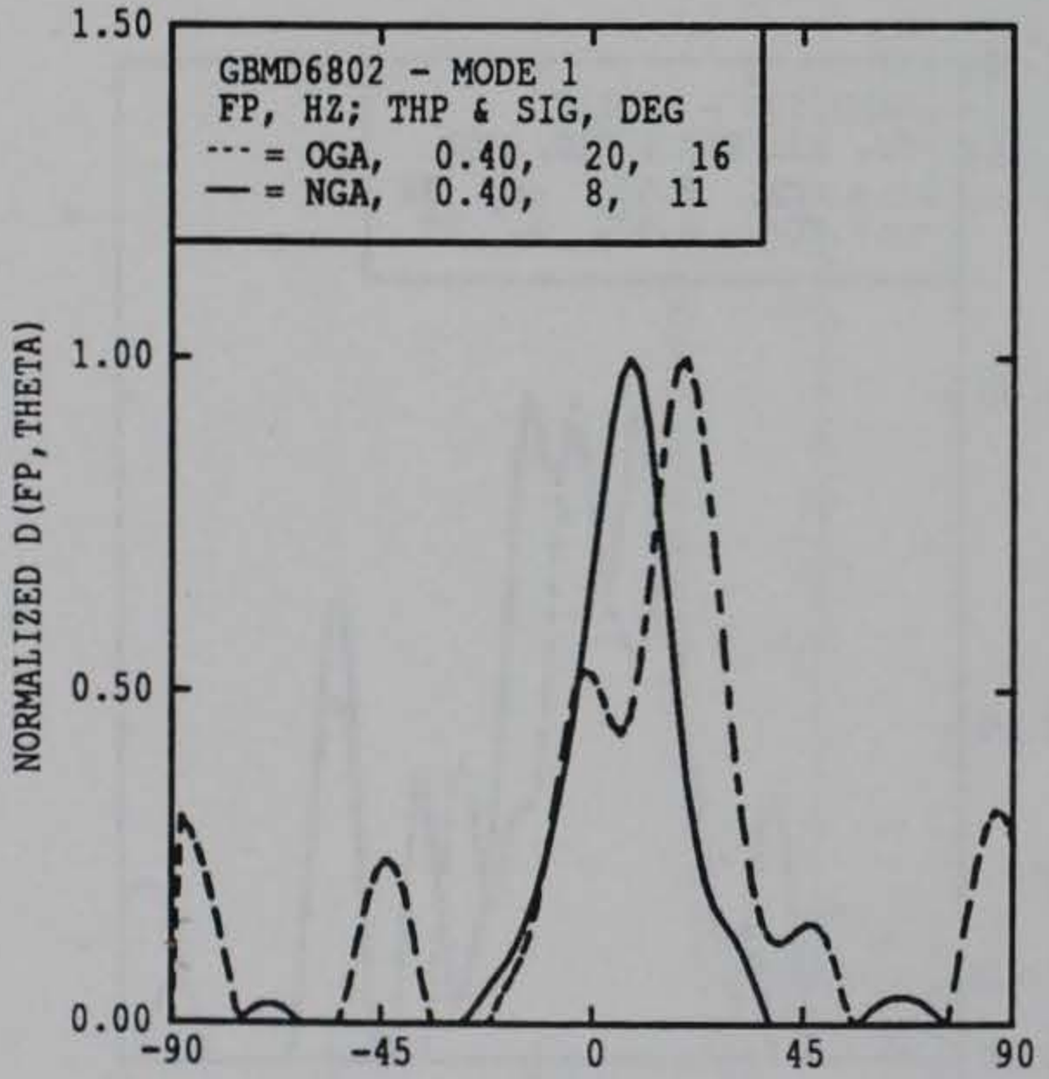

b. Bimodal case D68 with 20-deg Mode 1 wave direction

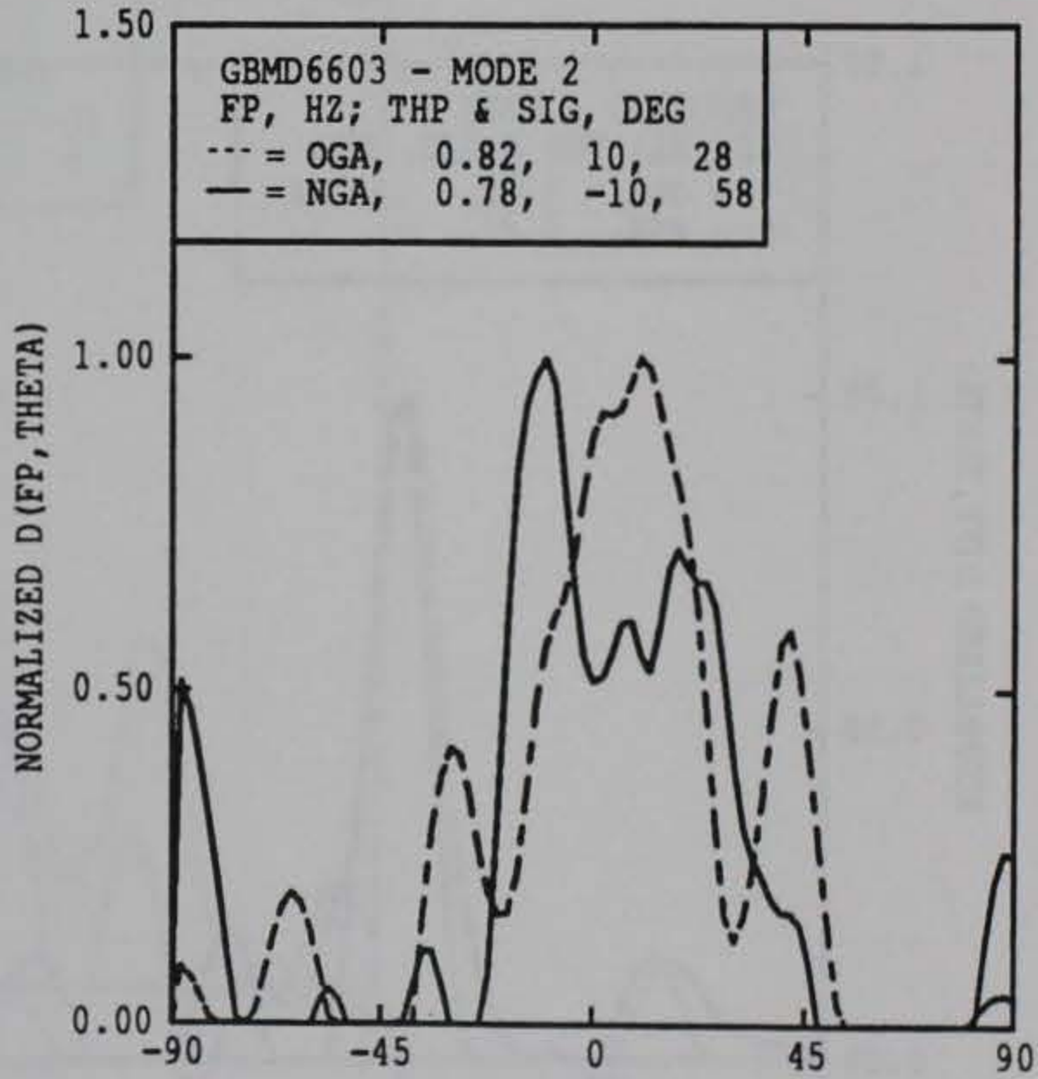

c. Bimodal case D66 with 20-deg Mode 2 wave direction

Figure 35. Wave direction transformation

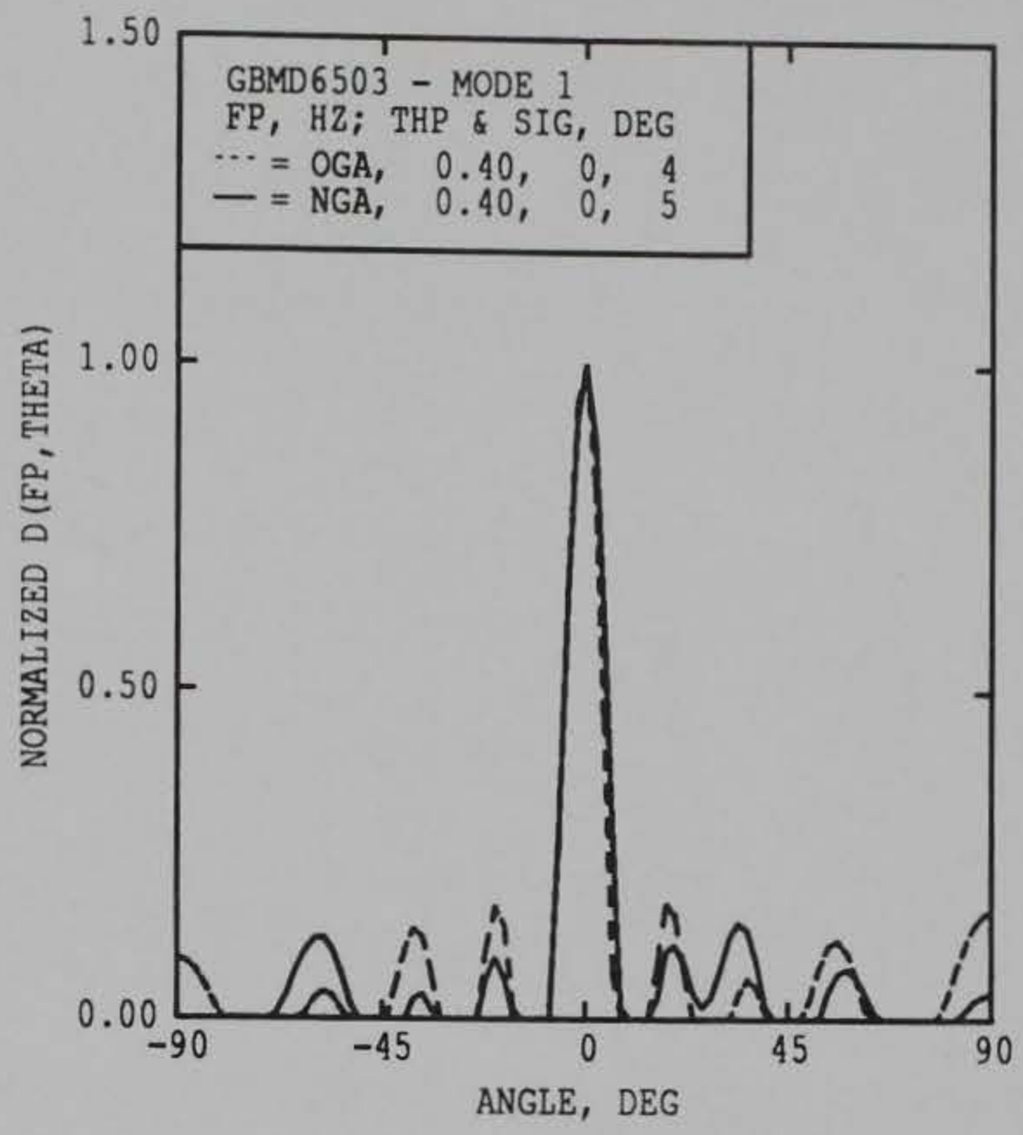

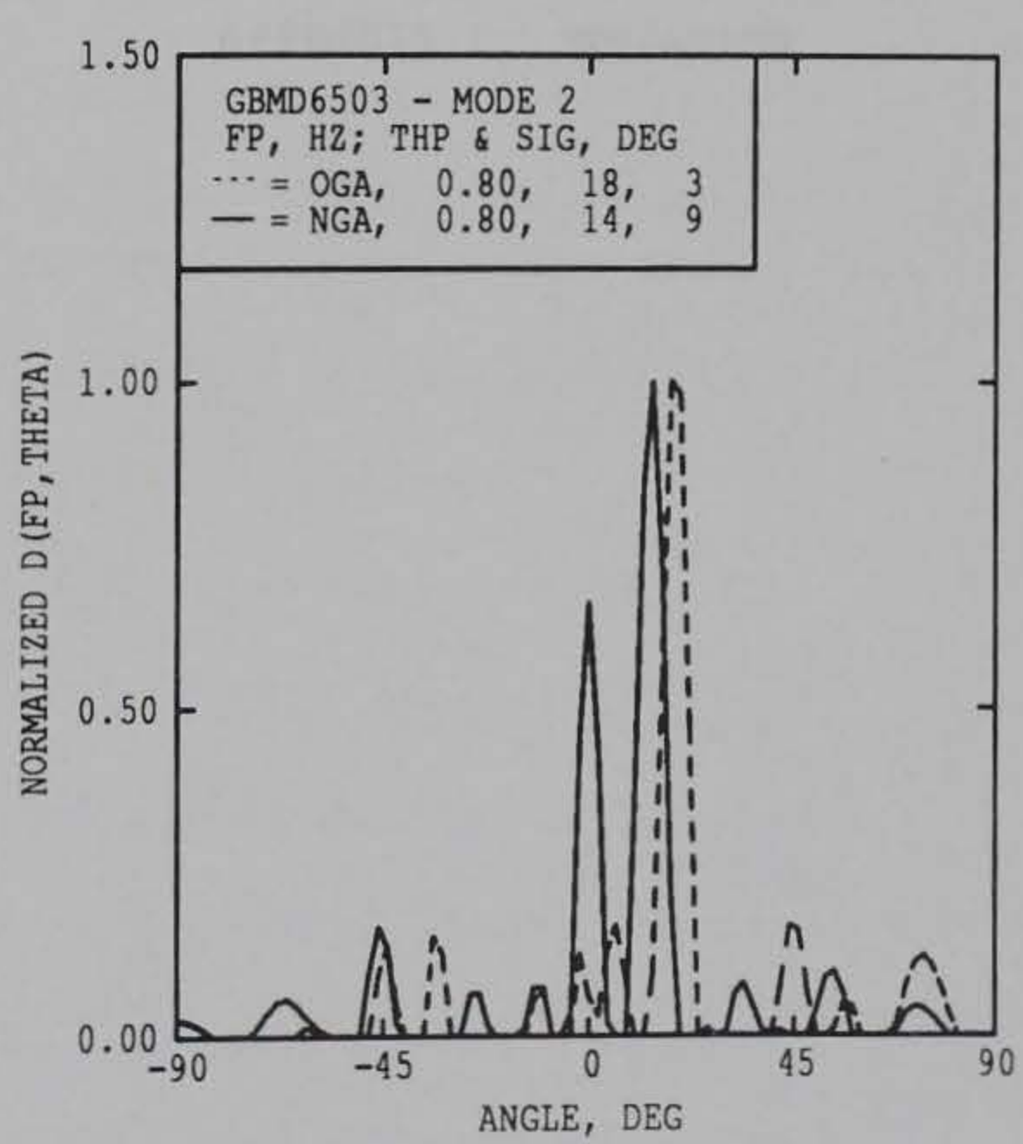

Figure 36. Formation of secondary directional peak, bimodal case D65

APPENDIX A: NOTATION

a_m	Real Fourier coefficient of spreading function
b_m	Imaginary Fourier coefficient of spreading function
B_e	Resolution bandwidth, Hz
$D(f,\Theta)$	Directional spreading function, 1/deg
f	Frequency, Hz
f_l	Lower cutoff frequency, Hz
f_p	Spectral peak frequency, Hz
f_u	Upper cutoff frequency, Hz
h	Water depth, cm
H	Wave height, cm
H_{m0}	Zero-moment wave height, cm
$H_{1/3,d}$	Zero downcrossing significant wave height, cm
$H_{m0,i}$	Zero-moment wave height of mode i, cm
H_σ	Significant wave height, four times standard deviation of the surface elevation time series, cm
L	Number of Fourier series harmonics
N	Number of gages in array
RAO	Response amplitude operator function
$S(f)$	Frequency spectrum, cm^2/Hz
$S(f,\Theta)$	Directional wave spectrum, $cm^2/Hz/deg$
$S_{ii}(f)$	Measured autospectral density for gage i, cm^2/Hz
$S_p(f)$	Predicted frequency spectrum, cm^2/Hz
$S_{200}(f)$	Frequency spectrum for 200 waves at T_p, half duration test, cm^2/Hz
$S_{400}(f)$	Frequency spectrum for 400 waves at T_p, full duration test, cm^2/Hz
$T_{1/3,d}$	Zero-downcrossing significant period, sec

T_p	Spectral peak period, sec
$T_{p,i}$	Spectral peak period of mode i, sec
T_r	Time series duration, sec
x	X-axis coordinate, m Random variable
y	Y-axis coordinate, m
α	Spectral parameter
γ	Spectral peakedness parameter
τ	Peak enhancement factor
Δf	Basic frequency increment, Hz
Δt	Time interval, sec
η	Water surface elevation, cm
$\bar{\eta}$	Average water surface elevation, cm
θ	Wave direction at frequency f , deg
$\bar{\Theta}$	Peak wave direction, overall mean wave direction for all frequencies, deg
$\bar{\Theta}_i$	Mean wave direction of mode i, deg
σ_a	Left spectral width parameter
σ_b	Right spectral width parameter
σ_m	Mean spreading standard deviation
$\sigma_{m,i}$	Directional spread of mode i
σ_n	Standard deviation of surface elevation time series, cm
υ	Degrees of freedom